Wireless Positioning Applications in Multipath Environments

Von der Fakultät für Ingenieurwissenschaften
Abteilung Elektrotechnik und Informationstechnik

der

Universität Duisburg-Essen

zur Erlangung des akademischen Grades

Doktors der Ingenieurwissenschaften (Dr.-Ing.)

genehmigte Dissertation

von

Shangbo Wang

aus

Henan, China

Referent: Prof. Dr.-Ing. Peter Jung
Korreferent: Prof. Dr.-Ing. Klaus Solbach

Tag der mündlichen Prüfung: 18. Juni 2014

Zusammenfassung

In den vergangenen Jahren wurde zunehmend Forschung im Bereich drahtlose Sensornetzwerk (engl. „Wireless Sensor Network“) betrieben. Lokalisierung im Innenraum ist ein vielversprechendes Forschungsthema, das in den Literaturen vielfältig diskutiert wird. Jedoch berücksichtigen die meisten Arbeiten einen wichtigen Faktor nicht, nämlich die Mehrwegeausbreitung, welche die Genauigkeit der Lokalisierung beeinflusst. Diese Arbeit bezieht sich auf Lokalisierungsanwendungen in UWB (Ultra-Breitband-Technologie)- und WLAN (drahtloses lokales Netzwerk)- Systemen im Fall von Mehrwegeausbreitung.

Zur Steigerung der Robustheit der Lokalisierungsanwendungen bei Mehrwegeausbreitung wurden neuartige Lokalisierungsalgorithmen, die auf der Auswertung der Ankunftszeit (engl. „Time of Arrival“, ToA), der empfangenen Signalstärke (engl. „Received Signal Strength“, RSS) und dem Einfallswinkel (engl. „Angle of Arrival“, AoA) basieren, vorgestellt und untersucht. Bei Mehrwegeausbreitung ist die Fragen den direkten Pfad zu lösen, da der direkte Pfad (engl. „Direct Path“, DP) schwächer als anderer Pfad sein kann. In dieser Arbeit werden daher neuartige Algorithmen zur Flankendetektion der empfangenen Signale für UWB Systeme entwickelt, um die Positionsbestimmung zu verbessern: Es gibt die kooperative Flankendetektion (engl. „Joint Leading Edge Detection“, JLED), die erweiterte maximalwahrscheinlichkeitbasierte Kanalschätzung (engl. „Improved Maximum Likelihood Channel Estimation“, IMLCE) und die Flankendetektion mit untervektorraumbasiertem Verfahren (engl. „Subspace based Approaches“, SbA).

Bei der kooperativen Flankendetektion werden zwei Kriterien herangezogen nämlich die minimale Fläche und das minimale mittlere Quadrat des Schätzfehlers (engl. „Minimum Mean Squared Error“, MMSE). Weiterhin wird ein monopulsbasierter Kanalschätzer (engl. „Monopulse based Channel Estimator“, MCE) entwickelt, um die möglicherweise falsche Kombinationen der Flanken (engl. „Leading Edge Combination“, LEC) auszuschließen. Zudem wird in der Arbeit der erweiterte MLCE vorgestellt, der aus einem groben und einem genauen Schätzungsschritt besteht.

Bei dem neuartigen untervektorraumbasierten Verfahren werden ein statischer und ein Schwundkanal untersucht. Im ersten Fall wird die Kombination der Rückwärtssuchalgorithmus mit untervektorraumbasierten Verfahren untersucht. Zudem wird im zweiten Fall ein untervektorraumbasierte Verfahren im Frequenzbereich vorgestellt.

Für die RSS-basierte Lokalisierung wird ein Fingerabdruckverfahren (engl. „Fingerprint Approach“) und ein neuartiger Entfernungsschätzer basierend auf der Kanalenergie entwickelt und implementiert.

Schließlich wird in der Arbeit ein Lokalisierungssystem mit Winkelschätzern inklusive einer entsprechenden Kalibrierung auf einer 802.11a/g Hardwareplattform vorgestellt. Dazu wird ein neuartiger Trägerschätzer und Kanalschätzer entwickelt.

Abstract

In the past several years there has been more growing research on Wireless Sensor Network (WSN). The indoor localization is a promising research topic, which is discussed variously in some literatures. However, the most work does not consider an important factor, i.e. the multi-path propagation, which affects the accuracy of the indoor localization. This work dealt with the indoor localization applied in UWB (Ultra Wide Band) and WLAN (Wireless Local Area Network) systems in the case of multi-path propagation.

To improve the robustness of the applications of localization in the case of multi-path propagation, novel localization algorithms based on the evaluation of the Time of Arrival (ToA), the Received Signal Strength (RSS) and the Angle of Arrival (AoA) were proposed and investigated. In the ToA based localization systems, the detection of shortest signal propagation time plays a critical role. In the case of multi-path propagation, the Direct Path (DP) needs to be resolved because the DP may be weaker than Multi Path Components (MPC). Thus the novel algorithms for leading edge detection were developed in this work in order to improve the accuracy of localization, namely Joint Leading Edge Detection (JLED), Improved Maximum Likelihood Channel Estimation (IMLCE) and the leading edge detection with Subspace based Approaches (SbA).

Two criteria were proposed and referenced for the JLED, namely Minimum Area (MA) and Minimum Mean Squared Error (MMSE). Furthermore, a monocycle-based channel estimator was developed to mitigate the fake LECs (Leading Edge Combination). The estimation error of JLED was theoretically analyzed and simulated for evaluation of the estimator. IMLCE consists of a coarse and a fine estimation step. The coarse position of the first correlation peak shall be found with the Search Back Algorithms (SBA), which is followed by MLCE-algorithms.

The novel SbA was investigated in a static and a fading channel. In the former case, the iterative algorithm, which combines SbA with SBA, was investigated. In the latter case, the FD-SbA (Frequency Domain - SbA) was proposed, which requires to calculate the covariance matrix in the FD.

For the RSS based localization, fingerprint approach and the novel channel energy based distance estimator were investigated and developed in this dissertation.

Finally, a localization system using AoA estimation and the initial calibration was presented on an 802.11a/g hardware platform. A novel Carrier Frequency Offset (CFO) estimator and channel estimator were investigated and developed. The measurement campaigns were made for one, two and four fixed stations, respectively.

Danksagung

"*Es ist absolut möglich, daß jenseits der Wahrnehmung unserer Sinne ungeahnte Welten verbogen sind*" – Albert Einstein

Die vorliegende Arbeit entstand im Rahmen meiner Tätigkeit als wissenschaftlicher Mitarbeiter am Lehrstuhl für Kommunikationstechnik der Fakultät für Ingenieurwissenschaften der Gerhard Mercator Universität Duisburg und als Doktorand an der Abteilung CT RTC ELE RFT-DE der Siemens AG.

Herrn Prof. Dr.-Ing. habil. Peter Jung, dem Leiter des Lehrstuhls für Kommunikationstechnik der Fakultät für Ingenieurwissenschaften der Universität Duisburg-Essen, danke ich herzlich für die engagierte Betreuung der vorliegenden Arbeit. Seine zahlreichen Anregungen und Vorschläge sowie seine stete Unterstützung bei der Bearbeitung der Aufgabenstellung trugen wesentlich zur Erstellung der vorliegenden Arbeit bei.

Weiterhin danke ich allen meinen Kolleginnen und Kollegen im Lehrstuhl für Kommunikationstechnik und in der Abteilung CT RTC ELE RFT-DE der Siemens AG für die sehr angenehme Arbeitsatmosphäre und die ausgezeichnete Zusammenarbeit. Insbesondere möchte ich mich bei den Dr. –Ing. Guido. H. Bruck, Andreas Waadt, Wei Chen, Dr. –Ing Jörg Hüttner, Dr. –Ing Andreas Ziroff, Markus Kaiser für ihre Hilfe, fachlichen Diskussionen und Anregungen bedanken.

Dank gilt allen Studierenden, Praktikanten deren Arbeiten zur Entstehung dieser Arbeit beitrugen.

Schließlich bedanke ich mich bei meiner Eltern und bei allen meinen Freunden für ihr Verständnis und ihre Unterstützung während der Fertigstellung dieser Arbeit.

Contents

1 Introduction

1.1 Motivation

Location Tracking (LT) applications and Quality of Service (QoS) parameter optimization in networks have become a hot research issue in the recent years. The most commonly available localization technology today is the Global Position System (GPS), which consists of 24 satellites in six orbital planes with four satellites in each plane [13]. The Standard Positioning Service (SPS) of GPS as a kind of real-time positioning system in the outdoor environment can achieve an accuracy of approximately 10m. However, the signals from GPS satellites are too weak to penetrate the buildings which are constructed from metal, concrete, etc. [13]. Hence, GPS is not an ideal candidate for the localization in the indoor environments. With the increase of economy and technologies, more Location Based Services (LBS) in the indoor environments such as objection positioning in warehouses, localization of exhibition items in museums, patients and nurses localization in hospital, position tracking of a robot's pose, etc. have taken place and are paid great research efforts. Indoor positioning technology can be roughly divided into two categories: radio positioning, which includes Radio-Frequency IDentification (RFID), Wireless Local Area Network (WLAN) and Ultra-Wideband (UWB), and non-radio positioning, which includes video cameras (optical), infrared, ultrasound [17]. RFID devices are attached to persons or to moveable objects so that the persons or objects can be tracked using fixed readers at different locations [18]. The disadvantages of RFID localization systems are the requirement of a large number of precoded RFID tags and the low localization accuracy (3-5m) [18]. Ultrasonic localization systems use ultrasonic waves to measure the distance between a fixed point station and the mobile station whose position shall be determined [18]. In the ultrasonic localization systems, the distance measurements can be disturbed by the multipath reception due to the extremely narrow signal bandwidth [18]. Localization using pulse-width modulated infrared signals in Non-line-of-sight (NLOS) and multipath environments has a low performance because infrared cannot penetrate obstacles.

To achieve better localization accuracy with relative lower hardware and software complexity in a multipath environment, UWB positioning systems have become a hot research issue in recent years. UWB is an excellent signaling choice for relatively high accuracy localization in short to medium distances due to its high time resolution and inexpensive circuitry [4]. It can also be considered as a unique signaling choice for short-range communication such as in WSNs [4]. The potential of UWB for high precision ranging, its possible applications and implementation process were extensively discussed and documented in IEEE 802.15.4a, on which the Low-Data-Rate (LDR) UWB was standardized [4][22]. Some of the UWB applications, localization range and their accuracy requirements are displayed in Table 1.1 to Table

1.4. From the four tables, it can be seen that UWB should be an excellent technology that can achieve sub-meter accuracy with the localization range smaller than 300m [4]. Due to the transmission range of UWB signal, the larger localization range requires the more UWB nodes in Wireless Sensor Networks (WSN).

Table 1.1: Key RTLS applications, ranges and accuracy requirements [6]

Core Real Time Location System (RTLS) applications	**Range**	**Accuracy Requirements**
High value inventory items (warehouses, ports, motor pools, manufacturing plants)	100-300m	30-300cm
Sports tracking (NASCAR, horse races, soccer)	100-300m	10-30cm
Cargo tracking at large depots including port facilities	300m	300cm
Vehicles for large automobile dealerships and heavy equipment rental establishments	100-300m	300cm
Key personnel in office/plant facility	100-300m	15cm
Children in large amusement parks	300m	300cm
Pet/cattle/wild-life tracking	300m	15-150cm

Table 1.2: Some non-commercial markets [6]

Non Commercial Market	Range	Accuracy Requirements
Robotic mowing and farming	300m	30cm
Supermarket carts	100-300m	30cm
Vehicle caravan	300m	30cm

Table 1.3: Some military applications [6]

Military Applications	Range	Accuracy Requirements
Military training facilities	300m	30cm
Military search & rescue: lost pilot, man-over-board, Coast Guard rescue operations	300m	300cm
Army small tactical unit "friendly forces" situational awareness-rural and urban	300m	30cm

Table 1.4: Main safety applications [6]

Civil Government / Safety Applications	Range	Accuracy
Tracking guards & prisoners	300m	30cm
Tracking firefighters and emergency responders	300m	30cm
Anti-collision system: aircraft / ground vehicles	300m	30cm
Tracking miners	300m	30cm

Aircraft landing systems	300m	30cm
Detecting avalanche victims	300m	30cm
Locating RF noise and interference sources	300m	30cm
Extension to LoJack vehicle theft recover system	300m	300cm

It has to be noted that the localization range of almost all applications has reached 100m, which requires the higher transmission power. During the development efforts for the US Navy, Multispectral Solutions, Inc. (MSSI) developed a spectrally-confined high power UWB transceiver which can achieve a communication range of 1km [44]. To adapt to the requirements of market, a number of UWB positioning products have been already developed. Some of the products and their available UWB localization technologies are listed in Table 1.5.

Table 1.5: Current UWB localization products [109][110][111]

Companies and Products	**Localization Technologies**	**Accuracy**
Ubisense	TDoA and AoA	30cm
Zebra Technologies (PAL650)	TDoA	up to 30.5cm
Zebra Technologies (Sapphire DART UWB)	TDoA	up to 30cm
Aetherwire	ToA	As low as centimeter accuracy

The Ubisense product is a small tag worn by a person or attached to an asset allowing it to be accurately located within an indoor environment. The PAL650 and Sapphire DART UWB systems are from MSSI, which has belonged to Zebra Technologies since 2007. Table 1.5 shows that the most UWB localization products utilize the ToA (Time of Arrival) or TDoA (Time Difference of Arrival) based localization techniques, which have the highest precision potential in comparison with RSS (Received Signal Strength) and AoA (Angle of Arrival). The reason is that the UWB signal has a very large bandwidth which can provide an extremely fine time resolution.

The most of aforementioned application scenarios and the products are required to work in harsh environments, which mean that the signal shall be transmitted through dense multipath environments and Line of Sight (LoS) may suffer from blockage and reflection. Meanwhile, the log-normal fading and multipath reception can negatively influence the localization accuracy. Nowadays, high localization accuracy is still an ambitious goal in such environments. Multipath propagation introduces challenges for UWB ranging due to a large number of Multipath Components (MPC) and relatively long excess delay compared to the transmitted pulse duration [4]. In practice, reflections from scatters in an environment arrive at a receiver as replicas of the transmitted signal with various attenuation levels and delays [4]. The maximum excess delay of the received multipath signal can be on the order of a hundred nanoseconds, and the strongest MPC may arrive much later than the first path [4]. For such a signal, the ToA or TDoA is no longer given by the maximum correlation peak. Hence, it is essential to investigate novel approaches featuring good performance in harsh environments.

Sampling rate is another key factor to determine the localization performance. Due to the extreme large bandwidth of UWB signal, the receiver sampling rate shall be large enough to provide a good localization performance. However, extreme high sampling rate is hardly realized due to the limitation of ADC (Analog Digital Converter). How to achieve acceptable localization accuracy with nyquist sampling rate even sub-nyquist sampling rate becomes a challenge issue.

Tracking as a real-time localization has become a hot research direction since there are more and more needs for indoor real-time LT systems to track people with special needs, e.g., the patients in hospital, the children who are away from the visual supervision [1]. In public safety and military applications, LT systems are used to track inmates in prisons and to guide policeman, firefighters, and soldiers in accomplishing their missions inside buildings [1]. Theoretically, the Kalman Filter can yield the optimal solution to the tracking problem for linear state and measurement equations. However, non-linear relations between the position of the target and the measurements let the Kalman filter not be implemented in many practical situations. Target tracking via Doppler spread may be another solution.

Although RSS-based LT cannot provide high accuracy in Impulse Radio (IR) UWB system in comparison with ToA/TDoA, it does not require clock synchronization among UWB receivers, which can decrease complexity of system design. Hence, it is clever idea to employ the RSS-based LT approaches to the LBS with low accuracy requirements (see Table 1.1).

Due to the wide deployment of WLAN equipment in indoor environment, there are many indoor LBSs which can also use WLAN signal to localize the object. Although Orthogonal Frequency Division Multiplexing (OFDM) exploited by WLAN systems has the narrowband characteristic which leads to lower localization accuracy in comparison with UWB, WLAN-based localizations have following advantages [19].

1. Ubiquitous coverage and scalability: The wireless network infrastructure already exists in many public places such as universities, corporations, airports, and shopping malls, providing a ubiquitous coverage.
2. No additional hardware required: Localization can be done by a software only method, thereby eliminating the need of for additional hardware. Hence there is no extra cost.
3. Extended range: Compared to other radio technologies, the range covered by WLAN is larger.
4. No LoS restrictions: Unlike the infrared localization systems, WLAN is not restricted to LoS.

However, there is little research about indoor localization using WLAN signal in the harsh environments.

The unreliability of state-of-the-art UWB and WLAN localization methods in harsh environments and the need for more accurate position location systems with low complexity motivate the research in this thesis.

1.2 State-of-the-art Localization Techniques

This section is to review the state-of-the-art localization techniques with the emphasis on their drawbacks in multipath environments. The current positioning techniques can be mainly classified into two categories: geometric localization and location fingerprinting. The former consists of two steps. First, signal metrics (ToA/TDoA, RSS, AoA) depending on the relative positions of AP (Access Point) and the target shall be extracted from the received signal via certain algorithms. For the next step, the position of the target shall be determined by the signal metrics via multi-lateration or multi-angulation [7][8]. One of the known multi-lateration is LS (Least Squares) algorithms, which are well understood and easily implemented on the hardware. The mathematical description of the multi-lateration via LS can be found in the section 2.3.2. In general, the accuracy of the geometric localization is determined by the following factors: SNR (Signal-to-Noise-Ratio) at the receiver, sampling rate, the propagation environment, number of APs, placement of array and estimation algorithms. It is clear that higher SNR can provide a better estimation for signal metrics. In a specific environment, the receiver SNR can only be improved via the spread spectrum technique or matched filter. In [10] and [11], the authors discuss the

CRLB (Cramer Rao Lower Bound) for joint AoA and ToA estimation in DS-CDMA (Direct-Sequence Code Division Multiple Access) systems. Despite higher sampling rate can achieve a better performance, high sampling cannot be considered as an appropriate strategy for the UWB localization because high sampling rate is not easily be implemented on the hardware. [84] and [86] introduces sub-sampling mixer, which can achieve a remarkable good performance with a reduced sampling rate. However, such sub-sampling mixer utilizes a broadband balun structure, which requires extra hardware infrastructure. The effects of number of APs and the placement of array on localization performance are discussed in [12]. The first-order and second-order error are analyzed for WLSE (Weight Least Squares Estimation) and MLE (Maximum Likelihood Estimation). The theoretical analysis and simulation results show that the localization accuracy can be improved with large number of APs and optimum placement of sensor array. In practice, however, equipping with large number of APs becomes unrealizable as more hardware and software are required. The propagation environment and the employed estimation algorithms play an essential role on the localization. In general, if the propagation channel has a strong LoS component, geometric position location techniques show a remarkable good performance. One of the important issues is to estimate signal metrics under the case that the NLoS component is stronger than LoS defined as harsh environment. The description of such scenario and its effect can be found in chapter 2. The key issue to localize the target in the harsh environment is to find leading edge of the receiving signal. Table 1.6 shows some important publications about leading edge detection in the harsh environments.

Table 1.6: Overview of publications for ToA/TDoA estimation

Citation	Main Content
[25] and [26]	● Time Delay and Path Amplitude estimation using LS method ● The number of paths is assumed to be known
[27] and [32]	● Time Delay estimation using ML method ● The number of paths is assumed to be known
[31]	Leading edge detection via coarse acquisition of PN codes
[33]	Leading edge detection via *single search, search and subtract, threshold and search*, *search subtract and readjust* algorithms
[34], [36] and [37]	Leading edge detection via GLRT (Generalized Likelihood Ratio Test)
[35] and [38]	Noisy template based timing acquisition
[81] and [82]	ToA estimation via search-back algorithms
[83]	Iterative peak subtraction
[85]	Matched Filter (MF) and first peak detection

In [25], [26], [27] and [32], the Least Squares (LS) and Maximum-Likelihood (ML) estimation of signal arriving time are discussed, respectively. The leading edge detection via LS followed by the Gauss-Newton algorithm is introduced in [25] and [26]. In [25], several different search methods are compared to Gauss-Newton algorithm including Coordinate Descent (CD) and linear prediction. The drawbacks mentioned in [25] are discussed and overcome in [26]. Time delay estimation using ML method is generally discussed in [27]. In [32], the ToA estimation for UWB signals in a dense multipath environment via ML method is investigated in both data-aided (DA) and non-data-aided (NDA) scenarios. However, aforementioned four literatures investigate the LS and ML only under the assumption that the number of paths in the multipath environments is known. In addition, the ML estimator cannot be directly implemented in practice because ML estimator has high computational complexity if the number of paths is large.

In [31], the data-aided coarse acquisition of pseudo noise (PN) codes is addressed. The time acquisition algorithm detects the presence of synchronization sequence by computing correlations with the expected PN sequence, for each position in the observation window, and comparing the maximum value with a threshold.

Unfortunately, it only achieves chip-level accuracy. To achieve better accuracy, shorter UWB monocycle shall be employed.

A frame-level blind timing acquisition algorithm is developed in [38]. The blind time acquisition algorithm requires no extra reference signal but a segment from the received signal as the dirty template. The blind time acquisition proposed in [38] can reduce the algorithm complexity. However, it can only achieve frame-level resolution. In [35], timing acquisition with dirty template is investigated in DA and NDA scenarios.

The leading edge detection via "single search, search and subtract, search subtract and readjust, threshold and search" algorithms are discussed and compared in [33]. These four algorithms are based on ML criterion, which has been discussed in [27] and [32].

In [34], the leading edge detection using Generalized Likelihood Ratio Test (GLRT) is investigated for Code Division Multiple Access (CDMA) systems. The GLRTs are employed to detect the UWB signal propagating through dense multipath and to estimate the associated timing in [36] and [37]. The complexity of hardware design is reduced by the symbol-rate sampling. However, only the frame-level timing acquisition can be achieved.

The ToA estimation using threshold-based energy detector is investigated in [81] and [82]. Based on the output of the energy detector, the search-back and threshold algorithms are used to estimate the first arrival. The simulation results in [81] show that the sub-meter ranging accuracy can be achieved. [83] introduces the iterative peak subtraction algorithms, which subtract multipath peaks from the received multipath signal using a clean template to obtain an accurate estimation of the first peak. However, [83] does not consider the pulse distortion and overlapping caused by the multipath effect.

It has to be noted that the aforementioned detection approaches do not consider the fading effect of the UWB channel. The description of large-scale and small-scale fading effect can be found in [19]. Generally, indoor UWB channel suffers from a log-normal fading effect, which leads to a variation of the local mean around the path loss [19]. The Matched Filter (MF) and ML based detectors will give erroneous results at the presence of such impact. In many case, the leading edge detection must be accomplished in low SNR environments, which make the design of the detection algorithm even more challenging. The cooperative localization method as an alternative research direction has been studied in [1]. The cooperative localization

using Wireless Sensor Networks (WSNs) requires the ranging information exchange between transponder and receiver or more than two receivers, which can increase network overhead. How to reduce the network overhead and simultaneously maintain the localization performance becomes a research issue.

Tracking performance depends on the mobility speed and the scanning time window at the receiver. Table 1.7 shows some important publications about UWB indoor tracking systems.

Table 1.7: Overview of publications for UWB indoor tracking

Citation	Main Content
[45]	Bias Tracking via MEKF (Modified Extended Kalman Filter) and MRPF (Modified Regularized Particle Filter)
[46] and [47]	Kalman filter with TDoA estimates
[48]	Tracking with RD (Range-Doppler) processing

In [46] and [47], a prototype UWB tracking system under development at the National Aeronautics and Space Administration (NASA)-Johanson Space Center was described. TDOA estimates are passed to a Kalman filter to upadate the current estimate of the position. The simulation results showed that Root Mean Squared Error (RMSE) achieved approximate 1.76m for the tracking range of 100m. [45] proposed to use modified extended Kalman Filter (MEKF) and the modified regularized particle filter (MRPF) to track large biases affecting estimated radiolocation metrics. Using the MEKF and MRPF is to process the nonlinearity of the radiolocation metrics. MRPF and MEKF are described in [49] and [50]. The Doppler spread is utilized in [48] to determine the radial component of the target velocity and the direction of motion.

In general, RSS-based LT contains two specific arts. The first one is path-loss based approach which estimates the RSS from the path-loss model. The second one is location fingerprinting technique. The former method has been discussed in [53], in which the RSSID (Received Signal Strength Indicator Difference) from three UWB nodes are exploited to perform localization procedure. [52] simulates the relation between transmission distance and the RSS for different channels in multiband OFDM UWB. Both [52] and [53] require the given path-loss model, which will be given in the subchapter 3.4.2. In practice, the deterministic path-loss propagation model shall be determined through the measurement campaign before the localization process is performed. The second approach has been discussed in [54]. However, there exist few researches on physical-layer based fingerprinting approach for UWB

systems. Especially in harsh environments, the determination of decay exponent for path loss model is even more challenging and signal arriving time cannot be accurately measured. Location fingerprinting may become the promising alternative LT approach. In [54], Channel Impulse Response (CIR) and signal energy are estimated and served as location fingerprints. For the CIR approach, the location fingerprinting systems can benefit from dense multipath propagation because the location fingerprints at different agent position become more distinct [54]. However, the deterministic formulation is not applicable to location fingerprints related to CIRs because wideband CIRs are very sensitive to the small scale effects. Table 1.8 shows several important literatures about the RSS-based localization in UWB systems.

Table 1.8: Several literatures about RSS/fingerprinting -based UWB localization

Citation	Main Content
[52] and [53]	Localization using the given path-loss model and the RSS measurements.
[54]	RSS-based location fingerprinting and CIR-based location fingerprinting

If there are more than one UWB mobile nodes whose position requires being determined simultaneously, the effect brought from Multi User Access (MUA) should be considered. There are many MUA mechanisms for localization. Orthogonal channels can be assigned in time, frequency, code or space domains [4]. In ad-hoc UWB networks, the most popular MUA technique is the Carrier Senses Multiple Accesses (CSMA). In CSMA, only a single user is allowed to access the channel within a certain time period [4]. However, CSMA mechanism needs the cooperation from each UWB mobile node. In DS-CDMA and THMA (Time-Hopping Multiple Access) UWB networks, each mobile node will be assigned a unique Pseudo Noise (PN) code and a unique time hopping code to spread its data, respectively. The performance of receiver depends strongly on the autocorrelation and cross correlation characteristics of the orthogonal code. In practice, the orthogonality may be destroyed by the imperfect design of the orthogognal code and the multiuser multipath scenario. Under such case, tracking of the leading edge is relatively challenging. [67] introduces a Multi User Interference (MUI) mitigation method which performs nonlinear filtering on the received signal energy. The advantage of the method is to use the non-coherent receiver which can reduce the computational complexity. However, nonlinear filter cannot mitigate the multipath effect at the presence of NLoS. Although NLoS assumption is made in the publication, the indoor environment cannot be determined beforehand.

WLAN localization modes can be categorized in Figure 1.1 [56]. The WLAN localization systems can be classified into two main categories: ad-hoc mode based systems and infrastructure mode based systems (see Figure 1.1). In ad-hoc mode, there are no access points and location determination systems. Therefore, these systems use empirical radio propagation models to triangulate the user location [102]. The localization systems based on the infrastructure mode take the access points as reference points and triangulate the user location relative to these access points. The infrastructure mode based techniques can be classified into three categories: AoA based localization, RSS based localization, ToA based localization and cell of origin based localization. With the estimated AoAs, it has two methods to determine the user location: direct triangulation and grid search [104][105]. RSS based localization can be classified into model based techniques and radio map based techniques. Model based techniques use empirical models to capture the relationship between the signal strength and distance [106]-[108]. Radio-map based techniques try to capture the signature of the access points at selected locations in the area of interest. Cell of origin based techniques limit the estimation accuracy to the range of the access point because they estimate the user location as the location of the access point that the wireless card is associated with [56]. Table 1.9 depicts some essential literatures about WLAN localization systems.

Table 1.9: Some important publications about WLAN localization systems

Citation	Main Content
[56]	Location fingerprinting related to signal strength distribution (non-parametric distribution and parametric distribution)
[58]	Delay measurement-based TDoA
[66]	Localization using time of flight (ToF) measurements
[102]	RSS based localization with the given path-loss model
[103]	AoA based localization AoA is estimated using SAGE (Space Alternating Generalized Expectation-Maximization) algorithm
[104]	GS (Gird Search) based Hybrid ToA/AoA Localization

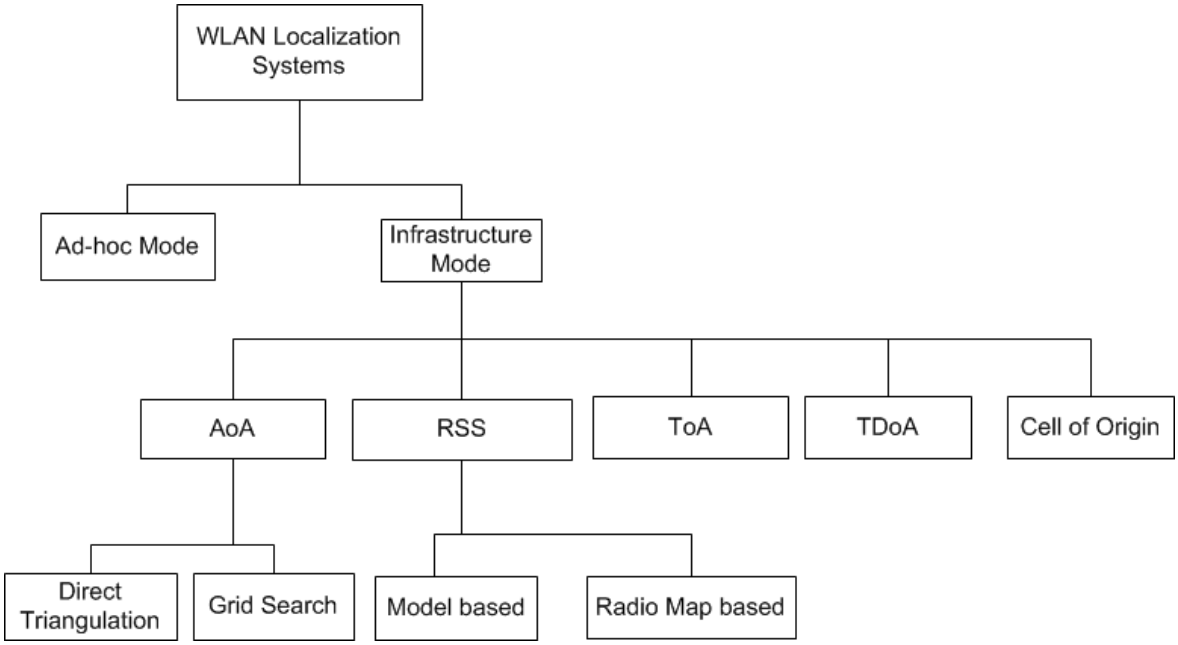

Figure 1.1: Category of WLAN Localization Systems [56]

The ToA/TDoA, RSS and AoA based WLAN localization systems are variously discussed in some literatures. [58] studied the possibility of overlaying geolocation functions in 802.11 DSSS WLANs. A delay measurement-based TDoA measuring method was proposed for 802.11 specifications, which can eliminate the requirement of initial synchronization in the conventional methods. [59] and [60] investigate the RSS-based location fingerprinting approaches in 802.11b. To reduce the software and hardware complexity, [61] introduces Hybrid of ToA and RSS approaches. In [62], ray tracing assisted RSS and ToA based algorithms were investigated. The advantage of ray tracing is that, besides obtaining the power level of a series of points, information can also be obtained about multipath effects [63]. The ToF (Time of Flight) based WLAN localization system is developed in [66]. Combining the ray tracing technique with the fingerprinting approach, the efficiency and accuracy can be improved. Due to the narrowband signal characteristic, the deployment of antenna array on WLAN transceiver is much cheaper than in UWB system. Antenna array provides an efficient mean to detect and process signals arriving from different directions. In comparison with a single omnidirectional antenna that is limited in directivity and bandwidth, antenna array has many advantages: it can adjust its beam pattern to a specific direction from which the signal is coming and the communication performance can be improved since signal-to-interference-ratio (SIR) for the specific direction can greatly increase. Hence, AoA estimation is an effective method to find the position of WLAN mobile target. The location of the desired target can be triangulated by the intersection of more than two direction lines, each formed by the circular radius from a WLAN base station to the WLAN mobile target [64]. SAGE algorithm is used in [103] to estimate the AoA. The SAGE algorithm is a modified form of the EM (Expectation Maximization), which can reduce the computational

complexity. However, the RMSE of the position estimation can only achieve approximate 2m, which cannot fulfill the requirements of the indoor localization.

The accuracy of AoA estimation depends heavily on the physical characteristics of deployed antenna array and propagation environments. The main advantage of AoA based localization in WLAN system is that the position can be determined using only two WLAN base stations for 2-D localization. Employing more than two WLAN receivers are not essential but it can enhance the localization performance. It should be noted that the incoming direction may be incorrectly determined to a wrong direction due to the multipath reflection at the presence of NLoS. If DP (Direct Path) between WLAN mobile target and WLAN receiver is completely blocked, correct AoA cannot be determined through the traditional methods: beamforming, MUSIC (Multi Signal Classification) and ESPRIT (Estimation of Signal Parameters via Rotational Invariance Techniques). Only solution in this case is to use ray tracing technique or AoA based fingerprinting approach. If DP is partially blocked, the received signal power from DP may be smaller than that from MPC in the harsh environments, e.g. metal wall. Channel estimation in such situation is required to separate the DP and the MPC. Figure 1.2 shows DP blocked multipath environment in which the estimated AoA may be determined to a wrong direction due to the shadowing and reflection effect caused by the obstacle and the wall between the transmitter and the receiver (see Figure 1.2). The detailed multipath effect on the AoA estimation can be found in section 4.3.

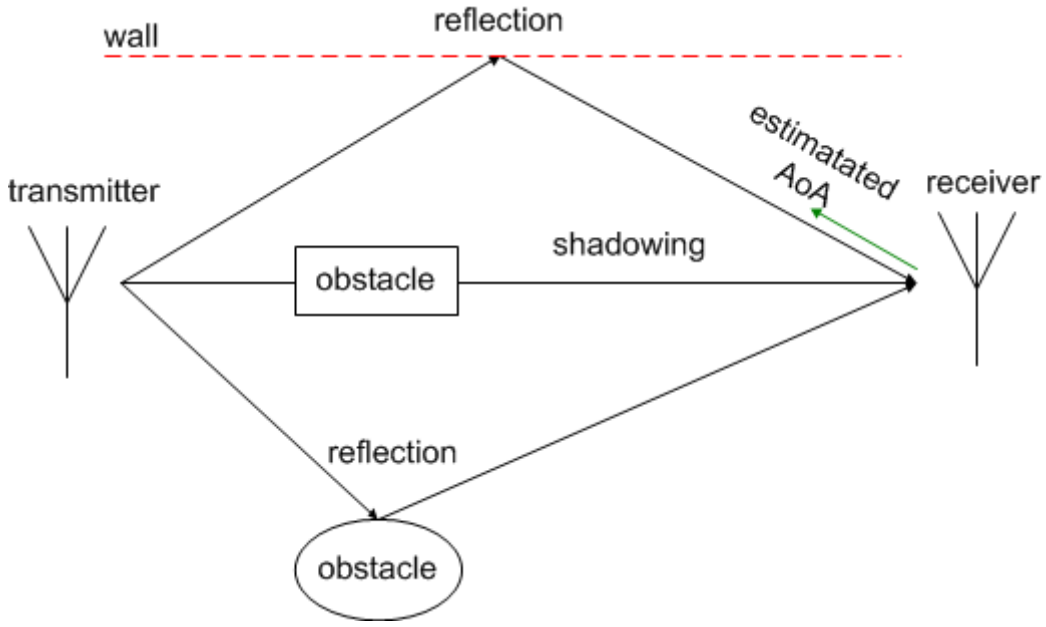

Figure 1.2: AoA estimation in a partially DP blocked multipath environment

1.3 Main Contributions

In this dissertation, the infrastructure of current localization systems and the conventional localization techniques (ToA/TDoA, RSS, AoA) are firstly presented

and described with the discussion of the error sources of each technique. The impact of the channel on the localization performance is highlighted. Then, the novel Joint Leading Edge Detection (JLED) approach is proposed to adapt to the multipath time hopping (TH) UWB systems and the low SNR environments. With the given estimation criteria with respect to the number of UWB receivers, the mathematical model of JLED approach is proposed. Finally, the estimation error of JLED approach is theoretically analyzed and the simulation results are given.

The leading edge detection via IMLCE is investigated in this dissertation. The general concept of Maximum Likelihood Estimation (MLE) and the mathematical expression of channel decay estimation and the time delay estimation are given in this dissertation. Then the detection error probability and the estimation error in the coarse detection and the fine estimation are analyzed, respectively. Finally, the simulation results of IMLCE based leading edge detection are given.

For TH-PAM (Time Hopping – Pulse Amplitude Modulation) UWB systems, the author proposes the leading edge detection via Subspace based Approach (SbA). The signal model of TH-PAM and the search-back based SbA algorithms are presented firstly. The author answers the question that why the random numbers shall be used to disturb the received data vector. It presents that the static channel is the premise for search-back based SbA. In the fading channel, the Frequency Domain (FD) SbA is proposed. Then the error probability of search-back based SbA is mathematically deduced and simulation results are given.

Novel RSS-based approaches as possible substitutes of the ToA are discussed in this dissertation. The Least Squares (LS) and Sub-Sampling Least Squares (SSLS) based fingerprint approaches are investigated and compared. From the given path-loss model, the LS and SSLS based fingerprint approaches are evaluated and the error probabilities of two approaches are deduced. Finally, the two approaches are implemented on the UWB demonstrator.

In the RSS based ranging, the transmission distance can be determined by the given path-loss model and the channel energy. In this dissertation, the author proposes the novel Channel Energy Estimation (CEE) approaches which exploit the Eigen Value Decomposition (EVD) of the Channel Auto Correlation Matrix (CACM) to get the channel energy. In relation to the CEE, noise power shall be estimated via the Singular Value Decomposition Approach (SVDA) and Eigen Value Decomposition Approach (EVDA), which are proposed in this dissertation.

In the research, an Angle of Arrival (AoA) estimation based positioning system was developed in Wireless LAN (WLAN) system. AoA estimation shall be executed in four WLAN based stations, each of which is equipped with a Uniform Linear Array (ULA), which consists of four antenna elements. Then, the position of the WLAN transmitter will be determined by the disjoint point of the four direction lines. Conventional beamforming and Root Multiple Signal Classification (RMUSIC) approaches are implemented to estimate the AoA from the WLAN transmitter. The narrow band characteristic of OFDM signal leads to coarse resolution of multipath in a harsh environment, which can degrade the AoA estimation performance. To overcome this drawback, the number of sources impinging on the array of sensors was estimated via information theoretic criterion. In addition, a novel OFDM channel estimator is designed and implemented in the receiver to distinguish the Direct Path (DP) and Multi Path Component (MPC) more accurately. To consider the decay factor during the transmission, an Automatic Gain Control (AGC) function is implemented in the signal processing module, which can adapt the system to the different transmission distance. Initial calibration process is adopted in the system to minimize the phase offset among the antenna elements. The employed antenna array parameters are optimized to achieve better estimation accuracy. Finally, the measurement campaigns are executed and the measurement results are evaluated.

1.4 Outline of the Dissertation

Firstly, infrastructure of the current LT system, conventional localization techniques and error sources are briefly introduced in chapter 2. At the beginning of chapter 3, the author introduces the indoor channel model, ranging-based UWB signal modulation formats, signal and the system model which were used in our research. The JLED, IMLCE and leading edge detection via SbA are discussed in the subchapter 3.3.1, 3.3.2 and 3.3.3, respectively. The error analysis and the simulation results are given in the subchapter 3.3.5, 3.3.6 and 3.3.7, respectively. The LS and SSLS based fingerprint methods are described in the subchapter 3.4.1. The error analysis and the measurement results of LS and SSLS based fingerprint methods are given in the subchapter 3.4.2. In 3.4.3 and 3.4.4, the CEE based distance estimation and its simulation results are proposed, respectively. Chapter 4 introduces our WLAN-based localization system. The optimization of antenna array parameters, initial calibration and the implemented AoA estimation algorithms are described in the subchapter 4.2. The perturbation of AoA estimation led by multipath component, the solution to solve the problem and the novel OFDM channel estimator are discussed in the subchapter 4.3. The subchapter 4.5 gives the simulation and measurements results. The UWB and WLAN demonstrators are described in the chapter 5. Finally, the conclusions are drawn in chapter 6, where the research is summarized and the future work will be suggested.

2 Infrastructure, Algorithms and Challenges of LT in Indoor Environments

2.1 Overview

This chapter will introduce general infrastructure of the current indoor LT systems. Based on this infrastructure, ToA/TDoA, RSS and AoA based approaches are introduced and illustrated. Finally, the error sources and fundamental limits of each approach are reviewed in this chapter.

2.2 Infrastructure of Indoor Localization Systems

There are mainly three different LT systems: active, passive and radar. To solve the "where am I" problem, the active localization system requires the cooperation between the target and the anchor nodes. The target under detect has the aim to find its own location. Firstly, it shall broadcast beacon signals to the anchor nodes continuously and the localization shall be accomplished by processing the received signal of each anchor node. Then the localization results shall be transmitted from the server to the target in order to let the target know its own position. For the passive localization, on the other hand, it shall solve the "where are you" problem, that means the server connected to the anchor node wants to know location of the target. Each anchor node within the range will capture the data signal once the target has transmitted any data to one or more certain anchor node for data communication. It is obvious that the difference between active and passive localization is that the target in the active localization system wants to find its own location and carry one part of its hardware as the receiver while the passive localization is not this. Radar is object-detection system which can use the radio waves to detect many parameters of the target without antenna. In this dissertation, only the passive LT systems are considered. Figure 2.1 illustrates the passive LT system. As can be seen from Figure 2.1, there are N targets under detect and four Access Points (APs) with known fixed coordinates in the LT system. There is one central sever which connects to the four APs via cable. The cable connection may use Ethernet or USB cable which transmits the location metrics from the four APs to the central server. The location metrics contains ToA/TDoA, RSS and AoA. After processing the location metrics in the central server, the LT results shall be transmitted to a monitor, on which the position of each target will be displayed. For different application, the radio link between targets and each AP can be UWB, WLAN, infrared, etc.

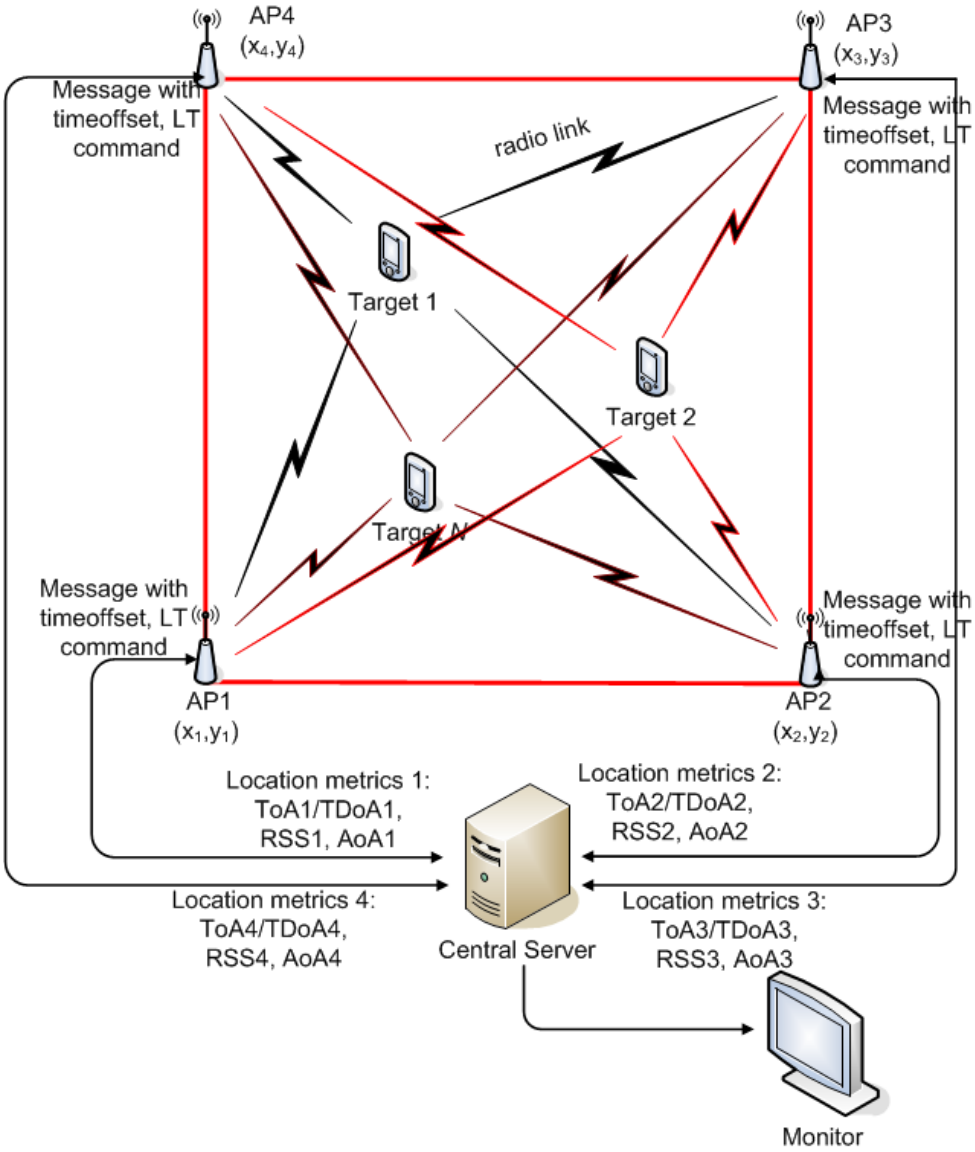

Figure 2.1: Infrastructure of passive LT system

In ToA based systems, the cable connections between the central server and APs are used to execute the synchronization process firstly. Then the clock drift between targets and APs can be eliminated through two-way ranging mechanisms which will be introduced in detail in the next subsection. After receiving the LT commands from the central server, the APs begin to listen to the ranging signals from the targets within the LT range. If one or more targets within the LT range transmit any signal for its own purpose, each AP will capture the waveform. From the captured waveform, the ToA metrics on each AP can be extracted using certain algorithms. TDoA based systems do not require synchronizations between target and APs because only the time offset between two APs is considered as the ranging metrics.

In RSS systems, the cable connections between the central server and APs are only used to transmit the LT commands and RSS metrics since no synchronizations are required any more. Each AP receives the signals from the target and total energy of

signals will be estimated via certain algorithms. Then the RSS as the ranging metric will be transmitted to the central server.

In AoA systems, the antenna array employed on each AP detects the direction of the incoming signal emitted from the target. Then the detected directions from each AP as the ranging metric shall be transmitted to the central server. AoA systems require no time synchronization between targets and APs but phase synchronizations among antenna elements are required.

2.3 Conventional Ranging Techniques

2.3.1 Layered Protocols

In any LT system, the ranging functionalities are accomplished by exchanging messages between involved parties. A ranging protocol is an agreement between two or more ranging devices on a ranging procedure. To reduce design complexity and provide flexibility, traditionally most network devices are considered and implemented as multiple layers [4], each layer offering its services to the higher layers [4]. This approach isolates the upper layers from the implementation details of the services it receives. In *n*-layer implementation of a network, *i*-th layers of local and peer devices communicate using protocol from layer *i*. Figure 2.2 shows the architecture of typical ranging devices.

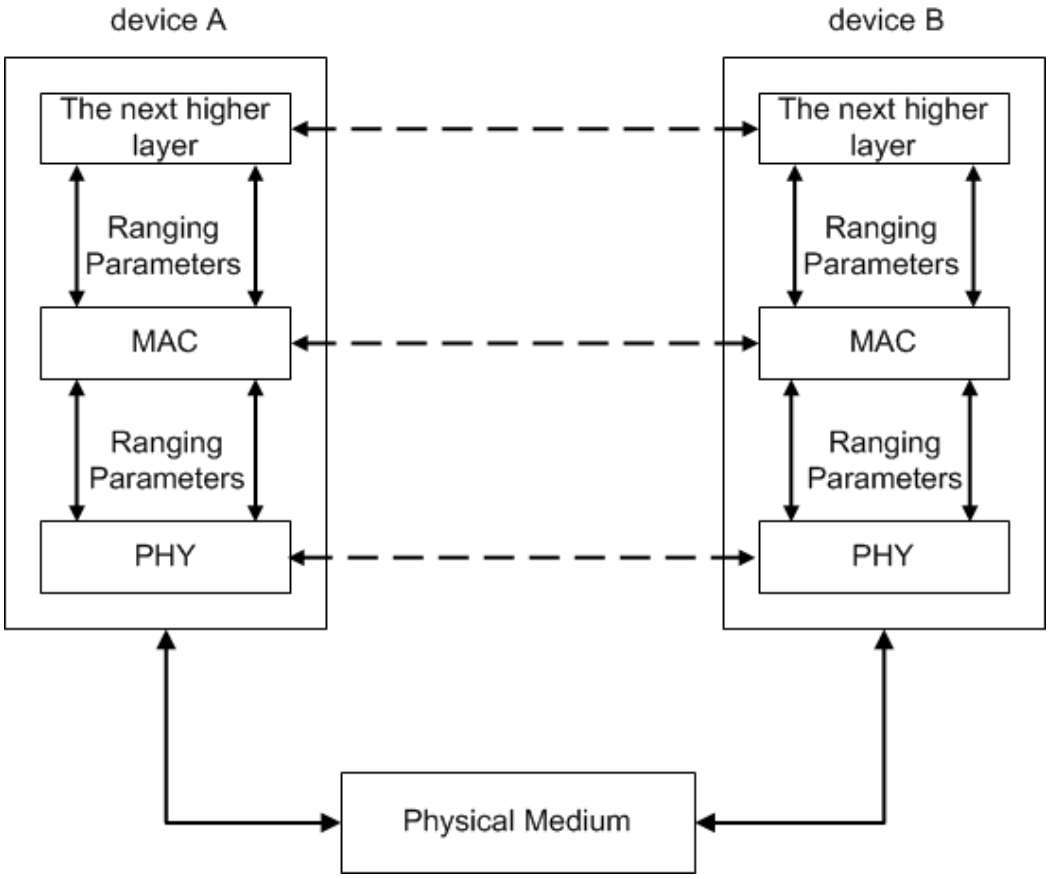

Figure 2.2: Architecture of ranging devices

As can be seen from Figure 2.2, ranging-related data such as ranging parameters, LT command, etc. are passed between the protocol layers. For instance, the higher layer can ask the MAC (Media Access Control) sub-layer to start the ranging process or to use a specific signal form. In the ToA based ranging systems, the MAC layer shall initiate a MAC layer protocol data unit (MPDU) containing the transmission timestamp for the synchronization process. The processing delay from MAC to PHY can lead to a perturbation of ranging parameters, which will be introduced in the next subsection.

2.3.2 ToA/TDoA based Ranging

ToA/TDoA is the most popular ranging mechanism because it can provide relatively high LT accuracy. To prevent ambiguity in ToA estimates, APs must have a common clock, or they must exchange its own clock information via certain mechanisms. Before synchronization, the local clock on each AP has not been aligned to each other. After synchronization, the clock of each AP shall be adjusted to the local cock on the central server. Figure 2.3 illustrates the synchronization process between APs and the central server with cable connection.

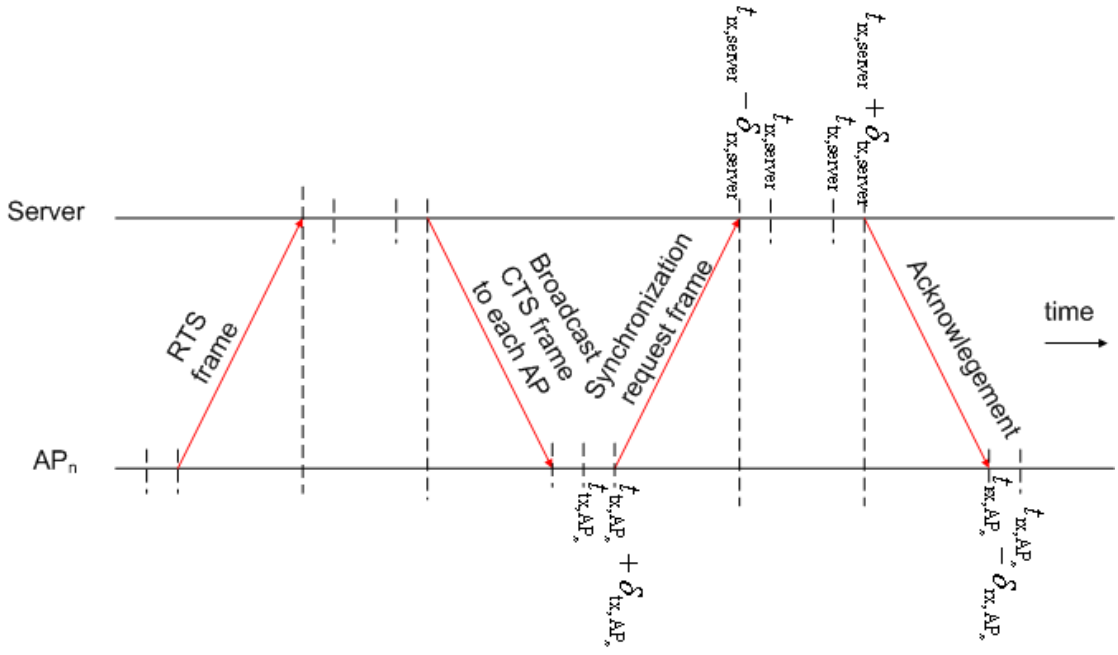

Figure 2.3: Synchronization process with RTS/CTS protocol

As can be seen from Figure 2.3, before start of synchronization process, RTS/CTS (Request to Send / Clear to Send) mechanisms shall be executed to avoid the collision between two or more APs. At $t_{\mathrm{tx},\mathrm{AP}_n}$, AP_n begins to transmit a synchronization request frame to the server and $t_{\mathrm{tx},\mathrm{AP}_n}$ will be recorded at the same time. The physical layer of AP_n will require a given processing time prior to the synchronization request can be transmitted. This signal processing delay shall be denoted by $\delta_{\mathrm{tx},\mathrm{AP}_n}$. Hence, the actual

transmission time is $t_{\text{tx,AP}_n} + \delta_{\text{tx,AP}_n}$. The server detects the arrived frame at $t_{\text{rx,server}}$, which can be expressed as

$$t_{\text{rx,server}} = t_{\text{rx,server,act}} + \delta_{\text{rx,server}}, \tag{2.1}$$

where $t_{\text{rx,server,act}}$ is the actual arriving time. Then the server shall extract the sequence number, the source address and the destination address from received request frame and check them.

The server initiates an acknowledgement at $t_{\text{tx,server}}$. This acknowledgement shall contain virtual transmission timestamp $t_{\text{tx,server}}$ and the frame processing time $t_{\text{tx,server}} - t_{\text{rx,server}}$. Due to the processing time of the physical layer of the server, the acknowledgement shall be broadcast to the APs at the timestamp $t_{\text{tx,server}} + \delta_{\text{tx,server}}$. AP_n detects the arrived acknowledgement at the virtual timestamp $t_{\text{rx,AP}_n}$ and the actual received timestamp can be expressed as:

$$t_{\text{rx,AP}_n\text{,act}} = t_{\text{rx,AP}_n} - \delta_{\text{rx,AP}_n}. \tag{2.2}$$

After extracting the received acknowledgement frame sent from server, the time delay of the cable can be estimated as:

$$T_{\text{d}} = \left(t_{\text{rx,AP}_n} - t_{\text{tx,AP}_n} - t_{\text{tx.server}} + t_{\text{rx,server}}\right)/2, \tag{2.3}$$

and the clock drift between the AP_n and the server can be expressed as

$$\varepsilon_{\text{AP}_n\text{,s}} = t_{\text{rx,AP}_n} - \left(t_{\text{tx,server}} + T_{\text{d}}\right). \tag{2.4}$$

Other APs on the network will start their RTS/CTS protocols if they have received the acknowledgement frame. It is obvious that the clock drift contains a perturbation factor, which is caused by the processing delay of the physical layer. Hence, the actual clock drift $\varepsilon_{\text{AP}_n\text{,s,act}}$ can be expressed as:

$$\varepsilon_{\text{AP}_n\text{,s,act}} = t_{\text{rx,AP}_n} - \delta_{\text{rx,AP}_n} - \left(t_{\text{tx,server}} + \delta_{\text{tx,server}} + \varepsilon\right), \tag{2.5}$$

with

$$\varepsilon = \frac{1}{2}\left(t_{\text{rx,AP}_n} - \delta_{\text{rx,AP}_n} - t_{\text{tx,AP}_n} - \delta_{\text{tx,AP}_n} - t_{\text{tx.server}} - \delta_{\text{tx,server}} + t_{\text{rx,server}} - \delta_{\text{rx,server}}\right). \tag{2.6}$$

The processing delays are not evitable since they are unknown to AP_n and server. The ToA system requires synchronization between target and each AP, which requires the cooperation of the target. If there is only one target in the LT range, no RTS/CTS protocol is needed. On the other hand, RTS/CTS protocols shall be employed to avoid the collisions if there are several targets within the LT range.

After the synchronization of the fixed mounted infrastructure and the targets have been accomplished, the LT process can be started. For the sake of simplicity, it just introduces the ranging protocol but no consideration of the path effect. Firstly, the

time axis shall be separated into several time slots each of which owns the equal time length. To evaluate the ranging time delay, the target shall transmit its ranging frame at the beginning of each time slot. It assumes that the transmission timestamp is T_0. Then it assumes that AP_n receives the ranging frame at the time stamp

$$T_{\mathrm{rx},n} = T_0 + \frac{d_n}{c}, \tag{2.7}$$

where d_n is the transmission distance between target and AP_n, c is the light speed. Hence, the d_n in (2.7) can be easily determined as $d_n = c\left(T_{\mathrm{rx},n} - T_0\right)$. Finally, each AP shall transmit a message containing d_n to the server. $T_{\mathrm{rx},n}$ is also called arriving time of leading edge, which is a key factor affecting the LT accuracy. Leading edge is heavily influenced by the channel status, the variance of Additive Gaussian Noise and detection algorithms. As mentioned in section 1.2, most of the ToA estimators are based on the maximum value of MF (Matched Filtering), ML (Maximum Likelihood) and MMSE (Minimum Mean Squared Error). The following context will briefly review the three estimators while the leading edge detection in harsh environments and the influences of the channel status will be discussed in chapter 3.

Let the received base band signal be expressed as

$$r(t) = \sum_{l=1}^{L} a_l s\left(t - \tau_l\right) + n(t), \tag{2.8}$$

where L is the number of paths. a_l and τ_l are the channel amplitude and delay, which are the unknown parameters. $n(t)$ is an additive noise which is assumed to be a zero-mean white Gaussian process with double-sided power spectral density $2\sigma_n^2$. This section only deals with the classical estimators. Hence, we assume that a_1 has the maximum value comparing with $a_{l,l=2\cdots L}$. The MF estimator can be defined as

$$\hat{\tau}_{\mathrm{toa,mf}} = \arg\max_{\tau}\left(z(\tau)\Big|_0^{T_{\mathrm{th}}}\right), \tag{2.9}$$

with

$$\begin{aligned} z(\tau) &= \frac{1}{\sqrt{E_{\mathrm{s}}}}\int_0^T s(t-\tau) r(t)\,\mathrm{d}t \\ &= \frac{1}{\sqrt{E_{\mathrm{s}}}}\sum_{l=1}^{L} a_l \int_0^T s(t-\tau)\, s\left(t-\tau_l\right)\mathrm{d}t + \frac{1}{\sqrt{E_{\mathrm{s}}}}\int_0^T s(t-\tau)\, n(t)\,\mathrm{d}t \\ &= \frac{1}{\sqrt{E_{\mathrm{s}}}}\sum_{l=1}^{L} a_l \int_0^T s(t-\tau)\, s\left(t-\tau_l\right)\mathrm{d}t + w(\tau) \\ &= \frac{1}{\sqrt{E_{\mathrm{s}}}}\sum_{l=1}^{L} a_l R\left(\tau-\tau_l\right) + w(\tau) \end{aligned}, \tag{2.10}$$

where T is the signal duration, E_{s} is the signal energy and $R(\tau)$ is the autocorrelation function of $s(t)$. $w(\tau)$ is a color noise process with the same first-

order and second-order statistics as $n(t)$ due to the normalized signal template. $w(\tau)$ is color because $n(t)$ is filtered by $s(t)$. T_{th} is the upper limit of the search space, which will be described in chapter 3.

From(2.8), the PDF (Probability Density Function) and the logarithm of the PDF of $r(t)$ can be written as

$$\begin{aligned} \mathrm{P}\left(r(t)\middle|\tau_1\right) &= \frac{1}{\sqrt{2\pi}\sigma_n}\exp\left(-\frac{\int_0^{T_{\text{th}}}\left|r(t)-\sum_{l=1}^{L}a_l s(t-\tau_l)\right|^2 \mathrm{d}t}{2\sigma_n^2}\right) \\ \Lambda\left(r(t)\middle|\tau_1\right) &= -\frac{\int_0^{T_{\text{th}}}\left|r(t)-\sum_{l=1}^{L}a_l s(t-\tau_l)\right|^2 \mathrm{d}t}{2\sigma_n^2} - \ln\left(\sqrt{2\pi}\sigma_n\right) \end{aligned} \tag{2.11}$$

The ML estimator can be expressed as

$$\begin{aligned} \hat{\tau}_{\text{toa,ml}} &= \arg\max_{\tau_1}\left(\Lambda\left(r(t)\middle|\tau_1\right)\right) \\ &= \arg\min_{\tau_1}\left(\int_0^{T_{\text{th}}}\left|r(t)-\sum_{l=1}^{L}a_l s(t-\tau_l)\right|^2 \mathrm{d}t\right). \end{aligned} \tag{2.12}$$

The MMSE estimator is to find $\hat{\tau}_{\text{toa,mmse}}$, which fulfills that $E\left(\left\|\hat{\tau}_{\text{toa,mmse}}-\tau_1\right\|^2\right)$ can approach the minimum value. From (2.8), we can see that the linear Bayesian model cannot be used. From the definition of MMSE estimator, we have

$$\begin{aligned} \hat{\tau}_{\text{toa,mmse}} &= E\left(\tau\middle|r(t)\right) \\ &= \int_0^{T_{\text{th}}}\tau\mathrm{P}\left(\tau\middle|r(t)\right)\mathrm{d}\tau \end{aligned}. \tag{2.13}$$

The important issue of MMSE estimation is to determine $\mathrm{P}\left(\tau\middle|r(t)\right)$. From Bayesian theorem, it has

$$\begin{aligned} \mathrm{P}\left(\tau\middle|r(t)\right) &= \frac{\mathrm{P}\left(r(t)\middle|\tau\right)\mathrm{P}(\tau)}{\mathrm{P}\left(r(t)\right)} \\ &= \frac{\mathrm{P}\left(r(t)\middle|\tau\right)\mathrm{P}(\tau)}{\int_0^{T_{\text{th}}}\mathrm{P}\left(r(t)\middle|\tau\right)\mathrm{P}(\tau)\mathrm{d}\tau} \end{aligned}. \tag{2.14}$$

Assuming τ_1 is uniformly distributed between 0 and T_{th}, (2.14) can be rewritten as

$$\mathrm{P}\left(\tau\middle|r(t)\right)=\frac{\exp\left(-\dfrac{\int_0^{T_{\text{th}}}\left|r(t)-a_1 s(t-\tau)-\sum_{l=2}^{L}a_l s(t-\tau_l)\right|^2 \mathrm{d}t}{2\sigma_n^2}\right)}{\int_0^{T_{\text{th}}}\exp\left(-\dfrac{\int_0^{T_{\text{th}}}\left|r(t)-a_1 s(t-\tau)-\sum_{l=2}^{L}a_l s(t-\tau_l)\right|^2 \mathrm{d}t}{2\sigma_n^2}\right)\mathrm{d}\tau}. \tag{2.15}$$

Setting the dominator of (2.15) to be ρ and substituting (2.15) into (2.13), it has

$$\hat{\tau}_{\text{toa,mmse}}=\frac{1}{\rho}\int_0^{T_{\text{th}}}\tau\exp\left(-\frac{\int_0^{T_{\text{th}}}\left|r(t)-a_1 s(t-\tau)-\sum_{l=2}^{L}a_l s(t-\tau_l)\right|^2 \mathrm{d}t}{2\sigma_n^2}\right)\mathrm{d}\tau. \tag{2.16}$$

The CRLB of ToA estimation for signal mode in (2.10) and the performance of MF, ML and MMSE estimator will be proposed in the section 2.3.5.

From the estimated ToA, the transmission distance can be easily calculated by $\hat{d}_n=c\left(\tau_{\text{toa}}-T_0\right)$. In the last step, the location of the target shall be determined by triangulation or Least Squares (LS) algorithms embedded in the server. Figure 2.4 illustrates two-dimensional localization, which requires at least three APs. As can be seen from Figure 2.3, there are four APs in the LT system and the red point represents the target under detect. d_1 to d_4 are the estimated distance from the target to the AP_1 to AP_4, respectively.

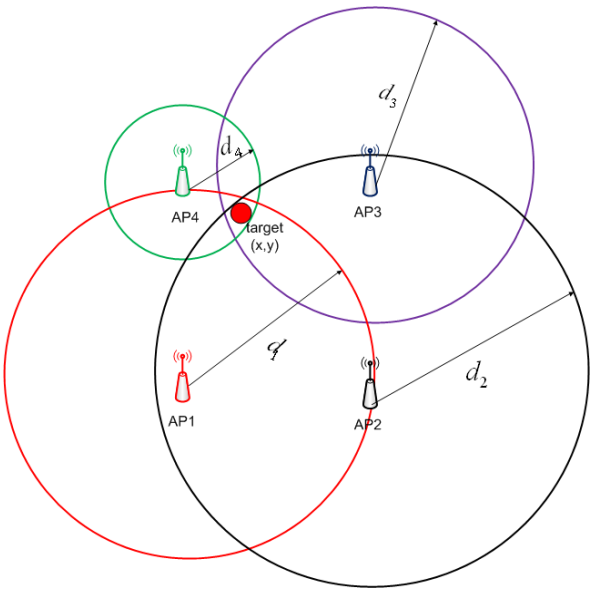

Figure 2.4: Two-dimensional localization

With the estimated distance $\hat{d}_n$, four circles centered at (x_n, y_n) can be defined (see Figure 2.4). Due to the perturbation in $T_{\mathrm{rx},n}$, the four circles cannot intersect at a single point. According to [71] and [72], the estimated distance $\hat{d}_n$ can be modeled as

$$\hat{d}_n = d_n + e_n + n_n = c\hat{t}_n, \tag{2.17}$$

where $\hat{t}_n$ is the time of flight estimate of the signal at the *n*-th AP. d_n is the true distance between *n*-th AP and the target. n_n is the Additive White Gaussian Noise (AWGN) with zero mean and variance σ_n^2. e_n is a non-negative distance bias introduced by the NLoS. Then the LS algorithm is to find a point $(\hat{x}, \hat{y})$, which fulfills the following conditions:

$$(\hat{x}, \hat{y}) = \arg\min_{(\hat{x},\hat{y})} \left(\sum_{n=1}^{N} \left(\hat{d}_n - \sqrt{(x - x_n)^2 + (y - y_n)^2} \right)^2 \right). \tag{2.18}$$

Conventionally, the ToA-based ranging requires synchronization among the target and the reference nodes or a certain protocol to exchange the time information. However, TDoA-based measurements can be obtained even in the absence of synchronization between the target and the AP, if there is only synchronization among the APs [73]. The difference between the arriving time of two signals traveling between the target and the two APs is estimated and considered as the ranging parameters [4]. One TDoA measurements defines a hyperbola between two relevant APs (see Figure 2.5).

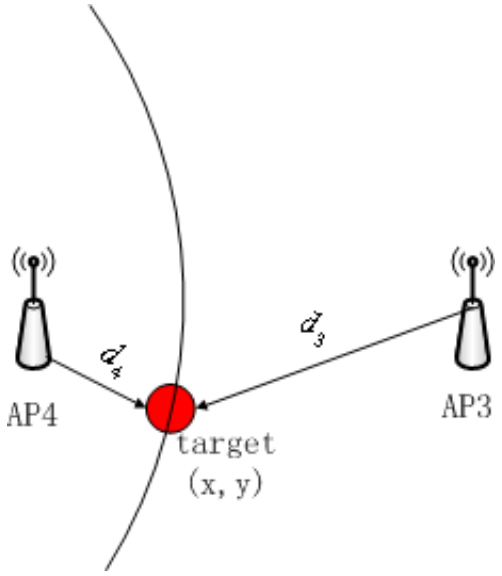

Figure 2.5: TDoA measurements define a hyperbola through the target

The position of the target can be determined as the intersection of two hyperbolas. More than two hyperbolas will take place if more than three APs are inspected. Under such case, the location estimation using LS can be expressed as:

$$(\hat{x},\hat{y}) = \underset{(\hat{x},\hat{y})}{\arg\min}\left(\sum_{n=1}^{N-1}\left(c\Delta\hat{t}_{n,n+1} - \left(\sqrt{(x-x_n)^2+(y-y_n)^2} - \sqrt{(x-x_{n+1})^2+(y-y_{n+1})^2}\right)\right)^2\right), \tag{2.19}$$

where $\Delta\hat{t}_{n,n+1} = \hat{t}_n - \hat{t}_{n+1}$.

2.3.3 RSS based Ranging

RSS based ranging systems provide information about the distance between the target and the APs based on certain channel characteristics. The main idea behind an RSS-based approach is that if the relation between distance and path loss is known, the RSS measurements at the APs can be used to estimate the distance between the AP and the target, assuming that the transmit power is known. We assume that the thermal noise is independent from the transmission distance. Then the known path loss model can be expressed as [4]

$$\overline{p}(d) = p_0 - 10\alpha\log_{10}(d/d_0), \tag{2.20}$$

where α is the path loss exponent, $\overline{p}(d)$ is the average received power in dBm at a distance d and p_0 is the received power in dBm at a reference distance d_0 [4]. In UWB systems, the shadowing effects are usually present in the received power $p(d)$, which are modeled as log-normal random variables [4]. Hence, the n-th received power within the k-th window $p_{k,n}(d_n)$ in dBm can be modeled as a Gaussian random variable with mean $\overline{p}_n(d_n)$. It has

$$\begin{aligned} &10\log_{10} p_{k,n}(d_n) \propto N\left(\overline{p}_n(d_n),\sigma^2\right) \\ &\propto N\left(p_0 - 10\alpha\log_{10}(d_n/d_0),\sigma^2\right) \quad , \\ &p_{k,n}(d_n) = \frac{1}{T}\int_{(k-1)T}^{kT} |r_n(t)|^2 \,\mathrm{d}t \end{aligned} \tag{2.21}$$

where σ^2 is the variance of log-normal fading. According to ergodic theorem and central limit theorem, it has

$$\hat{\overline{p}}_n(d_n) = \frac{10}{K}\log_{10}\left(\prod_{k=1}^{K} p_{k,n}(d_n)\right), \tag{2.22}$$

where K is the number of observation. The $\hat{\overline{p}}_n(d_n)$ will approach $\overline{p}_n(d_n)$ if K approaches unlimited number. From (2.21) and (2.22), the estimated $\overline{p}_n(d_n)$ can be expressed as

$$\hat{\overline{p}}_n(d_n) = \overline{p}_n(d_n) + w'_{K,n}, \tag{2.23}$$

where $w'_{K,n} \propto N(0,\sigma^2/K)$. Hence, the ML estimator can be written as

$$\hat{d}_n = \underset{d_n}{\arg\min}\left(\left|\hat{\overline{p}}_n(d_n) - \overline{p}_n(d_n)\right|^2\right), \tag{2.24}$$

where $\overline{p}_n(d_n)$ is the true received signal energy, which can be written as

$$\overline{p}_n(d_n) = p_0 - 10\alpha \log_{10}(d_n / d_0). \tag{2.25}$$

Substituting (2.25) into (2.24), it has

$$\hat{d}_n = \arg\min_{d_n}\left(\left|\hat{\overline{p}}_n(d_n) - p_0 + 10\alpha \log_{10}(d_n / d_0)\right|^2\right). \tag{2.26}$$

The CRLB and the performance of (2.26) will be given in section 2.3.5.

2.3.4 AoA based Ranging

Unlike the RSS measurement that provide received signal power, AoA based ranging system provides information about the direction of the incoming signal from the target. In general, Uniform Linear Array (ULA) is employed in order to measure the AoA of the signal. The angle information is obtained at the ULA by measuring the differences in arrival time of the incoming signal at different antenna elements. Figure 2.6 shows the AoA estimation using a ULA. d and θ represent the inter-element spacing and the actual AoA, respectively.

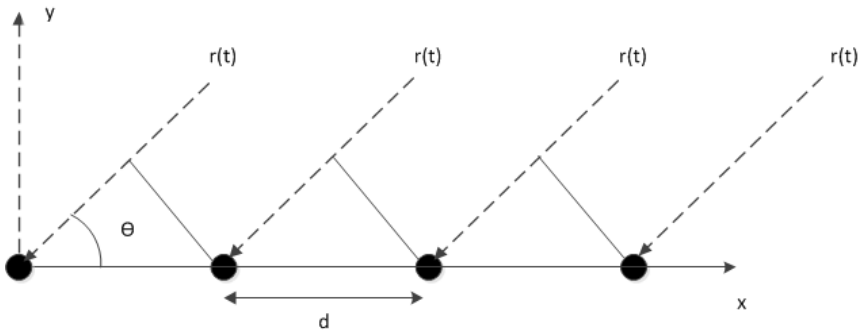

Figure 2.6: Signal arrival at the ULA

We assume that the target is enough far from the ULA and the signal is transmitted through an Additive White Gaussian Noise (AWGN) channel (AoA estimation under Multipath channel scenario will be given in Chapter 4). The Radio Frequency (RF) signals impinging on each antenna element can be expressed as

$$r(t) = s(t)e^{j2\pi f_c t} + n(t), \tag{2.27}$$

where $s(t)$ is the baseband signal. If the incoming direction of the signal is θ (see Figure 2.6), the phase difference between two antenna elements can be calculated as $\phi = 2\pi f_c d \cos\theta / c$. We set the left antenna element as the reference antenna, and then the received baseband signal on each antenna element can be expressed as a vector:

$$\underline{\boldsymbol{r}}(\boldsymbol{t}) = \begin{bmatrix} 1 \\ e^{j\phi} \\ \vdots \\ e^{j(N-1)\phi} \end{bmatrix} \underline{s}(t) + \begin{bmatrix} \underline{n}_1(t) \\ \underline{n}_2(t) \\ \vdots \\ \underline{n}_{N-1}(t) \end{bmatrix}. \tag{2.28}$$

It should be noted that (2.28) is only for narrow band signal which has $s(t) \approx s(t - d\cos\theta / c)$ if $d\cos\theta / c$ is small enough relative to $1/B_s$, where B_s is the signal bandwidth. For wideband systems, e.g. UWB, time-delayed versions of received signals should be considered since the time delay cannot be represented by a unique phase value for the UWB signal [4]. In this research, AoA-based approaches were investigated only for WLAN system. Hence, the AoA-based ranging for wideband systems will not be discussed in this dissertation. With the given $\underline{\boldsymbol{r}}(\boldsymbol{t})$, several AoA estimation methods such as conventional beamformer, MVDR (Minimum Variance Distortionless Respones) beamformer, ESPRIT (Estimation of Signal Parameter via Rotational Invariance Techniques) and MUSIC can be implemented to determine the AoA. For the conventional beamformer and MVDR beamformer based AoA estimation, the main lobe of the beamformer shall be adjusted to the different spatial directions to determine the received power from each direction. The different spatial directions shall be uniformly or opportunistically distributed over the whole angle range. Then the spatial direction with the maximum received power shall be considered to be the estimated AoA. The conventional beamformer is to use the spatial MF to maximize the SNR at the output of the beamformer [74]. MVDR beamformer and MMSE (Minimum Mean Squared Error) beamformer are adaptive beamformer, whose criteria is to maximize the Carrier-to-Interference (C/I) ratio and minimize the (MSE) Mean Squared Error between the output of the beamformer and the known reference signal. MUSIC is to exploit the orthogonality between the signal and noise subspace to get the spatial spectrum. The MUSIC, MMSE and MVDR can be referenced in [2], [75], [76] and [77]. It should be noted that the determination of noise subspace requires the number of targets in the system. Under the AWGN scenario, noise subspace can easily be determined since the number of targets can be easily determined by the information theoretic criterion. However, the determination of number of targets will become more complex under the multipath scenario. The Root MUSIC (RMUSIC) based AoA estimation under multipath scenario will be introduced in chapter 4. The CRLB of signal model in (2.28) will be proposed in 2.3.5.

2.3.5 Performance Analysis of Conventional Ranging Techniques

This section will give the CRLB for the aforementioned signal model and evaluate the performance of the aforementioned ranging techniques.

The expectation of the first derivative of (2.11) can be expressed as

$$E\left(-\frac{\partial\left(\ln \mathrm{P}\left(r(t);\tau_1\right)\right)}{\partial\tau_1}\right)=$$
$$=E\left(-\frac{a_1\int_0^{T_{\text{th}}}\left(r(t)-\sum_{l=1}^{L}a_l s(t-\tau_l)\right)\frac{\partial s(t-\tau_l)}{\partial\tau_1}\mathrm{d}t}{\sigma_n^2}\right) \tag{2.29}$$
$$=0$$

To get the expectation of the second derivate of logarithm PDF, (2.8) shall be transformed into Frequency Domain (FD)

$$r(f)=\sum_{l=1}^{L}a_l s(f)e^{-j2\pi f\tau_l}+w(f), \tag{2.30}$$

where $s(f)$ is the spectrum of $s(t)$. The expectation of the second derivate of logarithm PDF can be expressed as

$$E\left(-\frac{\partial^2\left(\ln p\left(r(f);\tau_1\right)\right)}{\partial\tau_1^2}\right)=\frac{4\pi^2a_1^2}{\sigma_n^2}\int_{-B}^{+B}\left|s(f)\right|^2 f^2\mathrm{d}f\ . \tag{2.31}$$

Hence, the CRLB for the signal model (2.10) can be expressed as

$$\mathrm{var}\left(\tau_{\text{toa}}\right)\geq\frac{\sigma_n^2}{4\pi^2a_1^2\left(\int_{-B}^{+B}\left|s(f)\right|^2 f^2\mathrm{d}f\right)}, \tag{2.32}$$

where B is the signal bandwidth. From (2.32), it can be concluded that the variance of ToA estimation is determined by signal bandwidth, PSD (Power Spectral Density) and the amplitude of first path.

The following context will evaluate the aforementioned ToA estimator: MF, ML and MMSE. Differentiating (2.10), we have

$$\frac{\partial z(\tau)}{\partial\tau}=\frac{1}{\sqrt{E_{\text{s}}}}\sum_{l=1}^{L}a_l R'(\tau-\tau_l)+w'(\tau). \tag{2.33}$$

If we directly set (2.33) to zero, τ is difficult to be solved. We assume that $z(\tau)$ is differentiable up to second order. Expanding $\partial z(\tau)/\partial\tau$ around τ_1, we have

$$\frac{\partial z(\tau)}{\partial\tau}=\left.\frac{\partial z(\tau)}{\partial\tau}\right|_{\tau=\tau_1}+(\tau-\tau_1)\left.\frac{\partial^2 z(\tau)}{\partial\tau^2}\right|_{\tau=\tau_1}+\mathrm{O}(\tau-\tau_1)^2. \tag{2.34}$$

Setting (2.34) to zero, it has

$$\left.\frac{\partial z(\tau)}{\partial\tau}\right|_{\tau=\tau_1}+(\tau-\tau_1)\left.\frac{\partial^2 z(\tau)}{\partial\tau^2}\right|_{\tau=\tau_1}+\mathrm{O}(\tau-\tau_1)^2=0. \tag{2.35}$$

According to [78], a $\tilde{\tau}_1$ can be selected between τ_1 and $\hat{\tau}_1$ to fulfill that

$$\left.\frac{\partial z(\tau)}{\partial \tau}\right|_{\tau=\tau_1} + (\tau-\tau_1)\left.\frac{\partial^2 z(\tau)}{\partial \tau^2}\right|_{\tau=\tilde{\tau}_1} = 0. \tag{2.36}$$

The quantity $\left.\frac{\partial^2 z(\tau)}{\partial \tau^2}\right|_{\tau=\tilde{\tau}_1}$ can converge to the $E\left(\left.\frac{\partial^2 z(\tau)}{\partial \tau^2}\right|_{\tau=\tau_1}\right)$ with the probability one.

Hence, the estimation error can be written as

$$\tau-\tau_1 = -\frac{\left.\frac{\partial z(\tau)}{\partial \tau}\right|_{\tau=\tau_1}}{E\left(\left.\frac{\partial^2 z(\tau)}{\partial \tau^2}\right|_{\tau=\tau_1}\right)}. \tag{2.37}$$

Hence, (2.33) can be rewritten as

$$\left.\frac{\partial z(\tau)}{\partial \tau}\right|_{\tau=\tau_1} = \frac{1}{\sqrt{E_s}}\sum_{l=1}^{L} a_l R'(\tau_1-\tau_l) + w'(\tau_1). \tag{2.38}$$

The expectation of second-order derivative of $z(\tau)$ can be expressed as

$$E\left(\left.\frac{\partial^2 z(\tau)}{\partial \tau^2}\right|_{\tau=\tau_1}\right) = \frac{1}{\sqrt{E_s}}\sum_{l=1}^{L} a_l R''(\tau_1-\tau_l). \tag{2.39}$$

Then (2.37) can be rewritten as

$$\tau-\tau_1 = -\frac{\frac{1}{\sqrt{E_s}}\sum_{l=1}^{L} a_l R'(\tau_1-\tau_l) + w'(\tau_1)}{\frac{1}{\sqrt{E_s}}\sum_{l=1}^{L} a_l R''(\tau_1-\tau_l)}. \tag{2.40}$$

The expectation and the variance of $\hat{\tau}_{\text{toa,mf}}$ can be written as

$$E\left(\hat{\tau}_{\text{toa,mf}}\right) = \tau_1 - \frac{\sum_{l=1}^{L} a_l R'(\tau_1-\tau_l)}{\sum_{l=1}^{L} a_l R''(\tau_1-\tau_l)}$$

$$E\left(\left(\hat{\tau}_{\text{toa,mf}} - E\left(\hat{\tau}_{\text{toa,mf}}\right)\right)^2\right) = E\left(\left(\tau_1 - \frac{\frac{1}{\sqrt{E_s}}\sum_{l=1}^{L} a_l R'(\tau_1-\tau_l) + w'(\tau_1)}{\frac{1}{\sqrt{E_s}}\sum_{l=1}^{L} a_l R''(\tau_1-\tau_l)} - \tau_1 + \frac{\sum_{l=1}^{L} a_l R'(\tau_1-\tau_l)}{\sum_{l=1}^{L} a_l R''(\tau_1-\tau_l)}\right)^2\right). \tag{2.41}$$

$$= E\left(\left(\frac{w'(\tau_1)}{\frac{1}{\sqrt{E_s}}\sum_{l=1}^{L} a_l R''(\tau_1-\tau_l)}\right)^2\right) = \frac{8\pi^2\sigma_n^2\int_{-B}^{B} f^2 |s(f)|^2 \,\mathrm{d}f}{\left(\sum_{l=1}^{L} a_l R''(\tau_1-\tau_l)\right)^2}$$

From (2.41), it can be concluded that the MF estimator may be a biased estimator under the multipath scenario while an unbiased estimator under the single-path scenario because $R^{'}(0)=0$. The bias and the variance depend on signal bandwidth, first-order and second-order autocorrelation function and SNR.

To evaluate the ML estimator, we firstly define the objective function according to (2.12)

$$\xi(\tau_{1\cdots L})=\int_0^{T_{\text{th}}}\left|r(t)-\sum_{l=1}^{L}a_l s(t-\tau_l)\right|^2 \mathrm{d}t \tag{2.42}$$

Differentiating the objective function with respect to τ and setting it to zero, we have

$$\begin{aligned}
\frac{\partial\xi(\tau_{1\cdots L})}{\partial\tau} &= \frac{\partial\int_0^{T_{\text{th}}}\left|r(t)-a_1 s(t-\tau)-\sum_{l=2}^{L}a_l s(t-\tau_l)\right|^2 \mathrm{d}t}{\partial\tau} \\
&= \frac{\partial\begin{pmatrix}\int_0^{T_{\text{th}}} r^2(t)\mathrm{d}t+a_1^2\int_0^{T_{\text{th}}} s^2(t-\tau)\mathrm{d}t+\int_0^{T_{\text{th}}}\left(\sum_{l=2}^{L}a_l s(t-\tau_l)\right)^2 \mathrm{d}t \\ -2a_1\int_0^{T_{\text{th}}} r(t)s(t-\tau)\mathrm{d}t+2a_1\int_0^{T_{\text{th}}}\left(\sum_{l=2}^{L}a_l s(t-\tau_l)\right)s(t-\tau)\mathrm{d}t \\ -2\int_0^{T_{\text{th}}} r(t)\left(\sum_{l=2}^{L}a_l s(t-\tau_l)\right)\mathrm{d}t\end{pmatrix}}{\partial\tau} \\
&= -2a_1^2\int_0^{T_{\text{th}}} s(t-\tau)s^{'}(t-\tau)\mathrm{d}t-\int_0^{T_{\text{th}}}\left(2a_1\left(\sum_{l=2}^{L}a_l s(t-\tau_l)\right)-2a_1 r(t)\right)s^{'}(t-\tau)\mathrm{d}t \\
&= 0
\end{aligned} \tag{2.43}$$

From (2.43), we can see that the optimal τ may be not unique and cannot be directly found. Suppose that $\tau_{l,l=2\cdots L}$ are unknown and deterministic and τ_1 is unknown and variable. Let us expand the first derivative of the objective function $\xi(\tau_{1\cdots L})$ around the true τ_1

$$\frac{\partial\xi(\tau_{1\cdots L})}{\partial\tau}=\frac{\partial\xi(\tau_{1\cdots L})}{\partial\tau}\bigg|_{\tau=\tau_1}+(\tau-\tau_1)\frac{\partial\xi^2(\tau_{1\cdots L})}{\partial\tau^2}\bigg|_{\tau=\tau_1}+\mathrm{O}\left((\tau-\tau_1)^2\right). \tag{2.44}$$

Similar with (2.37), the estimation error can be written as

$$\tau_{\text{toa,ml}}-\tau_1=-\frac{\left.\frac{\partial\xi(\tau_{1\cdots L})}{\partial\tau}\right|_{\tau=\tau_1}}{E\left(\left.\frac{\partial^2\xi(\tau_{1\cdots L})}{\partial\tau^2}\right|_{\tau=\tau_1}\right)}. \tag{2.45}$$

The numerator and dominator of (2.45) can be calculated as

$$\begin{aligned}
&\left.\frac{\partial \xi(\tau_{1\cdots L})}{\partial \tau}\right|_{\tau=\tau_1} = -2a_1^2 \int_0^{T_{\text{th}}} s(t-\tau)s'(t-\tau)\mathrm{d}t\Bigg|_{\tau=\tau_1} - \\
&-\int_0^{T_{\text{th}}} \left(2a_1\left(\sum_{l=2}^{L} a_l s(t-\tau_l)\right) - 2a_1 r(t)\right) s'(t-\tau)\,\mathrm{d}t\Bigg|_{\tau=\tau_1} \\
&= -2a_1^2 \int_0^{T_{\text{th}}} s(t-\tau_1)s'(t-\tau_1)\,\mathrm{d}t + 2a_1^2 \int_0^{T_{\text{th}}} s(t-\tau_1)s'(t-\tau_1)\,\mathrm{d}t \qquad (2.46) \\
&+2a_1 \int_0^{T_{\text{th}}} w(t)s'(t-\tau_1)\,\mathrm{d}t \\
&= 2a_1 \int_0^{T_{\text{th}}} w(t)s'(t-\tau_1)\,\mathrm{d}t
\end{aligned}$$

$$\begin{aligned}
E\left(\left.\frac{\partial^2 \xi(\tau_{1\cdots L})}{\partial \tau^2}\right|_{\tau=\tau_1}\right) &= E\left(\begin{array}{l} 2a_1^2\left[\int_0^{T_{\text{th}}} s'^2(t-\tau_1)\,\mathrm{d}t + \int_0^{T_{\text{th}}} s(t-\tau_1)s''(t-\tau_1)\,\mathrm{d}t\right] \\ -2a_1^2 \int_0^{T_{\text{th}}} s(t-\tau_1)s''(t-\tau_1)\,\mathrm{d}t - 2a_1 \int_0^{T_{\text{th}}} w(t)s''(t-\tau_1)\,\mathrm{d}t \end{array}\right) \\
&= E\left(2a_1^2 \int_0^{T_{\text{th}}} s'^2(t-\tau_1)\,\mathrm{d}t - 2a_1 \int_0^{T_{\text{th}}} w(t)s''(t-\tau_1)\,\mathrm{d}t\right) \qquad (2.47) \\
&= 8\pi^2 a_1^2 \int_{-B}^{+B} f^2 \left|s(f)\right|^2 \mathrm{d}f
\end{aligned}$$

Substituting (2.46) and (2.47) into (2.45), we have

$$\tau_{\text{toa,ml}} - \tau_1 = -\frac{\int_0^{T_{\text{th}}} w(t)s'(t-\tau_1)\,\mathrm{d}t}{4\pi^2 a_1 \int_{-B}^{+B} f^2 \left|s(f)\right|^2 \mathrm{d}f}. \qquad (2.48)$$

The bias and variance of ML estimator can be expressed as

$$E\left(\tau_{\text{toa,ml}}-\tau_1\right)=0$$

$$E\left(\left(\tau_{\text{toa,ml}}-\tau_1\right)^2\right)=E\left(\frac{1}{16\pi^4 a_1^2}\frac{\left(\int_0^{T_{\text{th}}} w(t)s'(t-\tau_1)\,\mathrm{d}t\right)^2}{\left(\int_{-B}^{+B} f^2\left|s(f)\right|^2\,\mathrm{d}f\right)^2}\right)$$

$$=\frac{\int_0^{T_{\text{th}}}\text{var}\left(w(t)\right)s'^2(t-\tau_1)\,\mathrm{d}t}{16\pi^4 a_1^2\left(\int_{-B}^{+B} f^2\left|s(f)\right|^2\,\mathrm{d}f\right)^2}$$

$$=\frac{4\pi^2\sigma_n^2\int_{-B}^{+B} f^2\left|s(f)\right|^2\,\mathrm{d}f}{16\pi^4 a_1^2\left(\int_{-B}^{+B} f^2\left|s(f)\right|^2\,\mathrm{d}f\right)^2}$$

$$=\frac{\sigma_n^2}{4\pi^2 a_1^2\left(\int_{-B}^{+B} f^2\left|s(f)\right|^2\,\mathrm{d}f\right)^2}\quad . \tag{2.49}$$

Comparing to (2.32), the ML estimator is an efficient estimator. In practice, however, ML estimator is an asymptotic efficient because $s(t)$ is replaced by its sampled vector $\boldsymbol{s}_N$.

The (2.16) can be rewritten as

$$\hat{\tau}_{\text{toa,mmse}}=\frac{\int_0^{T_{\text{th}}}\tau\exp\left(\frac{a_1^2R(\tau-\tau_1)-a_1\left(R_{ns}(\tau_1)-R_{ns}(\tau)\right)}{\sigma_n^2}\right)\mathrm{d}\tau}{\int_0^{T_{\text{th}}}\exp\left(\frac{a_1^2R(\tau-\tau_1)-a_1\left(R_{ns}(\tau_1)-R_{ns}(\tau)\right)}{\sigma_n^2}\right)\mathrm{d}\tau}, \tag{2.50}$$

where $R_{ns}(\tau)$ is the cross-correlation function of $s(t)$ and $n(t)$.

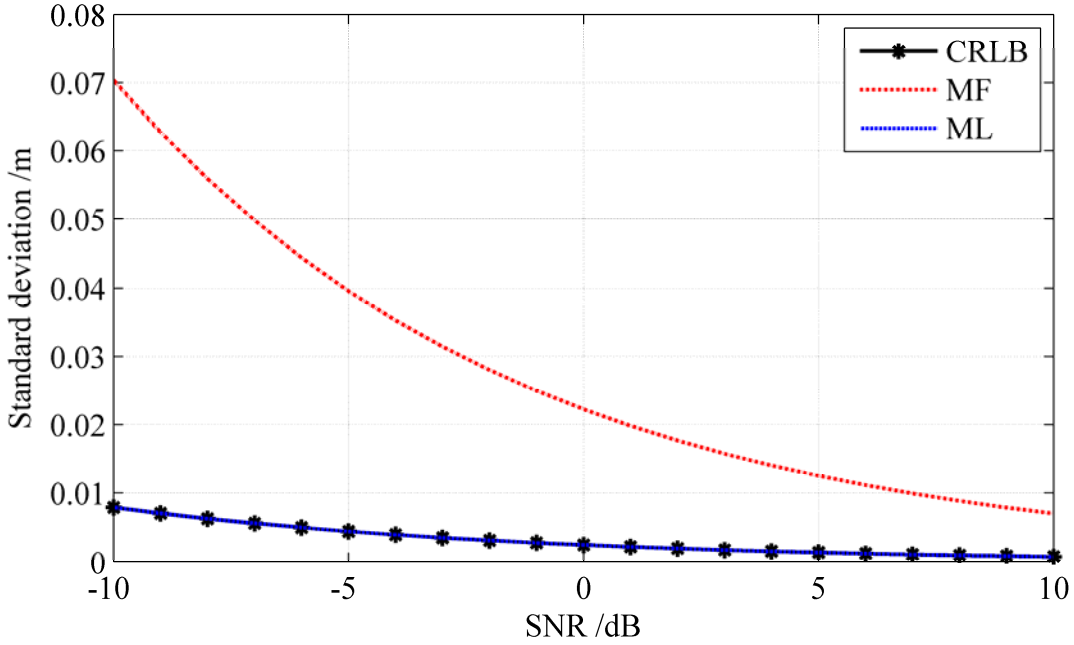

Figure 2.7: Standard deviation for MF and ML under the single-path scenario with 2-ns Gaussian monocycle

Figure 2.7 shows the standard deviation of MF and ML approaches. It is obvious that ML is better than MF.

From (2.21), the CRLB for estimating the distance in RSS-based ranging systems can be expressed as

$$\sqrt{\mathrm{var}\left(\hat{d}_n\right)} \geq \frac{\sigma \ln 10}{10\alpha\sqrt{K}} d_n, \tag{2.51}$$

where $\hat{d}_n$ represents an unbiased estimate of d_n. From (2.51), it can be seen that the lower bound increases with the increasing of the standard deviation of the shadowing and a larger transmission distance. The larger path loss exponent can result in better estimation accuracy. In all cases, the standard deviation for the error cannot be made smaller than 1m for distances larger than 6m [4]. From (2.26), we can define the objective function as

$$\zeta\left(\alpha, d_n\right) = \left|\hat{\bar{p}}_n\left(d_n\right) - p_0 + 10\alpha \log_{10}\left(d_n / d_0\right)\right|^2. \tag{2.52}$$

Differentiating $\zeta\left(\alpha, d_n\right)$ with respect to d_n and setting it to zero, we have

$$\hat{d}_n = d_0 10^{\frac{1}{10\alpha}\left(p_0 - \hat{\bar{p}}_n(d_n)\right)}. \tag{2.53}$$

The first-order and second-order statistics of $\hat{d}_n$ can be expressed as

$$E\left(\hat{d}_n\right)=E\left(d_0 10^{\frac{1}{10\alpha}\left(p_0-\hat{\bar{p}}_n(d_n)\right)}\right)$$

$$=d_0 E\left(10^{\frac{1}{10\alpha}\left(p_0-\hat{\bar{p}}_n(d_n)\right)}\right)$$

$$=d_n E\left(10^{\frac{w'_{K,n}}{10\alpha}}\right)$$

$$=\frac{10d_0\alpha}{\sqrt{\frac{2\pi}{K}}\sigma_n \ln 10}\int_0^{+\infty}\exp\left(-\frac{\left(p_0-10\alpha\log_{10}x-\bar{p}_n\left(d_n\right)\right)^2}{2\sigma_n^2/K}\right)\mathrm{d}x$$

$$=\frac{10d_0\alpha}{\sqrt{\frac{2\pi}{K}}\sigma_n \ln 10}\int_0^{+\infty}\exp\left(-\frac{\left(10\alpha\log_{10}\left(d_n/xd_0\right)\right)^2}{2\sigma_n^2/K}\right)\mathrm{d}x$$

$$=\frac{10d_n\alpha}{\sqrt{\frac{2\pi}{K}}\sigma_n \ln 10}\int_0^{+\infty}\exp\left(-\frac{50\alpha^2\log_{10}^2\left(x\right)}{\sigma_n^2/K}\right)\mathrm{d}x \qquad (2.54)$$

and

$$\mathrm{var}\left(\hat{d}_n\right)=E\left(\hat{d}_n^2\right)-E^2\left(\hat{d}_n\right)$$

$$=\frac{5d_n^2\alpha}{\sqrt{\frac{2\pi}{K}}\sigma_n \ln 10}\int_0^{+\infty}\exp\left(-\frac{25\alpha^2\log_{10}^2\left(x\right)}{2\sigma_n^2/K}\right)\mathrm{d}x- \qquad (2.55)$$

$$-\frac{50d_n^2\alpha^2K}{\pi\sigma_n^2\ln^2 10}\left(\int_0^{+\infty}\exp\left(-\frac{50\alpha^2\log_{10}^2\left(x\right)}{\sigma_n^2/K}\right)\mathrm{d}x\right)^2$$

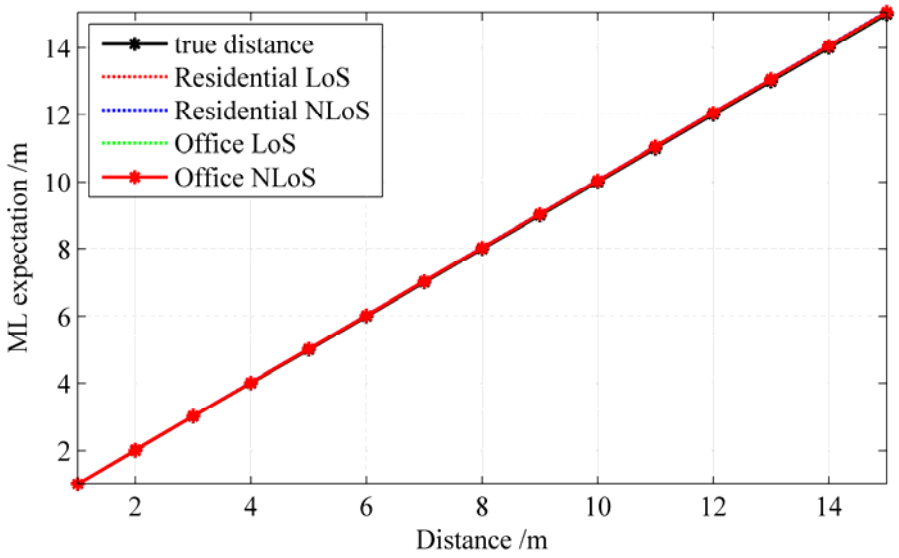

Figure 2.8: Expectation of ML estimator

Figure 2.8 depicts the expectation of ML estimator in residential LoS, residential NLoS, Indoor Office LoS and Indoor Office NLoS. It can be seen that (2.53) is a biased estimator, whose bias varies with α, σ and distance. For the specific α and σ, larger distance leads to larger bias. Table 2.1 shows the channel parameters for the environments investigated in and Figure 2.9.

Table 2.1: Channel parameters for different environments [4]

Environments	α	σ
Residential LOS	2.30	2.22
Residential NLOS	4.58	3.51
Indoor office LOS	2.10	1.90
Indoor office NLOS	3.07	3.90

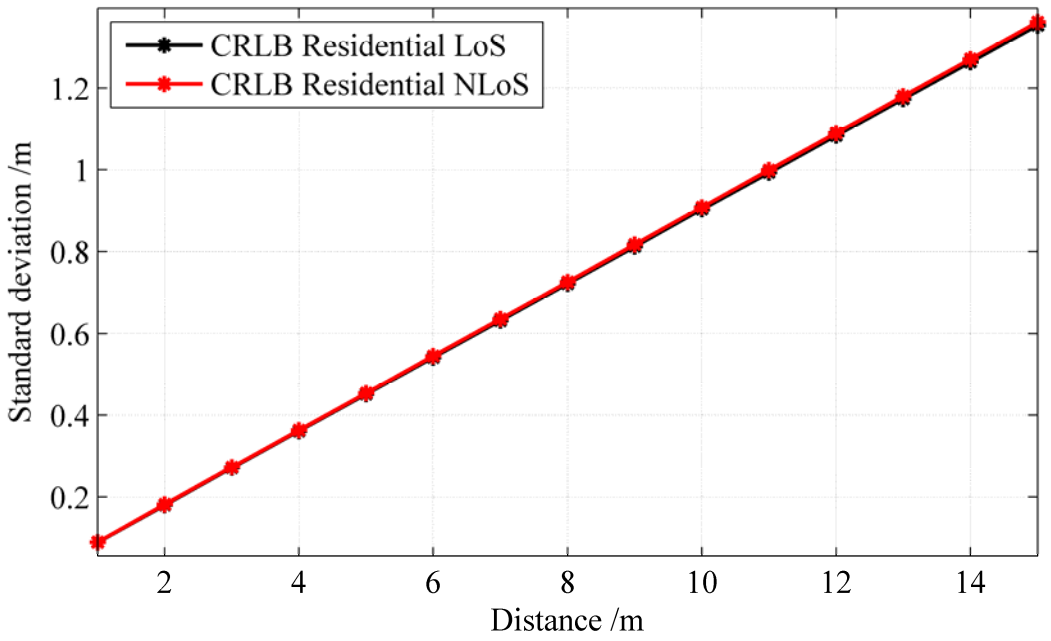

Figure 2.9: Standard deviation of ML estimator for residential LoS

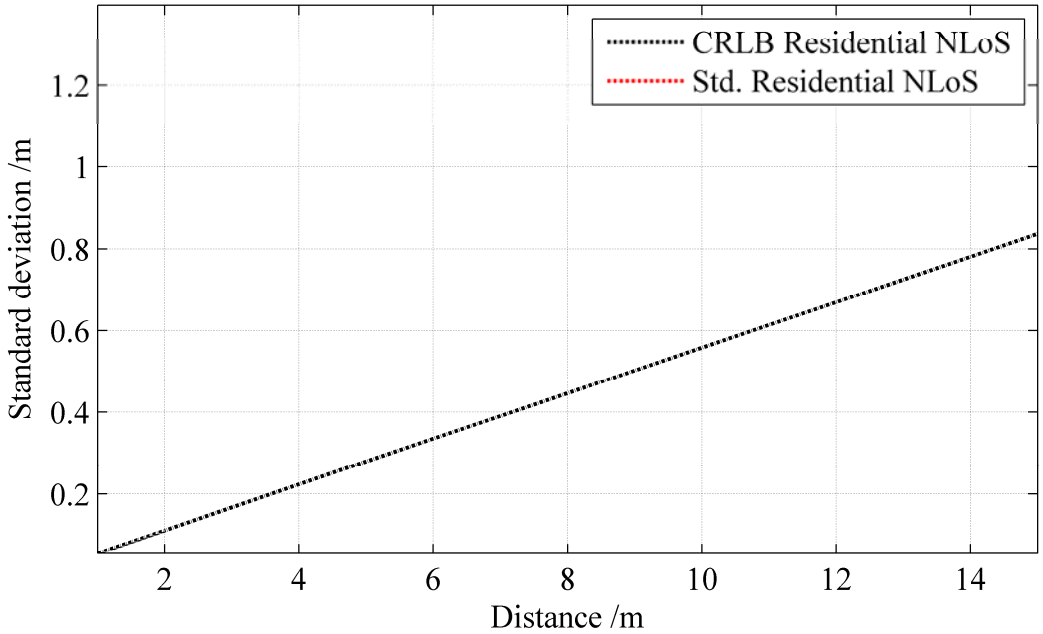

Figure 2.10: Standard deviation of ML estimator for residential NLoS

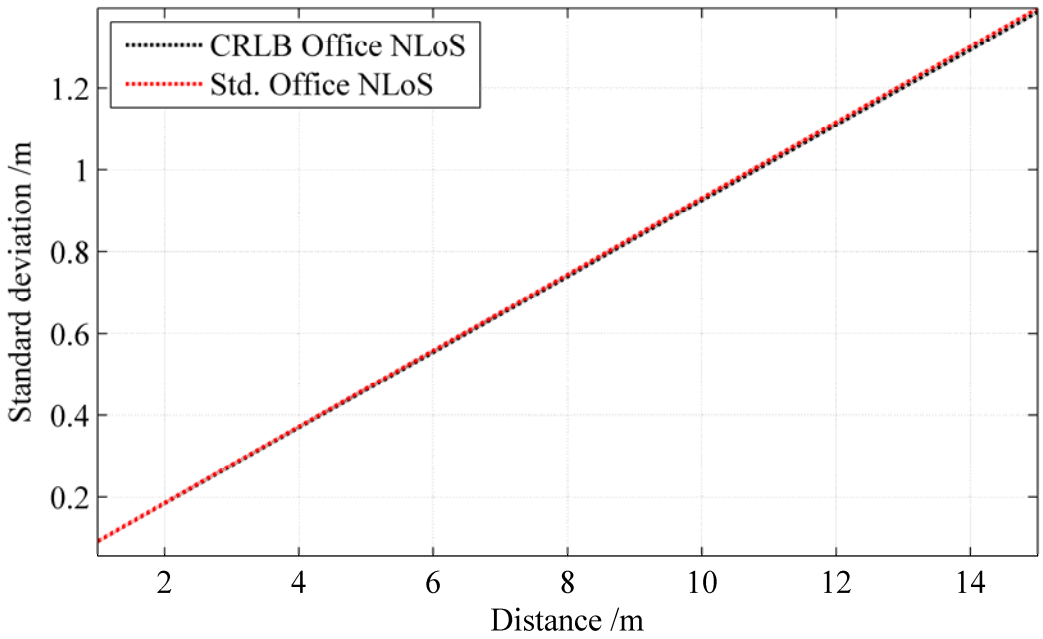

Figure 2.11: Standard deviation of ML estimator for office NLoS

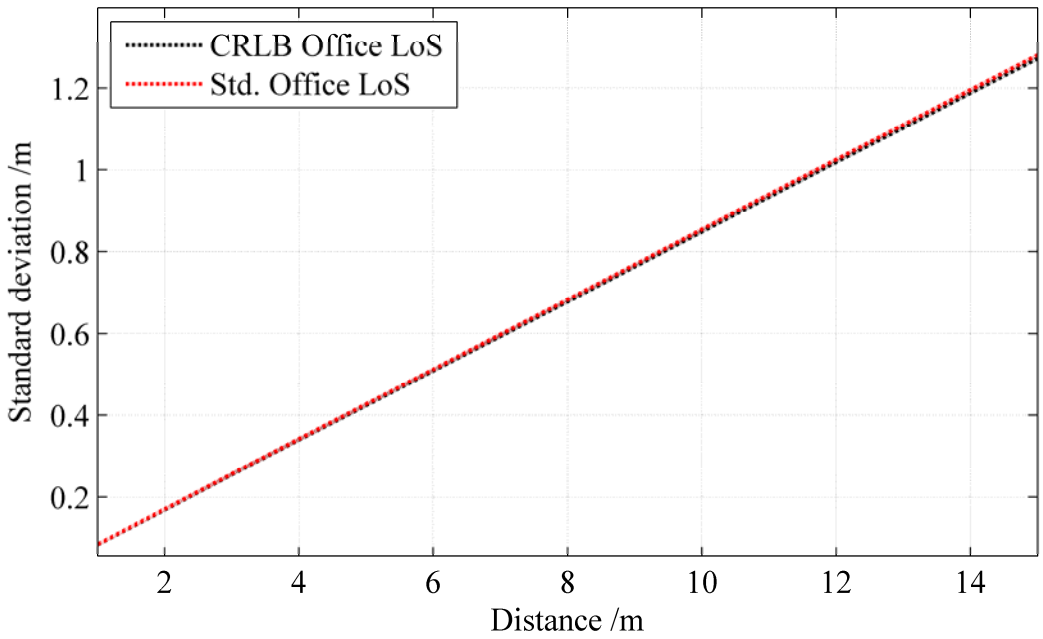

Figure 2.12: Standard deviation of ML estimator for office LoS

Figure 2.9 depicts the CRLB and standard deviation of (2.53) for the environments listed in Table 2.1. The accuracy of RSS measurements deteriorates as the distance between the transmitter and the receiver increases.

The following context will derive CRLB of AoA estimation for narrowband signal under single-path scenario. We rewrite (2.28) as

$$\underline{\boldsymbol{r}} = \underline{\boldsymbol{a}}\underline{s} + \underline{\boldsymbol{w}}, \tag{2.56}$$

where

$$\underline{\boldsymbol{a}} = \begin{bmatrix} 1 \\ e^{j\phi} \\ \vdots \\ e^{j(N-1)\phi} \end{bmatrix}, \underline{\boldsymbol{w}} = \begin{bmatrix} \underline{n}_1(t) \\ \underline{n}_2(t) \\ \vdots \\ \underline{n}_{N-1}(t) \end{bmatrix}. \tag{2.57}$$

Hence, the PDF of the received data can be expressed as

$$p(\underline{\boldsymbol{r}};\theta) = \frac{1}{\left(2\pi|\boldsymbol{R}_n|\right)^{\frac{N}{2}}} \exp\left(-\frac{\left(\underline{\boldsymbol{r}} - \underline{\boldsymbol{a}}\underline{s}\right)^{\mathrm{H}} \boldsymbol{R}_n^{-1} \left(\underline{\boldsymbol{r}} - \underline{\boldsymbol{a}}\underline{s}\right)}{2} \right), \tag{2.58}$$

where $\boldsymbol{R}_n$ is the covariance matrix of the noise vector $\underline{\boldsymbol{w}}$. Then the expectation of first derivative of the PDF can be expressed as

$$\begin{aligned} E\left(\frac{\partial\left(\ln p(\underline{\boldsymbol{r}};\theta)\right)}{\partial\theta} \right) &= E\left(-\left(\frac{\partial\left(\frac{\left(\underline{\boldsymbol{r}} - \underline{\boldsymbol{a}}\underline{s}\right)^{\mathrm{H}} \boldsymbol{R}_n^{-1} \left(\underline{\boldsymbol{r}} - \underline{\boldsymbol{a}}\underline{s}\right)}{2} \right)}{\partial \underline{\boldsymbol{a}}} \right)^{\mathrm{H}} \frac{\partial \underline{\boldsymbol{a}}}{\partial\phi} \frac{\partial\phi}{\partial\theta} \right) \\ &= -E\left(-\left(\underline{s}\boldsymbol{R}_n^{-1}\left(\underline{\boldsymbol{r}} - \underline{\boldsymbol{a}}\underline{s}\right)\right)^{\mathrm{H}} \frac{\partial \underline{\boldsymbol{a}}}{\partial\phi} \frac{\partial\phi}{\partial\theta} \right) \\ &= \left(\underline{s}\boldsymbol{R}_n^{-1}\left(E\left(\underline{\boldsymbol{r}}\right) - \underline{\boldsymbol{a}}\underline{s}\right)\right)^{\mathrm{H}} \frac{\partial \underline{\boldsymbol{a}}}{\partial\phi} \frac{\partial\phi}{\partial\theta} \\ &= 0 \end{aligned}. \tag{2.59}$$

The expectation of second derivative of the PDF can be written as

$$E\left(\frac{\partial\left(\left(\underline{s}\boldsymbol{R}_n^{-1}\left(\underline{\boldsymbol{r}} - \underline{\boldsymbol{a}}\underline{s}\right)\right)^{\mathrm{H}} \frac{\partial \underline{\boldsymbol{a}}}{\partial\phi} \frac{\partial\phi}{\partial\theta} \right)}{\partial\theta} \right) = -s^2 \left(\frac{\partial \underline{\boldsymbol{a}}}{\partial\phi} \frac{\partial\phi}{\partial\theta} \right)^{\mathrm{H}} \boldsymbol{R}_n^{-\mathrm{H}} \frac{\partial \underline{\boldsymbol{a}}}{\partial\phi} \frac{\partial\phi}{\partial\theta}. \tag{2.60}$$

Hence, the CRLB of AoA can be determined as

$$\begin{aligned} \mathrm{var}\left(\hat{\theta}\right) &\geq -\frac{1}{E\left(\frac{\partial^2\left(\ln\left(p(\underline{\boldsymbol{r}};\theta)\right)\right)}{\partial\theta^2} \right)} = \frac{1}{\|s\|^2 \left(\frac{\partial \underline{\boldsymbol{a}}}{\partial\phi} \frac{\partial\phi}{\partial\theta} \right)^{\mathrm{H}} \boldsymbol{R}_n^{-\mathrm{H}} \frac{\partial \underline{\boldsymbol{a}}}{\partial\phi} \frac{\partial\phi}{\partial\theta}} \\ &= \frac{c^2\sigma_n^2}{4\|s\|^2 \pi^2 f_c^2 d^2 \sin^2\theta \sum_{n=1}^{N} n^2} \end{aligned}. \tag{2.61}$$

It can be seen from (2.61) that the CRLB of AoA estimation is sensitive to the SNR, the number of antenna elements, carrier frequency and the inter-element spacing. Figure 2.13 shows the CRLB of AoA estimation for the AoA: 30°, 60° and 90°. The

number of antenna elements is four. Carrier frequency is 5.2GHz and the inter-element spacing is 4.43cm. The variance of AoA estimation using MUSIC and ML approach will not be discussed in this dissertation.

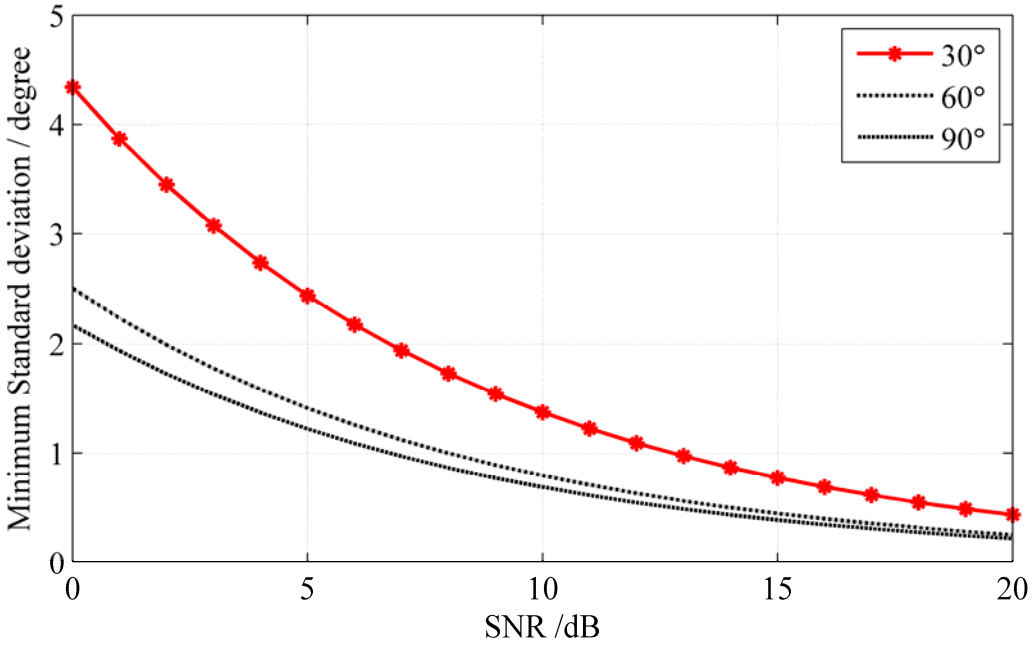

Figure 2.13: Minimum Standard Deviation for the AoA of 30°, 60° and 90°

2.3.6 Error Sources of ToA/TDoA based Ranging

For the ToA/TDoA UWB ranging systems, the timing imperfections among reference devices in infrastructure-based ranging and clock drifting between transmitter and receiver devices in the ToA measurements induce additional errors on range estimates [4]. In the ToA/TDoA based UWB ranging systems, multipath propagation introduces challenges for ranging due to a large number of MPCs and relatively long excess delays compared to the transmitted pulse duration. In the absence of multipath propagation, estimation of the arriving time of a signal is relatively easy via matched filter or energy detector, which has been investigated in several literatures. In practice, however, reflections from scatters in an environment arrive at a receiver as replicas of the transmitted signal with various attenuation levels and delays [4]. Due to the NLoS, antenna effect or the lognormal fading effect, the strongest path may arrive later than the leading edge [4]. Figure 2.14 and Figure 2.15 illustrate the UWB received signal under sparse multipath scenario. The sparse multipath scenario is characterized by an impulse response that only comprises a few significant multipath terms, the time gap between each pair of which is larger than the signal duration. Under sparse multipath scenario, the received signal suffers from no distortion. Figure 2.14 shows the scenario that the first path is the strongest path, which can be easily detected by the correlation peak, while Figure 2.15 illustrates that the strongest path arrives

sometimes later than the first path. In such case, the strongest correlation peak shows a wrong position of leading edge.

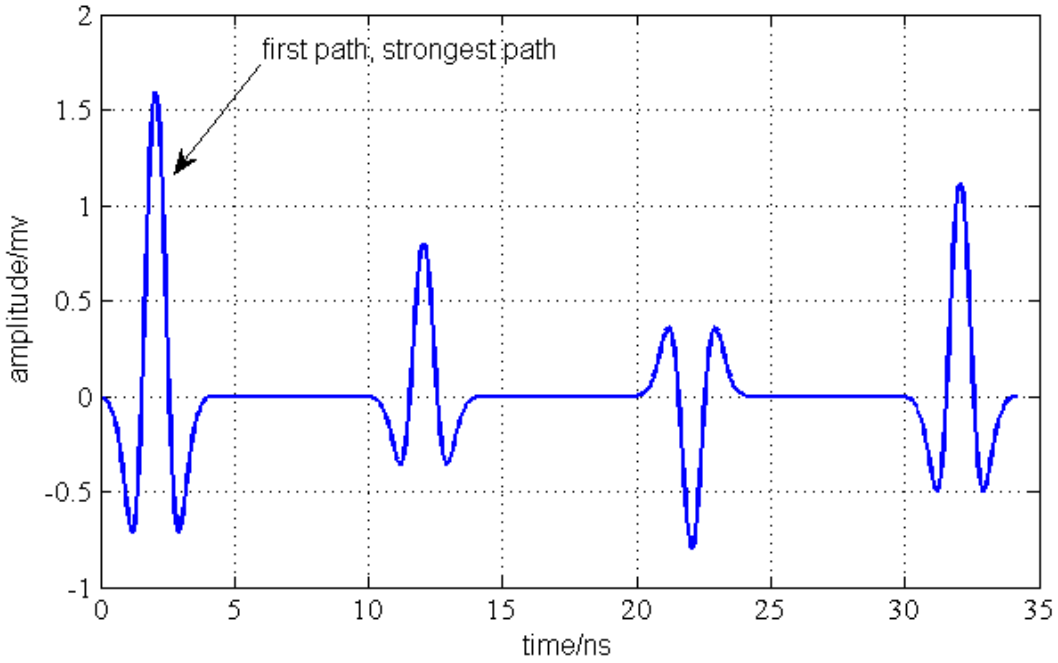

Figure 2.14: Received signal amplitude under sparse multipath scenario (strongest path is the first path)

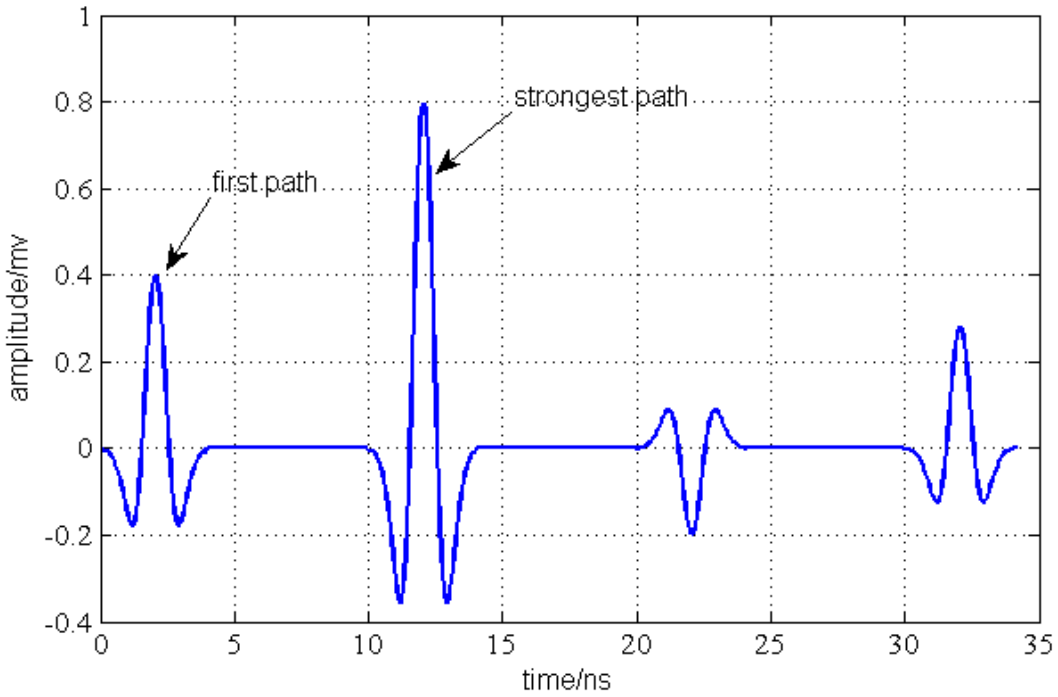

Figure 2.15: Received signal amplitude under sparse multipath scenario (strongest path is not the first path)

Another errors source for ToA/TDoA ranging systems is the imperfect autocorrelation characteristics of the transmitted signal or spreading sequences. In general, UWB ranging systems exploit second derivative of Gaussian monopulse as their signal format (see Figure 2.16). Under sparse multipath environments, the correlation peak always indicates the middle position of the Gaussian monopulse, which has the maximum signal power due to distortion-less of the received waveform (see Figure 2.14). In the dense multipath environments, the received waveform shall be modeled as superposition of multi reflections with different attenuations and time delays (see Figure 2.18). The correlation peak in such case may not indicate the middle position of Gaussian monopulse due to the Inter Pulse Interference (IPI) caused by the imperfect autocorrelation characteristics of the exploited pulse (see Figure 2.16). As can be seen from Figure 2.19, the black curve represents the correlation function of the signal without distortion, while the red one represents the correlation function of the actual received signal with distortion, whose correlation peak shows a time delay relative to the desired one.

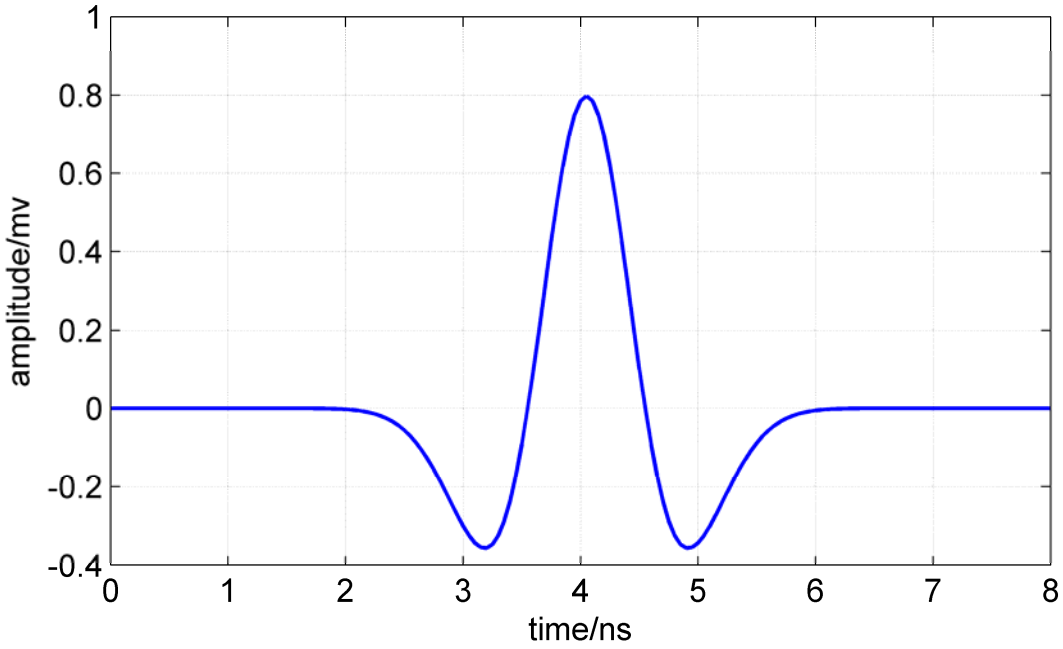

Figure 2.16: Second derivate of Gaussian mono-pulse without distortion

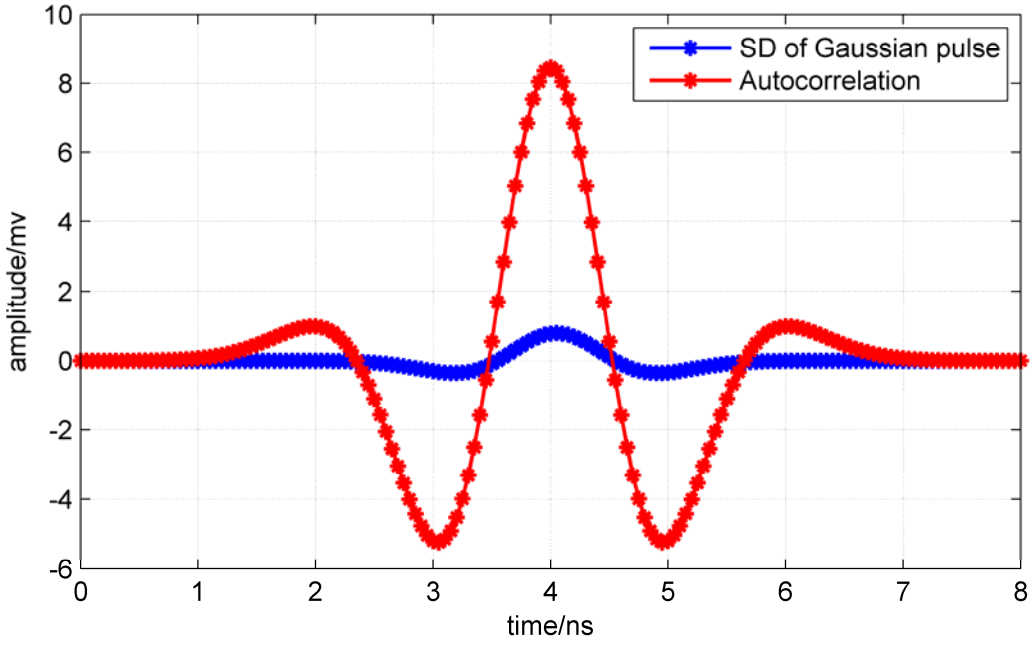

Figure 2.17: Autocorrelation of the received signal without distortion

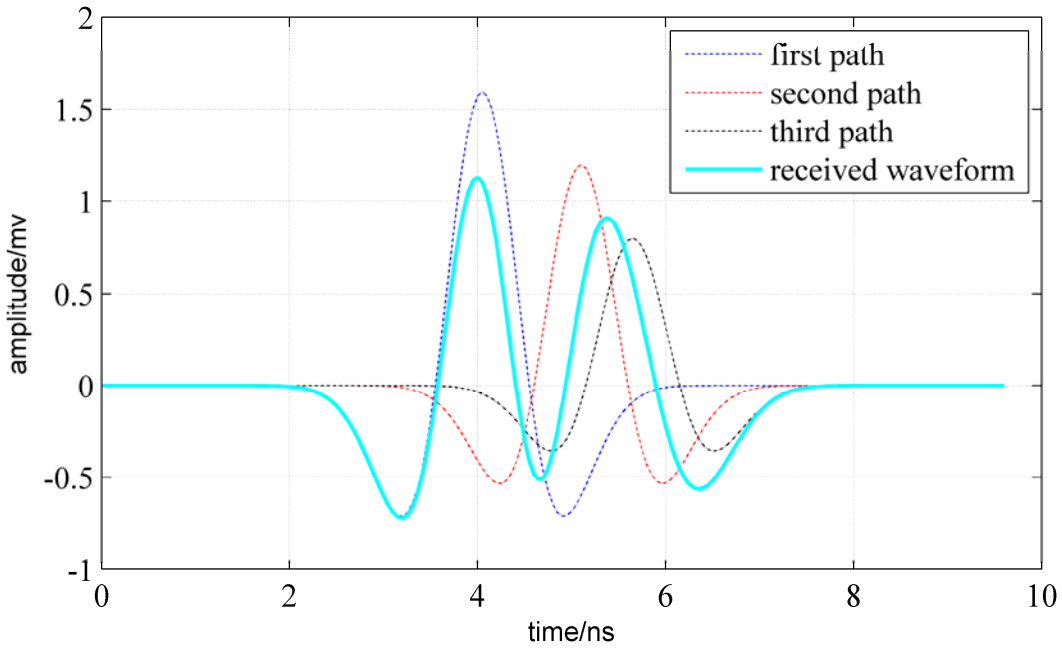

Figure 2.18: Signal distortion under dense multipath environments

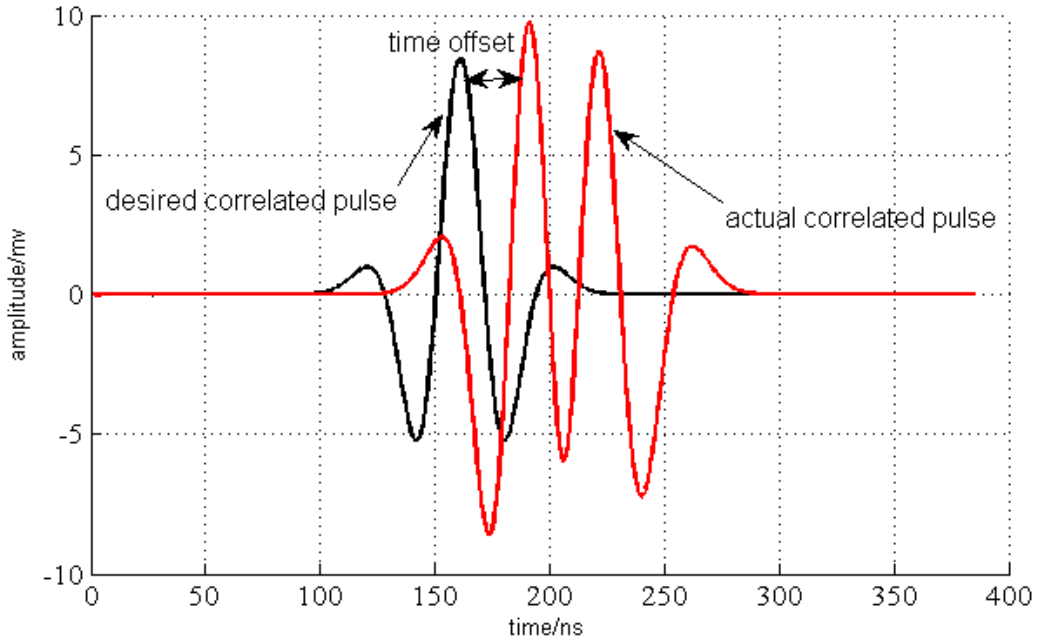

Figure 2.19: Time offset caused by signal distortion

Imperfect design of spreading sequences exploited by UWB ranging systems is another errors source. According to [22], UWB systems shall allocate a unique spreading sequence to each user in order to suppress the Multi User Interference (MUI) during the transmission. At the receiver, the signal shall be de-spread by the spreading sequence of the desired user to get the received signal. It then locks onto the correlation peak, and tries to identify the first arriving MPC preceding the correlation peak. If the spreading sequence of the desired user does not own perfect autocorrelation characteristics, the correlation side-lobes will appear between the correlation peaks [4], which can negatively influence detection of the leading edge.

If there are several UWB users under detect in the ranging system, the MUI will become another challenging issue. Under the single path scenario, the MUI can be suppressed or avoided by the perfect cross-correlation characteristics of the spreading sequences between each pair of users. Under multi path scenario, however, the MUI cannot be easily mitigated since the interference signal through each channel path with a different time delay may have a contribution to the MUI.

NLoS transmission is another error source for the ranging systems. If the Direct Path (DP) between the transmitter and the receiver is partially obstructed (e.g. obstructed by timber), the signal through the DP can be attenuated more than other MPCs, which can make the leading edge detection more challenging. If the DP is completely obstructed (e.g. obstructed by metal), the receiver can only detect the signal from other MPCs, whose leading edge has a time offset than that of DP. Then, it will introduce a positive bias to the ToA estimate. The positive bias was modeled as a Gaussian distribution random variable [84] or a constant along a time interval [87].

2.3.7 Error Sources of RSS based Ranging

It is obvious that lognormal fading effect can lead to estimation error in RSS based ranging. The description of lognormal fading effect on the estimation performance can be found in Section 2.3.3. Under multipath scenario, the received signal power shall be collected from each channel path. Figure 2.20 illustrates the determination of received signal power under multipath scenario.

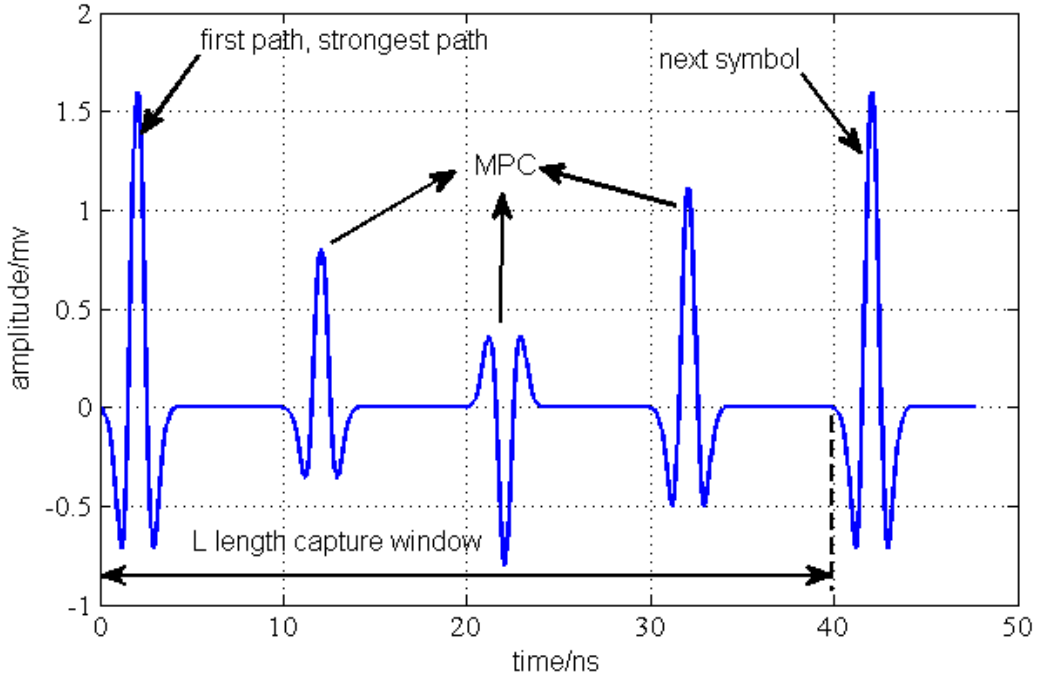

Figure 2.20: Determination of received signal power under multipath scenario

It can be concluded from Figure 2.20 that selection of the capture window length L is another key factor which affects the determination of received signal power. If $L < T_{\mathrm{d}}$, where T_{d} is the excess delay of the multipath channel, the received signal power cannot be entirely captured within the window so that

$$p'_{k,n}(d_n) = p_{k,n}(d_n) - \delta_p \tag{2.62}$$

where $p'_{k,n}(d_n)$ is the actual determined received signal power and δ_{p} is a power offset. Hence, it leads to $d'_n = d_n + \delta_{\mathrm{d}}$. In general, L is set to be equal to a Pulse Repetition Period (PRP) to avoid the pulse overlapping. However, if the channel excess delay is larger than PRP ($L < T_{\mathrm{d}}$), the fluctuation of $p_{k,n}(d_n)$ may be caused by two factors: pulse overlapping and smaller captured signal power. The hybrid of two factors can lead to an irregular fluctuation of $p_{k,n}(d_n)$: $p'_{k,n}(d_n) > p_{k,n}(d_n)$ with in-phase overlapping, $p'_{k,n}(d_n) < p_{k,n}(d_n)$ with out-of-phase overlapping and $p'_{k,n}(d_n) \approx p_{k,n}(d_n)$ without pulse overlapping. Obviously, MUI is another key factor which can degrade RSS based ranging performance to a large extent. Similar with

ToA based ranging systems, the spreading sequences shall be employed to suppress MUI.

2.3.8 UWB Indoor Channel

Large bandwidth of UWB systems leads to much difference in channel characterization compared to that of the narrow band systems. Due to the reflected materials and the characteristics of transmit and receive antennas, the UWB channel become always frequency selective, which can bring the frequency diversity gain at the receiver. For the ranging systems, however, the frequency selective property can negatively influence the ranging parameters since the received signal may suffer from distortion (see Figure 2.16).

There are two common methods for characterization of UWB channels. The first one is the deterministic channel modeling, which assumes that complete geometric information of the environment is available. The propagation characteristics of the environment can be generated by using ray-tracing techniques [88][89]. The main disadvantage of deterministic channel modeling is that the measured channel parameters are only applicable for the certain environment. Hence, in this dissertation, the author uses statistical channel modeling which need only determine the following parameters: power delay profile, path loss and shadowing, which are related to the ranging performance. The modified version of the original Saleh-Valenzula (S-V) model is employed in this dissertation. The *n*-th user's time variant channel impulse response can be given as [90]:

$$\underline{h}_n(t,\tau) = \sum_{k=1}^{K_n(\tau)} \sum_{l=1}^{L_n(\tau)} \alpha_{l,n}(\tau) e^{j\phi_{l,n}(\tau)} \delta\left(t - T_{k,n}(\tau) - \tau_{l,k,n}(\tau)\right), \tag{2.63}$$

where $\underline{h}_n(t,\tau)$ represents one channel realization for a given time τ. $T_{k,n}(\tau)$ is the function of τ, which represents the arrival time of the *k*-th cluster for the τ-th realization, and $\tau_{l,k,n}(\tau)$ represents the arrival time of the *l*-th path in *k*-th cluster for the τ-th realization. $T_{k,n}(\tau)$ and $\tau_{l,k,n}(\tau)$ are modeled as the Poisson distribution with the fixed rate Λ and λ, respectively. $\alpha_{l,n}(\tau)$ and $\phi_{l,n}(\tau)$ represents the channel coefficient and phase of the *l*-th path, respectively. According to [91], the coherence time of the indoor channel without presence of Doppler effect is a value on millisecond level. Hence, $T_{k,n}(\tau)$, $\tau_{l,k,n}(\tau)$, $\alpha_{l,n}(\tau)$ and $\phi_{l,n}(\tau)$ can be considered as constant values within one millisecond. Hence, (2.63) can be replaced by the time invariant channel model, which can be expressed as

$$\underline{h}_n(t) = \sum_{k=1}^{K_n} \sum_{l=1}^{L_{k,n}} \alpha_{l,n} e^{j\phi_{l,n}} \delta\left(t - T_{k,n} - \tau_{l,k,n}\right), \tag{2.64}$$

where K_n and $L_{k,n}$ are the number of clusters and the number of rays in the *k*-th cluster. In general, $T_{1,n}$ and $\tau_{l,1,n}$ are defined to be zero. According to [90], $T_{k,n}$ and $\tau_{l,k,n}$ can be described as the inter-arrival exponential probability density functions

$$p\left(T_{k,n} \mid T_{k-1,n}\right) = \Lambda e^{-\Lambda\left(T_{k,n}-T_{k-1,n}\right)}$$
$$p\left(\tau_{l,k,n} \mid \tau_{l-1,k,n}\right) = \lambda e^{-\lambda\left(\tau_{l,k,n}-\tau_{l-1,k,n}\right)}. \quad (2.65)$$

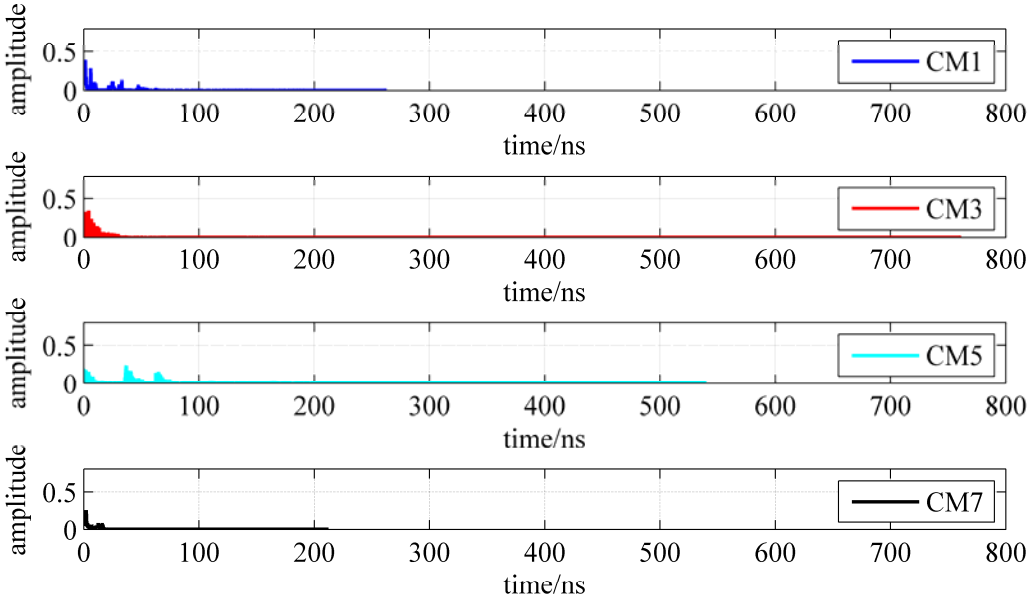

Figure 2.21: CM1, CM3, CM5 and CM7 channel realization

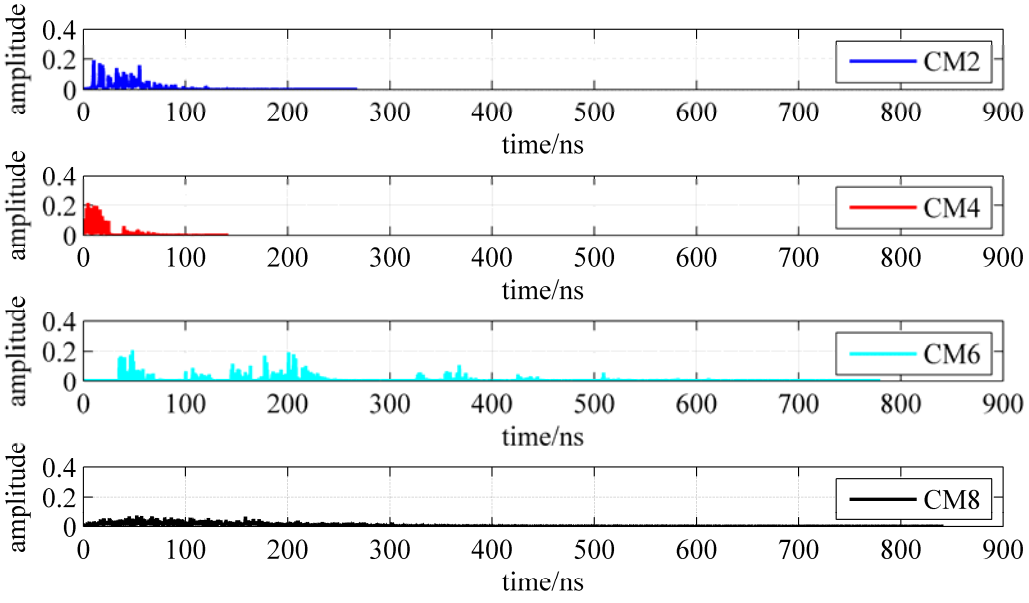

Figure 2.22: CM2, CM4, CM6 and CM8 channel realization

Figure 2.21 and Figure 2.22 show the channel realization of CM1 to CM8 , which are proposed by IEEE 802.15.4a. The channel realizations are sampled with the rate of 8GHz. According to [22], CM1, CM3, CM5 and CM7 are defined as residential LoS, indoor office LoS, outdoor LoS and industrial LoS, respectively. CM2, CM4, CM6 and CM8 are defined as residential NLoS, indoor office NLoS, outdoor NLoS and industrial NLoS, respectively. We can see that the first path always shows maximum

channel energy in the LoS scenario while the maximum path may arrive later than the first path in the NLoS scenario.

2.3.9 Ranging related Channel Parameters

For ToA/TDoA based UWB ranging, the MED (Maximum Excess Delay), 20dB-ED (20dB Excess Delay), MELER (Maximum Energy to Leading Energy Ratio), PLD (Peak to Leading edge Delay) are key factors determining the ranging accuracy. The 20dB-ED is defined to be the time delay during which the multipath energy falls to 20dB below the maximum peak. MELER is defined as the ratio between the maximum peak and the first peak. PLD is the time delay between the first peak and the maximum peak. The large 20dB-ED can lead to IPI (Inter Pulse Interference), which can negatively influence the maximum peak determination. MELER and PLD play important roles in the search-back algorithm, which has been discussed in [67]. From (2.64) and (2.65), we can see that MED, 20dB-ED, MELER and PLD are statistical numbers, which will give a different value for each channel realization. The CDF (Cumulative Distribution Function) of each parameter can be expressed as

$$\begin{aligned} \mathrm{cdf}_{\mathrm{mer}}(t) &\approx \mathrm{num}(\mathrm{MER} \le t)/N_{\mathrm{loop}} \\ \mathrm{cdf}_{\mathrm{20db\text{-}ed}}(t) &\approx \mathrm{num}(\mathrm{20dB\text{-}ED} \le t)/N_{\mathrm{loop}} \\ \mathrm{cdf}_{\mathrm{meler}}(R) &\approx \mathrm{num}(\mathrm{MELER} \le R)/N_{\mathrm{loop}} \\ \mathrm{cdf}_{\mathrm{pld}}(t) &\approx \mathrm{num}(\mathrm{PLD} \le t)/N_{\mathrm{loop}} \end{aligned}, \tag{2.66}$$

where N_{loop} is the number of Monto-Carlo simulation. It is obvious that (2.66) may converge to the true CDF if N_{loop} becomes larger. N_{loop} is set to be 1000 in this dissertation. $\mathrm{num}(\ )$ represents the number of simulations, which fulfill the specific condition. Figure 2.23 to Figure 2.32 show the CDF of MER, 20dB-ED, MELER and PLD for CM1, CM3 and CM5.

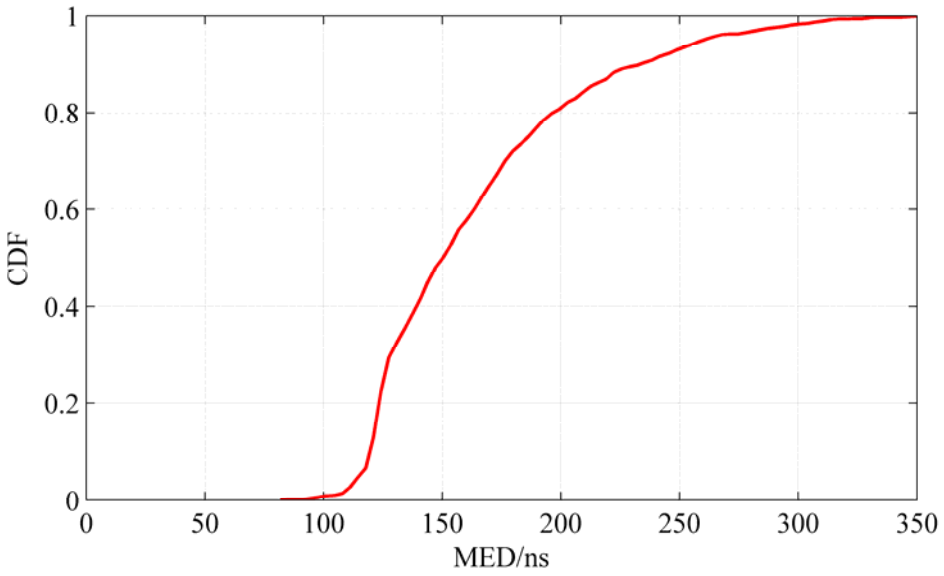

Figure 2.23: CDF of MED in CM1

From Figure 2.23, we can see that the MED is smaller than 400ns with approximate 100% in CM1.

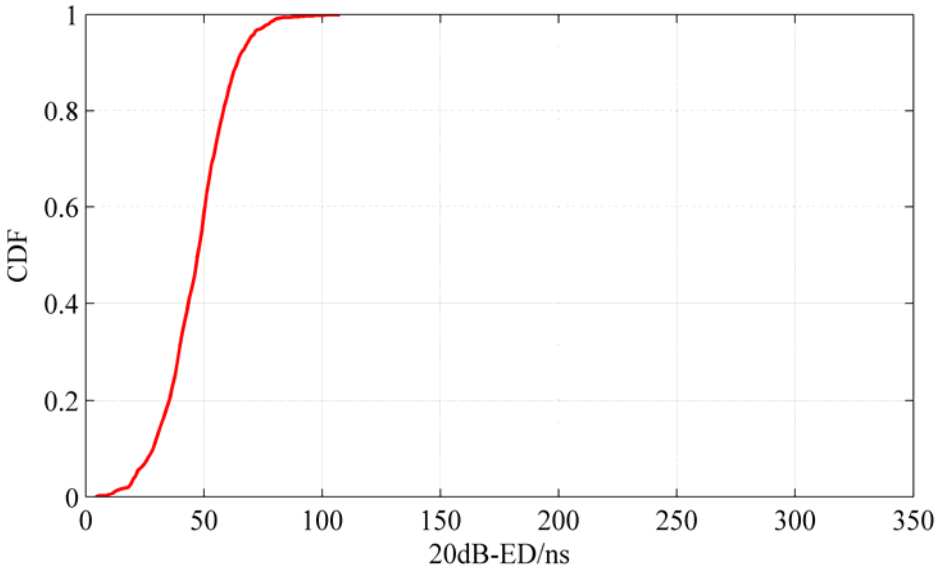

Figure 2.24: CDF of 20dB-ED in CM1

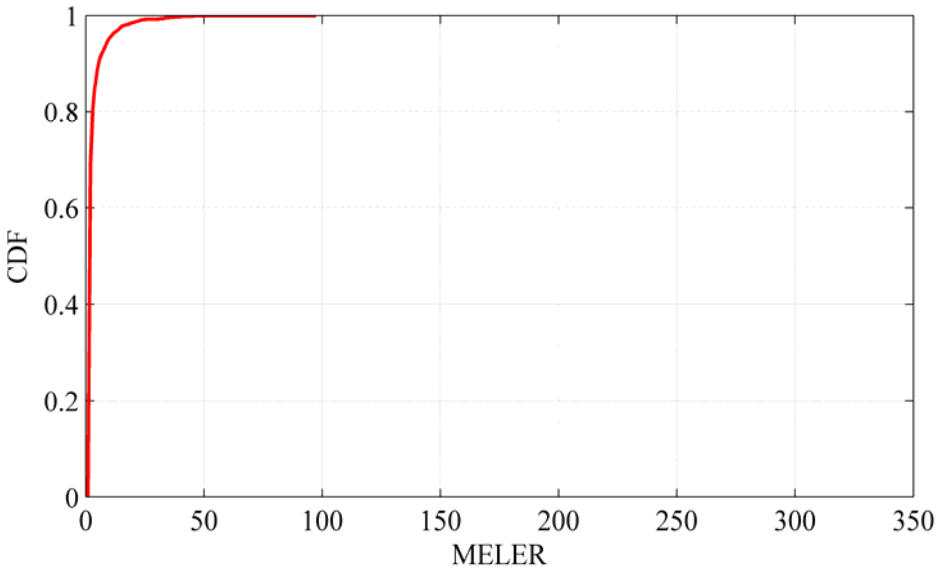

Figure 2.25: CDF of MELER in CM1

From Figure 2.24 and Figure 2.25, we can see that the 20dB-ED is smaller than 100ns with the probability of 100% and MELER is smaller than 60 with the probability of 100%.

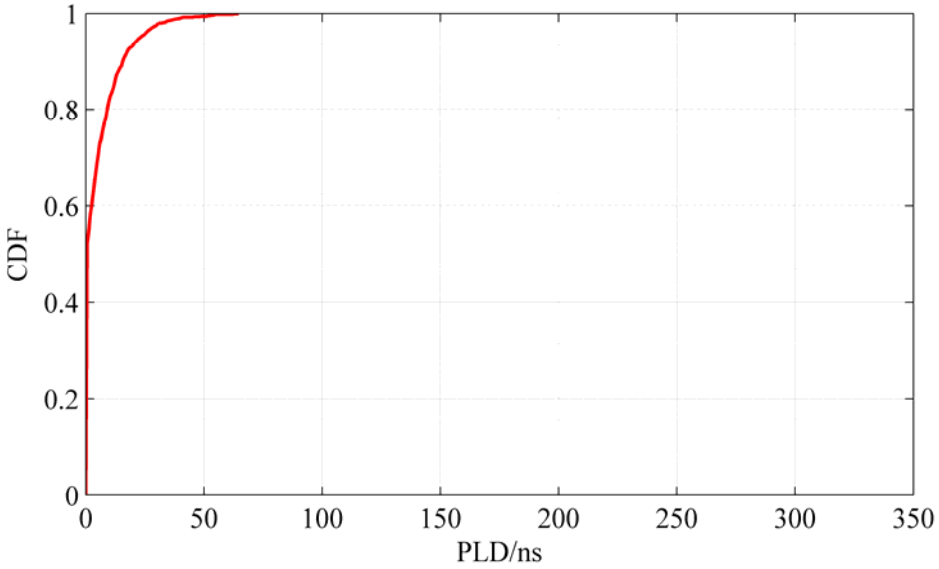

Figure 2.26: CDF of PLD in CM1

Figure 2.26 shows that the PLD is smaller than 60ns with 100% in CM1.

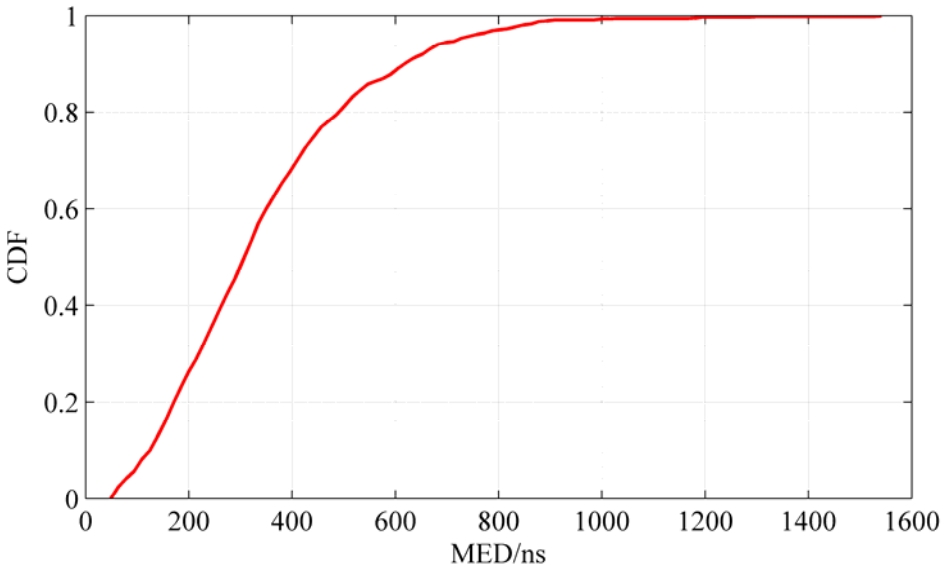

Figure 2.27: CDF of MED in CM3

Figure 2.27 shows that the MED is smaller than 1600ns with 100% in CM3.

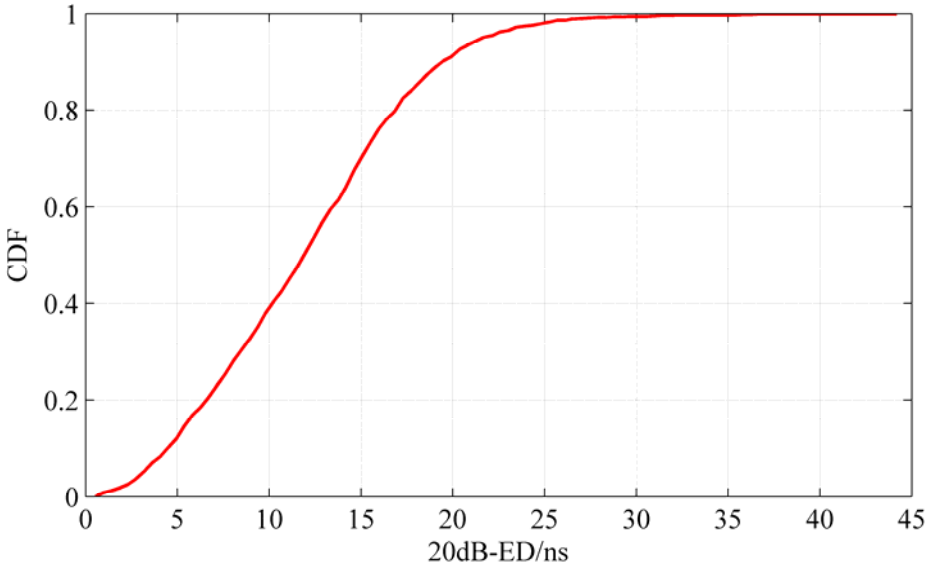

Figure 2.28: CDF of 20dB-ED in CM3

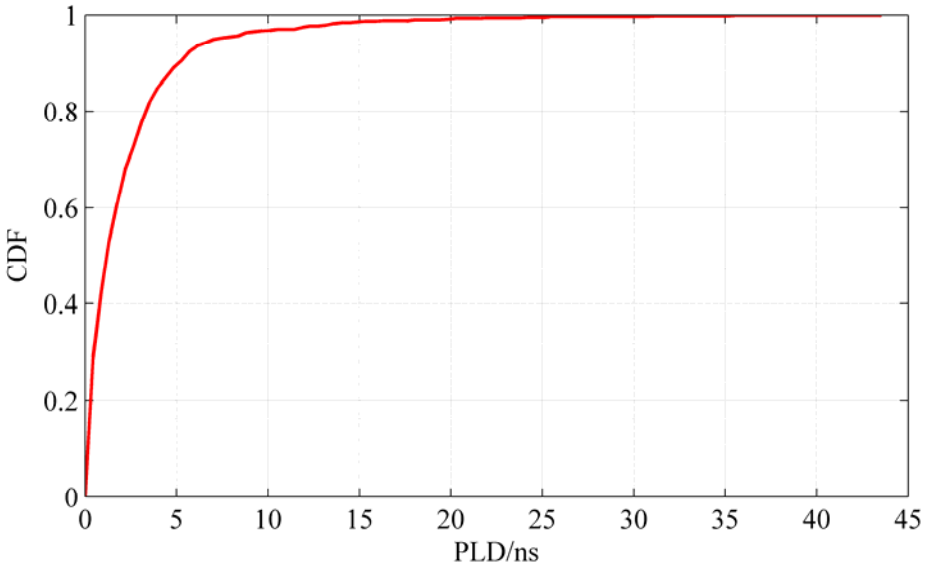

Figure 2.29: CDF of PLD in CM3

Figure 2.29 shows that the PLD is smaller than 25ns with approximate 100% in CM3.

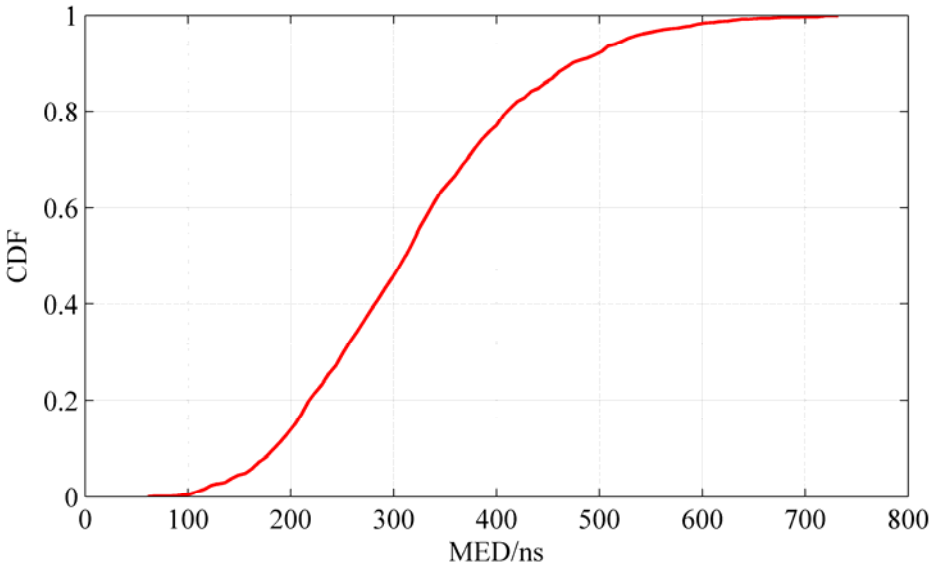

Figure 2.30: CDF of MED in CM5

Figure 2.30 shows that the MED is smaller than 700ns with approximate 100% in CM5

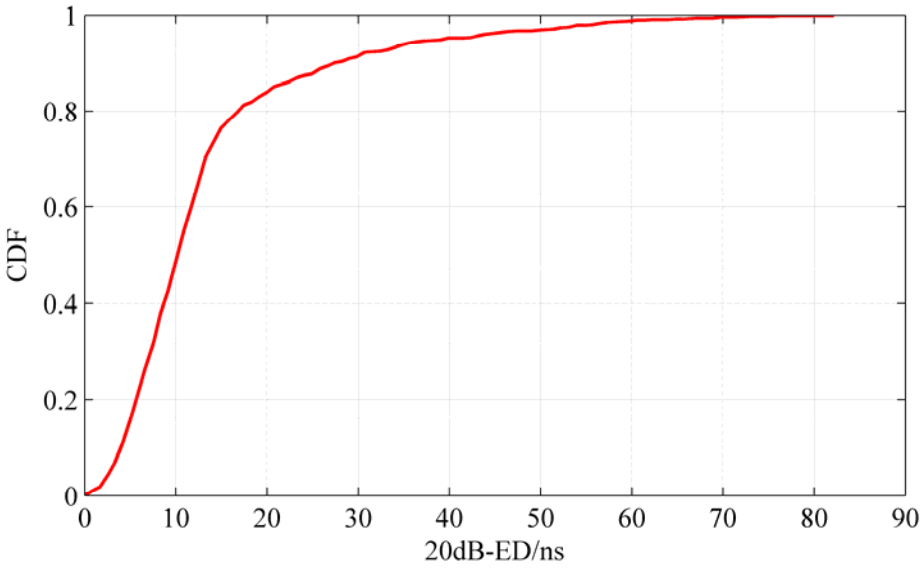

Figure 2.31: CDF of 20dB-ED in CM5

Figure 2.31 and show that the 20dB-ED is smaller than 70ns with approximate 100% and the MELER is smaller than 19400 with approximate 100% in CM5.

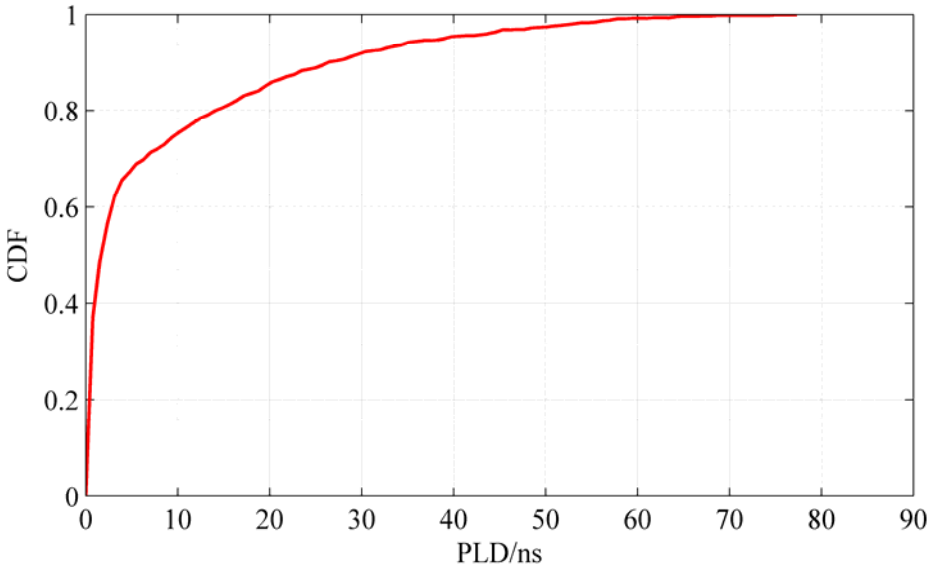

Figure 2.32: CDF of PLD in CM5

Figure 2.32 shows that the PLD is smaller than 70ns with approximate 100% in CM5. The aforementioned parameters are key factors, which determine the localization accuracy.

2.3.10 Error Sources of AoA based Ranging

In AoA based narrow band ranging systems (e.g. WLAN), the estimation error mainly comes from three sources:

1. Imperfect phase synchronization
2. Grating lobe of antenna array
3. Multipath transmission

Generally, one global Local Oscillator (LO) is deployed on the receiver to generate the reference clock with a constant phase offset while RF frontend chip for each channel is equipped with one independent Phase-Locked Loop (PLL). Ideally, the steady-state phase error should be zero and each PLL should output a clock with a constant phase offset since there is only one global LO. In practice, however, the average difference in time between the phases of the two signals when the PLL has achieved lock is a random number. Therefore, phase offset caused by PLL is not inevitable and that may seriously degrade the performance of AoA estimation. To suppress the effect of phase offset, initial calibration process before AoA estimation shall be performed. The detailed description of the calibration process can be found in chapter 4.

Grating lobe as the ambiguous direction with ideally the same radiation intensity is another error source for AoA estimation. Any actual radiation direction θ beyond the scope of clarity area of the antenna array will be detected to a mirror direction θ'. The relation between the actual and the mirror angle can be expressed as

$$\theta = \begin{cases} \arccos\left(\frac{\lambda}{d}\left(\frac{d}{\lambda}\cos\theta' + 1\right)\right), \text{if } \frac{d}{\lambda}\cos\theta' < \frac{d}{\lambda} - 1 \\ \arccos\left(\frac{\lambda}{d}\left(\frac{d}{\lambda}\cos\theta' - 1\right)\right), \text{if } \frac{d}{\lambda}\cos\theta' > 1 - \frac{d}{\lambda} \end{cases}, \tag{2.67}$$

where λ is the wavelength, which depends on the carrier frequency f_c, d is the inter-element spacing and θ is considered as the angle between wave impinging direction and the antenna array (see Figure 2.6). The clarity area of the antenna array can be calculated as

$$\arccos\left(\frac{\lambda}{2d}\right) \le \theta \le \arccos\left(-\frac{\lambda}{2d}\right). \tag{2.68}$$

It is obvious that $d = \lambda/2$ is the perfect case since the clarity area is between 0° and 180°.

Multipath transmission can negatively influence the performance of AoA estimation in terms of three aspects: inaccurate determination of number of paths, irresolvable paths, and the perturbation of received covariance matrix. We take subspace based estimation approach as an example. The number of copies of resolvable signals shall be estimated firstly to determine the number of signal subspace. In general, the Minimum Description Length (MDL), which is referred to as the Gaussian MDL (GMDL) is used to estimate the number of sources. It can be expressed as [95]

$$\hat{q}_{\text{GMDL}} = \underset{q=0,1,\ldots,N-1}{\arg\min}\left(-L\log\left(\frac{\prod_{i=q+1}^{N}\lambda_i}{\left(\frac{1}{N-q}\sum_{i=q+1}^{N}\lambda_i\right)^{N-q}} \right) + 0.5\left(q\left(2N-q\right)+1\right)\log L \right), \tag{2.69}$$

where N is the number of antenna elements, $\hat{q}_{\text{GMDL}}$ is the number of copies of resolvable signals and $\lambda_1 > \lambda_2 > \cdots > \lambda_N$ are the eigenvalues of the Auto Correlation Matrix (ACM) of the received data vector. If $\hat{q}_{\text{GMDL}} < N-1$, the signal subspace can correctly be detected to the real value. However, $\hat{q}_{\text{GMDL}} = N-1$ denote that the number of resolvable sources from reflected paths may be larger than N-1. Suppose that the received signal vector

$$\underline{\boldsymbol{r}}(t) = \underline{\boldsymbol{P}}\boldsymbol{s}(t) + \boldsymbol{n}(t), \tag{2.70}$$

where $\underline{\boldsymbol{P}}$ is a vandermonde matrix with size of $N \times L$ and $\boldsymbol{s}(t)$ is a $L \times 1$ vector. For the $N = L$ case, $\underline{\boldsymbol{P}}$ is a full rank square matrix. Hence, the signal subspace is with full rank and its eigenspace $\underline{\boldsymbol{U}}$ cannot form a basis for $\underline{\boldsymbol{P}}$. From $\hat{q}_{\text{GMDL}} = N-1$, $\underline{\boldsymbol{U}}$ can be

rewritten as $\left[\underline{\boldsymbol{U}}_{\mathrm{s}} \quad \underline{\boldsymbol{u}}_n\right]$, where $\underline{\boldsymbol{U}}_{\mathrm{s}}$ and $\underline{\boldsymbol{u}}_n$ are considered to be the signal subspace and noise subspace. Acutually, however, entire $\underline{\boldsymbol{U}}$ maybe signal space. Hence, the estimated steering matrix $\underline{\widehat{\boldsymbol{P}}}$ contains an offset, which can be written as $\underline{\widehat{\boldsymbol{P}}} = \underline{\boldsymbol{P}} + \Delta\underline{\boldsymbol{P}}$. The covariance matrix of $\underline{\boldsymbol{r}}(t)$ can be expressed as

$$\underline{\boldsymbol{\Phi}}_r = \underline{\boldsymbol{P}}\boldsymbol{S}\underline{\boldsymbol{P}}^{\mathrm{H}} + \boldsymbol{\Phi}_n, \tag{2.71}$$

where $\boldsymbol{\Phi}_n$ is the noise covariance matrix and $\boldsymbol{S}$ is the covariance matrix of $\boldsymbol{s}(t)$, which can be expressed as

$$\boldsymbol{S} = \begin{bmatrix} a_1^2 E_{\mathrm{s}} & a_1 a_2^* R_{\mathrm{s}}(\tau_2 - \tau_1) & \cdots & a_1 a_N^* R_{\mathrm{s}}(\tau_N - \tau_1) \\ a_2 a_1^* R_{\mathrm{s}}(\tau_1 - \tau_2) & a_2^2 E_{\mathrm{s}} & \cdots & a_2 a_N^* R_{\mathrm{s}}(\tau_N - \tau_2) \\ \vdots & \vdots & \ddots & \vdots \\ a_N a_1^* R_{\mathrm{s}}(\tau_1 - \tau_N) & a_N a_2^* R_{\mathrm{s}}(\tau_2 - \tau_N) & \cdots & a_N^2 E_{\mathrm{s}} \end{bmatrix}, \tag{2.72}$$

where $R_{\mathrm{s}}(\tau)$ is the autocorrelation function of $\boldsymbol{s}(t)$ and a_n is the decay factor of the n-th path. $\underline{\boldsymbol{\Phi}}_r$ can be expressed with its eigenvectors and eigenvalues:

$$\underline{\boldsymbol{\Phi}}_r = \underline{\boldsymbol{U}}\boldsymbol{\Lambda}\underline{\boldsymbol{V}}^{\mathrm{H}}, \tag{2.73}$$

where $\underline{\boldsymbol{U}}$ and $\underline{\boldsymbol{V}}$ are identical if $\underline{\boldsymbol{\Phi}}_r$ is a Hermitian matrix. Rewriting $\underline{\boldsymbol{P}}\boldsymbol{S}\underline{\boldsymbol{P}}^{\mathrm{H}}$ as $\underline{\boldsymbol{\Phi}}_{\mathrm{s}}$ and performing EVD (Eigen Value Decomposition), it has

$$\boldsymbol{\Phi}_{\mathrm{s}} = \underline{\boldsymbol{U}}_{\mathrm{s}}\boldsymbol{\Lambda}_{\mathrm{s}}\underline{\boldsymbol{V}}_{\mathrm{s}}^{\mathrm{H}}. \tag{2.74}$$

If $\underline{\boldsymbol{\Phi}}_n$ is a diagonal matrix with the same values on the main diagonal and $\boldsymbol{S}$ is a diagonal matrix, it has $\underline{\boldsymbol{U}} = \underline{\boldsymbol{U}}_{\mathrm{s}}$, $\underline{\boldsymbol{V}} = \underline{\boldsymbol{V}}_{\mathrm{s}}$ and $\boldsymbol{\Lambda} = \boldsymbol{\Lambda}_{\mathrm{s}} + \sigma_n^2\boldsymbol{I}$. According to [96], the eigenvalues and eigenvectors can be found via recursive QR decomposition.

$$\boldsymbol{\Phi}_{\mathrm{s}} = \underline{\boldsymbol{Q}}^{(1)} \cdots \underline{\boldsymbol{Q}}^{(k)} \underline{\boldsymbol{R}}_{\mathrm{s}}^{(k+1)} \underline{\boldsymbol{Q}}^{(k)\mathrm{H}} \cdots \underline{\boldsymbol{Q}}^{(1)\mathrm{H}}, \tag{2.75}$$

where $\underline{\boldsymbol{Q}}^{(k)}$ is unitary matrix for the k-th QR decomposition, $\underline{\boldsymbol{R}}_{\mathrm{s}}^{(k+1)}$ will become a diagonal matrix with the eigenvalues on the main diagonal and $\underline{\boldsymbol{Q}}^{(k)} \cdots \underline{\boldsymbol{Q}}^{(1)}$ becomes ist eigenspace as $k \to \infty$. However, the recursive algorithm becomes more complicated with the increase of k because the QR decomposition shall be performed for $\underline{\boldsymbol{R}}_{\mathrm{s}}^{(k)}\boldsymbol{Q}^{(k)}$ at each step. In this dissertation, the author proposes a novel approach with lower complexity to compute the eigenspace and eigenvalues. The following theorem can be shown:

THEOREM 1: Any normal matrix $\boldsymbol{\Phi}$ can be written as $\boldsymbol{\Phi} = \boldsymbol{Q}^{(1)}\boldsymbol{Q}^{(3)} \cdots \boldsymbol{Q}^{(2k+1)}\boldsymbol{R}^{(2k+2)\mathrm{H}}\boldsymbol{Q}^{(2k+2)\mathrm{H}}\boldsymbol{Q}^{(2k)\mathrm{H}} \cdots \boldsymbol{Q}^{(2)\mathrm{H}}$ (2.76), where $\boldsymbol{R}^{(2k)\mathrm{H}} = \boldsymbol{Q}^{(2k+1)}\boldsymbol{R}^{(2k+1)}$ and $\boldsymbol{R}^{(2k+1)\mathrm{H}} = \boldsymbol{Q}^{(2k+2)}\boldsymbol{R}^{(2k+2)}$, $\boldsymbol{R}^{(2k+1)}$ and $\boldsymbol{R}^{(2k+2)}$ are upper triangular matrices, $\boldsymbol{Q}^{(2k+1)}$ and $\boldsymbol{Q}^{(2k+2)}$ are unitary matrices, The matrix $\boldsymbol{R}^{(2k+1)}$ or $\boldsymbol{R}^{(2k+2)}$ tends to be a diagonal matrix as $k \to \infty$, the diagonal elements of which are the eigenvalues of $\boldsymbol{\Phi}$, $\boldsymbol{Q}^{(1)}\boldsymbol{Q}^{(3)} \cdots \boldsymbol{Q}^{(2k+1)}$ tends to be identical to $\boldsymbol{Q}^{(2)}\boldsymbol{Q}^{(4)} \cdots \boldsymbol{Q}^{(2k+2)}$ as $k \to \infty$.

PROOF:

From definition of QR decomposition, (2.76) can be easily derived. $\boldsymbol{\Phi}$ is a normal $N \times N$ matrix, which has $\boldsymbol{\Phi} = \boldsymbol{\Phi}^{\mathrm{H}}$. With (2.76), we can get $\boldsymbol{R}^{(2k+2)\mathrm{H}} = \boldsymbol{Q}_1^{\mathrm{H}} \boldsymbol{Q}_2 \boldsymbol{R}^{(2k+2)} \boldsymbol{Q}_1^{\mathrm{H}} \boldsymbol{Q}_2$, where $\boldsymbol{Q}_1 = \boldsymbol{Q}^{(1)} \cdots \boldsymbol{Q}^{(2k+1)}$ and $\boldsymbol{Q}_2 = \boldsymbol{Q}^{(2)} \cdots \boldsymbol{Q}^{(2k+2)}$. If we can prove $\boldsymbol{R}^{(2k+2)}$ converges to a diagonal matrix as $k \to \infty$, we can derive that $\boldsymbol{Q}_1 = \boldsymbol{Q}_2$ and $\boldsymbol{Q}_1$ is the eigenspace of $\boldsymbol{\Phi}$ as $k \to \infty$. Let us begin with $N = 2$ and rewrite $\boldsymbol{\Phi}$ as

$$\boldsymbol{\Phi} = \begin{bmatrix} \phi_{11} & \phi_{12} \\ \phi_{21} & \phi_{22} \end{bmatrix}, \tag{2.77}$$

where $\phi_{21} = \phi_{12}^*$. The QR decomposition can be written as

$$\begin{aligned} \underline{\boldsymbol{Q}}^{(1)} &= \begin{bmatrix} \dfrac{\phi_{11}}{\sqrt{\phi_{11}^2 + \phi_{21}^2}} & -\dfrac{\phi_{21}^*}{\sqrt{\phi_{11}^2 + \phi_{21}^2}} \\ \dfrac{\phi_{21}}{\sqrt{\phi_{11}^2 + \phi_{21}^2}} & \dfrac{\phi_{11}^*}{\sqrt{\phi_{11}^2 + \phi_{21}^2}} \end{bmatrix} \\ \boldsymbol{R}^{(1)} &= \begin{bmatrix} \sqrt{\phi_{11}^2 + \phi_{21}^2} & \dfrac{1}{\sqrt{\phi_{11}^2 + \phi_{21}^2}} \left(\phi_{11}^* \phi_{12} + \phi_{21}^* \phi_{22} \right) \\ 0 & \dfrac{1}{\sqrt{\phi_{11}^2 + \phi_{21}^2}} \det(\boldsymbol{\Phi}) \end{bmatrix} \end{aligned} \tag{2.78}$$

Then $\underline{\boldsymbol{Q}}^{(k)}$ and $\boldsymbol{R}^{(k)}$ can be calculated as

$$\begin{aligned} \boldsymbol{Q}^{(k)} &= \begin{bmatrix} \dfrac{\phi_{11}^{(k-1)}}{\sqrt{\left(\phi_{11}^{(k-1)}\right)^2 + \left(\phi_{21}^{(k-1)}\right)^2}} & -\dfrac{\phi_{21}^{(k-1)*}}{\sqrt{\left(\phi_{11}^{(k-1)}\right)^2 + \left(\phi_{21}^{(k-1)}\right)^2}} \\ \dfrac{\phi_{21}}{\sqrt{\left(\phi_{11}^{(k-1)}\right)^2 + \left(\phi_{21}^{(k-1)}\right)^2}} & \dfrac{\phi_{11}^*}{\sqrt{\left(\phi_{11}^{(k-1)}\right)^2 + \left(\phi_{21}^{(k-1)}\right)^2}} \end{bmatrix} \\ \boldsymbol{R}^{(k)} &= \begin{bmatrix} \sqrt{\left(\phi_{11}^{(k-1)}\right)^2 + \left(\phi_{21}^{(k-1)}\right)^2} & \dfrac{\left(\phi_{11}^{(k-1)*} \phi_{12}^{(k-1)} + \phi_{21}^{(k-1)*} \phi_{22}^{(k-1)}\right)}{\sqrt{\left(\phi_{11}^{(k-1)}\right)^2 + \left(\phi_{21}^{(k-1)}\right)^2}} \\ 0 & \dfrac{\det(\boldsymbol{\Phi})}{\sqrt{\left(\phi_{11}^{(k-1)}\right)^2 + \left(\phi_{21}^{(k-1)}\right)^2}} \end{bmatrix}, \end{aligned} \tag{2.79}$$

where $\boldsymbol{R}^{(k)\mathrm{H}} = \begin{bmatrix} \phi_{11}^{(k)} & 0 \\ \phi_{21}^{(k)} & \phi_{22}^{(k)} \end{bmatrix}$. The proof consists of two steps: I) convergence II) converge to a diagonal matrix. For the first step, we hypothesize that $\boldsymbol{R}^{(k)}$ cannot converge to a certain matrix as $k \to \infty$. From (2.79), it has $\phi_{11}^{(k+1)} = \sqrt{\left(\phi_{11}^{(k)}\right)^2 + \left(\phi_{21}^{(k)}\right)^2} > \phi_{11}^{(k)}$, if $\phi_{21}^{(k)} \neq 0$. According to the first hypothesis, it has $\lim_{k \to \infty} \left(\phi_{11}^{(k)} \right) = \infty$ and $\lim_{k \to \infty} \left(\phi_{22}^{(k)} \right) = 0$. Hence, the convergence can be proved. For the second

step, we hypothesize that $\boldsymbol{R}^{(k)\mathrm{H}} = \boldsymbol{R}^{(k+1)\mathrm{H}} = \begin{bmatrix} \phi_{11}^{(\infty)} & 0 \\ \phi_{21}^{(\infty)} & \phi_{22}^{(\infty)} \end{bmatrix}$ as $k \to \infty$ and $\phi_{21}^{(\infty)} \neq 0$. From (2.79), we can get $\phi_{11}^{(k+1)} = \sqrt{\left(\phi_{11}^{(k)}\right)^2 + \left(\phi_{21}^{(k)}\right)^2} = \sqrt{\left(\phi_{11}^{(k)}\right)^2 + c^2} > \phi_{11}^{(k)}$, which does not conform to second hypothesis. Hence, $\boldsymbol{R}^{(\infty)}$ must be diagonal matrix. Because diagonal matrix containing eigenvalues of $\boldsymbol{\Phi}$ is a unique diagonal matrix similar to $\boldsymbol{\Phi}$, it has $\boldsymbol{Q}_1 = \boldsymbol{Q}_2$ and $\boldsymbol{Q}_1$ is the eigenspace of $\boldsymbol{\Phi}$. Now we can expand to $N = L > 2$. $\boldsymbol{\Phi}$ can be written as

$$\begin{aligned} \boldsymbol{\Phi}^{(1)} = \boldsymbol{\Phi} &= \begin{bmatrix} \boldsymbol{f}_1^{(1)} & \cdots & \boldsymbol{f}_L^{(1)} \end{bmatrix} = \\ &= \begin{bmatrix} \phi_{11} & \phi_{12} & \cdots & \phi_{1L} \\ \phi_{21} & \phi_{22} & \cdots & \phi_{2L} \\ \vdots & \vdots & \ddots & \vdots \\ \phi_{L1} & \phi_{L2} & \cdots & \phi_{LL} \end{bmatrix} = \begin{bmatrix} \boldsymbol{A}^{(1)} & \boldsymbol{B}^{(1)} \\ \boldsymbol{C}^{(1)} & \boldsymbol{D}^{(1)} \end{bmatrix}. \end{aligned} \tag{2.80}$$

To simplify the calculation, the QR decomposition of $\boldsymbol{\Phi}^{(1)}$ shall be calculated with sub-matrices. We set $\boldsymbol{A}^{(1)} = \phi_{11}$, $\boldsymbol{B}^{(1)} = \begin{bmatrix} \phi_{12} & \cdots & \phi_{1L} \end{bmatrix}$, $\boldsymbol{C}^{(1)} = \begin{bmatrix} \phi_{21} & \cdots & \phi_{L1} \end{bmatrix}^{\mathrm{H}}$ and $\boldsymbol{D}^{(1)} = \begin{bmatrix} \phi_{22} & \cdots & \phi_{2L} \\ \vdots & \ddots & \vdots \\ \phi_{2L} & \cdots & \phi_{LL} \end{bmatrix}$. Then the QR decomposition of $\boldsymbol{\Phi}^{(k)}$ can be expressed as

$$\underline{\boldsymbol{Q}}^{(k)} = \boldsymbol{E}^{(k)} \boldsymbol{H}^{(k)} \boldsymbol{F}^{(k)} = \begin{bmatrix} \boldsymbol{q}_1^{(k)} & \boldsymbol{q}_2^{(k)} & \cdots & \boldsymbol{q}_L^{(k)} \end{bmatrix}, \tag{2.81}$$

where

$$\boldsymbol{E}^{(k)} = \begin{bmatrix} \dfrac{\boldsymbol{A}^{(k)}}{\sqrt{\mathrm{tr}\left(\boldsymbol{A}^{(k)\mathrm{H}} \boldsymbol{A}^{(k)} + \boldsymbol{C}^{(k)\mathrm{H}} \boldsymbol{C}^{(k)} \right)}} & \dfrac{\mathrm{tr}\left(\boldsymbol{A}^{(k)\mathrm{H}} \boldsymbol{A}^{(k)} + \boldsymbol{C}^{(k)\mathrm{H}} \boldsymbol{C}^{(k)} \right) \boldsymbol{B}^{(k)} - \boldsymbol{A}^{(k)} \boldsymbol{A}^{(k)\mathrm{H}} \boldsymbol{B}^{(k)} - \boldsymbol{A}^{(k)} \boldsymbol{C}^{(k)\mathrm{H}} \boldsymbol{D}^{(k)}}{\mathrm{tr}\left(\boldsymbol{A}^{(k)\mathrm{H}} \boldsymbol{A}^{(k)} + \boldsymbol{C}^{(k)\mathrm{H}} \boldsymbol{C}^{(k)} \right)} \\ \dfrac{\boldsymbol{C}^{(k)}}{\sqrt{\mathrm{tr}\left(\boldsymbol{A}^{(k)\mathrm{H}} \boldsymbol{A}^{(k)} + \boldsymbol{C}^{(k)\mathrm{H}} \boldsymbol{C}^{(k)} \right)}} & \dfrac{\mathrm{tr}\left(\boldsymbol{A}^{(k)\mathrm{H}} \boldsymbol{A}^{(k)} + \boldsymbol{C}^{(k)\mathrm{H}} \boldsymbol{C}^{(k)} \right) \boldsymbol{D}^{(k)} - \boldsymbol{C}^{(k)} \boldsymbol{A}^{(k)\mathrm{H}} \boldsymbol{B}^{(k)} - \boldsymbol{C}^{(k)} \boldsymbol{C}^{(k)\mathrm{H}} \boldsymbol{D}^{(k)}}{\mathrm{tr}\left(\boldsymbol{A}^{(k)\mathrm{H}} \boldsymbol{A}^{(k)} + \boldsymbol{C}^{(k)\mathrm{H}} \boldsymbol{C}^{(k)} \right)} \end{bmatrix}, \boldsymbol{H}^{(k)} = \boldsymbol{H}_1^{(k)} \cdots \boldsymbol{H}_{L-2}^{(k)} \tag{2.82}$$

$$\boldsymbol{H}_l^{(k)} = \begin{bmatrix} 1 & \cdots & 0 & 0 & \cdots & 0 \\ 0 & \ddots & 0 & 0 & \cdots & 0 \\ 0 & \cdots & 1 & h_{(l+1)(l+2)}^{(k)} & \cdots & h_{(l+1)L}^{(k)} \\ 0 & \cdots & 0 & h_{(l+2)(l+2)} & \cdots & 0 \\ \vdots & \cdots & 0 & 0 & \ddots & \vdots \\ 0 & \cdots & 0 & 0 & \cdots & h_{LL} \end{bmatrix}, \boldsymbol{E}^{(k)} \boldsymbol{H}^{(k)} = \begin{bmatrix} \boldsymbol{e}_1^{(k)} & \boldsymbol{e}_2^{(k)} & \cdots & \boldsymbol{e}_L^{(k)} \end{bmatrix} \tag{2.83}$$

$$\boldsymbol{F}^{(k)}=\begin{bmatrix} 1 & 0 & \cdots & 0 \\ 0 & 1/\sqrt{\mathrm{d}_1\left(\dfrac{\left(\overline{\boldsymbol{E}^{(k)}\boldsymbol{H}^{(k)}}\right)_1^{\mathrm{H}}}{\left(\boldsymbol{E}^{(k)}\boldsymbol{H}^{(k)}\right)_1}\right)} & \cdots & 0 \\ \vdots & \vdots & \ddots & \vdots \\ 0 & 0 & \cdots & 1/\sqrt{\mathrm{d}_{L-1}\left(\dfrac{\left(\overline{\boldsymbol{E}^{(k)}\boldsymbol{H}^{(k)}}\right)_1^{\mathrm{H}}}{\left(\boldsymbol{E}^{(k)}\boldsymbol{H}^{(k)}\right)_1}\right)} \end{bmatrix}. \tag{2.84}$$

In (2.82), "tr" is the trace function, "d_l" is to get the l-th diagonal element and $\overline{\left(\boldsymbol{E}^{(k)}\boldsymbol{H}^{(k)}\right)}_1=\left[\boldsymbol{e}_2^{(k)} \quad \cdots \quad \boldsymbol{e}_L^{(k)}\right]$. $\boldsymbol{H}^{(k)}$ is used to orthogonalize $\boldsymbol{E}^{(k)}$. Then $\boldsymbol{R}^{(k)}$ can be expressed as

$$\boldsymbol{R}^{(k)}=\begin{bmatrix} \sqrt{\mathrm{tr}\left(\boldsymbol{A}^{(k)\mathrm{H}}\boldsymbol{A}^{(k)}+\boldsymbol{C}^{(k)\mathrm{H}}\boldsymbol{C}^{(k)}\right)} & \dfrac{\boldsymbol{A}^{(k)\mathrm{H}}\boldsymbol{B}^{(k)}+\boldsymbol{C}^{(k)\mathrm{H}}\boldsymbol{D}^{(k)}}{\sqrt{\mathrm{tr}\left(\boldsymbol{A}^{(k)\mathrm{H}}\boldsymbol{A}^{(k)}+\boldsymbol{C}^{(k)\mathrm{H}}\boldsymbol{C}^{(k)}\right)}} \\ \boldsymbol{0} & \boldsymbol{G}^{(k)} \end{bmatrix}$$

$$\boldsymbol{G}^{(k)}=\begin{bmatrix} \boldsymbol{q}_2^{(k)}\boldsymbol{f}_2^{(k)} & \boldsymbol{q}_2^{(k)}\boldsymbol{f}_3^{(k)} & \cdots & \boldsymbol{q}_2^{(k)}\boldsymbol{f}_L^{(k)} \\ & \boldsymbol{q}_3^{(k)}\boldsymbol{f}_3^{(k)} & \cdots & \boldsymbol{q}_3^{(k)}\boldsymbol{f}_L^{(k)} \\ & & \ddots & \vdots \\ & & & \boldsymbol{q}_L^{(k)}\boldsymbol{f}_L^{(k)} \end{bmatrix}. \tag{2.82}$$

Then let

$$\boldsymbol{\Phi}^{(k+1)}=\boldsymbol{R}^{\mathrm{H}(k)}=\left[\boldsymbol{f}_1^{(k)} \quad \cdots \quad \boldsymbol{f}_L^{(k)}\right]. \tag{2.83}$$

The same as the case of $N=2$, $\dfrac{\boldsymbol{A}^{(k)\mathrm{H}}\boldsymbol{B}^{(k)}+\boldsymbol{C}^{(k)\mathrm{H}}\boldsymbol{D}^{(k)}}{\sqrt{\mathrm{tr}\left(\boldsymbol{A}^{(k)\mathrm{H}}\boldsymbol{A}^{(k)}+\boldsymbol{C}^{(k)\mathrm{H}}\boldsymbol{C}^{(k)}\right)}}$ shall vanish as $k\to\infty$. From (2.81) to (2.83), $\underline{\boldsymbol{Q}}^{(\infty)}$ can be written as

$$\underline{\boldsymbol{Q}}^{(\infty)}=\begin{bmatrix} q_{11}^{(\infty)} & \boldsymbol{0} \\ \boldsymbol{0} & \underline{\boldsymbol{Q}}_{L-1,\mathrm{sub}}^{(\infty)} \end{bmatrix}, \tag{2.84}$$

where $\underline{\boldsymbol{Q}}_{L-1}^{(\infty)}$ shall be a $(L-1)\times(L-1)$ unitary matrix. Hence, as $k\to\infty$, it has

$$\boldsymbol{\Phi}_{L-1,\mathrm{sub}}^{(\infty)}=\underline{\boldsymbol{Q}}_{L-1,\mathrm{sub}}^{(\infty)}\boldsymbol{G}^{(\infty)}, \tag{2.85}$$

where $\boldsymbol{\Phi}_{L-1,\mathrm{sub}}^{(\infty)}$ is the $(L-1)\times(L-1)$ right-down sub-matrix of $\boldsymbol{\Phi}^{(\infty)}$. Using the recursive method, we can get

$$\boldsymbol{\Phi}_{l,\mathrm{sub}}^{(\infty)}=\underline{\boldsymbol{Q}}_{l,\mathrm{sub}}^{(\infty)}\boldsymbol{G}_{l,\mathrm{sub}}^{(\infty)}, l=L-1,\cdots,2\ . \tag{2.86}$$

With (2.82), it can be concluded that $\boldsymbol{G}^{(\infty)}$ must be a diagonal matrix. Hence, THEOREM 1 is proved. Thus, $\underline{\boldsymbol{U}}$ can be estimated by

$$\underline{\widehat{\boldsymbol{U}}}\left(\boldsymbol{a},\boldsymbol{\tau},\boldsymbol{\varphi},R_{\mathrm{s}}\left(\tau\right)\right)=\underline{\boldsymbol{Q}}^{(1)}\underline{\boldsymbol{Q}}^{(3)}\cdots\underline{\boldsymbol{Q}}^{(2K+1)}, \tag{2.87}$$

where K shall be selected according to the coverage rate. The coverage rate of QR decomposition can be referenced in [96]. If the $\boldsymbol{\Phi}_r$ is perturbed by $\boldsymbol{\Delta\Phi}_r$ due to the finite data length, $\underline{\widehat{\boldsymbol{U}}}$ will be perturbed by $\boldsymbol{\Delta}\underline{\widehat{\boldsymbol{U}}}$, which can be expressed as [98]

$$\begin{aligned}
&\boldsymbol{\Delta}\widehat{\boldsymbol{U}}_{\mathrm{s}}\approx\widehat{\boldsymbol{U}}_n\widehat{\boldsymbol{U}}_n^{\mathrm{H}}\boldsymbol{\Delta\Phi}_r\widehat{\boldsymbol{U}}_{\mathrm{s}}\boldsymbol{\Omega}^{-1}\\
&\boldsymbol{\Delta}\widehat{\boldsymbol{U}}_n\approx-\widehat{\boldsymbol{U}}_{\mathrm{s}}\boldsymbol{\Omega}^{-1}\widehat{\boldsymbol{U}}_{\mathrm{s}}^{\mathrm{H}}\boldsymbol{\Delta\Phi}_r\widehat{\boldsymbol{U}}_n\\
&\boldsymbol{\Delta\Lambda}_{\mathrm{s}}\approx\widehat{\boldsymbol{U}}_{\mathrm{s}}^{\mathrm{H}}\boldsymbol{\Delta\Phi}_r\widehat{\boldsymbol{U}}_{\mathrm{s}},\boldsymbol{\Delta\Lambda}_n\approx\widehat{\boldsymbol{U}}_n^{\mathrm{H}}\boldsymbol{\Delta\Phi}_r\widehat{\boldsymbol{U}}_n,\\
&\boldsymbol{\Omega}=\boldsymbol{\Lambda}_{\mathrm{s}}-\boldsymbol{\Lambda}_n\\
&\boldsymbol{\Lambda}_{\mathrm{s}}=\mathrm{diag}\left(\lambda_1^2\quad\cdots\quad\lambda_p^2\right),\boldsymbol{\Lambda}_n=\sigma_n^2\boldsymbol{I}
\end{aligned} \tag{2.88}$$

where

$$\begin{aligned}
&\widetilde{\boldsymbol{U}}_{\mathrm{s}}=\widehat{\boldsymbol{U}}_{\mathrm{s}}+\boldsymbol{\Delta}\widehat{\boldsymbol{U}}_{\mathrm{s}},\widetilde{\boldsymbol{U}}_n=\widehat{\boldsymbol{U}}_n+\boldsymbol{\Delta}\widehat{\boldsymbol{U}}_n\\
&\widehat{\boldsymbol{U}}=\left[\widehat{\boldsymbol{U}}_{\mathrm{s}}\quad\widehat{\boldsymbol{U}}_n\right],\widetilde{\boldsymbol{U}}=\left[\widetilde{\boldsymbol{U}}_{\mathrm{s}}\quad\widetilde{\boldsymbol{U}}_n\right].
\end{aligned} \tag{2.89}$$

Suppose that $\phi_1<\cdots<\phi_N$, then the perturbed AoA can be expressed as

$$\hat{\phi}_{\mathrm{res}}=\arg\max_{\phi}\left(\underline{\boldsymbol{p}}_{\mathrm{est}}^{\mathrm{H}}\left(\phi\right)\widetilde{\boldsymbol{U}}_{\mathrm{s}}\widetilde{\boldsymbol{U}}_{\mathrm{s}}^{\mathrm{H}}\underline{\boldsymbol{p}}_{\mathrm{est}}\left(\phi\right)\right), \tag{2.90}$$

where

$$\underline{\boldsymbol{p}}_{\mathrm{est}}\left(\phi\right)=\left[1\quad e^{j\phi}\quad\cdots\quad e^{j(N-1)\phi}\right]^{\mathrm{T}}. \tag{2.91}$$

For the $N<L$ case, $\underline{\boldsymbol{P}}$ becomes a fat matrix, which contains K vandermonde vectors. $\underline{\boldsymbol{P}}$ can be rearranged to a square matrix $\underline{\boldsymbol{P}}'$, whose first $N-1$ columns are the same as those of $\underline{\boldsymbol{P}}$ and the last column is the weighted sum of last $L-N+1$ vandermonde vectors. If the signals are received from L irresolvable paths ($\left|\tau_i-\tau_j\right|\le 1/B$, B is the signal bandwidth), (2.70) can be rewritten as

$$\begin{aligned}
\underline{\boldsymbol{r}}\left(\boldsymbol{t}\right)&=\begin{bmatrix}1&\cdots&1\\e^{j\phi_1}&\cdots&e^{j\phi_L}\\\vdots&\ddots&\vdots\\e^{j(N-1)\phi_1}&\cdots&e^{j(N-1)\phi_L}\end{bmatrix}\begin{bmatrix}a_1s\left(t-\tau_1\right)\\a_2s\left(t-\tau_2\right)\\\vdots\\a_Ls\left(t-\tau_L\right)\end{bmatrix}+\begin{bmatrix}n_1\left(t\right)\\n_2\left(t\right)\\\vdots\\n_N\left(t\right)\end{bmatrix}\\
&\approx\begin{bmatrix}\sum_{l=1}^{L}a_l\\\sum_{l=1}^{L}a_le^{j\phi_l}\\\vdots\\\sum_{l=1}^{L}a_le^{j(N-1)\phi_l}\end{bmatrix}s\left(t\right)+\begin{bmatrix}n_1\left(t\right)\\n_2\left(t\right)\\\vdots\\n_N\left(t\right)\end{bmatrix}\\
&=\underline{\boldsymbol{p}}\left(\boldsymbol{\varphi},\boldsymbol{a}\right)\underline{s}\left(t\right)+\underline{\boldsymbol{n}}
\end{aligned}. \tag{2.92}$$

Thus the perturbed AoA can be expressed as

$$\hat{\phi}_{\text{irres}} = \arg\max_{\phi} \left(\left\| \underline{\boldsymbol{p}}_{\text{est}}^{\text{H}} (\phi)\, \underline{\boldsymbol{p}}(\boldsymbol{\varphi}, \underline{\boldsymbol{a}}) \right\|^2 \right). \tag{2.93}$$

The approaches, which can suppress the multipath effect, will be discussed in chapter 4.

3 Novel LT Approaches in Ultra Wideband Networks

3.1 Overview

The aforementioned novel LT approaches, which can effectively solve the problems formulated in chapter 2, will be discussed in this chapter. The employed UWB signal and ranging based multi user access formats: Time Hopping Multiple Access (THMA) are introduced. The novel LT techniques for ToA/TDoA based ranging systems and RSS based systems will be discussed in section 3.3 and section 3.4, respectively.

3.2 Employed UWB Monocycle

In this dissertation, the second derivative of nanosecond Gaussian monocycle is employed as the UWB transmitted signal, which can be expressed as

$$\omega(t) = A\left(1 - \frac{4\pi t^2}{\varepsilon^2}\right)e^{-2\pi t^2/\varepsilon^2}, \tag{3.1}$$

where $A > 0$ and ε are the parameters, which determine the pulse energy and width of the monocycle. $\omega(t)$ and its auto correlation function are illustrated in Figure 2.16, Figure 2.10 and Figure 2.18. Figure 3.1 shows the spectral power density of a normalized 2ns Gaussian monocycle.

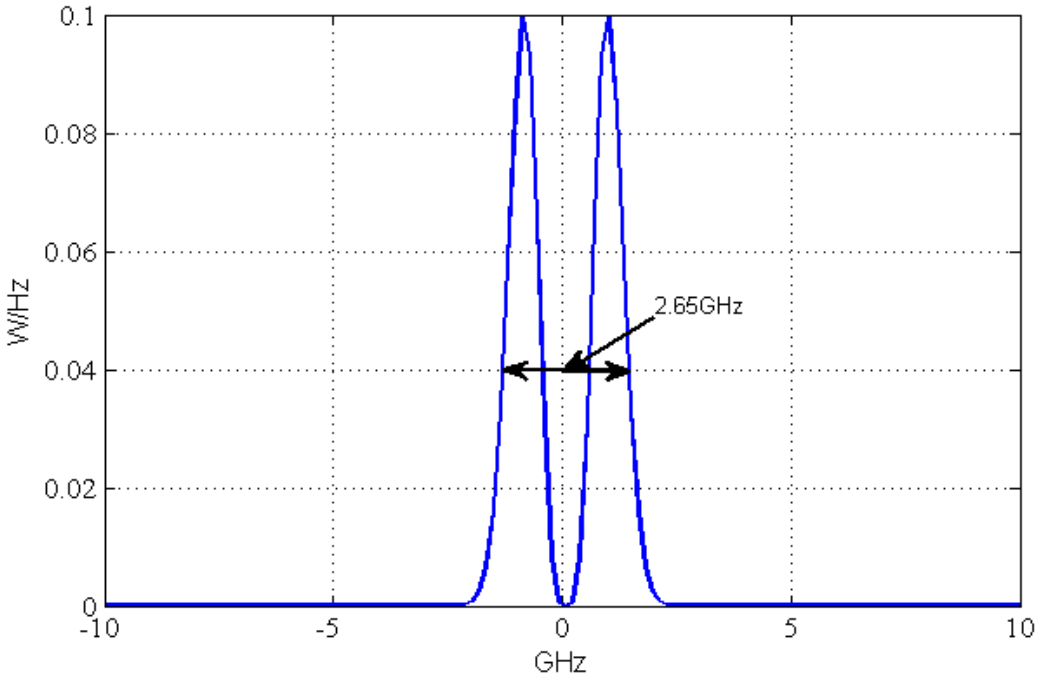

Figure 3.1: Spectral power density of 2ns Gaussian monocycle

It can be seen from Figure 3.1 that the half-power bandwidth of the employed 2ns-Gaussian monocycle is approximate 1.33 GHz, which requires at least 2.65 GHz sampling rate at the receiver according to the Nyquist-Shannon sampling theorem.

3.3 Time of Arrival (ToA) based Ranging

This section will propose several novel leading edge detection approaches: JLEDA, IMLCE and SbA. Finally, error sources of the leading edge detection for each estimator will be derived.

3.3.1 Joint Leading Edge Detection Approach (JLEDA)

The final goal of ranging systems is to determine the target position, which requires more than two UWB receivers for the two dimensional localization (see Figure 2.1 and Figure 2.4). For each *n*-th UWB receiver, $\hat{\tau}_{n,n=1,2\cdots N}$ and $\hat{d}_{n,n=1,2\cdots,N}$ are defined as the estimated ToA and distance parameters, respectively. In the ideal case, the N circles, each of which is drawn with the radius of $\hat{d}_n$, shall intersect in one point, which is considered as the target location. In practice, however, the intersection cannot be unique due to the detection offset. It proposes Joint Leading Edge Detection Approach (JLEDA) which requires the cooperation between each UWB receiver. JLEDA consists of four steps:

1. Output correlation
2. Correlated peak value selection
3. Search-back space determination
4. Minimum area search

The received signal can be modeled as

$$\begin{aligned} r_{\mathrm{g},n}(t) &= \sum_{l=1}^{L_m} \underline{a}_{l,n} g_n(t-\tau_l) + n_n(t) \\ g_n(t) &= s_n \otimes p(t) \otimes \delta_{L_\mathrm{p}} \end{aligned}, \tag{3.2}$$

where $\underline{a}_{l,n}$ and τ_l are the amplitude and time delay of the *l*-th channel for the *n*-th receiver, respectively. $g_n(t)$ is the *n*-th transmitted preamble signals. s_n is the *n*-th ternary code and $p(t)$ is the employed UWB monocycle (see Figure 2.16 and Figure 3.1). L_p is the length of the delta function, which determines the length of Pulse Repetition Period (PRP). From 2.3.9, we can see that the most of 20dB-ED in CM1 is smaller than 100ns. The paths with time delay larger than 100ns can be neglected due to their weak contributions to the received signal. It assumes that $T_\mathrm{p} L_\mathrm{p} > 100\mathrm{ns}$, where T_p is the pulse duration. Under this assumption, the Inter Symbol Interference (ISI) can be neglected. According to JLEDA, the received signal shall be correlated with a template signal and the output of the correlator can be expressed as

$$
\begin{aligned}
z_{g,n}(t) &= g_n(t) \otimes r_{\mathrm{g,n}}(t) \\
&= \int_{-\infty}^{\infty} g_n(\tau - t)\left(\sum_{l=1}^{L_n} \underline{a}_{l,n} g_n(\tau - \tau_l) + n(\tau) \right) d\tau \\
&= \underline{a}_{l,n} \sum_{l=1}^{L_n} \int_{-\infty}^{\infty} \left(g_n(\tau - t) g_n(\tau - \tau_l) \right) d\tau + \int_{-\infty}^{\infty} g_n(\tau - t) n(\tau) d\tau \\
&= \underline{a}_{l,n} \sum_{l=1}^{L_n} s(t - \tau_l) + \eta(t)
\end{aligned}
\tag{3.3}
$$

The first part of (3.3) is the delay-weight-sum of autocorrelation function of the normalized Gaussian pulse. $\eta(t)$ can be modeled as a Gaussian process with the same expectation and variance as that of $n(t)$. In addition, it should be noted that $z_{g,n}(t)$ has the time duration of $T_{\mathrm{th},n}$, which shall be determined firstly.

If N UWB receives are located at the fixed coordinates (x_n, y_n) and the localization area can be known (see Figure 2.1), $T_{\mathrm{th},n}$ can be determined as

$$
T_{\mathrm{th},n} = T_{\mathrm{ref}} + d_n / c + \mathrm{PLD}, \tag{3.4}
$$

where T_{ref} is the reference time stamp, which is usually set to be zero. PLD is approximate 60ns, which is depicted in 2.3.9. d_n is the possible maximum transmission distance for n-th receiver, which is determined by the geometry of the location of the receivers. c is the light velocity. From the first step, the maximum correlation peak $(t_{\mathrm{p},n}, v_{\mathrm{p},n})$ can be locked by

$$
(t_{\mathrm{p},n}, v_{\mathrm{p},n}) = \arg\max\left(\mathrm{abs}\left(z_{g,n}(t) \Big|_0^{T_{\mathrm{th},n}} \right) \right). \tag{3.5}
$$

From Figure 2.26, we can know that the first incoming path must be between zero and $t_{\mathrm{p},n}$. For the given $t_{\mathrm{p},n}, n = 1, 2, \cdots, N$, $\binom{2}{N}$ intersections can be determined by

$$
(x_{lk}, y_{lk}) = \underset{(x,y)}{\arg}\left(\begin{cases} (x - x_l)^2 + (y - y_l)^2 = (ct_{\mathrm{p},l})^2 \\ (x - x_k)^2 + (y - y_k)^2 = (ct_{\mathrm{p},k})^2 \end{cases}, l \neq k \right). \tag{3.6}
$$

From (3.6), the upper limit of the time search can be determined by

$$
\begin{aligned}
T_{\mathrm{s},n} &= \frac{\Delta L_n}{c} = \frac{ct_{\mathrm{p},n} - \min\left(d_{lk,n} \Big|_{\substack{l,k=1\cdots N \\ l,k \neq n}} \right)}{c} \\
d_{lk,n} &= \sqrt{(x_{lk} - x_n)^2 + (y_{lk} - y_n)^2} \\
n &= 1, 2, \cdots, N
\end{aligned}
\quad , \tag{3.7}
$$

For the sake of simplicity, an illustration for $N = 3$ case is illustrated in Figure 3.2.

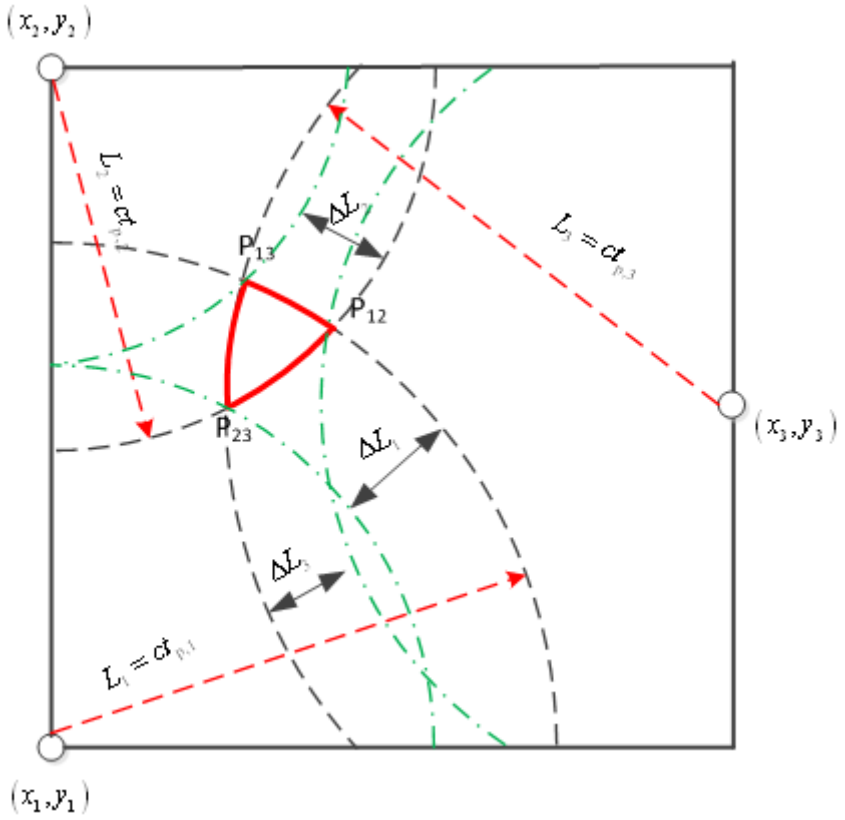

Figure 3.2: Determination of upper limit of the time search

We define the Maximum Energy to Leading Edge Energy Ratio (MER) as η_{MER}. Then the Virtual Leading Edge (VLE) can be detected as

$$t_{\text{vle},n} = \arg\min_{t}\left(\text{abs}\left(z_{g,n}(t)\right) \geq v_{\text{p},n} / \sqrt{\eta_{\text{MER}}}\right). \tag{3.8}$$

The VLE denotes the first selected peak value, which fulfills the power condition ($\geq v_{\text{p},n} / \sqrt{\eta_{\text{MER}}}$). From (3.7) and (3.8), the search-back space can be determined as $\left[\max\left(t_{\text{p},n} - T_{\text{s},n}, t_{\text{vle},n}\right) \quad t_{\text{p},n}\right]$. Then it assumes that M_n correlation peaks are found within the search-back space for the n-th receiver. If we select one peak form each receiver to form one CLEC (Candidate Leading Edge Combination), there are $Q = \prod_{n=1}^{N} M_n$ combinations that can be determined. It expresses the q-th CLEC as $\boldsymbol{t}_q = \left[t_{1,q} \quad t_{2,q} \quad \cdots \quad t_{N,q}\right]^{\text{T}}$. According to the geolocation and the number of receivers, two scenarios should be considered: I) $N = 3$ II) $N > 3$. For $N = 3$ case (see Figure 3.2), it defines two parameters: $A_q, q = 1,2,\cdots Q$ which is the area wrapped by $\text{P}_{mn,m=1,2,3,n=1,2,3,m\neq n}$, and $S_q, q = 1,2,\cdots Q$ which is sum of squared distance between the estimated location and each arcs. A_q and S_q are two essential criteria which are used to estimate the CLEC. It defines two functions $f_A(\bullet)$ and $f_S(\bullet)$ that project $\boldsymbol{t}_q$ to A_q and S_q, respectively:

$$\begin{aligned} A_q &= f_A\left(\boldsymbol{t}_q\right) = f_A\left(\boldsymbol{t}_{\text{r}} + \Delta\boldsymbol{t}_q\right) \\ S_q &= f_S\left(\boldsymbol{t}_q\right) = f_S\left(\boldsymbol{t}_{\text{r}} + \Delta\boldsymbol{t}_q\right) \end{aligned}, \tag{3.9}$$

where $\boldsymbol{t}_{\mathrm{r}}$ and $\Delta\boldsymbol{t}_q$ are the Actual Leading Edge Combination (ALEC) and the bias LEC vector. Clearly, $f_A(\boldsymbol{t}_{\mathrm{r}})$ and $f_S(\boldsymbol{t}_{\mathrm{r}})$ shall be zero. The followings are the derivate of $f_A(\bullet)$ from geometry (for $N = 3$ case).

$$f_A(\boldsymbol{t}_q)=\frac{1}{2}\sqrt{\prod_{l=1}^{2}\left(\begin{array}{l}\left(x_{\left(\left\lfloor\frac{l-1}{3}\right\rfloor+1\right)\left(\left\lfloor\frac{l}{3}\right\rfloor+1\right),q}-x_{\left(\left\lfloor\frac{l}{3}\right\rfloor+1\right)\left(\left\lfloor\frac{l+1}{3}\right\rfloor+1\right),q}\right)^2+\\ \left(y_{\left(\left\lfloor\frac{l-1}{3}\right\rfloor+1\right)\left(\left\lfloor\frac{l}{3}\right\rfloor+1\right),q}-y_{\left(\left\lfloor\frac{l}{3}\right\rfloor+1\right)\left(\left\lfloor\frac{l+1}{3}\right\rfloor+1\right),q}\right)^2\end{array}\right)}\sin\theta_q$$

$$\theta_q=\arccos\left(\frac{\sum_{j=1}^{3}\left(\begin{array}{l}\left(x_{\left(\left\lfloor\frac{j-1}{3}\right\rfloor+1\right)\left(\left\lfloor\frac{j}{3}\right\rfloor+1\right)}-x_{\left(\left\lfloor\frac{j}{3}\right\rfloor+1\right)\left(\left\lfloor\frac{j+1}{3}\right\rfloor+1\right)}\right)^2+\\ \left(y_{\left(\left\lfloor\frac{j-1}{3}\right\rfloor+1\right)\left(\left\lfloor\frac{j}{3}\right\rfloor+1\right)}-y_{\left(\left\lfloor\frac{j}{3}\right\rfloor+1\right)\left(\left\lfloor\frac{j+1}{3}\right\rfloor+1\right)}\right)^2\end{array}\right)}{2\sqrt{\prod_{l=1}^{2}\left(\begin{array}{l}\left(x_{\left(\left\lfloor\frac{l-1}{3}\right\rfloor+1\right)\left(\left\lfloor\frac{l}{3}\right\rfloor+1\right),q}-x_{\left(\left\lfloor\frac{l}{3}\right\rfloor+1\right)\left(\left\lfloor\frac{l+1}{3}\right\rfloor+1\right),q}\right)^2+\\ \left(y_{\left(\left\lfloor\frac{l-1}{3}\right\rfloor+1\right)\left(\left\lfloor\frac{l}{3}\right\rfloor+1\right),q}-y_{\left(\left\lfloor\frac{l}{3}\right\rfloor+1\right)\left(\left\lfloor\frac{l+1}{3}\right\rfloor+1\right),q}\right)^2\end{array}\right)}}\right), \tag{3.10}$$

where x_{mn} and y_{mn} are the coordinates of the intersections P_{mn} (see Figure 3.2), and they can be calculated as

$$\begin{aligned}x_{mn,q}&=\mathrm{re}\left(\left(x'_{mn,q}+iy'_{mn,q}\right)e^{i\varphi_{mn}}\right)+x_m\\ y_{mn,q}&=\mathrm{im}\left(\left(x'_{mn,q}+iy'_{mn,q}\right)e^{i\varphi_{mn}}\right)+y_m\end{aligned}. \tag{3.11}$$

To simplify the calculation, the coordinates of receivers shall be transformed to the reference coordinate systems. For the given X and Y aches, the transformed coordinates of receivers can be expressed as

$$\begin{aligned}x'_m&=\mathrm{re}\left(\left(x_m+iy_m\right)e^{-i\varphi_{mn}}\right)-x_m\\ y'_m&=\mathrm{im}\left(\left(x_m+iy_m\right)e^{-i\varphi_{mn}}\right)-y_m\\ x'_n&=\mathrm{re}\left(\left(x_n+iy_n\right)e^{-i\varphi_{mn}}\right)-x_n\\ y'_n&=\mathrm{im}\left(\left(x_n+iy_n\right)e^{-i\varphi_{mn}}\right)-y_n\end{aligned}, \tag{3.12}$$

where "re" and "im" are the real and imaginary part operator and φ_{mn} is the angle between the given X aches and the vector $\vec{v}_{mn}=\left(x_n-x_m\right)+i\left(y_n-y_m\right)$. With the reference coordinates, the coordinates of intersections P'_{ml} can be determined as

$$
\begin{aligned}
x'_{mn,q} &= \frac{c^2\left(t_{n,q}^2 - t_{m,q}^2\right) - \left(x_n'^2 - x_m'^2 + y_n'^2 - y_m'^2\right)}{2\left(x_n' - x_m'\right)} \\
y'_{mn,q} &= y_m' + \sqrt{c^2 t_{m,q}^2 - \left(x'_{mn} - x_m'\right)^2}
\end{aligned}
\tag{3.13}
$$

From (3.10) to (3.13), we can see that $f_A\left(\boldsymbol{t}_q\right)$ cannot be written as a linear function of $\boldsymbol{t}_q$. Hence, $f_A\left(\boldsymbol{t}_q\right)$ is considered as the *N*-variant function. Taking the second-order Taylor expansion around the real incoming time vector $\boldsymbol{t}_{\mathrm{r}}$, we can see that

$$
\begin{aligned}
f_A\left(\boldsymbol{t}_q\right) &= f_A\left(t_{1,r} + \Delta t_{1,q}, t_{2,r} + \Delta t_{2,q}, \cdots, t_{N,r} + \Delta t_{N,q}\right) \\
&= \sum_{n1=0}^{2}\sum_{n2=0}^{2}\cdots\sum_{nN=0}^{2}\left(\frac{\left(t_{1,q} - t_{1,r}\right)^{n1}\cdots\left(t_{N,q} - t_{N,r}\right)^{nN}}{n1!\cdots nN!}\left(\frac{\partial^{n1+\cdots+nN} f_A}{\partial t_{1,q}^{n1}\cdots\partial t_{N,q}^{nN}}\right)\left(\boldsymbol{t}_r\right)\right)
\end{aligned}
\tag{3.14}
$$

For $N = 3$, (3.14) can be simplified as

$$
\begin{aligned}
f_A\left(\boldsymbol{t}_q\right) \approx\ & f_A\left(\boldsymbol{t}_r\right) + \sum_{n=1}^{3}\frac{\partial f_A\left(\boldsymbol{t}_r\right)}{\partial t_{n,q}}\Delta t_{n,q} \\
& + \frac{\partial^2 f_A\left(\boldsymbol{t}_r\right)}{\partial t_{1,q}\partial t_{2,q}}\Delta t_{1,q}\Delta t_{2,q} + \frac{\partial^2 f_A\left(\boldsymbol{t}_r\right)}{\partial t_{1,q}\partial t_{3,q}}\Delta t_{1,q}\Delta t_{3,q} + \frac{\partial^2 f_A\left(\boldsymbol{t}_r\right)}{\partial t_{2,q}\partial t_{3,q}}\Delta t_{2,q}\Delta t_{3,q} \\
& + \frac{\partial^2 f_A\left(\boldsymbol{t}_r\right)}{2\partial t_{1,q}^2}\Delta t_{1,q}^2 + \frac{\partial^2 f_A\left(\boldsymbol{t}_r\right)}{2\partial t_{2,q}^2}\Delta t_{2,q}^2 + \frac{\partial^2 f_A\left(\boldsymbol{t}_r\right)}{2\partial t_{3,q}^2}\Delta t_{3,q}^2
\end{aligned}
\tag{3.15}
$$

The Jacobi vector and the Hessen matrix of $f_A\left(\boldsymbol{t}_r\right)$ can be expressed as

$$
\boldsymbol{j} = \begin{bmatrix} \dfrac{\partial f\left(\boldsymbol{t}_r\right)}{\partial t_{1,q}} & \dfrac{\partial f\left(\boldsymbol{t}_r\right)}{\partial t_{2,q}} & \dfrac{\partial f\left(\boldsymbol{t}_r\right)}{\partial t_{3,q}} \end{bmatrix}^{\mathrm{T}}
\tag{3.16}
$$

and

$$
\boldsymbol{H} = \begin{bmatrix}
\dfrac{\partial^2 f_A\left(\boldsymbol{t}_r\right)}{\partial t_{1,q}^2} & \dfrac{\partial^2 f_A\left(\boldsymbol{t}_r\right)}{\partial t_{1,q}\partial t_{2,q}} & \dfrac{\partial^2 f_A\left(\boldsymbol{t}_r\right)}{\partial t_{1,q}\partial t_{3,q}} \\
\dfrac{\partial^2 f_A\left(\boldsymbol{t}_r\right)}{\partial t_{2,q}\partial t_{1,q}} & \dfrac{\partial^2 f_A\left(\boldsymbol{t}_r\right)}{\partial t_{2,q}^2} & \dfrac{\partial^2 f_A\left(\boldsymbol{t}_r\right)}{\partial t_{2,q}\partial t_{3,q}} \\
\dfrac{\partial^2 f_A\left(\boldsymbol{t}_r\right)}{\partial t_{3,q}\partial t_{1,q}} & \dfrac{\partial^2 f_A\left(\boldsymbol{t}_r\right)}{\partial t_{3,q}\partial t_{2,q}} & \dfrac{\partial^2 f_A\left(\boldsymbol{t}_r\right)}{\partial t_{3,q}^2}
\end{bmatrix}
\tag{3.17}
$$

From (3.10), we can know that $\boldsymbol{j} \equiv 0$ and $\boldsymbol{H}$ is a positive-definite matrix. Hence, (3.15) can be rewritten as

$$
\begin{aligned}
f_A\left(\boldsymbol{t}_q\right) \approx\ & \underbrace{\frac{\partial^2 f_A\left(\boldsymbol{t}_r\right)}{\partial t_{1,q}\partial t_{2,q}}\Delta t_{1,q}\Delta t_{2,q} + \frac{\partial^2 f_A\left(\boldsymbol{t}_r\right)}{\partial t_{1,q}\partial t_{3,q}}\Delta t_{1,q}\Delta t_{3,q} + \frac{\partial^2 f_A\left(\boldsymbol{t}_r\right)}{\partial t_{2,q}\partial t_{3,q}}\Delta t_{2,q}\Delta t_{3,q}}_{\text{first term}} \\
& \underbrace{+ \frac{\partial^2 f_A\left(\boldsymbol{t}_r\right)}{2\partial t_{1,q}^2}\Delta t_{1,q}^2 + \frac{\partial^2 f_A\left(\boldsymbol{t}_r\right)}{2\partial t_{2,q}^2}\Delta t_{2,q}^2 + \frac{\partial^2 f_A\left(\boldsymbol{t}_r\right)}{2\partial t_{3,q}^2}\Delta t_{3,q}^2}_{\text{second term}}
\end{aligned}
\tag{3.18}
$$

To determine τ_q, $f_A(\tau_q)$ should be set to zero. Hence, the estimator can be written as

$$\hat{\tau}_q = \underset{\tau_q}{\text{roots}}\left(f_A(\tau_q) = 0 \right). \tag{3.19}$$

From (3.18), we can see that the roots of $f_A(\tau_q) = 0$ is not unique because of the first term. The multi roots $\hat{\tau}_{q_k, k=1,\cdots,K}$ shall be validated to get the correct unique root, where K is the number of roots of (3.19). The pulse based channel estimator is employed to find the correct τ_q. Figure 3.3 illustrates the Pulse based Channel Estimator (PCE).

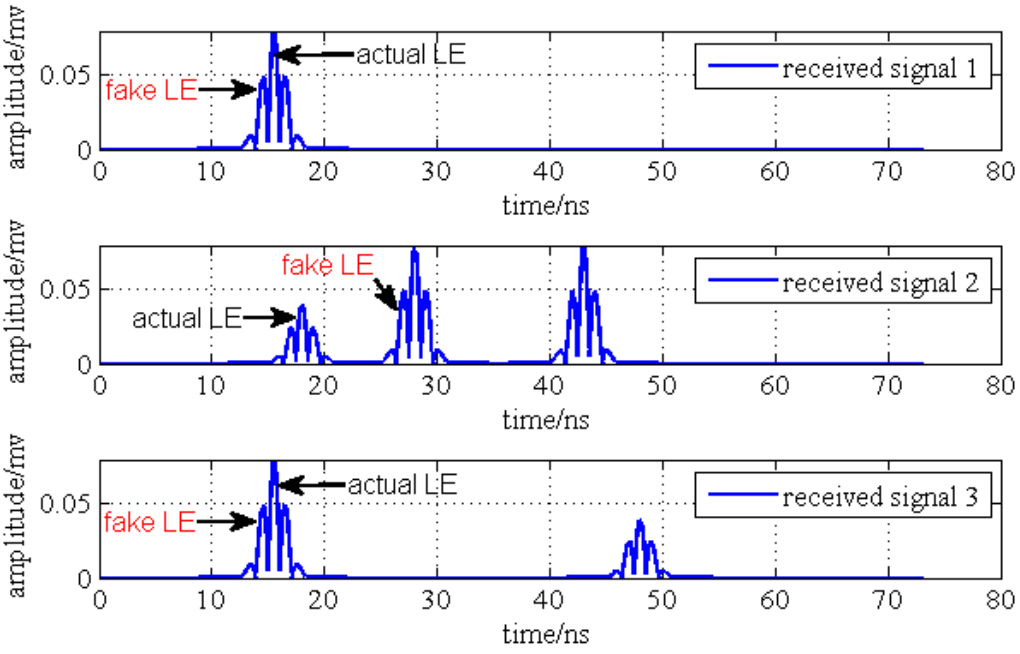

Figure 3.3: Fake LEC excluding via PCE

In Figure 3.3, it assumes that there are $K = 2$ estimated τ_q, one of which is the correct estimation (pointed by the black arrow) and another one is the fake LEC (pointed by the red arrow). Recall that the leading edge shall locate at the maximum point of the first auto-correlated Gaussian pulse (see (3.3)). For each τ_{q_k}, N rectangle functions $w_{n,q_k}(t) = \text{rect}\left(\frac{t - t_{n,q_k}}{2T_p} \right)$ are used to multiplied by $z_{g,n}(t), n = 1 \cdots N$, it has

$$z^s_{g,n,q_k}(t) = w_{n,q_k}(t) z_{g,n}(t), n = 1 \cdots N \tag{3.20}$$

Hence, the Time Domain (TD) channel can be estimated as

$$\underline{\boldsymbol{h}}_{n,q_k} = \boldsymbol{D}_{K_{T_p}} \left(\begin{bmatrix} \boldsymbol{I}_{2\omega T_p} \\ \boldsymbol{0}_{K_{T_p} \times 2\omega T_p} \end{bmatrix} \left(\boldsymbol{I}_{2\omega T_p} \boldsymbol{G}_{2\omega T_p \times K_{T_p}} \boldsymbol{s} \right)^{-1} \left(\boldsymbol{G}_{2\omega T_p \times K_{T_p}} \boldsymbol{z}^s_{g,n,q_k} \right) \right), \tag{3.21}$$

where

$$K_{T_p} = \lfloor 2T_p / t_s \rfloor \tag{3.22}$$

and $\boldsymbol{D}_{K_{T_p}}$ is a $K_{T_p} \times K_{T_p}$ squared matrix, which can be expressed as

$$\boldsymbol{D}_{K_{T_p}} = \begin{bmatrix} 1 & 1 & \cdots & 1 \\ 1 & \exp\left(-j\frac{2\pi}{K_{T_p}}\right) & \cdots & \exp\left(-j\frac{2\pi\left(K_{T_p}-1\right)}{K_{T_p}}\right) \\ \vdots & \vdots & \ddots & \vdots \\ 1 & \exp\left(-j\frac{2\pi\left(K_{T_p}-1\right)}{K_{T_p}}\right) & \cdots & \exp\left(-j\frac{2\pi\left(K_{T_p}-1\right)\left(K_{T_p}-1\right)}{K_{T_p}}\right) \end{bmatrix} \tag{3.23}$$

and

$$\begin{aligned} \boldsymbol{G}_{2\omega T_p \times K_{T_p}} &= \boldsymbol{F}_{2\omega T_p \times K_{T_p}} \boldsymbol{E}_{K_{T_p}} \boldsymbol{D}^{-1}_{K_{T_p}} \\ \boldsymbol{E}_{K_{T_p}} &= \begin{bmatrix} \boldsymbol{0} & \boldsymbol{I}_{K_{T_p}/2} \\ \boldsymbol{I}_{K_{T_p}/2} & \boldsymbol{0} \end{bmatrix} \\ \boldsymbol{F}_{2\omega T_p \times K_{T_p}} &= \begin{bmatrix} \boldsymbol{0}_{K_{T_p}/2-\omega T_p} & \boldsymbol{I}_{2\omega T_p} & \boldsymbol{0}_{K_{T_p}/2-\omega T_p} \end{bmatrix} \end{aligned} . \tag{3.24}$$

$\boldsymbol{I}_{K_{T_p}/2}$ represents $K_{T_p/2} \times K_{T_p/2}$ identity matrix and ω is the effective bandwidth of autocorrelation function of Gaussian pulse, which is defined by

$$\omega = \sqrt{\frac{\int_{-\infty}^{\infty} f^2 \left|s(f)\right|^2 df}{\int_{-\infty}^{\infty} \left|s(f)\right|^2 df}}, \tag{3.25}$$

with $s(f)$ being the Fourier transform of $s(t)$ given in (3.3). "$\lfloor \bullet \rfloor$" is the number rounding operator, $1/t_s$ is the sampling rate and $2T_p$ is the correlated pulse duration. $\boldsymbol{s}$ and $\boldsymbol{z}^{s}_{g,n,q_k}$ are the sampled $s(t)$ and $z^{s}_{g,n}(t)$ with $1/t_s$, respectively. In the ideal case (no noise, no pulse overlapping), $\underline{\boldsymbol{h}}_{n,q_k}$ shall be a delta function defined by $\delta_{K_{T_p},n,q_k}$, which is with K_{T_p} elements. For the correct $\boldsymbol{q}_k$, $\delta_{K_{T_p},n,q_k}$ can be expressed as

$$\boldsymbol{\delta}_{K_{T_p},n,q_k} = \begin{bmatrix} \underline{a}_{n,q_k} & 0 & \cdots & 0 \end{bmatrix}^{T}, \tag{3.26}$$

where $\underline{a}_{n,q_k}$ is the channel amplitude. For the fake $\boldsymbol{q}_k$, the corresponding $\underline{\boldsymbol{h}}_{n,q_k}$ is a time shift version of $\boldsymbol{\delta}_{K_{T_p},n,q_k}$. Hence, for ideal case, PCE can be written as

$$\begin{aligned} \widehat{m}_{n,q_k} &= \arg\max_{m=1\cdots K_{T_p}} \left(\boldsymbol{\delta}_{K_{T_p},n,q_k}\right) \\ \hat{q}_{\text{ideal}} &= \arg_{q_k}\left(\widehat{m}_{n,q_k}=1\right) \\ \hat{\boldsymbol{t}}_{\text{ideal}} &= \boldsymbol{t}_{\hat{q}_{\text{ideal}}} \end{aligned} . \tag{3.27}$$

In practice, due to the additive noise and the overlapped pulse, the maximum peak in (3.26) may shift to another position. With Least Squared Distance (LSD), (3.27) shall be rewritten as

$$\begin{aligned}
\hat{m}_{n,q_k} &= \arg\max_{m=1\cdots K_{T_p}} \left(\boldsymbol{\delta}_{K_{T_p},n,q_k} \right) \\
\hat{q} &= \arg\min_{q_k} \left(\sum_{n=1}^{N} \left(\hat{m}_{n,q_k} - 1 \right)^2 \right). \\
\hat{\boldsymbol{t}} &= \boldsymbol{t}_{\hat{q}}
\end{aligned} \tag{3.28}$$

So far the detection of leading edge for N=3 case is given. One of the essential issues is to determine the intersections for each CLEC in (3.11). According to the different CLECs, the intersection scenario can be divided into four modes, which are illustrated in Figure 3.4 to Figure 3.7.

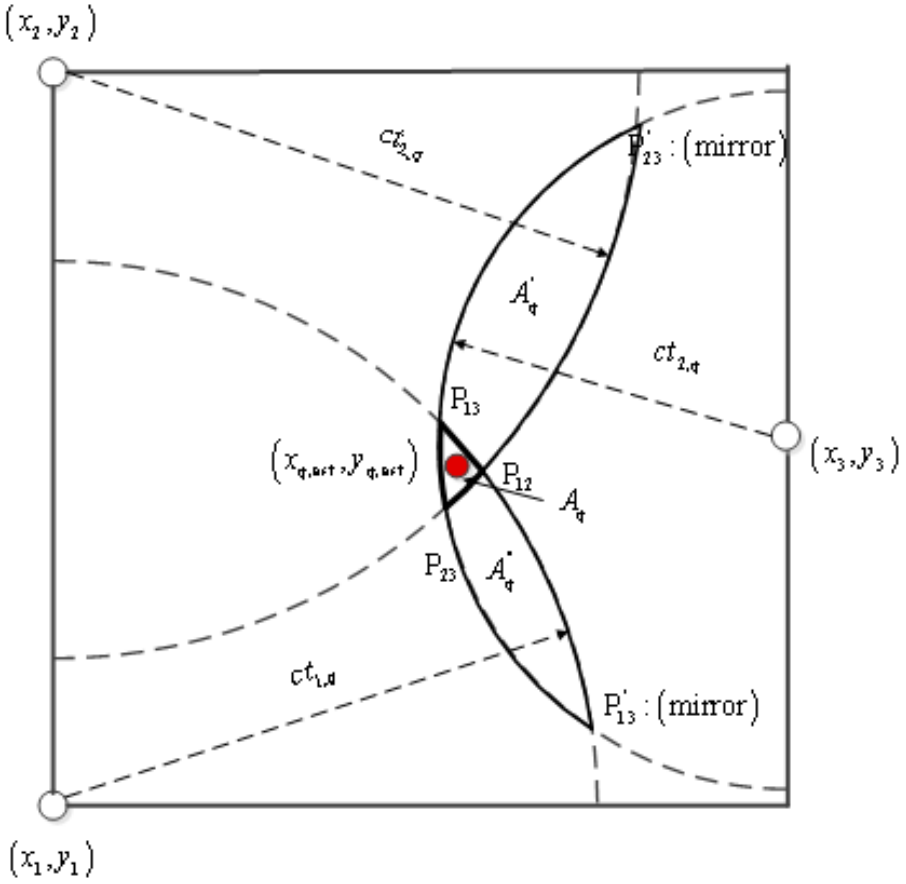

Figure 3.4: Determination of A_q and S_q (mode 1)

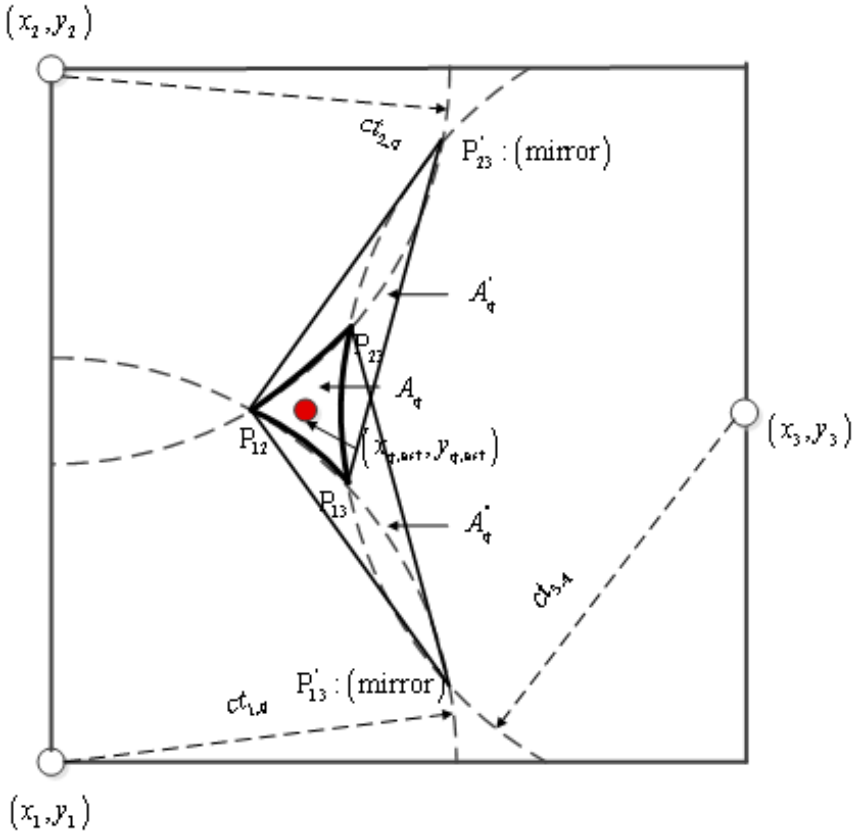

Figure 3.5: Determination of A_q and S_q (mode 2)

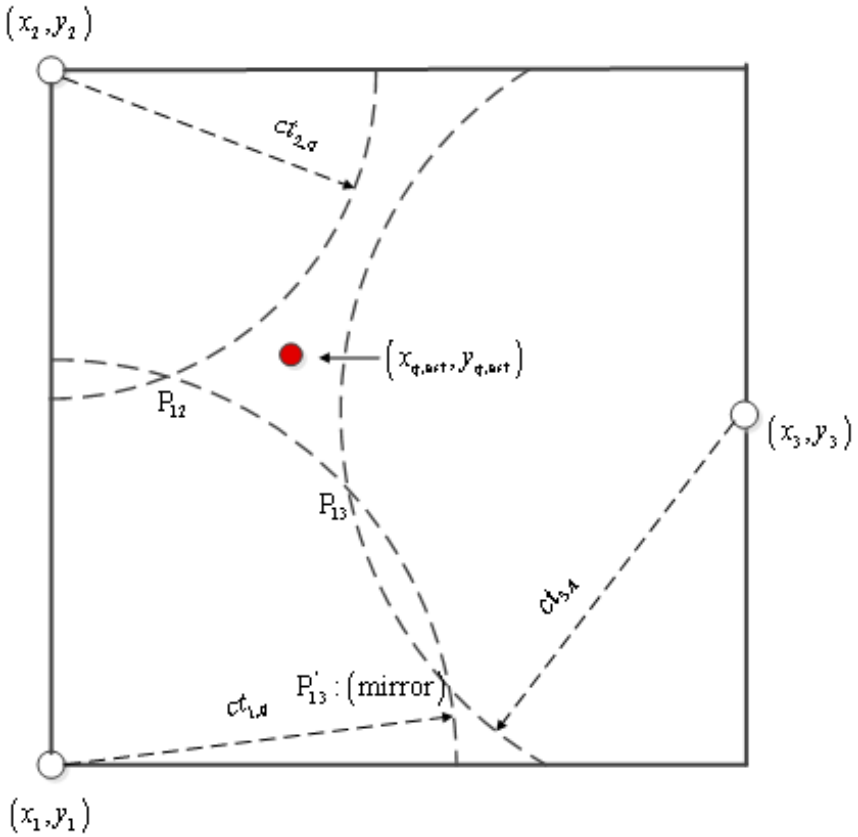

Figure 3.6: Determination of S_q (mode 3)

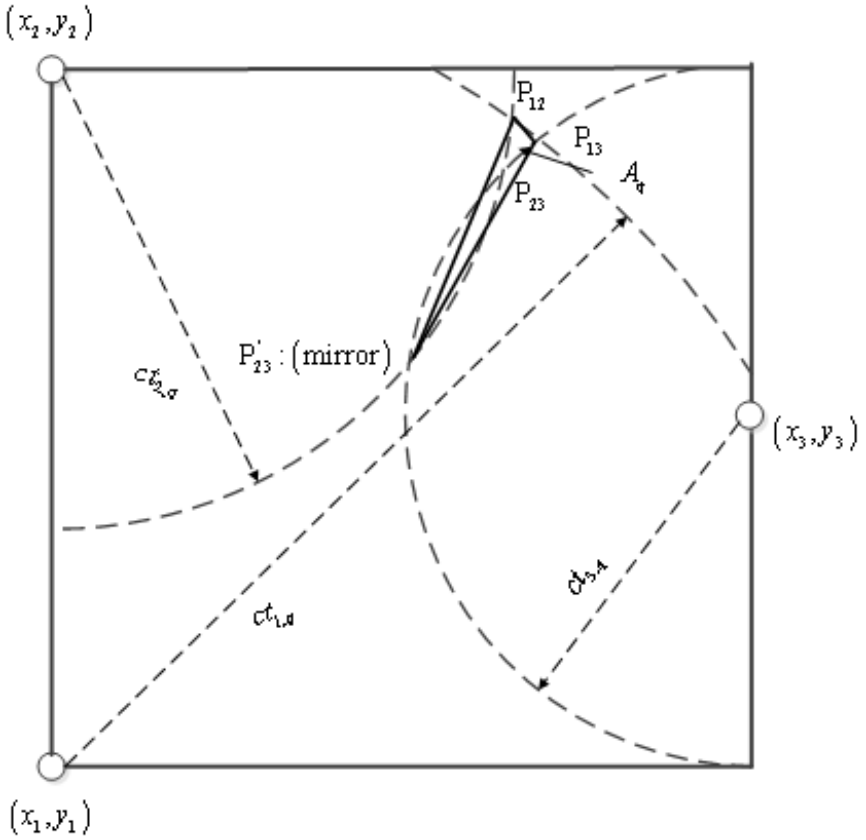

Figure 3.7: Determination of A_q and S_q (mode 4)

For the mode 1 (see Figure 3.4), the area A_q wrapped by P_{mn} is convex. It is reasonable that the possible location shall be within A_q but beyond $A_q^{'}$ and $A_q^{''}$. The mode 2 (Figure 3.5) illustrates that A_q is concave that let the possible location be within A_q, $A_q^{'}$ and $A_q^{''}$. In the mode 3 (Figure 3.6), only two intersections appears that let the calculation of A_q be impossible. In this case, A_q is assumed as an unlimited number. In the mode 4 (Figure 3.7), it appears a mirror intersection that makes the determination of A_q become more ambiguous. In this case, A_q shall be determined by the smaller wrapped area ($A_q = \min\left(A_q\left(P_{mn}\right), A_q\left(P_{mn}^{'}\right)\right)$). The determination of S_q shall be introduced latter. Due to the additive noise and rounding error of the calculation, (3.19) shall be rewritten as

$$\hat{\boldsymbol{t}}_q = \arg\min_{\boldsymbol{t}_q}\left(f_A\left(\boldsymbol{t}_q\right), K^{'} \right), \tag{3.29}$$

where $K^{'}$ represents the $K^{'}$ smallest values. Hence, selection of $K^{'}$ will influence the estimation performance.

Without loss of generality, JLED approach shall be expanded to $N \geq 3$ case, in which the squared distance S_q is considered as the unique criterion to determine the CLEC because determination of A_q become more complicated with the increase of number of intersections. From (3.9), we can see that (3.14) can be utilized for the $N \geq 3$ case.

Hence, second-order Taylor expansion around the true incoming time vector $\boldsymbol{t}_{\mathrm{r}}$ can be expressed as

$$\begin{aligned} f_S\left(\boldsymbol{t}_q\right) &\approx f_S\left(\boldsymbol{t}_r\right)+\sum_{n=1}^{N}\frac{\partial f_S\left(\boldsymbol{t}_r\right)}{\partial t_{n,q}}\Delta t_{n,q} \\ &+\sum_{n=1}^{N}\frac{\partial^2 f_S\left(\boldsymbol{t}_r\right)}{2\partial t_{n,q}^2}\Delta t_{n,q}^2+\sum_{m=1,n=1,m\neq n}^{N}\frac{\partial^2 f_S\left(\boldsymbol{t}_r\right)}{\partial t_{m,q}\partial t_{n,q}}\Delta t_{m,q}\Delta t_{n,q} \end{aligned} \tag{3.30}$$

Similar with that for $N=3$ case, $\boldsymbol{t}_q$ can be estimated via

$$\hat{\boldsymbol{t}}_q=\arg\min_{\boldsymbol{t}_q}\left(f_S\left(\boldsymbol{t}_q\right),K^{'}\right) \tag{3.31}$$

The followings are the derivate of $f_S(\bullet)$ for $N\geq 3$ case:

$$f_S\left(\boldsymbol{t}_q\right)=\sum_{n=1}^{N}\left(ct_{n,q}-\sqrt{\left(x_n-x_{\mathrm{est},q}\right)^2+\left(y_n-y_{\mathrm{est},q}\right)^2}\right), \tag{3.32}$$

where $\left(x_{\mathrm{est},q},y_{\mathrm{est},q}\right)$ shall be estimated via Least Squares (LS) method:

$$\begin{aligned} \begin{bmatrix} x_{\mathrm{est},q} \\ y_{\mathrm{est},q} \end{bmatrix} &= \left(\boldsymbol{A}^{\mathrm{H}}\boldsymbol{A}\right)^{-1}\boldsymbol{A}^{\mathrm{-H}}\boldsymbol{b}_q \\ \boldsymbol{A} &= 2\begin{bmatrix} x_2-x_1 & y_2-y_1 \\ x_3-x_2 & y_3-y_2 \\ \vdots & \vdots \\ x_1-x_N & y_1-y_N \end{bmatrix} \\ \boldsymbol{b}_q &= \begin{bmatrix} c\left(t_{1,q}^2-t_{2,q}^2\right)-\left(x_1^2-x_2^2+y_1^2-y_2^2\right) \\ c\left(t_{2,q}^2-t_{3,q}^2\right)-\left(x_2^2-x_3^2+y_2^2-y_3^2\right) \\ \vdots \\ c\left(t_{N,q}^2-t_{1,q}^2\right)-\left(x_N^2-x_1^2+y_N^2-y_1^2\right) \end{bmatrix} \end{aligned} . \tag{3.33}$$

Table 3.1: JLEDA algorithm

1. Find the maximum correlation peak $\left(t_{\mathrm{p},n}, v_{\mathrm{p},n}\right)$ over $\left(0 \quad T_{\mathrm{th},n}\right]$
2. Determine the M_n correlation peaks over $\left(0 \quad t_{\mathrm{p},n}\right]$ using the search-back algorithm: $t_{\mathrm{vle},m_n} = \mathrm{abs}\left(z_{g,n}(t)\Big|_0^{t_{\mathrm{p},n}}\right) \geq \dfrac{v_{\mathrm{p},n}}{\sqrt{\eta_{\mathrm{MER}}}}$
3. Calculate the $x_{mn,q}$, $y_{mn,q}$, $x_{q,\mathrm{est}}$ and $\mathrm{y}_{q,\mathrm{est}}$ for the q-th CLEC

For cnt =1: Q

switch(mode)

case: Mode 1 and Mode 2 ($x_{mn,q}$, $y_{mn,q}$, $x_{q,\mathrm{est}}$ and $\mathrm{y}_{q,\mathrm{est}}$ are real):

Calculate the A_q or S_q according to (3.9), (3.10) or (3.32)

case: Mode 3 ($x_{mn,q}$ and $y_{mn,q}$ have complex value):

Calculate the S_q according to (3.32) and set A_q to be $+\infty$

case: Mode 4 ($x_{mn,q}$ and $y_{mn,q}$ are real, $x_{q,\mathrm{est}}$ and $\mathrm{y}_{q,\mathrm{est}}$ are complex):

Determine the mirror point depicted in Figure 3.7

Calculate the A_q or S_q according to (3.9), (3.10) or (3.32)

end

end

Determine the $\hat{\boldsymbol{t}}_{q_k,k=1,\cdots,K}$ according to (3.19)

Estimate the $\hat{\boldsymbol{t}}$ according to (3.28)

So far the JLED approach has been investigated. The error analysis and simulation results will be given in subchapter 3.3.5.

3.3.2 Leading Edging Detection Using Improved Maximum Likelihood Channel Estimator (IMLCE)

As we know, Maximum Likelihood Estimator (MLE) can always provide the promising estimation results since it is an asymptotical Minimum Variance Unbiased (MVU) estimator [15]. To adapt to the dense multipath environment and reduce the computational complexity, the channel parameters shall be derived from subset of the Matched Filter (MF) output using Improved Maximum Likelihood Channel Estimator (IMLCE). The subset length is determined by the peak value position of the MF output (see (3.5)). MF can give a higher SNR at it output and channels can be separated if $\tau_l - \tau_k > 1/B$, where B is the system bandwidth. It denotes that partially overlapped pulses can be separated with MLCE as long as $1/B \leq T_{\mathrm{p}}$. The IMLCE consists of two steps: coarse estimation and fine estimation. Coarse estimation gives

coarse position of the first correlation peak using threshold-based search back algorithm. According to the estimated correlation peak, the local CIR shall be determined via MLCE in the second step (see Figure 3.8).

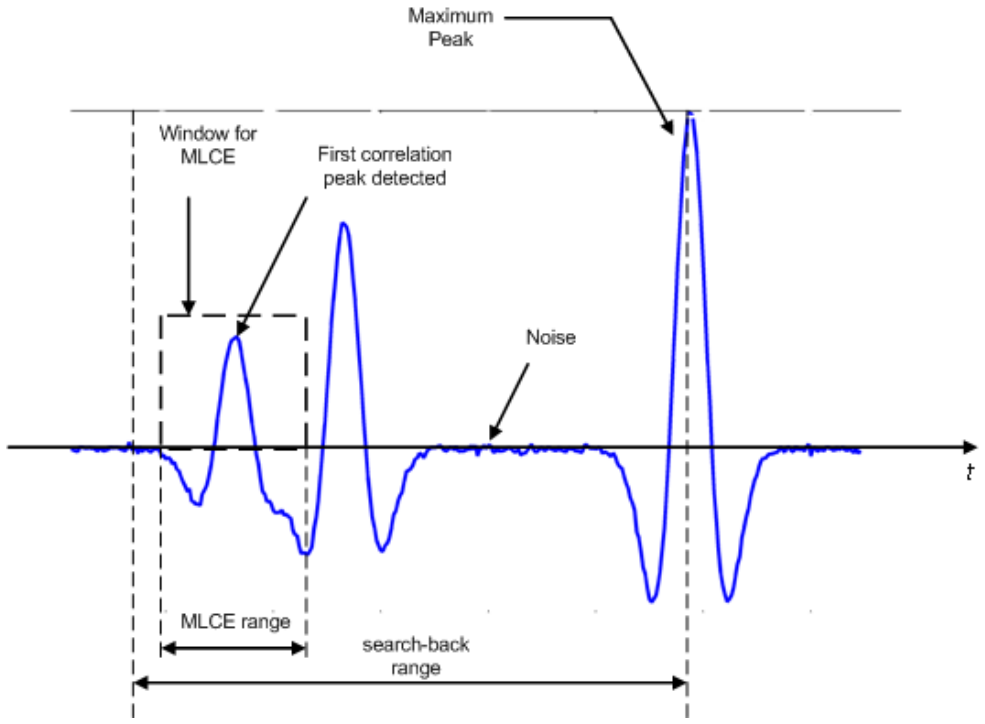

Figure 3.8: Leading edging detection via IMLCE

According to [22], the transmitted Time Hopping (TH) signal (data part) can be expressed as

$$s(t)=\sqrt{\frac{E_s}{N_s}}\sum_{k=0}^{K-1}\sum_{j=1}^{N_s}p\left(t-kT_s-jT_f-c_jT_c-d_k\varepsilon\right), \tag{3.34}$$

where E_s is the symbol energy, $p(t)$ is the normalized Gaussian pulse. K and N_s is the number of transmitted symbols and the number of pulse repetition period, respectively. T_s is the symbol duration, T_f is the pulse repetition time interval, T_c is the chip duration, d_k is the k-th information bit and $d_k \in \{0,1\}$ appearing with stochastically with equi-probability. ε is the Pulse Position Modulation (PPM) offset. The multipath channel in (2.64) can be rewritten as

$$\underline{h}_n(t)=\sum_{l=1}^{L_n}\underline{a}_{l,n}\Delta\left(\tau-\tau_{l,n}\right), \tag{3.35}$$

where the definition of $\underline{a}_{l,n}$ and $\tau_{l,n}$ are the same as (3.2). Hence, the received TH signal can be expressed as

$$\begin{aligned} r_n(t) &= \int_{-\infty}^{\infty} s(\tau)\underline{h}_n(t-\tau)\,d\tau + w_n(t) \\ &= \sqrt{\frac{E_s}{N_s}}\sum_{k=0}^{K-1}\sum_{j=1}^{N_s}\sum_{l=1}^{L}\underline{a}_{l,n}\,p\left(t-\tau_{l,n}-kT_s-jT_f-c_jT_c-d_k\varepsilon\right)+w_n(t) \end{aligned}. \tag{3.36}$$

The infrastructure of the coherent UWB receiver and the sampling circuit can be found in the section 3.3.4.

The template signal can be defined as

$$T(t)=\sqrt{\frac{E_{\mathrm{s}}}{N_{\mathrm{s}}}}\sum_{j=1}^{N_{\mathrm{s}}}p\left(t-jT_{\mathrm{f}}-c_jT_{\mathrm{c}}\right). \tag{3.37}$$

The output of correlator can be expressed as

$$\begin{aligned}
z_{\mathrm{d},n}(t)&=\int_{-\infty}^{\infty}T(\tau-t)r_n(\tau)d\tau\\
&=\int_{-\infty}^{\infty}\left(\sqrt{\frac{E_{\mathrm{s}}}{N_{\mathrm{s}}}}\sum_{j=1}^{N_{\mathrm{s}}}p\left(\tau-t-jT_{\mathrm{f}}-c_jT_{\mathrm{c}}\right)\right)\left(\sqrt{\frac{E_{\mathrm{s}}}{N_{\mathrm{s}}}}\sum_{k=0}^{K-1}\sum_{j=1}^{N_{\mathrm{s}}}\sum_{l=1}^{L_n}\underline{a}_{l,n}p\left(\tau-\tau_{l,n}-kT_{\mathrm{s}}-jT_{\mathrm{f}}-c_jT_{\mathrm{c}}-d_k\varepsilon\right)\right)d\tau\\
&+\int_{-\infty}^{\infty}T(\tau-t)w_n(\tau)d\tau\\
&=\frac{E_{\mathrm{s}}}{N_{\mathrm{s}}}\sum_{k=0}^{K-1}\sum_{l=1}^{L_n}\underline{a}_{l,n}s_{\mathrm{p}}\left(t-\tau_{l,n}-kT_{\mathrm{s}}-d_k\varepsilon\right)+\eta(t)
\end{aligned} \tag{3.38}$$

where $s_{\mathrm{p}}(t)$ is the autocorrelation function of $\sum_{j=1}^{N_{\mathrm{s}}}p\left(t-jT_{\mathrm{f}}-c_jT_{\mathrm{c}}\right)$. It can be expressed as

$$\begin{aligned}
s_{\mathrm{p}}(t)&=\int_{-\infty}^{\infty}\left(\sum_{j=1}^{N_s}p\left(t-\tau-jT_{\mathrm{f}}-c_jT_{\mathrm{c}}\right)\right)\left(\sum_{j=1}^{N_s}p\left(\tau-jT_{\mathrm{f}}-c_jT_{\mathrm{c}}\right)\right)d\tau\\
&=\sum_{j=1}^{N_s}s_{\mathrm{p}}^{'}\left(t-jT_{\mathrm{f}}-c_jT_{\mathrm{c}}\right)
\end{aligned}, \tag{3.39}$$

where $s_{\mathrm{p}}^{'}(t)$ is the autocorrelation function of $p(t)$.With the Nyquist-rate sampling and the resampling, the discrete received samples $z_{\mathrm{d},n}^{\mathrm{rs}}[i]$ can be determined. The same as (3.5), the maximum peak shall be determined via

$$\left(i_{\mathrm{p},n},v_{\mathrm{p},n}\right)=\arg\max_{i}\left(\mathrm{abs}\left(z_{\mathrm{d},n}^{\mathrm{rs}}\right)\Big|_0^{T_{\mathrm{th},n}}\right), \tag{3.40}$$

where $i_{\mathrm{p},n}$ denotes the *i*-th sample and $v_{\mathrm{p},n}=z_{i_{\mathrm{p},n},d,n}^{\mathrm{rs}}$. For the given η_{MER} and the search-back range T_{SB}, the coarse detection of leading edge can be expressed as

$$\hat{i}_{\mathrm{LD,COA}}=\min\left(\arg_{i=i_{\mathrm{p},n}-\lfloor T_{\mathrm{SB}}/t_{\mathrm{s}}\rfloor\,\mathrm{to}\,i_{\mathrm{p},n}}\left(z_{i,\mathrm{d},n}^{\mathrm{rs}}\geq\frac{v_{\mathrm{p},n}}{\sqrt{\eta_{\mathrm{MER}}}}\right)\right). \tag{3.41}$$

From Figure 2.25, it can find that the CDF of $\mathrm{MER}\leq 60$ is about 100% in CM1 ($\eta_{\mathrm{MER}}=60$). Determination of T_{SB} can utilize (3.4) and (3.7). In the ideal case (no noise, no pulse overlapping), the leading edge of *n*-th receiver can be detected as

$$\hat{t}_{n,\mathrm{COA}}=\left(\hat{i}_{\mathrm{LD,COA}}-1\right)t_{\mathrm{s}}. \tag{3.42}$$

Since the first received block may be distorted by overlapping with other reflected signals (see Figure 2.18 and Figure 2.19), $\hat{t}_n$ may have a large deviation from the actual incoming time. MLCE is an effective approach, which can separate two paths if $|\tau_l - \tau_k| \geq \frac{1}{B}$. For the estimated $\hat{i}_{\mathrm{LD,COA}}$, the employed window function can be expressed as

$$w_{n,\mathrm{rect}}(t) = \mathrm{rect}\left(\frac{t - \hat{t}_{n,\mathrm{COA}}}{2T_\mathrm{p}}\right). \tag{3.43}$$

Adding the windowing effect, the subset signal can be expressed as

$$\begin{aligned} z^\mathrm{s}_{\mathrm{d},n}(t) &= z_{\mathrm{d},n}(t)\, w_{n,\mathrm{rect}}(t) \\ &= \left(\frac{E_\mathrm{s}}{N_\mathrm{s}}\sum_{k=0}^{K-1}\sum_{l=1}^{L_n}\underline{a}_{l,n}s_\mathrm{p}\left(t-\tau_{l,n}-kT_\mathrm{s}-d_k\varepsilon\right)+\eta(t)\right)w_{n,\mathrm{rect}}(t). \\ &= \underbrace{\frac{E_\mathrm{s}}{N_\mathrm{s}}\sum_{k=0}^{K-1}\sum_{l=1}^{L_n}\underline{a}_{l,n}s_\mathrm{p}\left(t-\tau_{l,n}-kT_\mathrm{s}-d_k\varepsilon\right)w_{n,\mathrm{rect}}(t)}_{\text{signal}} + \underbrace{\eta'(t)}_{\text{noise}} \end{aligned} \tag{3.44}$$

Since $T_\mathrm{s} >> T_\mathrm{p}$, the signal portion in (3.44) can be rewritten as $\frac{E_\mathrm{s}}{N_\mathrm{s}}\sum_{l=1}^{L_n}\underline{a}_{l,n}s_\mathrm{p}\left(t-\tau_{l,n}-d_0\varepsilon\right)w_{n,\mathrm{rect}}(t)$. If the following definitions are made:

$$\begin{aligned} \boldsymbol{\tau}_n &= \begin{bmatrix}\tau_{1,n} & \tau_{2,n} & \cdots & \tau_{L_n,n}\end{bmatrix}^\mathrm{T} \\ \boldsymbol{s}_{\tau_{l,n}} &= \begin{bmatrix}s_{1,\tau_{l,n}} & s_{2,\tau_{l,n}} & \cdots & s_{M,\tau_{l,n}}\end{bmatrix}^\mathrm{T} \\ s_{j,\tau_{l,n}} &= \frac{E_\mathrm{s}}{N_\mathrm{s}}s_\mathrm{p}\left((m-1)t_\mathrm{s}-\tau_{l,n}-d_0\varepsilon\right)w_{n,\mathrm{rect}}\left((m-1)t_s\right) \end{aligned}. \tag{3.45}$$

Sampling $z^\mathrm{s}_{\mathrm{d},n}(t)$ with $1/t_\mathrm{s}$, it has

$$\boldsymbol{z}^\mathrm{s}_{\mathrm{d},n} = \boldsymbol{S}_n\boldsymbol{a}_n + \boldsymbol{\eta}', \tag{3.46}$$

where

$$\begin{aligned} \boldsymbol{S}_n &= \begin{bmatrix}\boldsymbol{s}_{\tau_{1,n}} & \boldsymbol{s}_{\tau_{2,n}} & \cdots & \boldsymbol{s}_{\tau_{L_n,n}}\end{bmatrix} \\ \boldsymbol{a}_n &= \begin{bmatrix}a_1 & a_2 & \cdots & a_{L_n}\end{bmatrix}^\mathrm{T} \end{aligned}. \tag{3.47}$$

In (3.46), $\boldsymbol{\eta}'$ can be considered as a Gaussian noise vector with zero mean and N_0-variance. The likelihood function can be expressed as

$$\mathrm{P}\left(\boldsymbol{z}^\mathrm{s}_{d,n} \mid \boldsymbol{a}_n, \boldsymbol{\tau}_n\right) = \frac{1}{(2\pi)^{M/2}\left(\det\left(\boldsymbol{R}_\eta\right)\right)^{1/2}}\exp\left(-\frac{1}{2}\left(\boldsymbol{z}^\mathrm{s}_{d,n}-\boldsymbol{S}_n\boldsymbol{a}_n\right)\boldsymbol{R}_\eta^{-1}\left(\boldsymbol{z}^\mathrm{s}_{d,n}-\boldsymbol{S}_n\boldsymbol{a}_n\right)^\mathrm{H}\right). \tag{3.48}$$

Then the ML estimation can be expressed as

$$\begin{aligned} \left(\boldsymbol{a}_{n,\mathrm{ML}}, \boldsymbol{\tau}_{n,\mathrm{ML}}\right) &= \arg\max_{(\boldsymbol{a}_n,\boldsymbol{\tau}_n)}\left(\mathrm{P}\left(\boldsymbol{z}^\mathrm{s}_{d,n} \mid \boldsymbol{a}_n, \boldsymbol{\tau}_n\right)\right) \\ &= \arg\min_{(\boldsymbol{a}_n,\boldsymbol{\tau}_n)}\left(\left(\boldsymbol{z}^\mathrm{s}_{d,n}-\boldsymbol{S}_n\boldsymbol{a}_n\right)\boldsymbol{R}_\eta^{-1}\left(\boldsymbol{z}^\mathrm{s}_{d,n}-\boldsymbol{S}_n\boldsymbol{a}_n\right)^\mathrm{H}\right) \end{aligned}. \tag{3.49}$$

$\boldsymbol{R}_\eta$ is considered as a diagonal matrix. Hence, (3.49) can be rewritten as

$$\begin{aligned}\left(\hat{\boldsymbol{a}}_{n,\mathrm{ML}},\hat{\boldsymbol{\tau}}_{n,\mathrm{ML}}\right)&=\underset{(\boldsymbol{a}_n,\boldsymbol{\tau}_n)}{\arg\min}\left(\boldsymbol{z}_{\mathrm{d},n}^{\mathrm{sH}}\boldsymbol{z}_{\mathrm{d},.n}^{\mathrm{s}}-\boldsymbol{z}_{\mathrm{d},n}^{\mathrm{sH}}\boldsymbol{S}_n\boldsymbol{a}_n-\boldsymbol{a}_n^{\mathrm{H}}\boldsymbol{S}_n^{\mathrm{H}}\boldsymbol{z}_{\mathrm{d},n}^{\mathrm{s}}+\boldsymbol{a}_n^{\mathrm{H}}\boldsymbol{S}_n^{\mathrm{H}}\boldsymbol{S}_n\boldsymbol{a}_n\right)\\&=\underset{(\boldsymbol{a}_n,\boldsymbol{\tau}_n)}{\arg\min}\left(\boldsymbol{a}_n^{\mathrm{H}}\boldsymbol{S}_n^{\mathrm{H}}\boldsymbol{S}_n\boldsymbol{a}_n-\boldsymbol{z}_{\mathrm{d},n}^{\mathrm{sH}}\boldsymbol{S}_n\boldsymbol{a}_n-\boldsymbol{a}_n^{\mathrm{H}}\boldsymbol{S}_n^{\mathrm{H}}\boldsymbol{z}_{\mathrm{d},n}^{\mathrm{s}}\right)\end{aligned} \tag{3.50}$$

Setting the first derivation to be zero, it has

$$\begin{aligned}&-\boldsymbol{z}_{\mathrm{d},n}^{\mathrm{sH}}\boldsymbol{S}_n-\boldsymbol{z}_{\mathrm{d},n}^{\mathrm{sH}}\boldsymbol{S}_n+2\boldsymbol{a}_{n,\mathrm{ML}}^{\mathrm{H}}\boldsymbol{S}_n^{\mathrm{H}}\boldsymbol{S}_n=\boldsymbol{0}\\&\hat{\boldsymbol{a}}_{n,\mathrm{ML}}^{\mathrm{H}}=\boldsymbol{z}_{\mathrm{d},n}^{\mathrm{sH}}\boldsymbol{S}_n\left(\boldsymbol{S}_n^{\mathrm{H}}\boldsymbol{S}_n\right)^{-1}\end{aligned}. \tag{3.51}$$

To get $\boldsymbol{\tau}_{n,\mathrm{ML}}$, it defines

$$\boldsymbol{x}\left(\boldsymbol{\tau}_n\right)=\left(\boldsymbol{S}_n^{\mathrm{H}}\boldsymbol{S}_n\right)^{-1}\boldsymbol{S}_n^{\mathrm{H}}\boldsymbol{z}_{\mathrm{d},n}^{\mathrm{s}}. \tag{3.52}$$

Then (3.50) can be rewritten as

$$\begin{aligned}&\boldsymbol{a}_n^{\mathrm{H}}\boldsymbol{S}_n^{\mathrm{H}}\boldsymbol{S}_n\boldsymbol{a}_n-\boldsymbol{z}_{\mathrm{d},n}^{\mathrm{sH}}\boldsymbol{S}_n\boldsymbol{a}_n-\boldsymbol{a}_n^{\mathrm{H}}\boldsymbol{S}_n^{\mathrm{H}}\boldsymbol{z}_{\mathrm{d},n}^{\mathrm{s}}=\\&=\left(\boldsymbol{a}_n-\boldsymbol{x}\left(\boldsymbol{\tau}_n\right)\right)^{\mathrm{H}}\boldsymbol{S}_n^{\mathrm{H}}\boldsymbol{S}_n\left(\boldsymbol{a}_n-\boldsymbol{x}\left(\boldsymbol{\tau}_n\right)\right)-\boldsymbol{x}\left(\boldsymbol{\tau}_n\right)^{\mathrm{H}}\boldsymbol{S}_n^{\mathrm{H}}\boldsymbol{S}_n\boldsymbol{x}\left(\boldsymbol{\tau}_n\right)\end{aligned}. \tag{3.53}$$

With (3.51), the first term of (3.53) shall disappear. The minimization of (3.50) can be rewritten as

$$\begin{aligned}\hat{\boldsymbol{\tau}}_{n,\mathrm{ML}}&=\underset{\boldsymbol{\tau}_n}{\arg\max}\left(\boldsymbol{x}\left(\boldsymbol{\tau}_n\right)^{\mathrm{H}}\boldsymbol{S}_n^{\mathrm{H}}\boldsymbol{S}_n\boldsymbol{x}\left(\boldsymbol{\tau}_n\right)\right)\\&=\underset{\boldsymbol{\tau}_n}{\arg\max}\left(\boldsymbol{z}_{\mathrm{d},n}^{\mathrm{sH}}\boldsymbol{S}_n\left(\boldsymbol{S}_n^{\mathrm{H}}\boldsymbol{S}_n\right)^{-1}\boldsymbol{S}_n^{\mathrm{H}}\boldsymbol{z}_{\mathrm{d},n}\right)\end{aligned}. \tag{3.54}$$

For a given number of channels L_n, (3.51) and (3.54) become a two dimensional optimization problem. It is obvious that $\hat{\boldsymbol{\tau}}_n$ can be determined independently from $\hat{\boldsymbol{a}}_n$. In general, determination of $\hat{\boldsymbol{\tau}}_n$ needs to compute the Jacobian matrix. It can be seen that right side of (3.54) is not a linear function that makes computation of Jacobian matrix become impossible. Therefore, an iterative method shall be employed, which begins with an initial $L_n\times 1$ time delay vector $\boldsymbol{\tau}_{n,\mathrm{ini}}$. $\boldsymbol{\tau}_{n,\mathrm{ini}}$ can be arbitrarily selected. Then $\tau_{l,l=1,2\cdots L_n,l\neq i}$ are kept fixed and $\boldsymbol{\tau}_{n,\mathrm{new}}=\left[\tau_{1,\mathrm{new}}\quad\tau_{2,\mathrm{new}}\quad\cdots\quad\tau_{L_n,\mathrm{new}}\right]^{\mathrm{T}}$ shall be renewed using (3.54). Then $\boldsymbol{\tau}_{n,\mathrm{ini}}$ shall be replaced by $\boldsymbol{\tau}_{n,\mathrm{new}}$ to begin the next iteration. This process needs to repeated until $\boldsymbol{\tau}_{n,\mathrm{new}}$ converges to a fixed vector. With $\hat{\boldsymbol{\tau}}_{n,\mathrm{ML}}$, $\hat{\boldsymbol{a}}_{n,\mathrm{ML}}$ can be estimated by (3.51).

In practice, however, L_n is unknown that makes (3.51) become a three dimensional optimization problem. (3.49) shall be rewritten as

$$\begin{aligned}\left(\boldsymbol{a}_{n,\mathrm{ML}},\boldsymbol{\tau}_{n,\mathrm{ML}},L_{n,\mathrm{ML}}\right)&=\underset{L_n=1\cdots c}{\arg\max}\left(\mathrm{P}\left(\boldsymbol{z}_{d,n}^{\mathrm{s}}\mid\hat{\boldsymbol{a}}_{n,L_n},\hat{\boldsymbol{\tau}}_{n,L_n}\right)\right)\\\left(\hat{\boldsymbol{a}}_{n,L_n},\hat{\boldsymbol{\tau}}_{n,L_n}\right)&=\underset{\left(\boldsymbol{a}_{n,L_n},\boldsymbol{\tau}_{n,L_n}\right)}{\arg\min}\left(\left(\boldsymbol{z}_{d,n}^{\mathrm{s}}-\boldsymbol{S}_{n,L_n}\boldsymbol{a}_{n,L_n}\right)\boldsymbol{R}_\eta^{-1}\left(\boldsymbol{z}_{d,n}^{\mathrm{s}}-\boldsymbol{S}_{n,L_n}\boldsymbol{a}_{n,L_n}\right)^{\mathrm{H}}\right),\end{aligned} \tag{3.55}$$

where $\boldsymbol{S}_{n,L_n}$ and $\boldsymbol{a}_{n,L_n}$ are defined in (3.47).

3.3.3 Leading Edge Detection via Subspace based Approach (SbA)

This sub-chapter proposes subspace based approach, which exploits the rank of received covariance matrix to determine $\left(\hat{\boldsymbol{a}}_{n,\mathrm{SbA}}, \hat{\boldsymbol{\tau}}_{n,\mathrm{SbA}}, \hat{L}_n\right)$ in the TH-PAM (Time-Hopping-Pulse Amplitude Modulation) UWB systems [22]. As an alternative modulation format, transmitted TH-PAM signal can be expressed as

$$s_{\mathrm{PAM}}(t) = \sqrt{\frac{E_{\mathrm{s}}}{N_{\mathrm{s}}}} \sum_{k=0}^{K-1} d_k \sum_{j=1}^{N_{\mathrm{s}}} p\left(t - kT_{\mathrm{s}} - jT_{\mathrm{f}} - c_j T_{\mathrm{c}}\right). \tag{3.56}$$

The received signal and the correlated signal can be expressed as

$$\begin{aligned} r_{n,\mathrm{PAM}}(t) &= \int_{-\infty}^{\infty} s_{\mathrm{PAM}}(\tau) \underline{h}_n(t-\tau)\, d\tau + w_n(t) \\ &= \sqrt{\frac{E_{\mathrm{s}}}{N_{\mathrm{s}}}} \sum_{k=0}^{K-1} d_k \sum_{j=0}^{N_{\mathrm{s}}-1} \sum_{l=1}^{L_n} \underline{a}_{l,n}\, p\left(t - \tau_{l,n} - kT_{\mathrm{s}} - jT_{\mathrm{f}} - c_j T_{\mathrm{c}}\right) + w_n(t) \end{aligned} \tag{3.57}$$

and

$$\begin{aligned} & z_{\mathrm{d},n,\mathrm{PAM}}(t) = \int_{-\infty}^{\infty} T(\tau - t)\, r_{n,\mathrm{PAM}}(\tau)\, d\tau \\ & = \int_{-\infty}^{\infty} \left(\sqrt{\frac{E_{\mathrm{s}}}{N_{\mathrm{s}}}} \sum_{j=0}^{N_s-1} p\left(\tau - t - jT_{\mathrm{f}} - c_j T_{\mathrm{c}}\right) \right) \left(\sqrt{\frac{E_{\mathrm{s}}}{N_{\mathrm{s}}}} \sum_{k=0}^{K-1} d_k \sum_{j=0}^{N_s-1} \sum_{l=1}^{L_n} \underline{a}_{l,n}\, p\left(\tau - \tau_{l,n} - kT_{\mathrm{s}} - jT_{\mathrm{f}} - c_j T_{\mathrm{c}}\right) \right) d\tau \\ & + \int_{-\infty}^{\infty} T(\tau - t)\, w_n(\tau)\, d\tau \\ & = \frac{E_{\mathrm{s}}}{N_{\mathrm{s}}} \sum_{k=0}^{K-1} d_k \sum_{l=1}^{L_n} \underline{a}_{l,n}\, s_{\mathrm{p,pam}}\left(t - \tau_{l,n} - kT_{\mathrm{s}}\right) + \eta(t) \\ & = \frac{E_{\mathrm{s}}}{N_{\mathrm{s}}} \sum_{k=0}^{K-1} d_k \sum_{j=1}^{N_{\mathrm{s}}} \sum_{l=1}^{L_n} \underline{a}_{l,n}\, s_{\mathrm{p}}'\left(t - \tau_{l,n} - jT_{\mathrm{f}} - c_j T_{\mathrm{c}} - kT_{\mathrm{s}}\right) + \eta(t) \end{aligned} \tag{3.58}$$

where $s_{\mathrm{p}}(t)$ is the autocorrelation function of $p(t)$. The same as JLDE and MLCE, it assumes that the maximum correlation peak is locked on $\left(i_{\mathrm{p,PAM},n}, v_{\mathrm{p,PAM},n}\right)$. Then the search-back algorithm shall be started, which is followed by the SbA (see Figure 3.9).

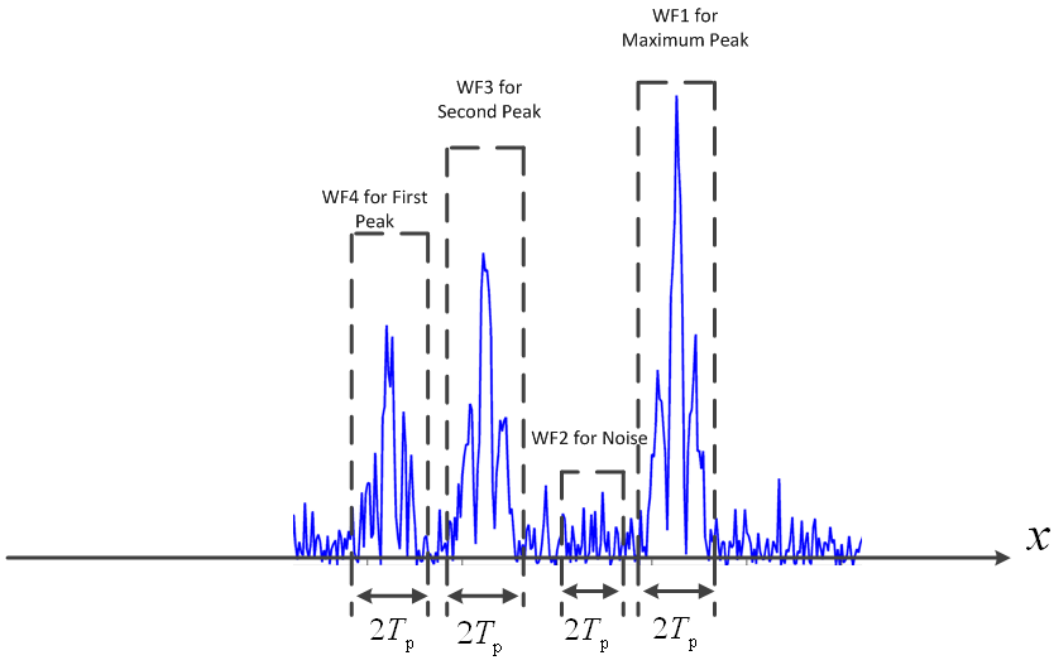

Figure 3.9: Determination of the main peaks

In this dissertation, SbA are investigated under two cases: I) channel remains static within one millisecond. II) channel experiences a multi-scale fading. In both cases, L_n keeps constant.

Proposition: In the former case, $\boldsymbol{a}_n$ and $\boldsymbol{\tau}_n$ cannot be directly determined by SbA because the number of signal subspace of the covariance matrix is equal to one.

Proof: Transforming (3.57) to Frequency Domain (FD), it has

$$\begin{aligned}\underline{R}_{n,\mathrm{PAM}}(f) &= \underbrace{\sqrt{\frac{E_\mathrm{s}}{N_\mathrm{s}}}\underline{P}(f)\sum_{k=0}^{K-1} d_k e^{-i2\pi fkT_\mathrm{s}} \sum_{j=0}^{N_\mathrm{s}-1} e^{-i2\pi f\left(jT_\mathrm{f}+c_j T_\mathrm{c}\right)} \sum_{l=1}^{L_n} \underline{a}_{l,n} e^{-i2\pi f\tau_{l,n}}}_{\text{signal}} + \underbrace{\underline{W}_n(f)}_{\text{noise}}, \\ &= \sum_{k=0}^{K-1} e^{-i2\pi fkT_\mathrm{s}} \underline{R}_{n,k,\mathrm{PAM}}(f) + \underline{W}_n(f)\end{aligned} \tag{3.59}$$

where $\underline{P}(f)$ is the Fourier Transformation of $p(t)$. (3.59) can be formulated into a matrix form.

$$\boldsymbol{r}_{n,k,\mathrm{PAM}} = \underline{\boldsymbol{D}}_\mathrm{p}\,\underline{\boldsymbol{A}}_n \boldsymbol{d}_{n,k} + \underline{\boldsymbol{w}}_{n,k}, \tag{3.60}$$

where

$$\underline{r}_{n,k,m,\mathrm{PAM}} = \underline{R}_{n,k,\mathrm{PAM}}\left(f_0 + (m-1)\Delta f\right), m = 1\cdots M, \tag{3.61}$$

and

$$\underline{\boldsymbol{D}}_{\mathrm{p}} = \mathrm{diag}\left(\left[\underline{P}\left(f_0\right) \quad \underline{P}\left(f_0+\Delta f\right) \quad \cdots \quad \underline{P}\left(f_0+\left(M-1\right)\Delta f\right)\right]\right)$$
$$\underline{\boldsymbol{A}}_n = \begin{bmatrix} 1 & 1 & \cdots & 1 \\ e^{-j2\pi\Delta f\tau_{1,n}} & e^{-j2\pi\Delta f\tau_{2,n}} & \cdots & e^{-j2\pi\Delta f\tau_{L_n,n}} \\ \vdots & \vdots & \ddots & \vdots \\ e^{-j2\pi(M-1)\Delta f\tau_{1,n}} & e^{-j2\pi(M-1)\Delta f\tau_{2,n}} & \cdots & e^{-j2\pi(M-1)\Delta f\tau_{L_n,n}} \end{bmatrix} \quad . \tag{3.62}$$
$$\boldsymbol{d}_{n,k} = \left[\sqrt{\frac{E_{\mathrm{s}}}{N_{\mathrm{s}}}}d_k a_{1,n} \quad \sqrt{\frac{E_{\mathrm{s}}}{N_{\mathrm{s}}}}d_k a_{2,n} \quad \cdots \quad \sqrt{\frac{E_{\mathrm{s}}}{N_{\mathrm{s}}}}d_k a_{L_n,n}\right]^{\mathrm{T}}$$

$\underline{\boldsymbol{w}}_n$ is considered as a zero mean Gaussian vector. The covariance matrix of $\boldsymbol{r}_{n,\mathrm{PAM}}$ can be determined as

$$\begin{aligned} E\left(\underline{\boldsymbol{r}}_{n,\mathrm{PAM}}\underline{\boldsymbol{r}}_{n,\mathrm{PAM}}^{\mathrm{H}}\right) &= \frac{1}{K}\sum_{k=1}^{K}\left(\underline{\boldsymbol{D}}_{\mathrm{p}}\underline{\boldsymbol{A}}_n\boldsymbol{d}_{n,k}+\underline{\boldsymbol{w}}_n\right)\left(\underline{\boldsymbol{D}}_{\mathrm{p}}\underline{\boldsymbol{A}}_n\boldsymbol{d}_{n,k}+\underline{\boldsymbol{w}}_n\right)^{\mathrm{H}} \\ &= \frac{1}{K}\sum_{k=1}^{K}\left(\underline{\boldsymbol{D}}_{\mathrm{p}}\underline{\boldsymbol{A}}_n\boldsymbol{d}_{n,k}\boldsymbol{d}_{n,k}^{H}\underline{\boldsymbol{A}}_n^{\mathrm{H}}\underline{\boldsymbol{D}}_{\mathrm{p}}^{\mathrm{H}}+\underline{\boldsymbol{D}}_{\mathrm{p}}\underline{\boldsymbol{A}}_n\boldsymbol{d}_{n,k}\underline{\boldsymbol{w}}_n^{\mathrm{H}}+\underline{\boldsymbol{w}}_n\boldsymbol{d}_{n,k}^{\mathrm{H}}\underline{\boldsymbol{A}}_n^{\mathrm{H}}\underline{\boldsymbol{D}}_{\mathrm{p}}^{\mathrm{H}}+\underline{\boldsymbol{w}}_n\underline{\boldsymbol{w}}_n^{\mathrm{H}}\right) \end{aligned} \quad . \tag{3.63}$$

With large K, $\frac{1}{K}\sum_{k=1}^{K}\underline{\boldsymbol{D}}_{\mathrm{p}}\underline{\boldsymbol{A}}_n\boldsymbol{d}_{n,k}\underline{\boldsymbol{w}}_n^{\mathrm{H}}$ and $\frac{1}{K}\sum_{k=1}^{K}\underline{\boldsymbol{w}}_n\boldsymbol{d}_{n,k}^{\mathrm{H}}\underline{\boldsymbol{A}}_n^{\mathrm{H}}\underline{\boldsymbol{D}}_{\mathrm{p}}^{\mathrm{H}}$ will vanish. $\frac{1}{K}\sum_{k=1}^{K}\underline{\boldsymbol{w}}_n\underline{\boldsymbol{w}}_n^{\mathrm{H}}$ will converge to a diagonal matrix. Recalling $a_k \in \{-1,1\}$ with equi-probability, it has $\mathrm{rank}\left(\frac{1}{K}\sum_{k=1}^{K}\underline{\boldsymbol{D}}_{\mathrm{p}}\underline{\boldsymbol{A}}_n\boldsymbol{d}_{n,k}\boldsymbol{d}_{n,k}^{H}\underline{\boldsymbol{A}}_n^{\mathrm{H}}\underline{\boldsymbol{D}}_{\mathrm{p}}^{\mathrm{H}}\right)=1$.

Trying to disturb $\boldsymbol{d}_{n,k}$ with random numbers, it has

$$\boldsymbol{d}_{n,k}^{'} = \boldsymbol{C}_{n,k}\boldsymbol{d}_{n,k}\,, \tag{3.64}$$

where $\boldsymbol{C}_{n,k} = \mathrm{diag}\left(\left[c_{1,n,k} \quad c_{2,n,k} \quad \cdots \quad c_{L_n,n,k}\right]\right)$. Hence, (3.62) can be rewritten as

$$\begin{aligned} &\boldsymbol{Q}_{n,k}\underline{\boldsymbol{D}}_{\mathrm{p}}^{-1}\boldsymbol{r}_{n,k,\mathrm{PAM}} = \boldsymbol{Q}_{n,k}\underline{\boldsymbol{A}}_n\boldsymbol{d}_{n,k}+\boldsymbol{Q}_{n,k}\underline{\boldsymbol{D}}_{\mathrm{p}}^{-1}\underline{\boldsymbol{w}}_{n,k} \\ &\boldsymbol{Q}_{n,k}\underline{\boldsymbol{A}}_n = \underline{\boldsymbol{A}}_n\boldsymbol{C}_{n,k} \\ &\boldsymbol{Q}_{n,k} = \left[\boldsymbol{q}_{1,n,k} \quad \boldsymbol{q}_{2,n,k} \quad \cdots \quad \boldsymbol{q}_{M,n,k}\right] \\ &\boldsymbol{q}_{m,n,k} = \left[q_{1,n,k} \quad q_{2,n,k} \quad \cdots \quad q_{M,n,k}\right]^{\mathrm{T}} \end{aligned} \quad . \tag{3.65}$$

$\boldsymbol{q}_{m,n,k}$ in (3.65) are the random vectors for each k-th received frame. Theoretically, the rank of $\boldsymbol{Q}_{n,k}$ shall be L_n and $\boldsymbol{Q}_{n,k}$ belongs to the same subspace as $\underline{\boldsymbol{A}}_n$ so that $\boldsymbol{Q}_{n,k}\underline{\boldsymbol{A}}_n$ can be replaced by $\underline{\boldsymbol{A}}_n\boldsymbol{C}_{n,k}$. It is obvious that the determination of $\boldsymbol{Q}_{n,k}$ requires to know $\underline{\boldsymbol{A}}_n$, which contains the unknown parameters L_n and $\boldsymbol{\tau}_n$. Therefore, it makes the determination of $\boldsymbol{Q}_{n,k}$ become impossible.

Hence, it is necessary to combine the search-back algorithm and SbA, which find the correlation peaks through Signal Subspace Indication (SSI). As can be seen from Figure 3.9, the random number shall be pulse-wisely multiplied by the suspected correlation peaks, which are filtered with Window Functions (WF). Then the number

of signal subspace can be determined by the Eigen Value Decomposition (EVD) of each covariance matrix. It assumes that the extracted maximum correlation peak can be expressed as

$$\begin{aligned} z^{\mathrm{s}}_{\mathrm{d},n,\mathrm{MP,PAM}}(t) &= z_{\mathrm{d},n,\mathrm{PAM}}(t)\, w_{n,\mathrm{rect,MP}}(t) \\ &= \left(\frac{E_{\mathrm{s}}}{N_{\mathrm{s}}} \sum_{k=0}^{K-1} d_{k,n} \sum_{l=1}^{L_n} \underline{a}_{l,n} s_{\mathrm{p,pam}}(t - \tau_{l,n} - kT_{\mathrm{s}}) + \eta(t) \right) w_{n,\mathrm{rect,MP}}(t) \\ &= \underbrace{\frac{E_{\mathrm{s}}}{N_{\mathrm{s}}} \sum_{k=0}^{K-1} d_{k,n} \sum_{l=1}^{L_n} \underline{a}_{l,n} s_{\mathrm{p,pam}}(t - \tau_{l,n} - kT_{\mathrm{s}})\, w_{n,\mathrm{rect,MP}}(t)}_{\text{signal}} + \underbrace{\eta'(t)}_{\text{noise}} \\ &= \sum_{k=0}^{K-1} d_{k,n} \sum_{j=0}^{N_{\mathrm{s}}-1} s_{\mathrm{p,mp,pam}}(t - kT_{\mathrm{s}} - jT_{\mathrm{f}}) + \eta'(t) \end{aligned}, \tag{3.66}$$

where

$$w_{n,\mathrm{rect,MP}}(t) = \sum_{k=0}^{K-1} \sum_{j=0}^{N_{\mathrm{s}}-1} \mathrm{rect}\left(\frac{t - kT_{\mathrm{s}} - jT_{\mathrm{f}} - \left(\hat{i}_{n,\mathrm{MP,PAM}} - 1\right) t_{\mathrm{s}}}{2T_{\mathrm{p}}} \right). \tag{3.67}$$

In (3.67), $\hat{i}_{n,\mathrm{MP,PAM}}$ and $\hat{v}_{n,\mathrm{MP,PAM}}$ shall be determined via (3.40). It can be seen that there are KN_{s} maximum correlation peaks which can be found by (3.66) and (3.67). Under $T_{\mathrm{f}} \geq 100\mathrm{ns}$, Inter-Pulse-Interference (IPI) can be effectively mitigated. With the search-back algorithm, the correlation peaks, which arrive before the first maximum correlation peak ($k = 0$), are expressed as $\hat{\boldsymbol{i}}_{n,\mathrm{PAM}} = \left[\hat{i}_{1,n,\mathrm{PAM}} \quad \cdots \quad \hat{i}_{M,n,\mathrm{PAM}} \right]$, which has $\hat{i}_{1,n,\mathrm{PAM}} < \hat{i}_{2,n,\mathrm{PAM}} < \cdots \hat{i}_{M,n,\mathrm{PAM}} < \hat{i}_{n,\mathrm{MP,PAM}}$. The recursive SbA shall inspect the correlated signal from $\hat{i}_{n,\mathrm{MP,PAM}}$ to $\hat{i}_{1,n,\mathrm{PAM}}$. The signal subspace shall be indicated by $\boldsymbol{R}_{lm,l=1\cdots M+1,m=1\cdots M+1,l\neq m}$, which can be expressed as

$$\begin{aligned} \boldsymbol{R}_{lm} &= E\left(\boldsymbol{z}'_{lm,n,\mathrm{PAM}} \boldsymbol{z}'^{\mathrm{H}}_{lm,n,\mathrm{PAM}} \right) \\ &= \frac{1}{Q} \sum_{q=1}^{Q} \boldsymbol{z}'_{lm,q,n,\mathrm{PAM}} \boldsymbol{z}'^{\mathrm{H}}_{lm,q,n,\mathrm{PAM}} \end{aligned}, \tag{3.68}$$

where $Q = KN_{\mathrm{s}}$ and

$$\begin{aligned} \boldsymbol{z}'_{lm,q,n,\mathrm{PAM}} &= \begin{bmatrix} \boldsymbol{z}'_{1,q,n} \\ \boldsymbol{z}'_{2,q,n} \end{bmatrix} \\ \boldsymbol{z}'_{1,q,n} &= \left[z_{\mathrm{d},n}\left(\left(\hat{i}_{l,n,\mathrm{PAM}} - \left\lfloor \frac{T_{\mathrm{p}}}{t_{\mathrm{s}}} \right\rfloor \right) t_{\mathrm{s}} + (q-1)T_{\mathrm{f}} \right) \quad \cdots \quad z_{\mathrm{d},n}\left(\left(\hat{i}_{m,n,\mathrm{PAM}} - \left\lfloor \frac{T_{\mathrm{p}}}{t_{\mathrm{s}}} \right\rfloor - 1 \right) t_{\mathrm{s}} + (q-1)T_{\mathrm{f}} \right) \right]^{\mathrm{T}} \\ \boldsymbol{z}'_{2,q,n} &= \left[c_{q,n} z_{\mathrm{d},n}\left(\left(\hat{i}_{m,n,\mathrm{PAM}} - \left\lfloor \frac{T_{\mathrm{p}}}{t_{\mathrm{s}}} \right\rfloor \right) t_{\mathrm{s}} + (q-1)T_{\mathrm{f}} \right) \quad \cdots \quad c_{q,n} z_{\mathrm{d},n}\left(\left(\hat{i}_{m,n,\mathrm{PAM}} + \left\lfloor \frac{T_{\mathrm{p}}}{t_{\mathrm{s}}} \right\rfloor \right) t_{\mathrm{s}} + (q-1)T_{\mathrm{f}} \right) \right]^{\mathrm{T}} \end{aligned}$$

. (3.69)

It is clear that $\boldsymbol{z}'_{lm,q,n,\mathrm{PAM}}$ consists of *l*-th correlation peak and disturbed *m*-th correlation peak. $c_{q,n}$ in (3.69) is the random number allocated for *q*-th correlation peak. Recall that *l*-th an *m*-th correlation peaks are just suspected one that consists of four

combinations: I) both are actual correlation peaks, II) "*l*-th" is noise, "*m*-th" is actual correlation peak, III) "*l*-th" is actual correlation peak, "*m*-th" is noise and IV) both are noises. From (3.68) and (3.69), it has

$$
\begin{aligned}
\boldsymbol{R}_{lm} &= E\left(\boldsymbol{z}'_{lm,n,\mathrm{PAM}}\boldsymbol{z}'^{\mathrm{H}}_{lm,n,\mathrm{PAM}}\right) \\
&= \frac{1}{Q}\sum_{q=1}^{Q}\left(\begin{bmatrix}\boldsymbol{z}'_{1,q,n}\\ \boldsymbol{z}'_{2,q,n}\end{bmatrix}\begin{bmatrix}\boldsymbol{z}'^{\mathrm{H}}_{1,q,n} & \boldsymbol{z}'^{\mathrm{H}}_{2,q,n}\end{bmatrix}\right) \\
&= \frac{1}{Q}\sum_{q=1}^{Q}\left(\begin{array}{l}\left(\begin{bmatrix}\boldsymbol{s}'_{l,\mathrm{p}} & \boldsymbol{0}\\ \boldsymbol{0} & \boldsymbol{s}'_{m,\mathrm{p}}\end{bmatrix}\begin{bmatrix}\frac{E_{\mathrm{s}}}{N_{\mathrm{s}}}d_{\left\lfloor\frac{q}{N_{\mathrm{s}}}\right\rfloor+1}a_{l,n}\\ \frac{E_{\mathrm{s}}}{N_{\mathrm{s}}}c_{q,n}d_{\left\lfloor\frac{q}{N_{\mathrm{s}}}\right\rfloor+1}a_{m,n}\end{bmatrix}+\begin{bmatrix}\boldsymbol{\eta}_{1,q}\\ \boldsymbol{\eta}_{2,q}\end{bmatrix}\right)\cdot \\ \cdot\left(\begin{bmatrix}\boldsymbol{s}'_{l,\mathrm{p}} & \boldsymbol{0}\\ \boldsymbol{0} & \boldsymbol{s}'_{m,\mathrm{p}}\end{bmatrix}\begin{bmatrix}\frac{E_{\mathrm{s}}}{N_{\mathrm{s}}}d_{\left\lfloor\frac{q}{N_{\mathrm{s}}}\right\rfloor+1}a_{l,n}\\ \frac{E_{\mathrm{s}}}{N_{\mathrm{s}}}c_{q,n}d_{\left\lfloor\frac{q}{N_{\mathrm{s}}}\right\rfloor+1}a_{m,n}\end{bmatrix}+\begin{bmatrix}\boldsymbol{\eta}_{1,q}\\ \boldsymbol{\eta}_{2,q}\end{bmatrix}\right)^{\mathrm{H}}\end{array}\right) \\
&= \frac{1}{Q}\sum_{q=1}^{Q}\left(\begin{array}{l}\underbrace{\begin{bmatrix}\boldsymbol{s}'_{l,\mathrm{p}} & \boldsymbol{0}\\ \boldsymbol{0} & \boldsymbol{s}'_{m,\mathrm{p}}\end{bmatrix}\begin{bmatrix}\frac{E_{\mathrm{s}}}{N_{\mathrm{s}}}d_{\left\lfloor\frac{q}{N_{\mathrm{s}}}\right\rfloor+1}a_{l,n}\\ \frac{E_{\mathrm{s}}}{N_{\mathrm{s}}}c_{q,n}d_{\left\lfloor\frac{q}{N_{\mathrm{s}}}\right\rfloor+1}a_{m,n}\end{bmatrix}\begin{bmatrix}\frac{E_{\mathrm{s}}}{N_{\mathrm{s}}}d_{\left\lfloor\frac{q}{N_{\mathrm{s}}}\right\rfloor+1}a_{l,n} & \frac{E_{\mathrm{s}}}{N_{\mathrm{s}}}c_{q,n}d_{\left\lfloor\frac{q}{N_{\mathrm{s}}}\right\rfloor+1}a_{m,n}\end{bmatrix}\begin{bmatrix}\boldsymbol{s}'^{\mathrm{H}}_{l,\mathrm{p}} & \boldsymbol{0}^{\mathrm{H}}\\ \boldsymbol{0}^{\mathrm{H}} & \boldsymbol{s}'^{\mathrm{H}}_{m,\mathrm{p}}\end{bmatrix}}_{\boldsymbol{S}\text{: signal subspace}} \\ +\underbrace{\begin{bmatrix}\boldsymbol{\eta}_{1,q}\\ \boldsymbol{\eta}_{2,q}\end{bmatrix}\begin{bmatrix}\boldsymbol{\eta}^{\mathrm{H}}_{1,q} & \boldsymbol{\eta}^{\mathrm{H}}_{2,q}\end{bmatrix}}_{\text{noise subspace}}\end{array}\right),
\end{aligned}
\tag{3.70}
$$

where $\boldsymbol{s}'_{l,\mathrm{p}}$ and $\boldsymbol{s}'_{m,\mathrm{p}}$ are the digitalized $s'_{\mathrm{p}}\left(t-\left(\hat{i}_{l,n,\mathrm{PAM}}-1\right)t_{\mathrm{s}}\right)$ and $s'_{\mathrm{p}}\left(t-\left(\hat{i}_{m,n,\mathrm{PAM}}-1\right)t_{\mathrm{s}}\right)$, respectively. $\boldsymbol{0}$ in (3.70) is $\left(\hat{i}_{m,n,\mathrm{PAM}}-\hat{i}_{l,n,\mathrm{PAM}}+1\right)\times 1$ vector. $\boldsymbol{\eta}_{1,q}$ and $\boldsymbol{\eta}_{2,q}$ are the Gaussian noise vector with the length of $\hat{i}_{m,n,\mathrm{PAM}}-\hat{i}_{l,n,\mathrm{PAM}}+1$ and $\left\lfloor 2T_{\mathrm{p}}/t_{\mathrm{s}}\right\rfloor$, respectively. For the I) case, both $\boldsymbol{s}'_{l,\mathrm{p}}$ and $\boldsymbol{s}'_{m,\mathrm{p}}$ are pulse correlation vectors that let $\mathrm{rank}\left(\boldsymbol{S}\right)=2$. For the II) and III) cases, $\boldsymbol{s}'_{l,\mathrm{p}}$ or $\boldsymbol{s}'_{m,\mathrm{p}}$ is noise, by which (3.70) can be rewritten as

$$
\boldsymbol{R}_{lm} = \frac{1}{Q}\sum_{q=1}^{Q}\left(\begin{bmatrix}\boldsymbol{s}'_{l,\mathrm{p}}\\ \boldsymbol{0}\end{bmatrix}\left[\left(\frac{E_{\mathrm{s}}}{N_{\mathrm{s}}}d_{\left\lfloor\frac{q}{N_{\mathrm{s}}}\right\rfloor+1}a_{l,n}\right)^{2}\right]\begin{bmatrix}\boldsymbol{s}'^{\mathrm{H}}_{l,\mathrm{p}} & \boldsymbol{0}^{\mathrm{H}}\end{bmatrix}+\begin{bmatrix}\boldsymbol{\eta}_{1,q}\\ \boldsymbol{\eta}_{2,q}\end{bmatrix}\begin{bmatrix}\boldsymbol{\eta}^{\mathrm{H}}_{1,q} & \boldsymbol{\eta}^{\mathrm{H}}_{2,q}\end{bmatrix}\right) \tag{3.71}
$$

or

$$
\boldsymbol{R}_{lm} = \frac{1}{Q}\sum_{q=1}^{Q}\left(\begin{bmatrix}\boldsymbol{0}\\ \boldsymbol{s}'_{m,\mathrm{p}}\end{bmatrix}\left[\left(\frac{E_{\mathrm{s}}}{N_{\mathrm{s}}}c_{q,n}d_{\left\lfloor\frac{q}{N_{\mathrm{s}}}\right\rfloor+1}a_{m,n}\right)^{2}\right]\begin{bmatrix}\boldsymbol{0}^{\mathrm{H}} & \boldsymbol{s}'^{\mathrm{H}}_{m,\mathrm{p}}\end{bmatrix}+\begin{bmatrix}\boldsymbol{\eta}_{1,q}\\ \boldsymbol{\eta}_{2,q}\end{bmatrix}\begin{bmatrix}\boldsymbol{\eta}^{\mathrm{H}}_{1,q} & \boldsymbol{\eta}^{\mathrm{H}}_{2,q}\end{bmatrix}\right). \tag{3.72}
$$

It is obvious that the number of signal subspace in (3.71) and (3.72) is one. For the IV) case, the number of signal subspace shall be zero as both $\boldsymbol{s}'_{l,\mathrm{p}}$ and $\boldsymbol{s}'_{m,\mathrm{p}}$ are noise. It

assumes that the Eigenvalues of $\boldsymbol{R}_{lm}$ are $\lambda_{i,i=1\cdots N}$. Then the number of signal subspace shall be determined via MDL (see (2.69)).

Table 3.2: Algorithm for recursive SbA

1. Correlate the received signal via (3.58)
2. Find the maximum correlation peak $\left(t_{\mathrm{p},n}, v_{\mathrm{p},n}\right)$ over $\left(0 \quad T_{\mathrm{th},n}\right]$
3. Find the *M* main peaks depicted in Figure 3.9 using search-back algorithm
4. Impose the windowing function on the *M* main peaks via (3.66) and (3.67),.

Set the initial inspected *l*-th and *m*-th peak: *M*-th peak and (*M*-1)-th peak

idx_est = [*l*];

while (true)

1. Disturb the *l*-th and *m*-th peak with random vectors via (3.64), (3.65) and (3.69)
2. Determine the $\boldsymbol{R}_{lm}$ via (3.68) and (3.70)
3. Determine the Eigenvalues of $\boldsymbol{R}_{lm}$ and estimate the number of signal subspace L via (2.69).

switch (L)

case $L = 0$: //no signal determined

$l = m$ - 1;

$m = l$ -1;

case $L = 1$: //signal subspace is 1, *l*-th peak is signal, *m*-th peak is noise

$m = m$ -1;

case $L \geq 2$: // signal subspace is 2. Both *l*-th peak and *m*-th peak are signals

$l = m$;

idx_est = [idx_est *m*];

$m = m$ -1;

end

if(*m* is equal to zero)

break;

end

end

toa_est = idx_est(end)-th peak

In Table 3.2, it can be seen that SbA shall be started from the maximum peak. In the first iteration, the covariance matrix of two neighboring correlation peaks shall be

determined. Then the covariance matrix determination for the next iteration shall be indicated by the signal subspace in the current iteration. The recursive SbA shall run until touching the $\hat{i}_{1,n,\mathrm{PAM}}$ -th correlation peak. "idx_est" in Table 3.2 is used to store each detected correlation peak. The last element is the first estimated correlation peak.

So far the SbA based leading edge detection in the static channel scenario has been discussed. If the channel experiences a multi-scale fading, the recursive SbA is not valid as $\boldsymbol{a}_n$ and $\boldsymbol{\tau}_n$ are not constant value, which makes the calculation of $\boldsymbol{R}_{lm}$ become impossible. Here, it assumes that $\boldsymbol{a}_n$ and $\boldsymbol{\tau}_n$ keep asymptotically static within T_s (one received symbol). Hence, the multichannel shall be rewritten as $\underline{h}_{k,n}(t)=\sum_{l=1}^{L_n}\underline{a}_{l,k,,n}\Delta\left(\tau-\tau_{l,k,n}\right), k=1\cdots K$. (3.57) can be rewritten as

$$\begin{aligned} r_{k,n,\mathrm{PAM,f}}(t) &= \int_{(k-1)T_\mathrm{s}}^{kT_\mathrm{s}} s_{\mathrm{PAM}}(\tau)\underline{h}_{k,n}(t-\tau)\,d\tau + w_{k,n}(t) \\ &= \sqrt{\frac{E_\mathrm{s}}{N_\mathrm{s}}}d_k\sum_{j=0}^{N_\mathrm{s}-1}\sum_{l=1}^{L_n}\underline{a}_{l,k,n}\,p\left(t-\tau_{l,k,n}-jT_\mathrm{f}-c_jT_\mathrm{c}\right)+w_{k,n}(t) \end{aligned} . \tag{3.73}$$

Transforming $r_{k,n,\mathrm{PAM,f}}(t)$ to Frequency Domain (FD) and sampling it with Δf , it has

$$\underline{\boldsymbol{r}}_{k,n,\mathrm{PAM,f}} = \underline{\boldsymbol{D}}_\mathrm{p}\,\underline{\boldsymbol{A}}_{k,n}\boldsymbol{d}_{k,n}+\underline{\boldsymbol{w}}_{k,n}, \tag{3.74}$$

where $\underline{\boldsymbol{D}}_\mathrm{p}$ is defined in (3.59) and (3.62), and

$$\underline{\boldsymbol{A}}_{k,n}=\begin{bmatrix} 1 & 1 & \cdots & 1 \\ e^{-j2\pi\Delta f\tau_{1,k,n}} & e^{-j2\pi\Delta f\tau_{2,k,n}} & \cdots & e^{-j2\pi\Delta f\tau_{L_n,k,n}} \\ \vdots & \vdots & \ddots & \vdots \\ e^{-j2\pi(M-1)\Delta f\tau_{1,k,n}} & e^{-j2\pi(M-1)\Delta f\tau_{2,k,n}} & \cdots & e^{-j2\pi(M-1)\Delta f\tau_{L_n,k,n}} \end{bmatrix} \tag{3.75}$$

and

$$\boldsymbol{d}_{k,n}=\begin{bmatrix}\sqrt{\frac{E_\mathrm{s}}{N_\mathrm{s}}}d_k a_{1,k,n} & \sqrt{\frac{E_\mathrm{s}}{N_\mathrm{s}}}d_k a_{2,k,n} & \cdots & \sqrt{\frac{E_\mathrm{s}}{N_\mathrm{s}}}d_k a_{L_n,k,n}\end{bmatrix}^\mathrm{T}. \tag{3.76}$$

Recall that our task is just to determine $\boldsymbol{\tau}_{1,n}$ that needs only to inspect the first received symbol. Dividing $\underline{\boldsymbol{r}}_{1,n,\mathrm{PAM,f}}$ into I sub-blocks, (3.74) can be rewritten as

$$\begin{aligned} &\underline{\boldsymbol{r}}_{1,n,\mathrm{PAM,f}} = \begin{bmatrix}\underline{\boldsymbol{r}}_{1,n,\mathrm{PAM,f}}^{(1)\mathrm{H}} & \underline{\boldsymbol{r}}_{1,n,\mathrm{PAM,f}}^{(2)\mathrm{H}} & \cdots & \underline{\boldsymbol{r}}_{1,n,\mathrm{PAM,f}}^{(I)\mathrm{H}}\end{bmatrix}^\mathrm{H} \\ &\underline{\boldsymbol{D}}_\mathrm{p}^{(i)-1}\underline{\boldsymbol{r}}_{1,n,\mathrm{PAM,f}}^{(i)} = \underline{\boldsymbol{A}}_{1,n}^{(i)}\boldsymbol{d}_{1,n}+\underline{\boldsymbol{D}}_\mathrm{p}^{(i)-1}\underline{\boldsymbol{w}}_{1,n}^{(i)} \\ &i=1\cdots I \end{aligned} . \tag{3.77}$$

From (3.77), it has

$$\underline{\boldsymbol{D}}_{\mathrm{p}}=\begin{bmatrix}\underline{\boldsymbol{D}}_{\mathrm{p}}^{(1)} & & \\ & \ddots & \\ & & \underline{\boldsymbol{D}}_{\mathrm{p}}^{(I)}\end{bmatrix}$$
$$\underline{\boldsymbol{A}}_{1,n}=\begin{bmatrix}\underline{\boldsymbol{A}}_{1,n}^{(1)\mathrm{H}} & \cdots & \underline{\boldsymbol{A}}_{1,n}^{(I)\mathrm{H}}\end{bmatrix}^{\mathrm{H}}. \tag{3.78}$$
$$\underline{\boldsymbol{w}}_{1,n}=\begin{bmatrix}\underline{\boldsymbol{w}}_{1,n}^{(1)\mathrm{H}} & \cdots & \underline{\boldsymbol{w}}_{1,n}^{(I)\mathrm{H}}\end{bmatrix}^{\mathrm{H}}$$

In (3.77), $\underline{\boldsymbol{r}}_{1,n,\mathrm{PAM,f}}^{(i)}$ is $M/I\times 1$ vectors. The FD covariance matrix can be expressed as

$$\begin{aligned}\underline{\boldsymbol{R}}_{\boldsymbol{r}} &\approx \frac{1}{I}\sum_{i=1}^{I}\left(\underline{\boldsymbol{D}}_{\mathrm{p}}^{(i)-1}\underline{\boldsymbol{r}}_{1,n,\mathrm{PAM,f}}^{(i)}\right)\left(\underline{\boldsymbol{D}}_{\mathrm{p}}^{(i)-1}\underline{\boldsymbol{r}}_{1,n,\mathrm{PAM,f}}^{(i)}\right)^{\mathrm{H}}\\ &=\frac{1}{I}\sum_{i=1}^{I}\left(\underline{\boldsymbol{A}}_{1,n}^{(i)}\boldsymbol{d}_{1,n}+\underline{\boldsymbol{D}}_{\mathrm{p}}^{(i)-1}\underline{\boldsymbol{w}}_{1,n}^{(i)}\right)\left(\underline{\boldsymbol{A}}_{1,n}^{(i)}\boldsymbol{d}_{1,n}+\underline{\boldsymbol{D}}_{\mathrm{p}}^{(i)-1}\underline{\boldsymbol{w}}_{1,n}^{(i)}\right)^{\mathrm{H}}\\ &=\underline{\boldsymbol{A}}_{1,n}^{(1)}\left(\frac{1}{I}\sum_{i=1}^{I}\left(\underline{\boldsymbol{E}}_{i,n}\boldsymbol{d}_{1,n}\boldsymbol{d}_{1,n}^{\mathrm{H}}\underline{\boldsymbol{E}}_{i,n}^{\mathrm{H}}\right)\right)\underline{\boldsymbol{A}}_{1,n}^{(1)\mathrm{H}}+\frac{1}{I}\sum_{i=1}^{I}\left(\underline{\boldsymbol{A}}_{1,n}^{(i)}\boldsymbol{d}_{1,n}\underline{\boldsymbol{w}}_{1,n}^{(i)\mathrm{H}}\underline{\boldsymbol{D}}_{\mathrm{p}}^{(i)-\mathrm{H}}\right)+\\ &+\frac{1}{I}\sum_{i=1}^{I}\left(\underline{\boldsymbol{D}}_{\mathrm{p}}^{(i)-1}\underline{\boldsymbol{w}}_{1,n}^{(i)}\boldsymbol{d}_{1,n}^{\mathrm{H}}\underline{\boldsymbol{A}}_{1,n}^{(i)\mathrm{H}}\right)+\frac{1}{I}\sum_{i=1}^{I}\underline{\boldsymbol{D}}_{\mathrm{p}}^{(i)-1}\underline{\boldsymbol{w}}_{1,n}^{(i)}\underline{\boldsymbol{w}}_{1,n}^{(i)\mathrm{H}}\underline{\boldsymbol{D}}_{\mathrm{p}}^{(i)-\mathrm{H}}\end{aligned} \tag{3.79}$$

where

$$\underline{\boldsymbol{E}}_{i,n}=\begin{bmatrix}e^{-j2\pi(i-1)\frac{M}{I}f_{\mathrm{d}}\tau_{1,1,n}} & & \\ & \ddots & \\ & & e^{-j2\pi(i-1)\frac{M}{I}f_{\mathrm{d}}\tau_{L,1,n}}\end{bmatrix} \tag{3.80}$$

Theoretically, the second and third terms in (3.79) will disappear if I is large enough. The last term will converge to a diagonal matrix if two conditions are fulfilled: I) the number of FFT (Fast Fourier Transform) points is large enough. II) $\underline{\boldsymbol{D}}_{\mathrm{p}}^{(i)}=\underline{\boldsymbol{D}}_{\mathrm{p}}^{(j)}$ for $i\neq j$ and the diagonal elements of $\underline{\boldsymbol{D}}_{\mathrm{p}}^{(i)}$ have the same power. The rank of $\frac{1}{I}\sum_{i=1}^{I}\left(\underline{\boldsymbol{E}}_{i,n}\boldsymbol{d}_{1,n}\boldsymbol{d}_{1,n}^{\mathrm{H}}\underline{\boldsymbol{E}}_{i,n}^{\mathrm{H}}\right)$ is L_n since I is assumed to be larger than L_n.

Proof of the two conditions

To prove the first condition, it assumes that $\underline{\boldsymbol{D}}_{\mathrm{p}}^{(i)}$ is a unity matrix, which can be ignored in (3.79). The last term in (3.79) can be rewritten as

$$\begin{aligned}\underline{\boldsymbol{R}}_{\underline{\boldsymbol{w}}} &= E\left(\boldsymbol{FFT}_{M/I\times M/I}\boldsymbol{w}_{1,n,t}\boldsymbol{w}_{1,n,t}^{\mathrm{H}}\boldsymbol{FFT}_{M/I\times M/I}^{H}\right)\\ &=\boldsymbol{FFT}_{M/I\times M/I}E\left(\boldsymbol{w}_{1,n,t}\boldsymbol{w}_{1,n,t}^{\mathrm{H}}\right)\boldsymbol{FFT}_{M/I\times M/I}^{H}\\ &=\boldsymbol{FFT}_{M/I\times M/I}\begin{bmatrix}\sigma_{n,1}^{2} & & & \\ & \sigma_{n,2}^{2} & & \\ & & \ddots & \\ & & & \sigma_{n,M/I}^{2}\end{bmatrix}\boldsymbol{FFT}_{M/I\times M/I}^{H}\end{aligned}, \tag{3.81}$$

where $\boldsymbol{FFT}_{M/I\times M/I}$ is FFT operation and $\boldsymbol{w}_{1,n,t}$ is the TD noise vector. To keep $\underline{\boldsymbol{R}}_{\underline{\boldsymbol{w}}}$ to be diagonal matrix, $E\left(\boldsymbol{w}_{1,n,t}\boldsymbol{w}_{1,n,t}^{\mathrm{H}}\right)$ shall be a diagonal matrix with the same elements on it's diagonal. It is obvious that small N will lead to $\sigma_{n,k}^2 \neq \sigma_{n,l}^2$, which can destroy the diagonal characteristic of $\underline{\boldsymbol{R}}_{\underline{\boldsymbol{w}}}$. For the second condition, $\underline{\boldsymbol{R}}_{\underline{\boldsymbol{w}}}$ can be rewritten as

$$\begin{aligned}
\underline{\boldsymbol{R}}_{\underline{\boldsymbol{w}}} &= E\left(\underline{\boldsymbol{D}}_{\mathrm{p}}^{-1}\boldsymbol{FFT}_{M/I\times M/I}\boldsymbol{w}_{1,n,t}\boldsymbol{w}_{1,n,t}^{\mathrm{H}}\boldsymbol{FFT}_{M/I\times M/I}^{\mathrm{H}}\underline{\boldsymbol{D}}_{\mathrm{p}}^{-\mathrm{H}}\right) \\
&= E\left(\boldsymbol{FFT}_{M/I\times M/I}\underline{\boldsymbol{C}}_{\mathrm{p}}\boldsymbol{w}_{1,n,t}\boldsymbol{w}_{1,n,t}^{\mathrm{H}}\underline{\boldsymbol{C}}_{\mathrm{p}}^{\mathrm{H}}\boldsymbol{FFT}_{M/I\times M/I}^{\mathrm{H}}\right) \\
&= \boldsymbol{FFT}_{M/I\times M/I}\underline{\boldsymbol{C}}_{\mathrm{p}}\begin{bmatrix}\sigma_{n,1}^2 & & & \\ & \sigma_{n,2}^2 & & \\ & & \ddots & \\ & & & \sigma_{n,\frac{M}{I}}^2\end{bmatrix}\underline{\boldsymbol{C}}_{\mathrm{p}}^{\mathrm{H}}\boldsymbol{FFT}_{M/I\times M/I}^{\mathrm{H}} \\
\underline{\boldsymbol{C}}_{\mathrm{p}} &= \boldsymbol{FFT}_{M/I\times M/I}^{\mathrm{H}}\underline{\boldsymbol{D}}_{\mathrm{p}}^{-1}\boldsymbol{FFT}_{M/I\times M/I}
\end{aligned} \tag{3.82}$$

It is obvious that $\underline{\boldsymbol{C}}_{\mathrm{p}}$ shall be a circulant matrix with orthogonal column vector as $\underline{\boldsymbol{D}}_{\mathrm{p}}^{-1}$ is a diagonal matrix. To keep $\underline{\boldsymbol{C}}_{\mathrm{p}}\boldsymbol{w}_{1,n,t}\boldsymbol{w}_{1,n,t}^{\mathrm{H}}\underline{\boldsymbol{C}}_{\mathrm{p}}^{\mathrm{H}}$ being a diagonal matrix, the diagonal elements of $\underline{\boldsymbol{D}}_{\mathrm{p}}^{-1}$ shall asymptotically have the same power.

3.3.4 UWB Receiver Design for ToA based Ranging

In general, rake receiver shall be implemented in each receiver to detect the transmitted information bit. The benefit of rake receiver is that it uses the Maximum Ratio Combining (MRC) to maximize the output SNR. In this research, the Matched Filter (MF) is utilized to correlate the received signal. The correlation shall be followed by a sampling circuit, which consists of Nyquist-rate sampling and a resampling process. To achieve fine time resolution, the correlation output shall be sampled at a high sampling frequency, which may be higher than the Nyquist rate. In practice, however, ADC sampling at such high sampling rate is hardly realizable and requires high power consumption. In this research, a sinc filter is utilized to resample the signal at a high frequency after the Nyquist sampling. The designed UWB receiver for ToA ranging is presented in Figure 3.31.

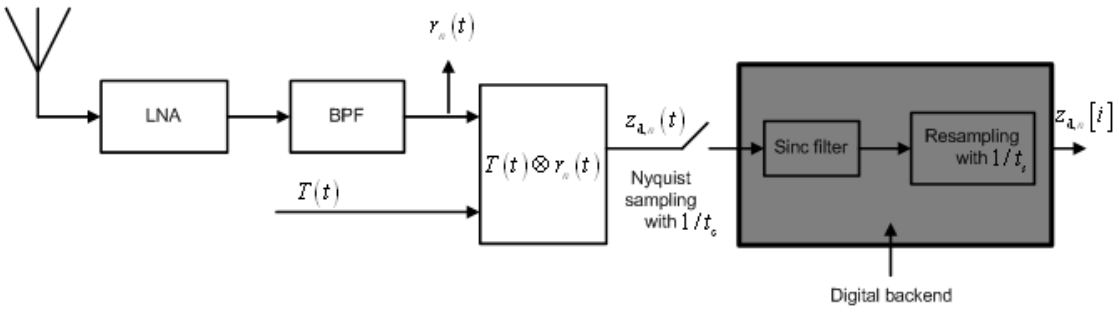

Figure 3.10: Infrastructure of coherent receiver and sampling circuit

In Figure 3.31, $T(t)$ is the template signal, which is used to correlate the received signal. $1/t_c$ and $1/t_s$ are the Nyquist sampling rate and the resampling rate, respectively. The input of the sinc filter is defined as $\boldsymbol{z}_{d,n}^{ns} = \left[z_{1,d,n}^{ns} \quad z_{2,d,n}^{ns} \quad \cdots \quad z_{K,d,n}^{ns} \right]$ and the sinc filter can be expressed as $\mathrm{si}(t) = \sin(\pi t / t_c) / (\pi t / t_c)$. If the resampling output is defined as $\boldsymbol{z}_{d,n}^{rs} = \left[z_{1,d,n}^{rs} \quad z_{2,d,n}^{rs} \quad \cdots \quad z_{I,d,n}^{rs} \right]$, $z_{m,d,n}^{rs}$ can be expressed as

$$z_{i,d,n}^{rs} = \sum_{k=1}^{K} z_{k,d,n}^{ns} \mathrm{si}\left((i-1)t_s - (k-1)t_c \right). \tag{3.83}$$

The resampling process can be performed in the digital backend, which can be realized in software module.

3.3.5 Error Analysis and Simulation Results of JLED

It can be concluded from 3.3.1 that the accuracy of JLED is mainly determined by two aspects: I) M_n correlation peaks determination. II) K' determination (see (3.29)). To determine K', it is necessary firstly to determine ΔA_q and ΔS_q, which can be calculated by (3.15) and (3.30).

$$\begin{aligned} \Delta A_q \approx & \sum_{n=1}^{3} \frac{\partial f_A(\boldsymbol{t}_r)}{\partial t_{n,q}} \Delta t_{n,q} \\ & + \frac{\partial^2 f_A(\boldsymbol{t}_r)}{\partial t_{1,q} \partial t_{2,q}} \Delta t_{1,q} \Delta t_{2,q} + \frac{\partial^2 f_A(\boldsymbol{t}_r)}{\partial t_{1,q} \partial t_{3,q}} \Delta t_{1,q} \Delta t_{3,q} + \frac{\partial^2 f_A(\boldsymbol{t}_r)}{\partial t_{2,q} \partial t_{3,q}} \Delta t_{2,q} \Delta t_{3,q} \\ & + \frac{\partial^2 f_A(\boldsymbol{t}_r)}{2\partial t_{1,q}^2} \Delta t_{1,q}^2 + \frac{\partial^2 f_A(\boldsymbol{t}_r)}{2\partial t_{2,q}^2} \Delta t_{2,q}^2 + \frac{\partial^2 f_A(\boldsymbol{t}_r)}{2\partial t_{3,q}^2} \Delta t_{3,q}^2 \end{aligned} \tag{3.84}$$

and

$$\begin{aligned} \Delta S_q \approx & \sum_{n=1}^{N} \frac{\partial f_S(\boldsymbol{t}_r)}{\partial t_{n,q}} \Delta t_{n,q} \\ & + \sum_{n=1}^{N} \frac{\partial^2 f_S(\boldsymbol{t}_r)}{2\partial t_{n,q}^2} \Delta t_{n,q}^2 + \sum_{m=1, n=1, m \neq n}^{N} \frac{\partial^2 f_S(\boldsymbol{t}_r)}{\partial t_{m,q} \partial t_{n,q}} \Delta t_{m,q} \Delta t_{n,q} \end{aligned} . \tag{3.85}$$

It is obvious that ΔA_q and ΔS_q are positive numbers. It defines false alarm probabilities $P_{fa,n}$ for n-th receiver, with which the probability that the time shift of the first correlation peak being within $\tau_{th,n}$ is $(1 - P_{fa,n})$. It can be expressed as

$$\mathrm{P}\left(\left| \Delta t_{n,q} \right| < \tau_{th,n} \right) = 1 - P_{fa,n}, \tag{3.86}$$

where $\tau_{th,n}$ is the threshold of time shift. Hence, the expression of $\Delta t_{n,q} = \tau_{n,q} - \hat{\tau}_{n,q}$ shall be determined. From (3.48), the likelihood function for the $i_{q,n}$ correlation peak can be rewritten as

$$\mathrm{P}\left(z_{g,n}\left(t\right)\Big|_{t_1=i_{q,n}t_s-T_\mathrm{p}}^{t_2=i_{q,n}t_s+T_\mathrm{p}} \Big| a_n,\tau_n \right)=\frac{1}{\sqrt{2\pi}N_\eta}\exp\left(-\frac{\int_{t_1}^{t_2}\left(z_{g,n}\left(t\right)-a_n s_n\left(t-\tau_n\right)\right)^2 \mathrm{dt}}{2N_\eta} \right). \tag{3.87}$$

For ML estimator, the objective function is defined as

$$\begin{aligned}\zeta\left(a_n,\tau_n\right)&=-\frac{1}{2N_\eta}\int_{t_1=i_{q,n}t_s-T_\mathrm{p}}^{t_2=i_{q,n}t_s+T_\mathrm{p}}\left(z_{g,n}\left(t\right)-a_n s_n\left(t-\tau_n\right)\right)^2 \mathrm{dt}\\ &=-\frac{1}{2N_\eta}\int_{t_1=i_{q,n}t_s-T_\mathrm{p}}^{t_1=i_{q,n}t_s+T_\mathrm{p}} z_{g,n}^2\left(t\right)\mathrm{dt}-\frac{a_n^2 E_\mathrm{p}}{2N_\eta}+\frac{a_n}{N_\eta}\int_{t_1=i_{q,n}t_s-T_\mathrm{p}}^{t_1=i_{q,n}t_s+T_\mathrm{p}} z_{g,n}\left(t\right)s_n\left(t-\tau_n\right)\mathrm{dt}\end{aligned}, \tag{3.88}$$

where E_p is the energy of the autocorrelation function $s\left(t\right)$. $z_{g,n}\left(t\right)$ in (3.88) contains $\left(a_{q,n},\tau_{q,n}\right)$, which are the true amplitude and time delay. If we can determine $\left.\frac{\partial\zeta\left(a_n,\tau_n\right)}{\partial\tau_n}\right|_{\tau_n=\tau_{n,q}}$ and expectation value of $\left.\frac{\partial^2\zeta\left(a_n,\tau_n\right)}{\partial\tau_n^2}\right|_{\tau_n=\tau_{n,q}}$, the time delay estimation error will converge to [15]

$$\hat{\tau}_n-\tau_{n,q}\cong-\frac{\left.\frac{\partial\zeta\left(a_n,\tau_n\right)}{\partial\tau_n}\right|_{\tau_n=\tau_{n,q}}}{E_n\left(\left.\frac{\partial^2\zeta\left(a_n,\tau_n\right)}{\partial\tau_n^2}\right|_{\tau_n=\tau_{n,q}}\right)}, \tag{3.89}$$

where "$E_n\left(\bullet\right)$" represents the expectation operation with respect to noise. From (3.89), the $\tau_{\mathrm{th},n}$ can be found via (3.86). The first derivative of (3.88) can be expressed as

$$\begin{aligned}\left.\frac{\partial\zeta\left(a_n,\tau_n\right)}{\partial\tau_n}\right|_{\tau_n=\tau_{n,q}}&=\left.\frac{a_n}{N_\eta}\frac{\partial\left(\int_{t_1=i_{q,n}t_s-T_\mathrm{p}}^{t_1=i_{q,n}t_s+T_\mathrm{p}} z_{g,n}\left(t\right)s_n\left(t-\tau_n\right)\mathrm{dt}\right)}{\partial\tau_n}\right|_{\tau_n=\tau_{n,q}}\\ &=\left.\frac{a_n}{N_\eta}\int_{t_1=i_{q,n}t_s-T_\mathrm{p}}^{t_2=i_{q,n}t_s+T_\mathrm{p}} z_{g,n}\left(t\right)\frac{\partial s_n\left(t-\tau_n\right)}{\partial\tau_n}\mathrm{dt}\right|_{\tau_n=\tau_{n,q}}\\ &=-\frac{a_n}{N_\eta}\int_{t_1=i_{q,n}t_s-T_\mathrm{p}}^{t_2=i_{q,n}t_s+T_\mathrm{p}} z_{g,n}\left(t^{'}+\tau_{n,q}\right)\frac{\mathrm{d}s_n\left(t^{'}\right)}{\mathrm{d}t^{'}}\mathrm{d}t^{'}\\ &=-\frac{a_n}{N_\eta}\int_{t_1=i_{q,n}t_s-T_\mathrm{p}}^{t_2=i_{q,n}t_s+T_\mathrm{p}}\left(a_{n,q}s_n\left(t^{'}+\tau_{n,q}-\tau_{n,q}\right)+\eta\left(t^{'}+\tau_{n,q}\right)\right)\mathrm{d}s_n\left(t^{'}\right)\\ &=-\frac{a_n a_{n,q}}{2N_\eta}s_n^2\left(t^{'}\right)\Big|_{t_1=i_{q,n}t_s-T_\mathrm{p}}^{t_2=i_{q,n}t_s+T_\mathrm{p}}-\frac{a_n}{N_\eta}\int_{t_1=i_{q,n}t_s-T_\mathrm{p}}^{t_2=i_{q,n}t_s+T_\mathrm{p}}\eta\left(t^{'}+\tau_{n,q}\right)s_n^{'}\left(t^{'}\right)\mathrm{d}t^{'}\end{aligned}. \tag{3.90}$$

It is obvious that the first term of (3.90) is zero. It defines $\rho_n^{'}(\tau)=\int_{t_1=i_{q,n}t_s-T_p}^{t_2=i_{q,n}t_s+T_p}\eta(t+\tau)s_n^{'}(t)\mathrm{d}t$. Hence,

$$\left.\frac{\partial\zeta(a_n,\tau_n)}{\partial\tau_n}\right|_{\tau_n=\tau_{n,q}}=-\frac{a_n}{N_\eta}\rho_n^{'}(\tau_{n,q}). \tag{3.91}$$

The second derivative can be determined from (3.90).

$$\begin{aligned}
&\left.\frac{\partial^2\zeta(a_n,\tau_n)}{\partial\tau_n^2}\right|_{\tau_n=\tau_{n,q}}=-\frac{a_n}{N_\eta}\int_{t_1}^{t_2}\frac{\partial z_{g,n}(t^{'}+\tau_n)}{\partial\tau_n}\mathrm{d}s_n(t^{'})\Bigg|_{\tau_n=\tau_{n,q}}\\
&=\frac{a_n a_{n,q}}{N_\eta}\int_{t_2}^{t_1}\frac{\partial s_n(t^{'}-\tau_{g,n}+\tau_n)}{\partial\tau_n}\mathrm{d}s_n(t^{'})+\frac{a_n}{N_\eta}\int_{t_2}^{t_1}\frac{\partial\eta(t^{'}+\tau_n)}{\partial\tau_n}\mathrm{d}s_n(t^{'})\Bigg|_{\tau_n=\tau_{n,q}}.\\
&=\frac{a_n a_{n,q}}{N_\eta}\int_{t_2}^{t_1}\left(\frac{\mathrm{d}s_n(t^{'})}{\mathrm{d}t^{'}}\right)^2\mathrm{d}t^{'}-\frac{a_n}{N_\eta}\rho_n^{''}(\tau_{n,q})\\
&=-\frac{4\pi^2 a_n a_{n,q}E_p\omega^2}{N_\eta}-\frac{a_n}{N_\eta}\rho_n^{''}(\tau_{n,q})
\end{aligned} \tag{3.92}$$

In (3.92), ω is the effective bandwidth of $s_n(t)$, which was defined in (3.25). $\rho_n^{''}(\tau)=\int_{t_1=i_{q,n}t_s-T_p}^{t_2=i_{q,n}t_s+T_p}\eta^{'}(t+\tau)s_n^{'}(t)\mathrm{d}t$. As $\eta(t)$ is a white Gaussian process, $\eta^{'}(t)$ is a color Gaussian process, whose expectation is the same as that of $\eta(t)$. Hence, $E_n\left(\rho_n^{''}(\tau_{n,q})\right)=0$. The expectation of (3.92) can be expressed as

$$\begin{aligned}
&E_n\left(\left.\frac{\partial^2\zeta(a_n,\tau_n)}{\partial\tau_n^2}\right|_{\tau_n=\tau_{n,q}}\right)=E_n\left(-\frac{4\pi^2 a_n a_{n,q}E_p\omega^2}{N_\eta}-\frac{a_n}{N_\eta}\rho_n^{''}(\tau_{n,q})\right).\\
&=-\frac{4\pi^2 a_n a_{n,q}E_p\omega^2}{N_\eta}
\end{aligned} \tag{3.93}$$

From (3.89), it can get

$$\begin{aligned}
\hat{\tau}_n-\tau_{n,q}&\cong\frac{\frac{a_n}{N_\eta}\rho_n^{'}(\tau_{n,q})}{\frac{4\pi^2 a_n a_{n,q}E_p\omega^2}{N_\eta}}.\\
&=\frac{\rho_n^{'}(\tau_{n,q})}{4\pi^2 a_{n,q}E_p\omega^2}
\end{aligned} \tag{3.94}$$

From (3.94), it can be concluded that the estimation error of time delay can be decreased with larger pulse energy and effective pulse bandwidth. (3.86) can be rewritten as

$$\mathrm{P}\left(\frac{\rho_n^{'}\left(\tau_{n,q}\right)}{4\pi^2 a_{n,q} E_{\mathrm{p}} \omega} < \tau_{\mathrm{th},n}\right) = 1 - P_{\mathrm{fa},n}\,. \tag{3.95}$$

To determine $\tau_{\mathrm{th},n}$, the PDF of $\rho_n^{'}\left(\tau_{n,q}\right)$ shall be known. The variance of $\rho_n^{'}\left(\tau_{n,q}\right)$ can be expressed as

$$\mathrm{var}\left(\rho_n^{'}\left(\tau_{n,q}\right)\right) = \mathrm{var}\left(\int_{t_1}^{t_2} \eta\left(t+\tau_{n,q}\right) s_n^{'}\left(t\right)\mathrm{d}t\right). \tag{3.96}$$

Since $\eta(t)$ is a white Gaussian process with free mean and N_η variance, (3.96) can be rewritten as

$$\begin{aligned}&\mathrm{var}\left(\int_{t_1}^{t_2} \eta\left(t+\tau_{n,q}\right) s_n^{'}\left(t\right)\mathrm{d}t\right) = \int_{t_1+\tau_{n,q}}^{t_2} s_n^{'2}\left(t\right)\mathrm{var}\left(\eta\left(t\right)\right)\mathrm{d}t \\ &= N_\eta \int_{t_1+\tau_{n,q}}^{t_2} s_n^{'2}\left(t\right)\mathrm{d}t\end{aligned}\,. \tag{3.97}$$

Hence, $\rho_n^{'}\left(\tau_{n,q}\right)$ can be considered as a variable conforming to Gaussian distribution $\left(\mu_\rho = 0, \sigma_\rho^2 = N_\eta \int_{t_1+\tau_{n,q}}^{t_2} s_n^{'2}\left(t\right)\mathrm{d}t\right)$. From (3.95), it can get

$$\begin{aligned}\tau_{\mathrm{th},n} &= \sigma_{\mathrm{p}} Q^{-1}\left(P_{\mathrm{fa}}\right) \\ &= N_\eta Q^{-1}\left(P_{\mathrm{fa}}\right) \int_{t_1+\tau_{n,q}}^{t_2} s_n^{'2}\left(t\right)\mathrm{d}t\end{aligned}\,, \tag{3.98}$$

where $Q(\bullet)$ is the Q-function. With $\tau_{\mathrm{th},n}, n = 1\cdots N$, ΔA_{th} and ΔS_{th} can be determined from (3.84) and (3.85). Then $K^{'}$ can be determined as

$$\begin{aligned}K_A^{'} &= \mathrm{count}\left\{\Delta A_q \le \Delta A_{\mathrm{th}}\right\} \\ K_S^{'} &= \mathrm{count}\left\{\Delta S_q \le \Delta S_{\mathrm{th}}\right\}\end{aligned}\,, \tag{3.99}$$

where "count" is to find the number of LECs, which fulfill the condition from (3.99).

The simulation parameters can be found in Table 3.3. Three UWB receivers are employed in this research for the two dimensional localization. The three UWB receivers are located at (0m, 0m), (0m, 10m) and (10m, 5m), respectively.

Table 3.3: Simulation parameters

Simulation Parameters	Description	Value
N	The number of UWB receivers	3
(x_n, y_n)	Coordinates	(0m, 0m) (0m, 10m) (10m, 5m)
T_p	Duration of Gaussian monocycle	2ns
L_p	Length of Delta function	64
$1/t_c$	Sampling frequency	2.65GHz
$1/t_s$	resampling frequency	20GHz
K'	The number of selected LECs	referenced from (3.99)
SNR	Signal to Noise Ratio	0dB

Within the localization area, 10 candidate positions are selected as $\mathbf{p} = (1\text{m} + k\Delta x, 1\text{m} + k\Delta y), k = 1 \cdots 10$, which are shown as the black nodes in Figure 3.11. To evaluate the performance of JLED, 100 measurement campaigns are performed at each candidate position (see Figure 3.11)

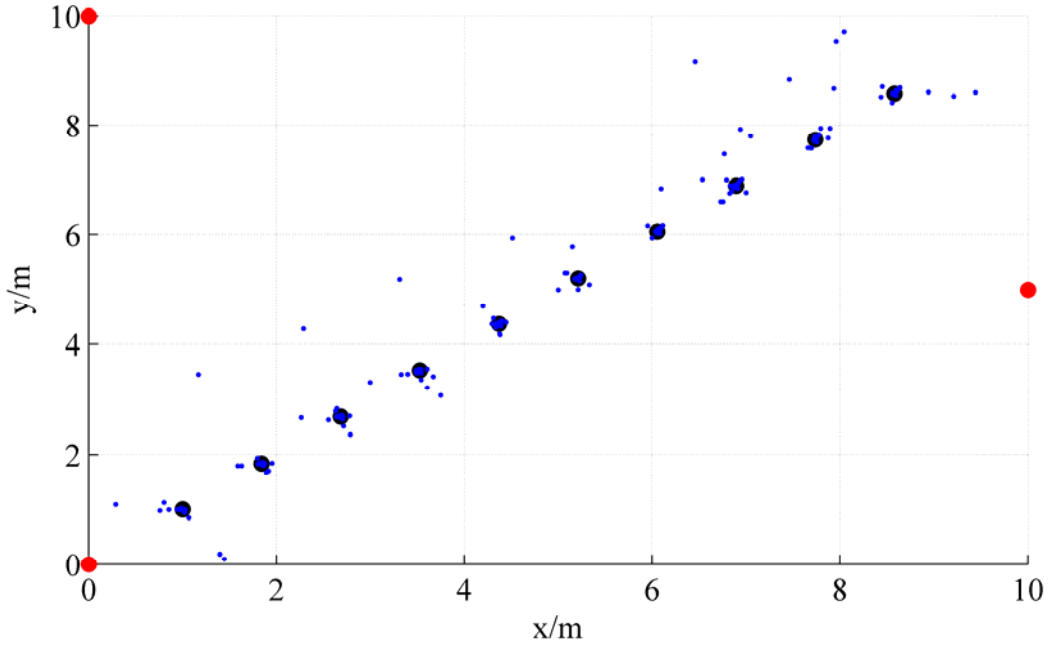

Figure 3.11: 100 measurements at 10 selected candidate positions

The three red points in Figure 3.11 represent the UWB receivers and the black points represent the 10 candidate positions. Each blue point is one measurement campaign which takes place at each candidate position.

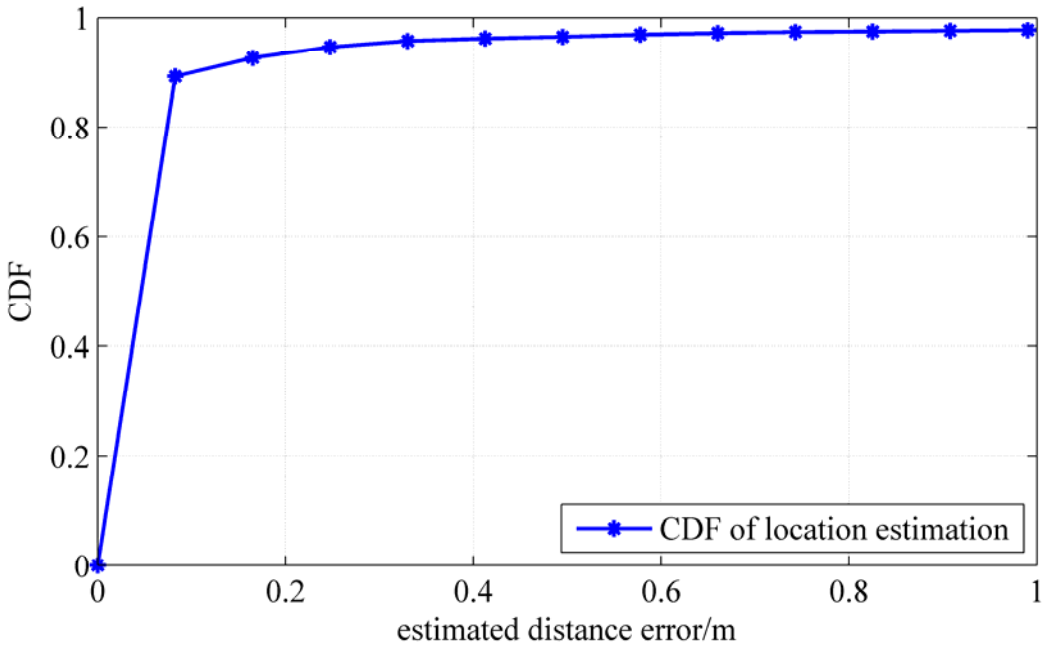

Figure 3.12: CDF of estimated distance error

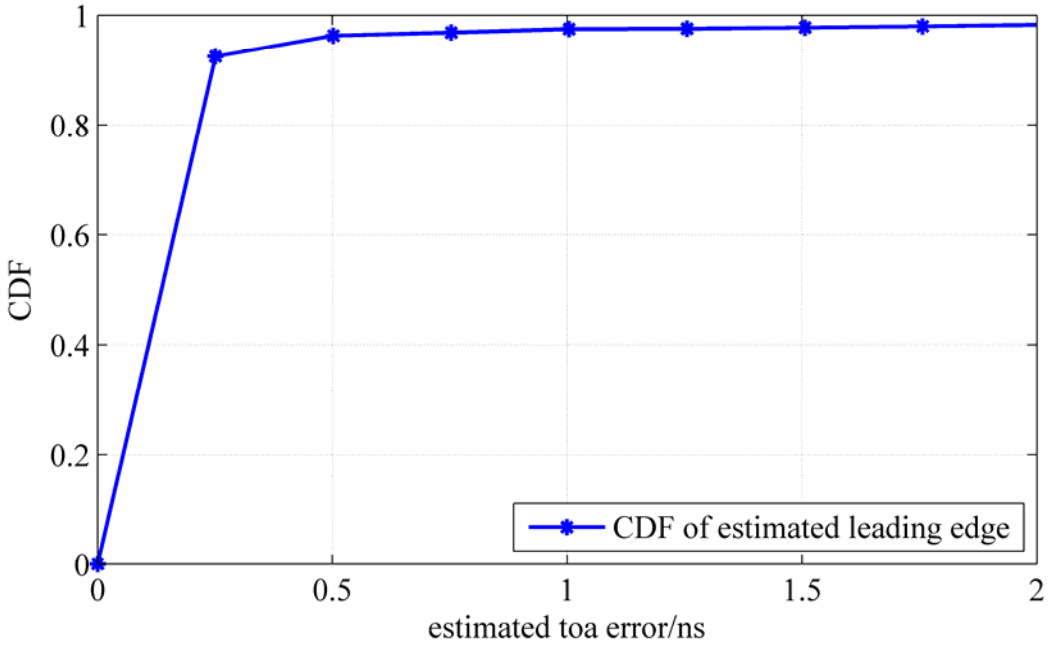

Figure 3.13: CDF of estimated ToA error

It can be seen from Figure 3.13 and Figure 3.13 that the estimated distance error is smaller than 40cm with approximate 96% and the estimated ToA error is smaller than 1ns with more than 97%. Figure 3.14 and Figure 3.15 show the RMSE (Root Mean Squared Error) and the standard deviation of the location measurements and the leading edge detection, respectively. The simulation results show that RMSE of the

location measurement and the leading edge detection with JLEDA can achieve 50.14cm and 0.99ns, respectively.

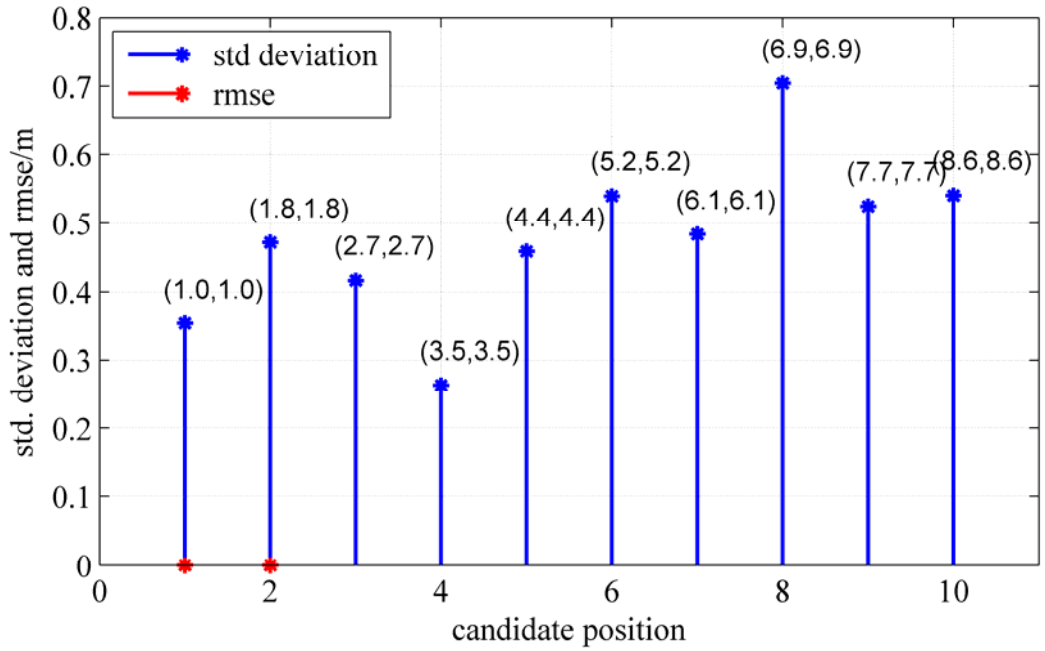

Figure 3.14: RMSE and standard deviation of the location estimation at each selected candidate position

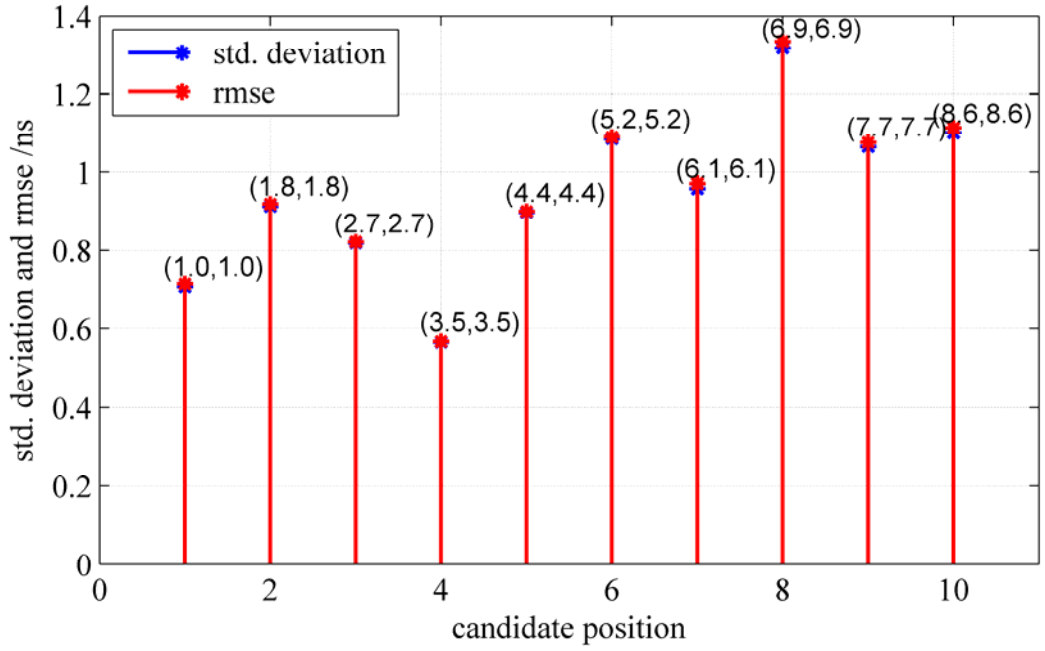

Figure 3.15: RMSE and standard deviation of estimated leading edge at each selected candidate position

3.3.6 Error Analysis and Simulation Results of Improved MLCE

From 3.3.2, it is clear that the estimation error of IMLCE mainly comes from I) search-back based coarse detection and II) fine estimation via MLCE. From (3.41), it can be seen that the accuracy of coarse detection is determined by η_{MER} , the length of search-back window and noise power. Before the search-back algorithm is started, the threshold $v_{\mathrm{th},n}=\dfrac{v_{\mathrm{p},n}}{\sqrt{\eta_{\mathrm{MER}}}}$ shall be selected appropriately. Recall that Figure 2.25 and Figure 2.26 give the CDF of the MELER and PLD for CM1, respectively. After the first derivative, the Probability Density Function (PDF) of MELER and PLD $\mathrm{P}_{\mathrm{mer}}(m)$ and $\mathrm{P}_{\mathrm{pld}}(t)$ can be determined. Hence, the estimation error probability of the coarse detection can be expressed as

$$P_{\mathrm{e,coa}}=1-\int_{0}^{T_{\mathrm{pld}}}\left(\left(1-2Q\left(\frac{v_{\mathrm{th},n}}{\sqrt{N_\eta}}\right)\right)^{\left\lfloor (T_{\mathrm{SB}}-t)/t_{\mathrm{s}}\right\rfloor}\mathrm{P}\left(\eta_{\mathrm{MER}}\le\left(\frac{v_{\mathrm{p},n}}{v_{\mathrm{th},n}}\right)^2\right)\right)\mathrm{P}_{\mathrm{pld}}(t)\,\mathrm{dt}\,. \tag{3.100}$$

In (3.100), $\mathrm{P}\left(\eta_{\mathrm{MER}}\le\left(\dfrac{v_{\mathrm{p},n}}{v_{\mathrm{th},n}}\right)^2\right)$ is the probability which can be determined from CDF of MELER. $\left\lfloor (T_{\mathrm{SB}}-t)/t_{\mathrm{s}}\right\rfloor$ is the number of the consecutive noise samples before the first correlation peak. Next, the estimation error in the fine estimation will be given. Recall that the number of channels L_n is unknown. Hence, (3.94) can only apply to $L_n=1$ case. Without loss of generality, (3.88) can be expanded to

$$\begin{aligned}
&\zeta\left(a_{1,n}\cdots a_{L_n,n},\tau_{1,n}\cdots\tau_{L_n,n},L_n\right)=-\frac{1}{2N_\eta}\int_{t_1=\hat{i}_{\mathrm{LD,COA}}t_{\mathrm{s}}-T_{\mathrm{p}}}^{t_2=\hat{i}_{\mathrm{LD,COA}}t_{\mathrm{s}}+T_{\mathrm{p}}}\left(z_{\mathrm{d},n}(t)-\sum_{l=1}^{L_n}a_{l,n}s_n\left(t-\tau_{l,n}\right)\right)^2\mathrm{dt}\\
&=-\frac{1}{2N_\eta}\int_{t_1=\hat{i}_{\mathrm{LD,COA}}t_{\mathrm{s}}-T_{\mathrm{p}}}^{t_2=\hat{i}_{\mathrm{LD,COA}}t_{\mathrm{s}}+T_{\mathrm{p}}}z_{\mathrm{d},n}^2(t)\,\mathrm{dt}-\frac{1}{2N_\eta}\int_{t_1=\hat{i}_{\mathrm{LD,COA}}t_{\mathrm{s}}-T_{\mathrm{p}}}^{t_2=\hat{i}_{\mathrm{LD,COA}}t_{\mathrm{s}}+T_{\mathrm{p}}}\left(\sum_{l=1}^{L_n}a_{l,n}s_n\left(t-\tau_{l,n}\right)\right)^2\mathrm{dt}+\\
&+\frac{1}{2N_\eta}\int_{t_1=\hat{i}_{\mathrm{LD,COA}}t_{\mathrm{s}}-T_{\mathrm{p}}}^{t_2=\hat{i}_{\mathrm{LD,COA}}t_{\mathrm{s}}+T_{\mathrm{p}}}z_{\mathrm{d},n}(t)\sum_{l=1}^{L_n}a_{l,n}s_n\left(t-\tau_{l,n}\right)\mathrm{dt}\\
&=-\frac{1}{2N_\eta}\int_{t_1=\hat{i}_{\mathrm{LD,COA}}t_{\mathrm{s}}-T_{\mathrm{p}}}^{t_2=\hat{i}_{\mathrm{LD,COA}}t_{\mathrm{s}}+T_{\mathrm{p}}}z_{\mathrm{d},n}^2(t)\,\mathrm{dt}-\frac{E_{\mathrm{p}}\sum_{l=1}^{L_n}a_{l,n}^2}{2N_\eta}-\\
&-\frac{1}{2N_\eta}\sum_{l=1,m=1;l\neq m}^{L_n}\int_{t_1=\hat{i}_{\mathrm{LD,COA}}t_{\mathrm{s}}-T_{\mathrm{p}}}^{t_2=\hat{i}_{\mathrm{LD,COA}}t_{\mathrm{s}}+T_{\mathrm{p}}}a_{l,n}a_{m,n}s_n\left(t-\tau_{l,n}\right)s_n\left(t-\tau_{m,n}\right)\mathrm{dt}+\\
&+\frac{1}{2N_\eta}\int_{t_1=\hat{i}_{\mathrm{LD,COA}}t_{\mathrm{s}}-T_{\mathrm{p}}}^{t_2=\hat{i}_{\mathrm{LD,COA}}t_{\mathrm{s}}+T_{\mathrm{p}}}z_{\mathrm{d},n}(t)\sum_{l=1}^{L_n}a_{l,n}s_n\left(t-\tau_{l,n}\right)\mathrm{dt}
\end{aligned}\tag{3.101}$$

The first derivative can be expressed as

$$\left.\frac{\partial\zeta\left(a_{1,n}\cdots a_{L_n,n},\tau_{1,n}\cdots\tau_{L_n,n},L_n\right)}{\partial\tau_{1,n}}\right|_{\tau_{l,n}=\tau_{l,q,n},a_{l,n}=a_{l,q,n}},$$

$$=-\frac{1}{2N_\eta}\sum_{m=2}^{L_n}a_{1,q,n}a_{m,q,n}R_{s,n}^{'}\left(\tau_{1,q,n}-\tau_{m,q,n}\right)+\frac{1}{2N_\eta}\sum_{m=2}^{L_n}a_{1,q,n}a_{m,q,n}\rho_{s,n}^{'}\left(\tau_{1,q,n}-\tau_{m,q,n}\right)-\frac{a_{1,q,n}}{N_\eta}\rho_n^{'}\left(\tau_{1,q,n}\right) \quad (3.102)$$

where $R_{s,n}^{'}(\tau)=\dfrac{\mathrm{d}\left(\int_{-T_\mathrm{p}}^{T_\mathrm{p}}s_n(t+\tau)s_n(t)\mathrm{d}t\right)}{\mathrm{d}\tau}$ and $\rho_{s,n}^{'}(\tau)=\int_{-T_\mathrm{p}}^{T_\mathrm{p}}s_n(t+\tau)\mathrm{d}s_n(t)$. The second derivative can be expressed as

$$\left.\frac{\partial^2\zeta\left(a_{1,n}\cdots a_{L_n,n},\tau_{1,n}\cdots\tau_{L_n,n},L_n\right)}{\partial\tau_{1,n}^2}\right|_{\tau_{l,n}=\tau_{l,q,n},a_{l,n}=a_{l,q,n}},$$

$$=-\frac{1}{2N_\eta}\sum_{m=2}^{L_n}a_{1,q,n}a_{m,q,n}R_{s,n}^{''}\left(\tau_{1,q,n}-\tau_{m,q,n}\right)+\frac{1}{2N_\eta}\sum_{m=2}^{L_n}a_{1,q,n}a_{m,q,n}\rho_{s,n}^{''}\left(\tau_{1,q,n}-\tau_{m,q,n}\right)-\frac{a_{1,q,n}}{N_\eta}\rho_n^{''}\left(\tau_{1,q,n}\right) \quad (3.103)$$

where $\rho_{s,n}^{''}(\tau)=\int_{-T_\mathrm{p}}^{T_\mathrm{p}}s_n^{'}(t+\tau)s_n^{'}(t)\mathrm{d}t$. Hence, the fine estimation error can converge to

$$\hat{\tau}_{1,n}-\tau_{1,q,n}\cong-\frac{\left.\dfrac{\partial\zeta\left(a_{1,n}\cdots a_{L_n,n},\tau_{1,n}\cdots\tau_{L_n,n},L_n\right)}{\partial\tau_{1,n}}\right|_{\tau_{l,n}=\tau_{l,q,n},a_{l,n}=a_{l,q,n}}}{E\left(\left.\dfrac{\partial^2\zeta\left(a_{1,n}\cdots a_{L_n,n},\tau_{1,n}\cdots\tau_{L_n,n},L_n\right)}{\partial\tau_{1,n}^2}\right|_{\tau_{l,n}=\tau_{l,q,n},a_{l,n}=a_{l,q,n}}\right)},$$

$$=\frac{\dfrac{1}{2N_\eta}\sum_{m=2}^{L_n}a_{1,q,n}a_{m,q,n}R_{s,n}^{'}\left(\tau_{1,q,n}-\tau_{m,q,n}\right)-\dfrac{1}{2N_\eta}\sum_{m=2}^{L_n}a_{1,q,n}a_{m,q,n}\rho_{s,n}^{'}\left(\tau_{1,q,n}-\tau_{m,q,n}\right)+\dfrac{a_{1,q,n}}{N_\eta}\rho_n^{'}\left(\tau_{1,q,n}\right)}{-\dfrac{1}{2N_\eta}\sum_{m=2}^{L_n}a_{1,q,n}a_{m,q,n}R_{s,n}^{''}\left(\tau_{1,q,n}-\tau_{m,q,n}\right)+\dfrac{1}{2N_\eta}\sum_{m=2}^{L_n}a_{1,q,n}a_{m,q,n}\rho_{s,n}^{''}\left(\tau_{1,q,n}-\tau_{m,q,n}\right)} \quad (3.104)$$

It is obvious that the estimation error is influenced by the number of channels, amplitude of each channel and relative time delay between the first channel and the other one.

The simulation parameters of IMLCE are the same as that of JLED. Figure 3.16 gives the illustration of 100 measurements at each selected candidate position. It can be seen from Figure 3.18 and Figure 3.18 that the estimated distance error is smaller than 40cm with approximate 98% and the estimated ToA error is smaller than 1ns with more than 96%. In comparison with JLEDA, IMLCE can provide better estimation performance (see Figure 3.19 and Figure 3.20). RMSE of the location measurements and the leading edge detection with IMLCE can achieve 26.21cm and 0.66ns, respectively.

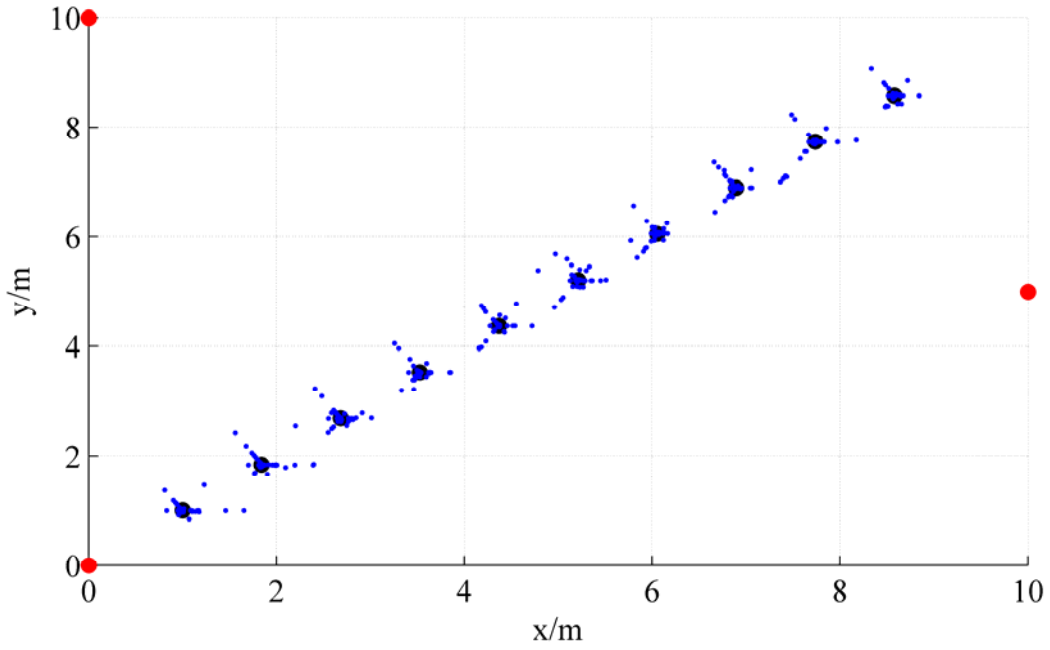

Figure 3.16: 100 measurements at 10 candidate positions (IMLCE)

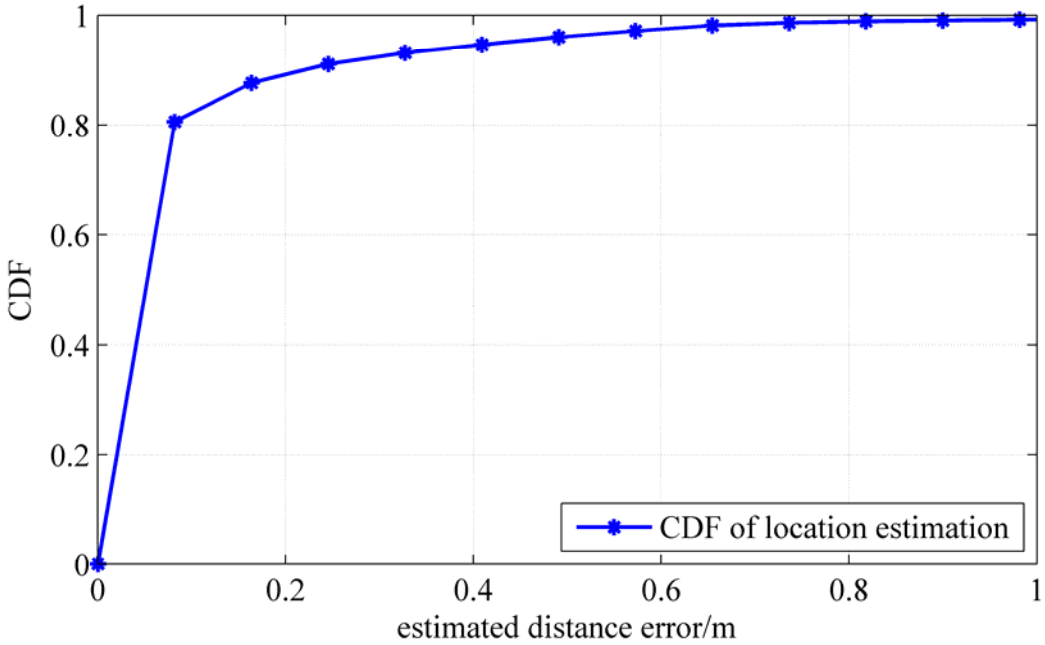

Figure 3.17: CDF of estimated distance error (IMLCE)

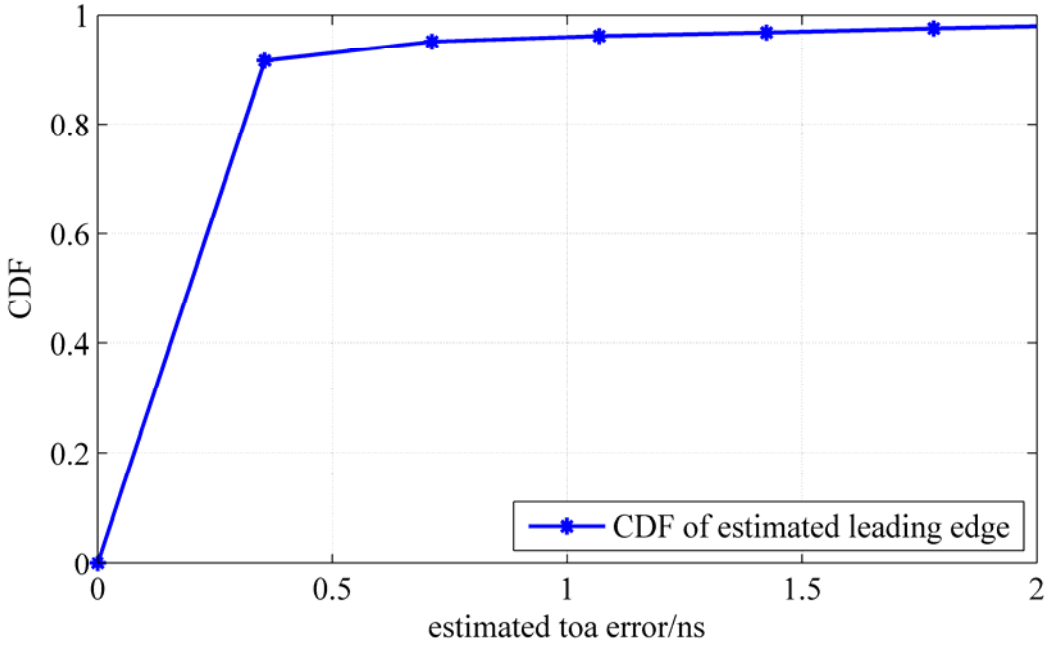

Figure 3.18: CDF of estimated ToA error (IMLCE)

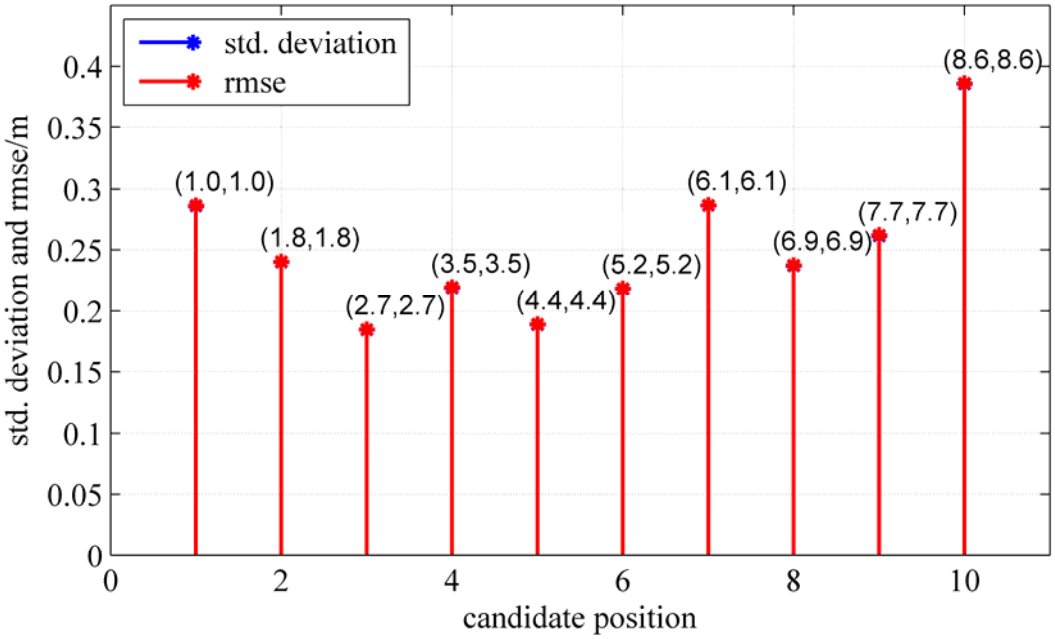

Figure 3.19: RMSE and standard deviation of the location measurements (IMLCE)

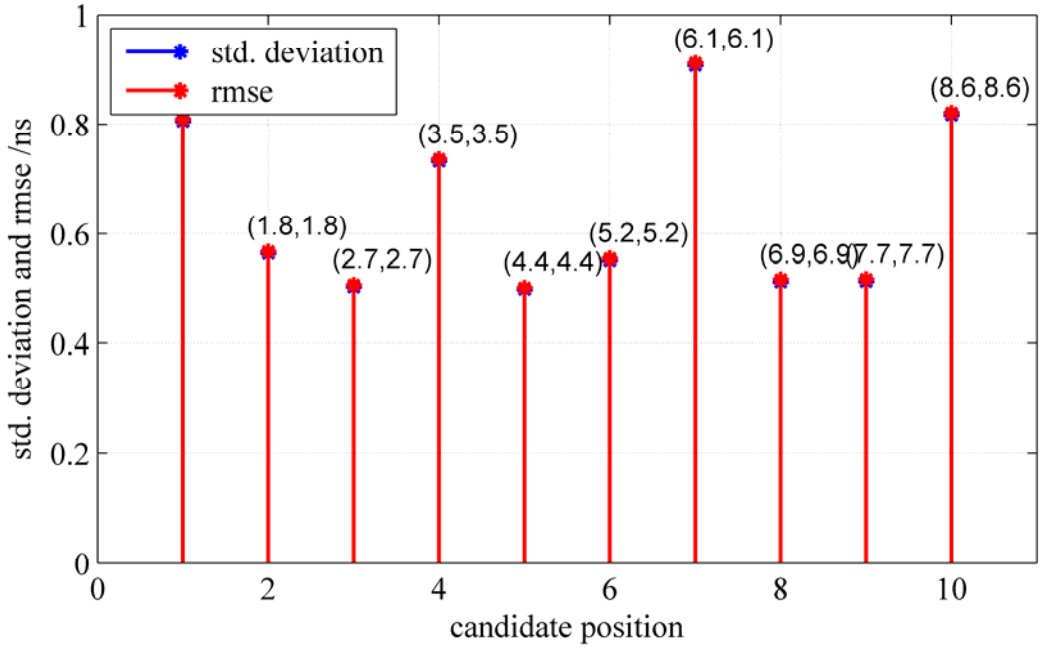

Figure 3.20: RMSE and standard deviation of leading edge detection (IMLCE)

3.3.7 Error Analysis and Simulation Results of Subspace based Approach

From 3.3.3, it is clear that the estimation error of the recursive SbA is mainly influenced by I) number of sources determination via (2.69) and II) perturbation of covariance matrix from (3.70). Before the expression of the estimation error probability is proposed, two assumptions shall be made: a) maximum correlation peak can be correctly determined by (3.40) and b) $c_{q,n} \in \{1,-1\}$. Firstly, let us analyze the number of sources determination via Gaussian Minimum Description Length (GMDL from (2.69)). Due to the additive Gaussian noise and limited number Q, the $\boldsymbol{R}_{lm}$ in (3.70) can be rewritten as

$$\begin{aligned} \boldsymbol{R}_{lm} &= \boldsymbol{R}_{lm,\mathrm{t}} + \Delta\boldsymbol{R}_{lm} \\ &= \boldsymbol{U}_{\mathrm{s},lm}\boldsymbol{\Lambda}_{\mathrm{s},lm}\boldsymbol{U}_{\mathrm{s},lm}^{\mathrm{H}} + \boldsymbol{U}_{n,lm}\boldsymbol{\Lambda}_{n,lm}\boldsymbol{U}_{n,lm}^{\mathrm{H}} + \Delta\boldsymbol{R}_{lm} \\ &= \boldsymbol{U}_{lm}^{'}\boldsymbol{\Lambda}_{lm}^{'}\boldsymbol{V}_{lm}^{'\mathrm{H}} \\ \boldsymbol{U}_{lm}^{'} &= \boldsymbol{U}_{\mathrm{s},lm} + \Delta\boldsymbol{U}_{\mathrm{s},lm} \end{aligned}, \tag{3.105}$$

where $\boldsymbol{U}_{\mathrm{s},lm}$ and $\boldsymbol{U}_{n,lm}$ span the signal and noise column subspace of the perfect covariance matrix $\boldsymbol{R}_{lm,\mathrm{t}}$, respectively. $\Delta\boldsymbol{R}_{lm}$ is the perturbation matrix. $\boldsymbol{\Lambda}_{\mathrm{s},lm}$ and $\boldsymbol{\Lambda}_{n,lm}$ are diagonal matrices. Due to $\Delta\boldsymbol{R}_{lm}$, the elements of $\boldsymbol{\Lambda}_{lm}^{'}$ may have complex number and $\boldsymbol{U}_{lm}^{'}$ and $\boldsymbol{V}_{lm}^{'\mathrm{H}}$ are not unitary matrices. The relation between $\Delta\boldsymbol{R}_{lm}$ and $\Delta\boldsymbol{U}_{\mathrm{s},lm}$ will be given later. From Figure 3.9, the error probability of the first correlation peak detection can be expressed as

$$P_{\mathrm{e,sba}} = 1 - \sum_{l=1}^{L_n-2}\sum_{j=1}^{\binom{l}{L_n-2}} \mathrm{P}_{j,l}\,, \tag{3.106}$$

$\mathrm{P}_{j,l}$ in (3.106) represents the detection probability for *j*-th combination, which contains $l+2$ correlation peaks. It is denoted as $\boldsymbol{p}_{j,l,n}=\left[\begin{array}{cccc} i_{\mathrm{L},n} & \underbrace{i_{j,1} \quad \cdots \quad i_{j,l+2}}_{l} & \hat{i}_{n,\mathrm{MP}} \end{array}\right]$. It defines $\boldsymbol{u}_{p_{m,m+1}}$ as the vector, which contains the correlation peaks between *m*-th and *m*+1-th peaks in $\boldsymbol{p}_{j,l,n}$. It is obvious that the number of elements in each $\boldsymbol{u}_{p_{m,m+1}}$ is different. It is defined as $K_{p_{m,m+1}}$. Hence, $\mathrm{P}_{j,l}$ can be expressed as

$$\begin{array}{l} \mathrm{P}_{j,l}=\prod_{m=1}^{l+2}\mathrm{P}\left(\mathrm{GMDL}_{p_{m,m+1}}(2)>\mathrm{GMDL}_{p_{m,m+1}}(1)\right) \\ \prod_{k=1}^{K_{p_{m,m+1}}}\mathrm{P}\left(\mathrm{GMDL}_{u_{k,p_{m+1}}}(2)<\mathrm{GMDL}_{u_{k,p_{m+1}}}(1)\right) \end{array} . \tag{3.107}$$

In (3.107), $\mathrm{P}\left(\mathrm{GMDL}(2)>\mathrm{GMDL}(1)\right)$ and $\mathrm{P}\left(\mathrm{GMDL}(2)<\mathrm{GMDL}(1)\right)$ represent the probabilities that there are two and one detected correlation peaks, respectively. The next step, the two probabilities from (3.105) will be determined. For the subsets of correlated signal $z'_{lm,q,n,\mathrm{PAM}}, q=1\cdots Q$, the likelihood function can be expressed as

$$\begin{aligned} &\mathrm{P}\left(z'_{lm,1,n}\cdots z'_{lm,Q,n}\middle|\theta\right)=\mathrm{P}\left(\mathrm{GMDL}(\theta)\right) \\ &=\frac{1}{(2\pi)^{\frac{Q\left(\hat{i}_{m,n,\mathrm{PAM}}-\hat{i}_{l,n,\mathrm{PAM}}+\left\lfloor\frac{2T_\mathrm{p}}{t_\mathrm{s}}\right\rfloor\right)}{2}}\det{}^{-Q}\left(\boldsymbol{R}_\eta\right)}\exp\left(-\sum_{q=1}^{Q}\frac{1}{2}\left(\left(z'_{lm,q,n}-\sum_{l'=1}^{\theta}a'_{l',q}s'_{l',\mathrm{p}}\right)^{\mathrm{H}}\boldsymbol{R}_\eta^{-1}\left(z'_{lm,q,n}-\sum_{l'=1}^{\theta}a'_{l',q}s'_{l',\mathrm{p}}\right)\right)\right), \end{aligned} \tag{3.108}$$

where $s'_{l',\mathrm{p}}$ was defined in (3.70) and $a'_{l',q}$ shall be derived from $\boldsymbol{R}_{lm}$. θ is the number of correlated signals. Hence, it has

$$\begin{aligned} &\mathrm{P}\left(\mathrm{GMDL}(\theta_1)>\mathrm{GMDL}(\theta_2)\right) \\ &=\mathrm{P}\left(\begin{array}{l} \sum_{q=1}^{Q}\frac{1}{2}\left(\left(z'_{lm,q,n}-\sum_{l'=1}^{\theta_1}a'_{l',q}s'_{l',\mathrm{p}}\right)^{\mathrm{H}}\boldsymbol{R}_\eta^{-1}\left(z'_{lm,q,n}-\sum_{l'=1}^{\theta_1}a'_{l',q}s'_{l',\mathrm{p}}\right)\right)< \\ <\sum_{q=1}^{Q}\frac{1}{2}\left(\left(z'_{lm,q,n}-\sum_{l'=1}^{\theta_2}a'_{l',q}s'_{l',\mathrm{p}}\right)^{\mathrm{H}}\boldsymbol{R}_\eta^{-1}\left(z'_{lm,q,n}-\sum_{l'=1}^{\theta_2}a'_{l',q}s'_{l',\mathrm{p}}\right)\right) \end{array}\right) \end{aligned} . \tag{3.109}$$

The objective function can be rewritten as

$$
\begin{aligned}
\zeta(\theta_1) &= \sum_{q=1}^{Q}\frac{1}{2}\left(\left(\boldsymbol{z}'_{lm,q,n}-\sum_{l'=1}^{\theta_1}a'_{l',q}\boldsymbol{s}'_{l',\mathrm{p}}\right)^{\mathrm{H}}\boldsymbol{R}_{\eta,\theta_1}^{-1}\left(\boldsymbol{z}'_{lm,q,n}-\sum_{l'=1}^{\theta_1}a'_{l',q}\boldsymbol{s}'_{l',\mathrm{p}}\right)\right)\\
&=\frac{1}{2}\sum_{q=1}^{Q}\mathrm{tr}\left(\left(\boldsymbol{z}'_{lm,q,n}-\sum_{l'=1}^{\theta_1}a'_{l',q}\boldsymbol{s}'_{l',\mathrm{p}}\right)^{\mathrm{H}}\boldsymbol{R}_{\eta,\theta_1}^{-1}\left(\boldsymbol{z}'_{lm,q,n}-\sum_{l'=1}^{\theta_1}a'_{l',q}\boldsymbol{s}'_{l',\mathrm{p}}\right)\right)\\
&=\frac{1}{2}\sum_{q=1}^{Q}\mathrm{tr}\left(\left(\boldsymbol{z}'_{lm,q,n}-\sum_{l'=1}^{\theta_1}a'_{l',q}\boldsymbol{s}'_{l',\mathrm{p}}\right)\left(\boldsymbol{z}'_{lm,q,n}-\sum_{l'=1}^{\theta_1}a'_{l',q}\boldsymbol{s}'_{l',\mathrm{p}}\right)^{\mathrm{H}}\boldsymbol{R}_{\eta,\theta_1}^{-1}\right)\\
&=\frac{1}{2}\mathrm{tr}\left(\sum_{q=1}^{Q}\left(\boldsymbol{z}'_{lm,q,n}\boldsymbol{z}'^{\mathrm{H}}_{lm,1,n}-\boldsymbol{z}'_{lm,q,n}\sum_{l'=1}^{\theta_1}a'^{*}_{l',q}\boldsymbol{s}'^{\mathrm{H}}_{l',\mathrm{p}}-\sum_{l'=1}^{\theta_1}a'_{l',q}\boldsymbol{s}'_{l',\mathrm{p}}\boldsymbol{z}'^{\mathrm{H}}_{lm,q,n}+\sum_{l'=1}^{\theta_1}a'_{l',q}\boldsymbol{s}'_{l',\mathrm{p}}\sum_{l'=1}^{\theta_1}a'^{*}_{l',q}\boldsymbol{s}'^{\mathrm{H}}_{l',\mathrm{p}}\right)\boldsymbol{R}_{\eta,\theta_1}^{-1}\right)
\end{aligned}
\qquad ,(3.110)
$$

where "tr" is used to determine the trace of the matrix. $\boldsymbol{R}_{\eta,\theta_1}$ is the noise covariance matrix which changes with θ_1. Clearly, $\sum_{q=1}^{Q}\boldsymbol{z}'_{lm,q,n}\boldsymbol{z}'^{\mathrm{H}}_{lm,q,n}$ can be replaced by $Q\boldsymbol{R}_{lm}$ and $\sum_{q=1}^{Q}\left(\sum_{l'=1}^{\theta_1}a'_{l',q}\boldsymbol{s}'_{l',\mathrm{p}}\sum_{l'=1}^{\theta_1}a'^{*}_{l',q}\boldsymbol{s}'^{\mathrm{H}}_{l',\mathrm{p}}\right)$ can be replaced by $Q\boldsymbol{U}'_{\theta_1,lm}\left(\boldsymbol{\Lambda}'_{\theta_1,lm}-\sigma_\eta^2\boldsymbol{I}_{\theta_1}\right)\boldsymbol{V}'^{\mathrm{H}}_{\theta_1,lm}$, where $\boldsymbol{U}'_{lm}=\left[\boldsymbol{U}'_{\theta_1,lm}\quad \boldsymbol{U}'_{\hat{i}_{m,n,\mathrm{PAM}}-\hat{i}_{l,n,\mathrm{PAM}}+\left\lfloor\frac{2T_\mathrm{p}}{t_\mathrm{s}}\right\rfloor-\theta_1,lm}\right]$ and $\boldsymbol{V}'_{lm}=\left[\boldsymbol{V}'_{\theta_1,lm}\quad \boldsymbol{V}'_{\hat{i}_{m,n,\mathrm{PAM}}-\hat{i}_{l,n,\mathrm{PAM}}+\left\lfloor\frac{2T_\mathrm{p}}{t_\mathrm{s}}\right\rfloor-\theta_1,lm}\right]$,

$\hat{\sigma}_\eta^2=\dfrac{1}{\hat{i}_{m,n,\mathrm{PAM}}-\hat{i}_{l,n,\mathrm{PAM}}+\left\lfloor\frac{2T_\mathrm{p}}{t_\mathrm{s}}\right\rfloor-\theta_1}\mathrm{tr}\left(\boldsymbol{\Lambda}'_{\hat{i}_{m,n,\mathrm{PAM}}-\hat{i}_{l,n,\mathrm{PAM}}+\left\lfloor\frac{2T_\mathrm{p}}{t_\mathrm{s}}\right\rfloor-\theta_1,lm}\right)$, $\boldsymbol{R}_{\eta,\theta_1}=\hat{\sigma}_\eta^2\boldsymbol{I}_{\hat{i}_{m,n,\mathrm{PAM}}-\hat{i}_{l,n,\mathrm{PAM}}+\left\lfloor\frac{2T_\mathrm{p}}{t_\mathrm{s}}\right\rfloor}$.

Then

$$
\begin{aligned}
&\sum_{q=1}^{Q}\boldsymbol{z}'_{lm,q,n}\sum_{l'=1}^{\theta_1}a'^{*}_{l',q}\boldsymbol{s}'^{\mathrm{H}}_{l',\mathrm{p}}\\
&=\sum_{q=1}^{Q}\left(\left(\sum_{l''=1}^{L_{n,\mathrm{s}}}a''_{l'',q}\boldsymbol{s}''_{l'',\mathrm{p}}+\boldsymbol{\eta}_q\right)\sum_{l'=1}^{\theta_1}a'^{*}_{l',q}\boldsymbol{s}'^{\mathrm{H}}_{l',\mathrm{p}}\right)\\
&=\sum_{q=1}^{Q}\left(\left(\sum_{l''=1}^{L_{n,\mathrm{s}}}a''_{l'',q}\boldsymbol{s}''_{l'',\mathrm{p}}\sum_{l'=1}^{\theta_1}a'^{*}_{l',q}\boldsymbol{s}'^{\mathrm{H}}_{l',\mathrm{p}}\right)+\boldsymbol{\eta}_q\sum_{l'=1}^{\theta_1}a'^{*}_{l',q}\boldsymbol{s}'^{\mathrm{H}}_{l',\mathrm{p}}\right)
\end{aligned}
\qquad , \qquad (3.111)
$$

where $a''_{l'',q}$ is the true amplitude of $\boldsymbol{z}'_{lm,q,n}$ and $L_{n,\mathrm{s}}$ is the number of multipath for $\boldsymbol{z}'_{lm,q,n}$. $\boldsymbol{s}''_{l'',\mathrm{p}}$ is the digitalized $s'_\mathrm{p}\left(t-\tau''_{l''}\right)$. $a'_{l',q}$ shall be determined by the given θ_1. From aforementioned two assumptions and (3.105), $a'_{l',q}$ can be expressed as

$$
\boldsymbol{a}'_q=\begin{bmatrix}a'_{1,q}\\a'_{2,q}\\\vdots\\a'_{\theta_1,q}\end{bmatrix}=\pm\mathrm{sqrt}\left(\mathrm{diag}\left(\boldsymbol{X}_{\theta_1,lm}\boldsymbol{\Lambda}_{\theta_1,lm}\boldsymbol{Y}_{\theta_1,lm}\right)\right), \qquad (3.112)
$$

where

$$\begin{aligned}
&\boldsymbol{X}_{\theta_1,lm}=\left(\boldsymbol{U}_{\theta_1,lm}^{\mathrm{H}}\boldsymbol{U}_{\theta_1,lm}\right)^{-1}\boldsymbol{U}_{\theta_1,lm}^{\mathrm{H}}\boldsymbol{S}_{\mathrm{p}}^{'}\\
&\boldsymbol{Y}_{\theta_1,lm}=\boldsymbol{S}_{\mathrm{p}}^{'\mathrm{H}}\boldsymbol{V}_{\theta_1,lm}\left(\boldsymbol{V}_{\theta_1,lm}^{\mathrm{H}}\boldsymbol{V}_{\theta_1,lm}\right)\\
&\boldsymbol{S}_{\mathrm{p}}^{'}=\left[\begin{array}{cccc}\boldsymbol{s}_{1,p}^{'} & \boldsymbol{s}_{2,p}^{'} & \cdots & \boldsymbol{s}_{\theta_1,p}^{'}\end{array}\right]
\end{aligned}\quad . \tag{3.113}$$

The "±" in (3.112) denotes that each correlation peak may have reverse polarity due to $c_{q,n}$. Hence, (3.110) can be rewritten as

$$\begin{aligned}
\zeta\left(\theta_1\right)&=\frac{\widehat{\sigma}_{\eta}^{-2}}{2}\mathrm{tr}\left(\begin{array}{l}
Q\boldsymbol{R}_{lm}+Q\boldsymbol{U}_{\theta_1,lm}^{'}\left(\boldsymbol{\Lambda}_{\theta_1,lm}^{'}-\widehat{\sigma}_{\eta}^{2}\boldsymbol{I}_{\theta_1}\right)\boldsymbol{V}_{\theta_1,lm}^{'\mathrm{H}}-\\
-\sum_{q=1}^{Q}\left(\left(\sum_{l^{''}=1}^{L_{s,n}}a_{l^{''},q}^{''}\boldsymbol{s}_{l^{''},\mathrm{p}}^{''}\sum_{l^{'}=1}^{\theta_1}a_{l^{'},q}^{'}\boldsymbol{s}_{l^{'},\mathrm{p}}^{'\mathrm{H}}\right)+\boldsymbol{\eta}_q\sum_{l^{'}=1}^{\theta_1}a_{l^{'},q}^{'}\boldsymbol{s}_{l^{'},p}^{'\mathrm{H}}\right)-\\
-\sum_{q=1}^{Q}\left(\left(\sum_{l^{'}=1}^{\theta_1}a_{l^{'},q}^{'}\boldsymbol{s}_{l^{'},p}^{'}\sum_{l^{''}=1}^{L_{s,n}}a_{l^{''},q}^{''}\boldsymbol{s}_{l^{''},\mathrm{p}}^{''\mathrm{H}}\right)+\sum_{l^{'}=1}^{\theta_1}a_{l^{'},q}^{'}\boldsymbol{s}_{l^{'},p}^{'}\boldsymbol{\eta}_q^{\mathrm{H}}\right)
\end{array}\right)\\
&=\frac{\widehat{\sigma}_{\eta}^{-2}}{2}\left(Q\left(\mathrm{tr}\left(\boldsymbol{\Lambda}_{lm}^{'}\right)+\mathrm{tr}\left(\boldsymbol{\Lambda}_{\theta_1,lm}^{'}\right)-\theta_1\widehat{\sigma}_{\eta}^{2}\right)-2Q\sum_{l^{''}=1}^{L_{s,n}}\sum_{l^{'}=1}^{\theta_1}a_{l^{''},q}^{''}a_{l^{'},q}^{'}\mathrm{tr}\left(\boldsymbol{R}_{s,l^{''}l^{'}}\right)+\eta^{'}\right)
\end{aligned}\quad , \tag{3.114}$$

where $\eta^{'}$ is Gaussian noise with

$$E\left(\eta^{'}\right)=0,\mathrm{var}\left(\eta^{'}\right)=Q\left\|\boldsymbol{s}_{\mathrm{p}}^{'}\right\|^2\sigma_{\eta,n}^{2}\sum_{l^{'}=1}^{\theta_1}a_{l^{'},q}^{'2}\ . \tag{3.115}$$

In (3.115), $\sigma_{\eta,n}^{2}$ is the true variance of $\eta(t)$ in (3.58). Hence, (3.109) can be rewritten as

$$\begin{aligned}
&\mathrm{P}\left(\mathrm{GMDL}\left(\theta_1\right)>\mathrm{GMDL}\left(\theta_2\right)\right)\\
&=\mathrm{P}\left(\begin{array}{l}
\frac{\widehat{\sigma}_{\eta}^{-2}}{2}Q\left(\mathrm{tr}\left(\boldsymbol{\Lambda}_{lm}^{'}\right)+\mathrm{tr}\left(\boldsymbol{\Lambda}_{\theta_1,lm}^{'}\right)-\theta_1\widehat{\sigma}_{\eta}^{2}-2\sum_{l^{''}=1}^{L_{s,n}}\sum_{l^{'}=1}^{\theta_1}a_{l^{''},q}^{''}a_{l^{'},q}^{'}\mathrm{tr}\left(\boldsymbol{R}_{s,l^{''}l^{'}}\right)\right)+\frac{\widehat{\sigma}_{\eta}^{-2}}{2}\eta^{'}\\
<\frac{\widehat{\sigma}_{\eta}^{-2}}{2}Q\left(\mathrm{tr}\left(\boldsymbol{\Lambda}_{lm}^{'}\right)+\mathrm{tr}\left(\boldsymbol{\Lambda}_{\theta_2,lm}^{'}\right)-\theta_2\widehat{\sigma}_{\eta}^{2}-2\sum_{l^{''}=1}^{L_{s,n}}\sum_{l^{'}=1}^{\theta_2}a_{l^{''},q}^{''}a_{l^{'},q}^{'}\mathrm{tr}\left(\boldsymbol{R}_{s,l^{''}l^{'}}\right)\right)+\frac{\widehat{\sigma}_{\eta}^{-2}}{2}\eta^{'}
\end{array}\right)
\end{aligned}. \tag{3.116}$$

From (3.115), it can be known that the variance of $\eta^{'}$ is dependent on the number of assumed correlation peaks. It sets

$$\begin{aligned}
\mu_1&=\frac{\widehat{\sigma}_{\eta}^{-2}}{2}Q\left(\mathrm{tr}\left(\boldsymbol{\Lambda}_{lm}^{'}\right)+\mathrm{tr}\left(\boldsymbol{\Lambda}_{\theta_1,lm}^{'}\right)-\theta_1\widehat{\sigma}_{\eta}^{2}-2\sum_{l^{''}=1}^{L_{s,n}}\sum_{l^{'}=1}^{\theta_1}a_{l^{''},q}^{''}a_{l^{'},q}^{'}\mathrm{tr}\left(\boldsymbol{R}_{s,l^{''}l^{'}}\right)\right)\\
\mu_2&=\frac{\widehat{\sigma}_{\eta}^{-2}}{2}Q\left(\mathrm{tr}\left(\boldsymbol{\Lambda}_{lm}^{'}\right)+\mathrm{tr}\left(\boldsymbol{\Lambda}_{\theta_2,lm}^{'}\right)-\theta_2\widehat{\sigma}_{\eta}^{2}-2\sum_{l^{''}=1}^{L_{s,n}}\sum_{l^{'}=1}^{\theta_2}a_{l^{''},q}^{''}a_{l^{'},q}^{'}\mathrm{tr}\left(\boldsymbol{R}_{s,l^{''}l^{'}}\right)\right)\\
\sigma_{1,\eta}^{'2}&=\frac{\widehat{\sigma}_{n}^{-4}}{4}Q\left\|\boldsymbol{s}_{\mathrm{p}}^{'}\right\|^2\sigma_{\eta,n}^{2}\sum_{l^{'}=1}^{\theta_1}a_{l^{'},q}^{'2}\\
\sigma_{2,\eta}^{'2}&=\frac{\widehat{\sigma}_{n}^{-4}}{4}Q\left\|\boldsymbol{s}_{\mathrm{p}}^{'}\right\|^2\sigma_{\eta,n}^{2}\sum_{l^{'}=1}^{\theta_2}a_{l^{'},q}^{'2}
\end{aligned}. \tag{3.117}$$

Then $\mu^{'}$ can be found that let

$$\frac{1}{\sqrt{2\pi}\sigma_{1,\eta}^{'}}\exp\left(-\frac{\left(\mu^{'}-\mu_1\right)^2}{2\sigma_{1,\eta}^{'}}\right)=\frac{1}{\sqrt{2\pi}\sigma_{2,\eta}^{'}}\exp\left(-\frac{\left(\mu^{'}-\mu_2\right)^2}{2\sigma_{2,\eta}^{'}}\right). \quad (3.118)$$

Then $\mathrm{P}\left(\mathrm{GMDL}\left(\theta_1\right)>\mathrm{GMDL}\left(\theta_2\right)\right)$ can be written as

$$\mathrm{P}\left(\mathrm{GMDL}\left(\theta_1\right)>\mathrm{GMDL}\left(\theta_2\right)\right)=\begin{cases}\frac{1}{2}\left(1-\mathrm{Q}\left(\left|\frac{\mu^{'}-\mu_1}{\sigma_{1,\eta}^{'}}\right|\right)+\mathrm{Q}\left(\left|\frac{\mu^{'}-\mu_2}{\sigma_{2,\eta}^{'}}\right|\right)\right), \mu_1<\mu_2 \\ \frac{1}{2}\left(1-\mathrm{Q}\left(\left|\frac{\mu^{'}-\mu_2}{\sigma_{2,\eta}^{'}}\right|\right)+\mathrm{Q}\left(\left|\frac{\mu^{'}-\mu_1}{\sigma_{1,\eta}^{'}}\right|\right)\right), \mu_1>\mu_2\end{cases}. \quad (3.119)$$

From (3.106) and (3.107), $P_{\mathrm{e,sba}}$ can be determined. The simulation parameters of SbA can be found in Table 3.4. Figure 3.21 depicts the simulation results of SbA based leading edge detection. In the low SNR environment, SbA based leading edge detection in static channel scenario gives much better performance than that in fading channel scenario. The gap will become smaller with the higher SNR. With SNR = 0dB, the RMSE of SbA based leading edge detection in static channel and the fading channel can achieve 1 and 2.4ns, respectively.

Table 3.4: Simulation parameters of SbA

Simulation Parameters	**Description**	**Value**
N	The number of UWB receivers	1
T_{p}	Duration of Gaussian pulse	2ns
L_{p}	Length of Delta function	64
$1/t_{\mathrm{c}}$	Sampling frequency	2.65GHz
$1/t_{\mathrm{s}}$	Resampling frequency	20GHz
SNR	Signal to Noise Ratio	-20 to 20 dB
N_{loop}	The number of Monte-Carlo simulation	500

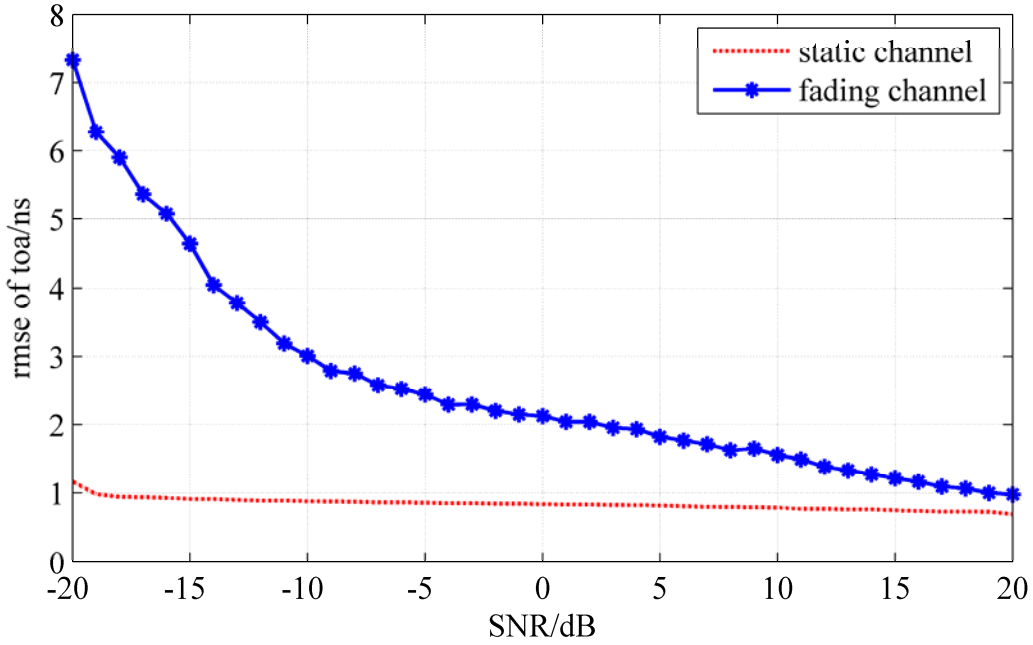

Figure 3.21: RMSE of SbA based leading edge detection

3.4 Novel Power based Location Estimator

In this section, the novel power based location estimators: RSSI based fingerprint approach and Channel Energy Estimation (CEE) based distance estimator will be proposed. The former uses sub-sampling least squares to reduce the computational complexity and increase the localization accuracy. The latter extracts channel energy from the received signal and compare the channel energy among each receiver. The simulation and measurement results of two approaches will be given in section 3.4.2 and 3.4.4.

3.4.1 Sub-Sampling Least Squares (SSLS) based Fingerprint Approach

Let's begin with Least Squares (LS) based fingerprint method. It assumes that there is a rectangular localization region A with length L and width H (see Figure 2.1). Firstly, the candidate positions $\boldsymbol{loc} = [\mathrm{loc}_1 \quad \mathrm{loc}_2 \quad \cdots \quad \mathrm{loc}_M]$ shall be selected through regularly sampling with spatial interval ΔL (see Figure 3.22). At each candidate position, the reference RSSI value shall be pre measured and recorded for each receiver. It can be formulated into a matrix form:

$$\boldsymbol{RSSI}_{\text{ref}} = \left[\boldsymbol{rssi}_{\text{loc}_1} \quad \boldsymbol{rssi}_{\text{loc}_2} \quad \cdots \quad \boldsymbol{rssi}_{\text{loc}_M} \right] = \begin{bmatrix} rssi_{1,\text{loc}_1} & rssi_{1,\text{loc}_2} & \cdots & rssi_{1,\text{loc}_M} \\ rssi_{2,\text{loc}_1} & rssi_{2,\text{loc}_2} & \cdots & rssi_{2,\text{loc}_M} \\ \vdots & \vdots & \ddots & \vdots \\ rssi_{N,\text{loc}_1} & rssi_{N,\text{loc}_2} & \cdots & rssi_{N,\text{loc}_M} \end{bmatrix}, \tag{3.120}$$

where $rssi_{n,\text{loc}_m}$ represents the RSSI value at m-th candidate location for n-th receiver. It assumes that the measured RSSI vector is $\boldsymbol{rssi}_{\text{mes}} = \left[rssi_{1,\text{mes}} \quad rssi_{2,\text{mes}} \quad \cdots \quad rssi_{N,\text{mes}} \right]^{\text{T}}$. The LS method is to find the location, at which the Euclidean Distance (ED) between the measured RSSI and the recorded one is least. It can be expressed as

$$\widehat{m} = \arg\min_{m} \left(\left(\boldsymbol{rssi}_{\text{mes}} - \boldsymbol{rssi}_{\text{loc}_m} \right)^{\text{H}} \left(\boldsymbol{rssi}_{\text{mes}} - \boldsymbol{rssi}_{\text{loc}_m} \right) \right). \tag{3.121}$$

In general, ΔL shall be kept to be small enough to get the high accuracy. In other side, however, smaller ΔL can lead to higher computational cost. To solve the problem, we propose the SSLS. The SSLS needs not compare the squared value for each candidate location, but down-sample the candidate locations with ΔL_1, which has $\Delta L_1 = k\Delta L$. k is an integer number larger than one (see Figure 3.22). Hence, the reference RSSI values at the down-sampled candidate location can be expressed as

$$\boldsymbol{RSSI}_{\text{ref,d}} = \left[\boldsymbol{rssi}_{\text{loc}_1,\text{d}} \quad \boldsymbol{rssi}_{\text{loc}_2,\text{d}} \quad \cdots \quad \boldsymbol{rssi}_{\text{loc}_{\lfloor M/k^2 \rfloor},\text{d}} \right] = \begin{bmatrix} rssi_{1,\text{loc}_1,\text{d}} & rssi_{1,\text{loc}_2,\text{d}} & \cdots & rssi_{1,\text{loc}_{\lfloor M/k^2 \rfloor},\text{d}} \\ rssi_{2,\text{loc}_1,\text{d}} & rssi_{2,\text{loc}_2,\text{d}} & \cdots & rssi_{2,\text{loc}_{\lfloor M/k^2 \rfloor},\text{d}} \\ \vdots & \vdots & \ddots & \vdots \\ rssi_{N,\text{loc}_1,\text{d}} & rssi_{N,\text{loc}_2,\text{d}} & \cdots & rssi_{N,\text{loc}_{\lfloor M/k^2 \rfloor},\text{d}} \end{bmatrix}. \tag{3.122}$$

For the measured RSSI, $\widehat{m}_{\text{d}}$ can be estimated as

$$\widehat{m}_{\text{d}} = \arg\min_{m_{\text{d}}} \left(\left(\boldsymbol{rssi}_{\text{mes}} - \boldsymbol{rssi}_{\text{loc}_{m_{\text{d}}},\text{d}} \right)^{\text{H}} \left(\boldsymbol{rssi}_{\text{mes}} - \boldsymbol{rssi}_{\text{loc}_{m_{\text{d}}},\text{d}} \right) \right). \tag{3.123}$$

The suspected location region can be expressed as $R_{\text{s}} = \left(x_{\text{loc}_{\widehat{m}_{\text{d}}}} - \Delta L_1 / 2, x_{\text{loc}_{\widehat{m}_{\text{d}}}} + \Delta L_1 / 2 \right) \times \left(y_{\text{loc}_{\widehat{m}_{\text{d}}}} - \Delta L_1 / 2, y_{\text{loc}_{\widehat{m}_{\text{d}}}} + \Delta L_1 / 2 \right)$. Extracting the recorded RSSIs from the candidate locations within R_{s} to constitute a new matrix:

$$\boldsymbol{RSSI}_{\text{ref},\text{s}} = \left[\boldsymbol{rssi}_{\text{loc}_{1,\text{s}}} \quad \boldsymbol{rssi}_{\text{loc}_{2,\text{s}}} \quad \cdots \quad \boldsymbol{rssi}_{\text{loc}_{M',\text{s}}} \right] = \begin{bmatrix} rssi_{1,\text{loc}_{1,\text{s}}} & rssi_{1,\text{loc}_{2,\text{s}}} & \cdots & rssi_{1,\text{loc}_{M',\text{s}}} \\ rssi_{2,\text{loc}_{1,\text{s}}} & rssi_{2,\text{loc}_{2,\text{s}}} & \cdots & rssi_{2,\text{loc}_{M',\text{s}}} \\ \vdots & \vdots & \ddots & \vdots \\ rssi_{N,\text{loc}_{1,\text{s}}} & rssi_{N,\text{loc}_{2,\text{s}}} & \cdots & rssi_{N,\text{loc}_{M',\text{s}}} \end{bmatrix}, \tag{3.124}$$

$$\boldsymbol{loc}_{\text{s}} = \left[\text{loc}_{1,\text{s}} \quad \text{loc}_{2,\text{s}} \quad \cdots \quad \text{loc}_{M',\text{s}} \right]$$

Then the fine location in R_s can be estimated as

$$\hat{m}' = \arg\min_{m'} \left(\left(\boldsymbol{rssi}_{\text{mes}} - \boldsymbol{rssi}_{\text{loc}_{m',s}} \right)^{\text{H}} \left(\boldsymbol{rssi}_{\text{mes}} - \boldsymbol{rssi}_{\text{loc}_{m',s}} \right) \right). \tag{3.125}$$

$\text{loc}_{\hat{m}',s}$ is considered as the estimated location.

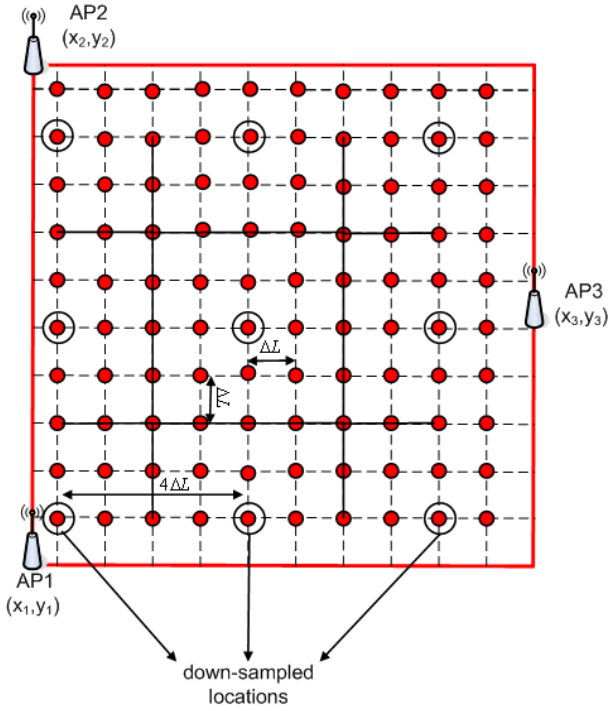

Figure 3.22: Illustration of SSLS based fingerprint method

Figure 3.22 illustrates the localization region, within which the candidate locations are selected with the regular sampling. Each small red point represents one candidate location, at which the RSS shall be premeasured. The points marked with the circles represent the down-sampled locations, which are the candidate locations using SSLS. Figure 3.22 shows $k = 4$.

3.4.2 Performance Evaluation and Measurement Results of LS and SSLS based Fingerprint Methods

The received signal power can be written as

$$P_{\text{rx}} = P_{\text{tx}} - \left(P_{\text{L}}\left(f_{\text{g}}, d_0 \right) + 10\alpha \log_{10}\left(\frac{d}{d_0} \right) + \eta\left(0, \sigma_{\text{a}}\right) \right), \tag{3.126}$$

where $\eta\left(0, \sigma_{\eta}\right)$ denotes the Gaussian distributed random variable with 0dB average and stand deviation σ_{η}. To minimize the log-normal fading effect, each reference RSSI shall be measured many times and

$$rssi_{n,\text{loc}_m} = \sum_{k=1}^{K} rssi_{n,\text{loc}_m}^{k}, \tag{3.127}$$

where $rssi_{n,\mathrm{loc}_m}^{k}$ is the k-th measured RSSI value and K is the number of measurement campaigns. In the real-time localization, the measured RSSI at the location (x,y) can be expressed as

$$rssi_{n,\mathrm{mes}}(x,y) = rssi_{n,\mathrm{t}}(x,y) + \eta\,, \tag{3.128}$$

where $rssi_{n,\mathrm{t}}(x,y)$ is the true RSSI at the location (x,y). It assumes that loc_m is the candidate position, from which to (x,y) the ED is the least (see Figure 3.23).

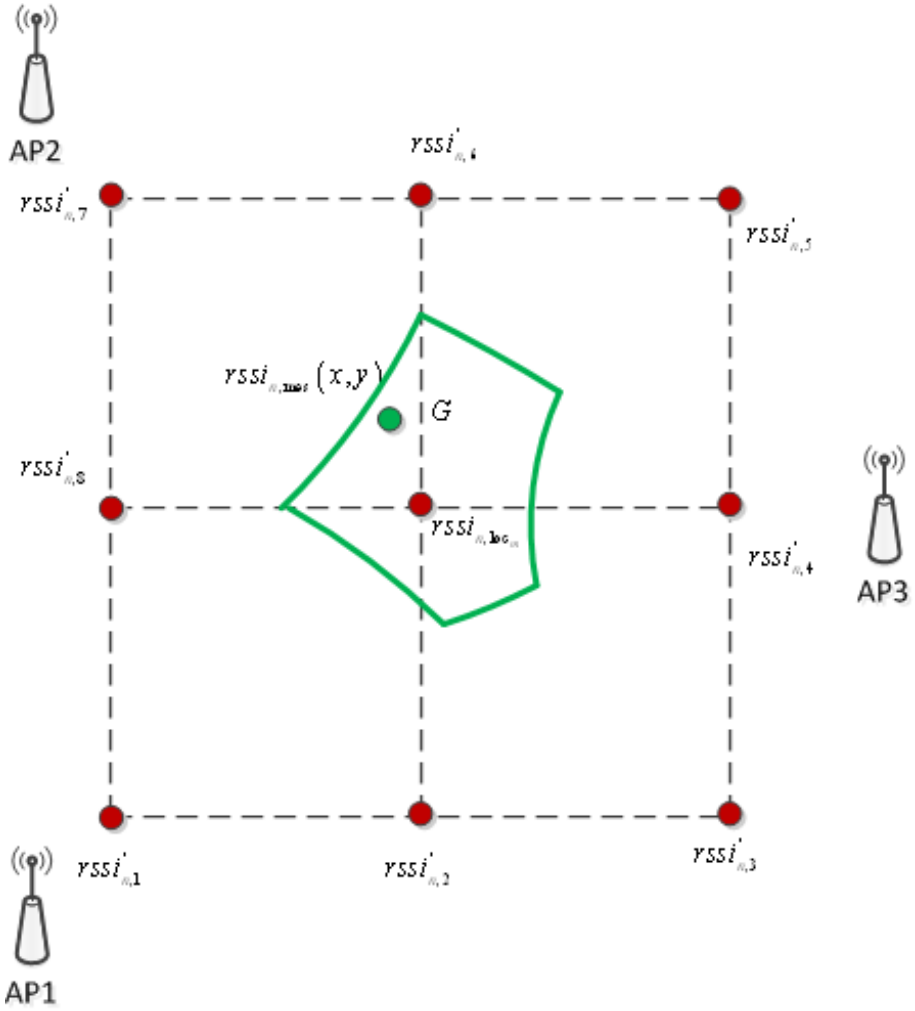

Figure 3.23: Position decision of a measured RSSI

It assumes that (x,y) is located within G, where G is the joint area, within which the position decision shall be loc_m. From $rssi'_{n,k,k=1\cdots8}$ and $rssi_{n,\mathrm{loc}_m}$, G can be determined as

$$\begin{aligned}
&G = G_1 \cap G_2 \cap \cdots \cap G_N \\
&G_n \propto \underset{(x,y)}{\arg}\left(rssi_{n,\min} \le rssi_{n,\mathrm{t}}(x,y) \le rssi_{n,\max}\right) \\
&rssi_{n,\mathrm{loc}_m,\min} = rssi_{n,\mathrm{loc}_m} - \frac{rssi_{n,\mathrm{loc}_m} - \max\left(rssi'_{n,k} \middle| rssi'_{n,k} < rssi_{n,\mathrm{loc}_m}\right)}{2}. \\
&rssi_{n,\mathrm{loc}_m,\max} = \frac{\min\left(rssi'_{n,k} \middle| rssi'_{n,k} > rssi_{n,\mathrm{loc}_m}\right) - rssi_{n,\mathrm{loc}_m}}{2} - rssi_{n,\mathrm{loc}_m}
\end{aligned} \tag{3.129}$$

From (3.128), the decision error probability for loc_m can be expressed as

$$\mathrm{P}_{\mathrm{e},\mathrm{loc}_m}=1-\frac{1}{A(G)}\iint_G\left(\prod_{n=1}^{N}\left(\begin{array}{l}1-\mathrm{Q}\left(\dfrac{\left|rssi_{n,\mathrm{loc}_m,\min}-rssi_{n,\mathrm{t}}(x,y)\right|}{\sigma_\eta}\right)-\\ -\mathrm{Q}\left(\dfrac{\left|rssi_{n,\mathrm{loc}_m,\max}-rssi_{n,\mathrm{t}}(x,y)\right|}{\sigma_\eta}\right)\end{array}\right)\right)\mathrm{d}x\mathrm{d}y\,, \tag{3.130}$$

where $A(G)$ is the area of G. Hence, the error probability of LS can be expressed as

$$\mathrm{P}_{\mathrm{e,LS}}=\frac{1}{M}\sum_{m=1}^{M}\mathrm{P}_{\mathrm{e},\mathrm{loc}_m}\,. \tag{3.131}$$

SSLS consists of two steps. In the first step, G shall be expanded to G_d since $\Delta L_1>\Delta L$. Hence, the detection probability of the first step can be rewritten as

$$\mathrm{P}_{\mathrm{det},\mathrm{loc}_{m_\mathrm{d}},\mathrm{coa}}=\frac{1}{A(G_\mathrm{d})}\iint_{G_\mathrm{d}}\left(\prod_{n=1}^{N}\left(\begin{array}{l}1-\mathrm{Q}\left(\dfrac{\left|rssi_{n,\mathrm{loc}_{m_\mathrm{d}},\min}-rssi_{n,\mathrm{t}}(x,y)\right|}{\sigma_\eta}\right)-\\ -\mathrm{Q}\left(\dfrac{\left|rssi_{n,\mathrm{loc}_{m_\mathrm{d}},\max}-rssi_{n,\mathrm{t}}(x,y)\right|}{\sigma_\eta}\right)\end{array}\right)\right)\mathrm{d}x\mathrm{d}y\,. \tag{3.132}$$

Then the decision error probability for $\mathrm{loc}_{m_\mathrm{d}}$ can be written as

$$\mathrm{P}_{\mathrm{e},\mathrm{loc}_{m_\mathrm{d}},\mathrm{fine}}=1-\mathrm{P}_{\mathrm{det},\mathrm{loc}_{m_\mathrm{d}},\mathrm{coa}}\mathrm{P}_{\mathrm{det},\mathrm{loc}_{m_\mathrm{d}},\mathrm{fine}}\,, \tag{3.133}$$

where

$$\mathrm{P}_{\mathrm{det},\mathrm{loc}_{m_\mathrm{d}},\mathrm{fine}}=\frac{1}{M'}\sum_{m'=1}^{M'}\frac{1}{A(G)}\iint_G\left(\prod_{n=1}^{N}\left(\begin{array}{l}1-\mathrm{Q}\left(\dfrac{\left|rssi_{n,\mathrm{loc}_{m'},\min}-rssi_{n,\mathrm{t}}(x,y)\right|}{\sigma_\eta}\right)-\\ -\mathrm{Q}\left(\dfrac{\left|rssi_{n,\mathrm{loc}_{m'},\max}-rssi_{n,\mathrm{t}}(x,y)\right|}{\sigma_\eta}\right)\end{array}\right)\right)\mathrm{d}x\mathrm{d}y \tag{3.134}$$

Hence, the error probability of SSLS can be expressed as

$$\mathrm{P}_{\mathrm{e,SSLS}}=\frac{1}{M_\mathrm{d}}\sum_{m_\mathrm{d}=1}^{M_\mathrm{d}}\mathrm{P}_{\mathrm{e},\mathrm{loc}_{m_\mathrm{d}},\mathrm{fine}}\,. \tag{3.135}$$

It is obvious that the SSLS has the lower complexity than LS if ΔL is small enough. From Figure 3.22, it has

$$M\approx\frac{LH}{\Delta L^2},M_\mathrm{d}\approx\frac{LH}{k^2\Delta L^2},M'\approx k^2\,. \tag{3.136}$$

From (3.130) to (3.135), it is clear that the computational complexity of SSLS is much lower than that of LS.

$$O(\mathrm{SSLS}) < O(\mathrm{LS})$$
$$O(\mathrm{SSLS}) = M_{\mathrm{d}} + M^{'} = \frac{LH}{k^2 \Delta L^2} + k^2 \,. \tag{3.137}$$
$$O(\mathrm{LS}) = M = \frac{LH}{\Delta L^2}$$

The parameters of the measurement can be found in Table 3.5.

Table 3.5: Parameters of measurement campaign

Measurement Parameters	**Description**	**Value**
N	The number of UWB receivers	3
	Modulation Format	MB-OFDM
(x_n, y_n)	Coordinates	(0m,0m) (1.76m,1m) (0m,2m)
	The employed sub channel	15
L	Width of localization region	1.76m
H	Height of localization region	2m
ΔL	Spatial interval	5cm
k		4

The measurement campaign was executed based on ECMA-368. According to [93], the PHY of multiband OFDM operates in the 3.1 – 10.6 GHz frequency band, which can be separated into 14 sub-bands. Time-Frequency Codes (TFC) are used to get the frequency diversity. In our research, frequency hopping shall be avoided during the transmission in order to keep the transmission power constant. Hence, the 15th channel is used since it only uses the 3rd sub band to transmit signal. Figure 3.24 depicts the relation between received power and the transmission distance for 15th channel.

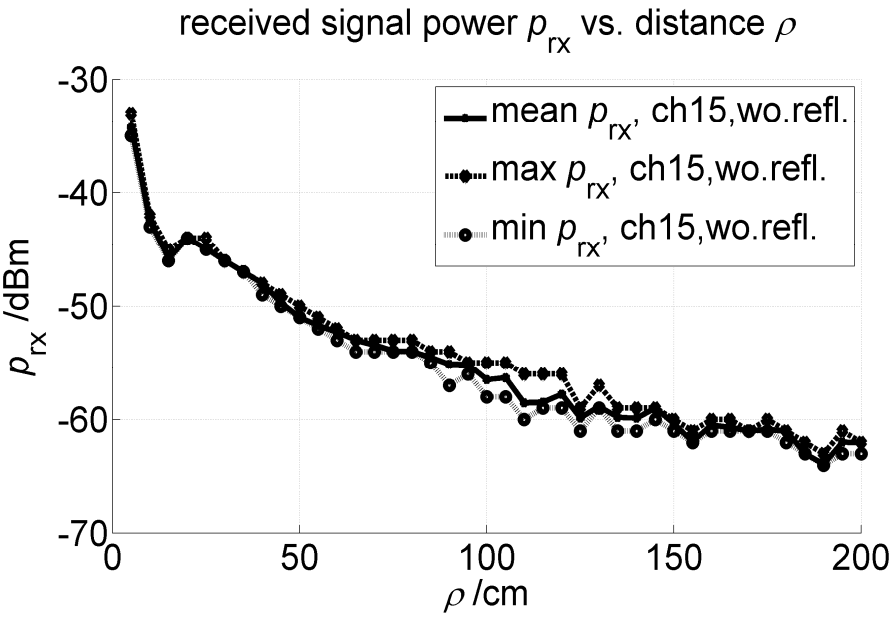

Figure 3.24: RSSI vs transmission distance for 15th channel

and illustrate the Probability Density Function (PDF) of estimation error with LS and SSLS, respectively. The variance of log-normal fading in our environment is approximate 3.0. It can be seen from two figures that SSLS outperforms LS.

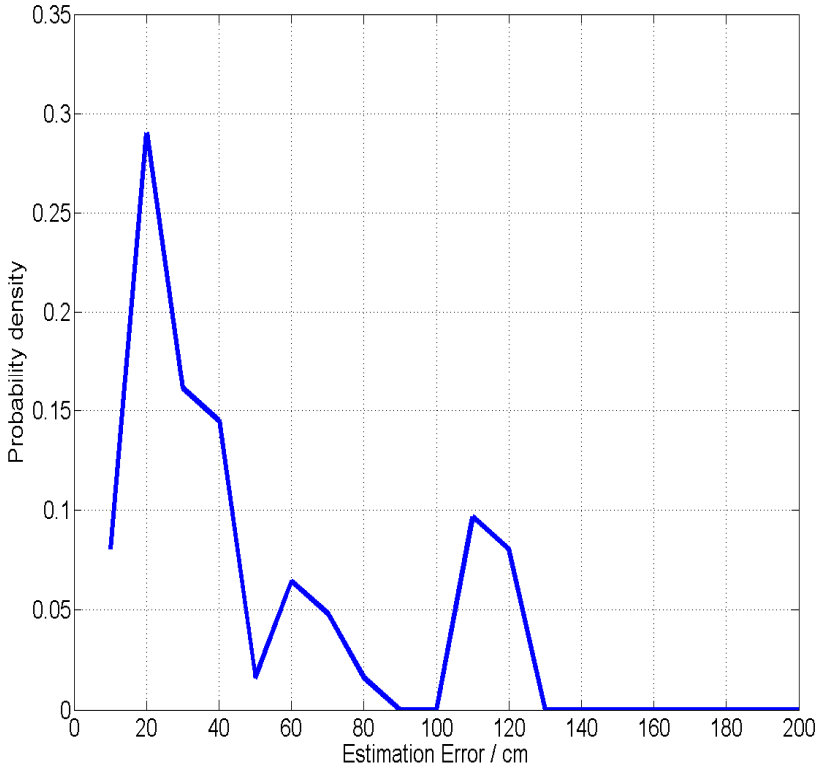

Figure 3.25: PDF of estimation error (LS, $\sigma_\eta \approx 3.0$, RMSE = 55.4cm)

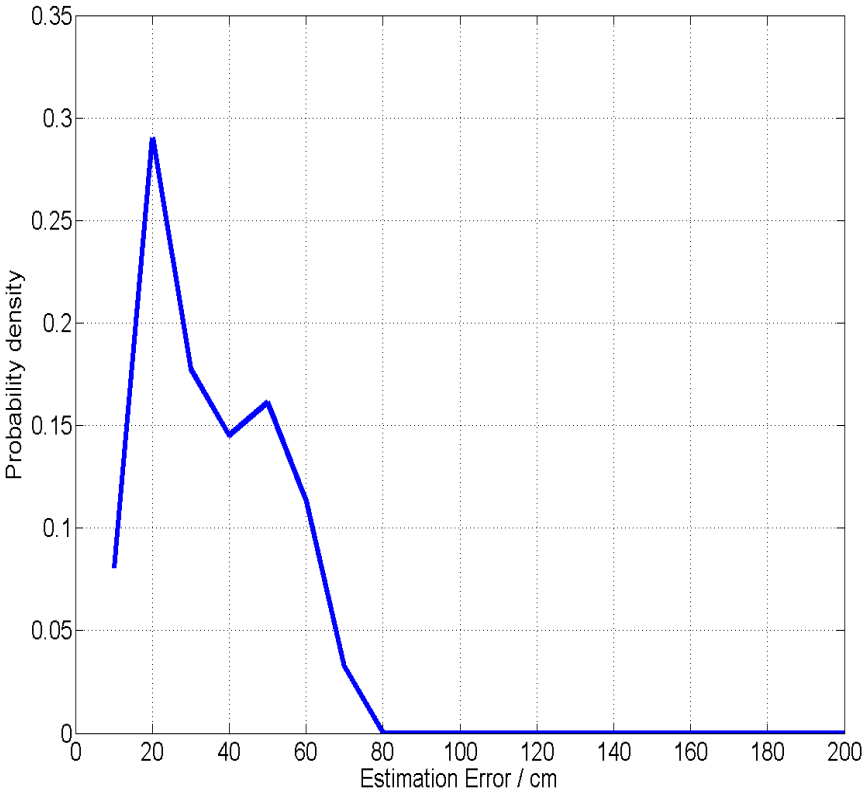

Figure 3.26: PDF of estimation error (SSLS, $\sigma_\eta \approx 3.0$, RMSE = 33.0cm)

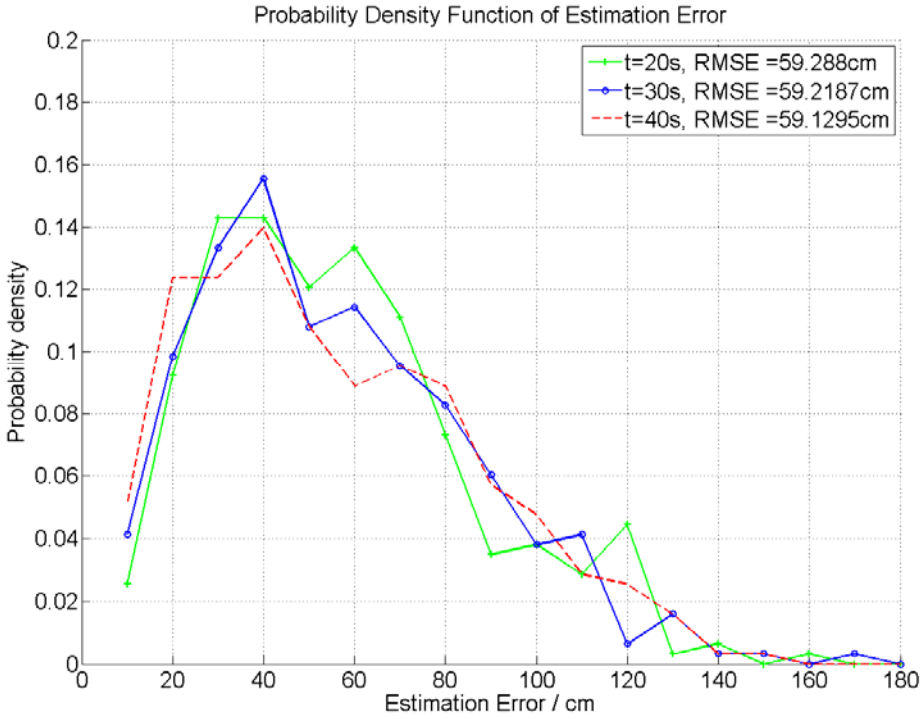

Figure 3.27: PDF of estimation error for passive LT (*L* = 20s, 30s and 40s)

Figure 3.27 depicts the performance of passive LT procedure. In the passive LT procedure, the LT duration is set to 20s, 30s and 40s. As can be seen from this figure, the LT performance can be improved with the increased LT duration since the log-normal fading effect can be reduced with the increased LT duration.

3.4.3 Distance Estimation via Channel Energy Estimator

The fingerprint methods depend heavily on the localization environment and the estimation accuracy will go worse with the lower SNR. In this subsection, distance estimation based on channel energy is proposed. Path loss is reflected by the estimated channel energy. The channel energy shall be estimated via I) Singular Value Decomposition Approach (SVDA) and II) Eigen Value Decomposition Approach (EVDA). According to [22], the discrete IR-UWB symbol from *n*-th receiver can be illustrated as:

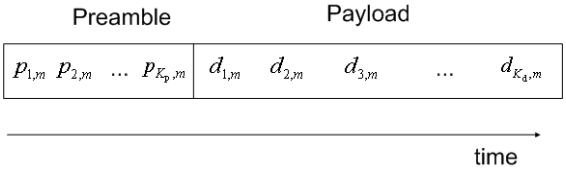

Figure 3.28: Structure of transmitted frame

From (3.2), the spread preamble sequence can be illustrated as

$$\begin{aligned} \boldsymbol{p} &= \begin{bmatrix} \boldsymbol{p}_1 & \boldsymbol{p}_2 & \cdots & \boldsymbol{p}_I \end{bmatrix} \\ &= \begin{bmatrix} g_0 & g_1 & \cdots & g_{K-1} \end{bmatrix}^{\mathrm{T}} \\ p_i &= \begin{bmatrix} p_1 \otimes \delta_{L_\mathrm{p}} & p_2 \otimes \delta_{L_\mathrm{p}} & \cdots & p_{K_\mathrm{p}} \otimes \delta_{L_\mathrm{p}} \end{bmatrix}, \\ &= \begin{bmatrix} g_0 & g_1 & \cdots & g_{K_\mathrm{p}L_\mathrm{p}-1} \end{bmatrix} \end{aligned} \tag{3.138}$$

where $K = IK_\mathrm{p}L_\mathrm{p}$ and I is the number of spread preamble symbols contained in one spread preamble sequence. It defines $\underline{\boldsymbol{H}}_n$ as the channel matrix between the transmitter and the *n*-th UWB receiver. As known that $\underline{\boldsymbol{H}}_n$ is a $(W_n + K - 1) \times K$ toeplitz matrix with shifted and zero-padded versions of $\begin{bmatrix} \underline{h}_{0,n} & \underline{h}_{1,n} & \cdots & \underline{h}_{W_n-1,n} & 0 & \cdots & 0 \end{bmatrix}^{\mathrm{T}}$ on its columns, where $\underline{h}_{w,n}, w = 0 \cdots W_n$ is the discrete CIR. Then the received vector $\boldsymbol{r}_{n,\mathrm{p}}$ can be expressed as

$$\begin{aligned} \underline{\boldsymbol{r}}_{n,\mathrm{p}} &= \underline{\boldsymbol{H}}_n \boldsymbol{p} + \underline{\boldsymbol{n}}_n \\ &= \boldsymbol{G}_n \underline{\boldsymbol{h}}_n + \underline{\boldsymbol{n}}_n \end{aligned}, \tag{3.139}$$

where $\underline{\boldsymbol{n}}_n$ is discrete additive Gaussian noise at *n*-th UWB receiver. $\boldsymbol{G}_n$ is a $L_{\mathrm{r},n} \times W_n$ matrix with shifted and zero-padded versions of $\begin{bmatrix} g_0 & g_1 & \cdots & g_{K-1} & 0 & \cdots & 0 \end{bmatrix}^{\mathrm{T}}$ on its columns and $\underline{\boldsymbol{h}}_n = \begin{bmatrix} \underline{h}_{0,n} & \underline{h}_{1,n} & \cdots & \underline{h}_{W_n-1,n} \end{bmatrix}^{\mathrm{T}}$. It assumes that $L_{\mathrm{r},n} \times W_n$ and $\underline{\boldsymbol{h}}_n$ keeps unchanged during the transmission of K preambles as there is weak Doppler Effect in the indoor environment. With SVD of $\boldsymbol{G}_n$, the (3.139) can be rewritten as

$$\underline{\boldsymbol{r}}_{n,\mathrm{p}} = \boldsymbol{U}\boldsymbol{S}_n\boldsymbol{V}^{\mathrm{H}} \underline{\boldsymbol{h}}_n + \underline{\boldsymbol{n}}_n, \tag{3.140}$$

where

$$\begin{aligned} \boldsymbol{G}_n &= \boldsymbol{U}\boldsymbol{S}_n\boldsymbol{V}^{\mathrm{H}} \\ \boldsymbol{S}_n &= \begin{bmatrix} \boldsymbol{D}_{W_n} \\ \boldsymbol{0}_{\left(L_{\mathrm{r},n}-W_n\right)\times W_n} \end{bmatrix}. \end{aligned} \tag{3.141}$$

In (3.141), $\boldsymbol{D}_{W_n}$ is a diagonal matrix which contains W_n Eigen values. $\boldsymbol{U}$ and $\boldsymbol{V}$ are $L_{\mathrm{r},n}\times L_{\mathrm{r},n}$ and $W_n\times W_n$ unitary matrices, respectively. Hence, (3.140) can be transformed into

$$\boldsymbol{U}^{-1}\underline{\boldsymbol{r}}_{n,\mathrm{p}} = \boldsymbol{S}_n\boldsymbol{V}^{\mathrm{H}}\underline{\boldsymbol{h}}_n + \boldsymbol{U}^{-1}\underline{\boldsymbol{n}}_n\,. \tag{3.142}$$

As $\boldsymbol{U}$ is a unitary matrix, (3.142) can be rewritten as

$$\boldsymbol{U}^{\mathrm{H}}\underline{\boldsymbol{r}}_{n,\mathrm{p}} = \boldsymbol{S}_n\boldsymbol{V}^{\mathrm{H}}\underline{\boldsymbol{h}}_n + \boldsymbol{U}^{\mathrm{H}}\underline{\boldsymbol{n}}_n\,, \tag{3.143}$$

where

$$\boldsymbol{S}_n\boldsymbol{V}^{\mathrm{H}}\underline{\boldsymbol{h}}_n = \begin{bmatrix} \underline{\boldsymbol{h}}_n^{'} \\ \boldsymbol{0} \end{bmatrix}. \tag{3.144}$$

$\underline{\boldsymbol{h}}_n^{'}$ and $\boldsymbol{0}$ are $W_n\times 1$ and $\left(L_{\mathrm{r},n}-W_n\right)\times 1$ vectors, respectively, The first W_n elements of $\boldsymbol{S}_n\boldsymbol{V}^{\mathrm{H}}\underline{\boldsymbol{h}}_n$ are products of the W_n Eigen values and the W_n multi-taps while the rest elements are 0. The (3.143) can be rewritten as

$$\begin{aligned} \underline{\boldsymbol{r}}_n^{'} &= \begin{bmatrix} \underline{\boldsymbol{h}}_n^{'} \\ \boldsymbol{0} \end{bmatrix} + \begin{bmatrix} \underline{\boldsymbol{n}}_{1,n}^{'} \\ \underline{\boldsymbol{n}}_{2,n}^{'} \end{bmatrix} \\ \begin{bmatrix} \underline{\boldsymbol{n}}_{1,n}^{'} \\ \underline{\boldsymbol{n}}_{2,n}^{'} \end{bmatrix} &= \boldsymbol{U}^{\mathrm{H}}\underline{\boldsymbol{n}}_n \end{aligned}. \tag{3.145}$$

In (3.145), $\underline{\boldsymbol{n}}_{1,n}^{'}$ and $\underline{\boldsymbol{n}}_{2,n}^{'}$ are $W_n\times 1$ and $\left(L_{\mathrm{r},n}-W_n\right)\times 1$ vectors, respectively. If $L_{\mathrm{r},n}-W_n$ is large enough, noise power at *n*-th UWB receiver can be estimated by

$$\widehat{N}_{0,n,\mathrm{svd}} = \frac{1}{L_{\mathrm{r},n}-W_n}\underline{\boldsymbol{n}}_{2,n}^{'\mathrm{H}}\underline{\boldsymbol{n}}_{2,n}^{'}\,. \tag{3.146}$$

Next, the noise power estimation via EVD of Auto Correlation Matrix (ACM) of the received preamble vector will be proposed. The same as that of SVDE, it assumes that the channel keeps static during transmission of *K* preambles. According to [22], it has $W_n < K_{\mathrm{p}}L_{\mathrm{p}}$, which denotes that Inter Preamble Interference (IPI) only take place between two adjacent preambles. From (3.138) and (3.139), $\boldsymbol{G}_n$ can be separated into

$$\begin{aligned} \boldsymbol{G}_n &= \begin{bmatrix} \boldsymbol{G}_{n,\mathrm{sub}} \\ \boldsymbol{R}_n \end{bmatrix} \\ \boldsymbol{G}_{n,\mathrm{sub}} &= \begin{bmatrix} \boldsymbol{G}_{n,\mathrm{sub}}^{(1)} \\ \boldsymbol{G}_{n,\mathrm{sub}}^{(2)} \\ \vdots \\ \boldsymbol{G}_{n,\mathrm{sub}}^{(I)} \end{bmatrix}, \end{aligned} \tag{3.147}$$

where $\boldsymbol{G}_{n,\mathrm{sub}}$ is with the size of $K \times W_n$ while $\boldsymbol{R}_n$ is the rest matrix with the size of $(W_n - 1) \times W_n$. $\boldsymbol{G}_{n,\mathrm{sub}}^{(i)}$ is a $K_\mathrm{p} L_\mathrm{p} \times W_{mn}$ circulant matrix with shifted version of $\begin{bmatrix} g_0 & g_1 & \cdots & g_{K_\mathrm{p}L_\mathrm{p}-1} \end{bmatrix}$ on its columns. $\underline{\boldsymbol{r}}_{n,\mathrm{p}}$ can be rewritten as

$$\underline{\boldsymbol{r}}_{n,\mathrm{p}} = \begin{bmatrix} \underline{\boldsymbol{r}}_{n,\mathrm{p}}^{(1)} \\ \underline{\boldsymbol{r}}_{n,\mathrm{p}}^{(2)} \\ \vdots \\ \underline{\boldsymbol{r}}_{n,\mathrm{p}}^{(I+1)} \end{bmatrix} \quad . \tag{3.148}$$

$$\underline{\boldsymbol{r}}_{n,\mathrm{p}}^{(i)} = \boldsymbol{G}_{n,\mathrm{sub}}^{(i)} \underline{\boldsymbol{h}}_n + \underline{\boldsymbol{n}}_n^{(i)}, i = 1,2,...,I$$

In (3.148), the vector $\underline{\boldsymbol{r}}_{n,\mathrm{p}}^{(i)}, i = 1 \cdots I$ has the length of $K_\mathrm{p} L_\mathrm{p}$. The ACM of the received preamble vector can be determined by

$$\begin{aligned} \underline{\boldsymbol{R}}_{\underline{r}_n} &= \mathrm{E}\left(\underline{\boldsymbol{r}}_{mn}^{\mathrm{p},(i)} \underline{\boldsymbol{r}}_{mn}^{\mathrm{p},(i)\mathrm{H}} \right) \\ &\approx \frac{1}{I} \sum_{i=1}^{I} \left(\left(\boldsymbol{G}_{n,\mathrm{sub}}^{(i)} \underline{\boldsymbol{h}}_n + \underline{\boldsymbol{n}}_n^{(i)} \right) \left(\boldsymbol{G}_{n,\mathrm{sub}}^{(i)} \underline{\boldsymbol{h}}_n + \underline{\boldsymbol{n}}_n^{(i)} \right)^{\mathrm{H}} \right) \\ &= \frac{1}{I} \sum_{i=1}^{I} \left(\boldsymbol{G}_{n,\mathrm{sub}}^{(i)} \underline{\boldsymbol{h}}_n \underline{\boldsymbol{h}}_n^{\mathrm{H}} \boldsymbol{G}_{n,\mathrm{sub}}^{(i)\mathrm{H}} + \boldsymbol{G}_{n,\mathrm{sub}}^{(i)} \underline{\boldsymbol{h}}_n \underline{\boldsymbol{n}}_n^{(i)\mathrm{H}} + \underline{\boldsymbol{n}}_n^{(i)} \underline{\boldsymbol{h}}_n^{\mathrm{H}} \boldsymbol{G}_{n,\mathrm{sub}}^{(i)\mathrm{H}} + \underline{\boldsymbol{n}}_n^{(i)} \underline{\boldsymbol{n}}_n^{(i)\mathrm{H}} \right), \\ &= \frac{1}{I} \sum_{i=1}^{I} \boldsymbol{G}_{n,\mathrm{sub}}^{(i)} \underline{\boldsymbol{h}}_n \underline{\boldsymbol{h}}_n^{\mathrm{H}} \boldsymbol{G}_{n,\mathrm{sub}}^{(i)\mathrm{H}} + N_{0,n} \boldsymbol{I}_{K_\mathrm{p}L_\mathrm{p}} + \Delta \underline{\boldsymbol{R}}_n \\ &= \underline{\boldsymbol{R}}_\mathrm{p} + N_{0,n} \boldsymbol{I}_{K_\mathrm{p}L_\mathrm{p}} + \Delta \underline{\boldsymbol{R}}_n \end{aligned} \tag{3.149}$$

where rank of $\underline{\boldsymbol{R}}_\mathrm{p}$ is one and $\Delta \underline{\boldsymbol{R}}_n$ is the perturbation matrix. After EVD of $\underline{\boldsymbol{R}}_{\underline{r}_n}$, $K_\mathrm{p} L_\mathrm{p}$ Eigenvalues $\begin{bmatrix} \lambda_{1,n}^{'} & \lambda_{2,n}^{'} & \cdots & \lambda_{K_\mathrm{p}L_\mathrm{p},n}^{'} \end{bmatrix}$ can be determined and

$$\begin{aligned} &\lambda_{1,n}^{'} \geq \lambda_{2,n}^{'} \geq ... \geq \lambda_{K_\mathrm{p}L_\mathrm{p},n}^{'} \\ &\lambda_{1,n}^{'} = \lambda_n + N_{0,n} + \Delta\lambda_1 \\ &\lambda_{j,n}^{'} = N_{0,n} + \Delta\lambda_j \\ &j = 2 \cdots K_\mathrm{p} L_\mathrm{p} \end{aligned} \quad , \tag{3.150}$$

where $\Delta\lambda_1 \cdots \Delta\lambda_{K_\mathrm{p}L_\mathrm{p}}$ are perturbed Eigen values. Then the $N_{0,n}$ can be estimated by

$$\widetilde{N}_{0,n} = \frac{1}{K_\mathrm{p} L_\mathrm{p} - 1} \sum_{i=2}^{K_\mathrm{p}L_\mathrm{p}} \lambda_{i,n}^{'} \, . \tag{3.151}$$

So far the noise power density of $N_{0,n}$ has been estimated by (3.146) and (3.151), which shall be further exploited to estimate the channel energy. From (3.148), $\boldsymbol{G}_{n,\mathrm{sub}}^{(i)} \underline{\boldsymbol{h}}_n$ can be calculated as

$$\boldsymbol{G}_{n,\mathrm{sub}}^{(i)}\underline{\boldsymbol{h}}_n=\begin{bmatrix} g_{0,i} & g_{K_\mathrm{p}L_\mathrm{p}-1,i} & \cdots & g_{K_\mathrm{p}L_\mathrm{p}-W_n+1,i} \\ g_{1,i} & g_{0,i} & \cdots & g_{K_\mathrm{p}L_\mathrm{p}-W_n+2,i} \\ \vdots & \vdots & \ddots & \vdots \\ g_{K_\mathrm{p}L_\mathrm{p}-1,i} & g_{K_\mathrm{p}L_\mathrm{p}-2,i} & \cdots & g_{K_\mathrm{p}L_\mathrm{p}-W_n+2,i} \end{bmatrix}\begin{bmatrix} \underline{h}_{0,n} \\ \underline{h}_{1,n} \\ \vdots \\ \underline{h}_{W_n-1,n} \end{bmatrix}$$
$$=\begin{bmatrix} \sum_{j=0}^{0} g_{j,i}\underline{h}_{j,n}+\sum_{k=1}^{W_n-1} g_{K_\mathrm{p}L_\mathrm{p}-k,i}\underline{h}_{k,n} \\ \sum_{j=0}^{1} g_{1-j,i}\underline{h}_{j,n}+\sum_{k=2}^{W_n-1} g_{K_\mathrm{p}L_\mathrm{p}-k+1,i}\underline{h}_{k,n} \\ \vdots \\ \sum_{j=0}^{W_n-1} g_{K_\mathrm{p}L_\mathrm{p}-1-j,i}\underline{h}_{j,n} \end{bmatrix}. \quad (3.152)$$

The diagonal elements of $\underline{\boldsymbol{R}}_\mathrm{p}$: $\underline{d}_{jj,i,n}, j=1,2,...,K_\mathrm{p}L_\mathrm{p}$ can be approximated as

$$\underline{d}_{jj,n}\approx\sum_{k=0}^{W_n-1}\left(g_{\left(K_\mathrm{p}L_\mathrm{p}+j-k-1\right)\bmod\left(K_\mathrm{p}L_\mathrm{p}\right)}\right)^2\underline{h}_{k,n}\underline{h}_{k,n}^{*}, j=1,2,...,K_\mathrm{p}L_\mathrm{p}. \quad (3.153)$$

Since the preamble sequence of each sub-block is asymptotic orthogonal [22]:

$$\sum_{k=0}^{K_\mathrm{p}L_\mathrm{p}-1} g_{k,i}g_{k+\delta,i}\approx 0,\delta\neq 0. \quad (3.154)$$

λ_n in (3.150) can be estimated by

$$\begin{aligned}\lambda_n&\approx\lambda_{1,n}^{'}-N_{0,n}=\sum_{j=1}^{K_\mathrm{p}L_\mathrm{p}}\underline{d}_{jj,n}\\&\approx\left(\sum_{l=0}^{K_\mathrm{p}L_\mathrm{p}-1}\left(g_{l,n}\right)^2\right)\left(\sum_{w=0}^{W_n-1}\left(\underline{h}_{w,n}\underline{h}_{w,n}^{*}\right)\right).\\&=\left(\sum_{l=0}^{K_\mathrm{p}L_\mathrm{p}-1}\left(g_{l,n}\right)^2\right)E_{h_n}\end{aligned} \quad (3.155)$$

From (3.150), (3.146), (3.151) and (3.155), the channel energy E_{h_n} can be estimated. According to E_{h_n} and (3.126), the transmission distance can be estimated as

$$\hat{d}=d_0\left(1+10^{\left(\frac{10\log_{10}\left(E_{h_n}\right)-P_\mathrm{L}\left(f_g,d_0\right)}{10\alpha}\right)}\right), \quad (3.156)$$

where d_0 is the reference distance, which is generally set to one meter and $P_\mathrm{L}\left(f_g,d_0\right)$ is the path loss at the reference distance, which shall be determined by the measurement campaign.

3.4.4 Simulation Results of Distance Estimation

The simulation parameters are depicted in Table 3.6.

Table 3.6: Simulation Parameters of Distance Estimation

Parameter	Definition	Value
N	Number of receivers	1
M	Number of transmitters	1
d	Transmission distance	7m
α	Decay exponent	2.5
SNR	Signal to Noise Ratio	0 – 10 dB
N_{loop}	Number of Monte-Carlo Simulation	500
SVDE	Singular Value Decomposition Estimation	
EVDE	Eigen Value Decomposition Estimation	

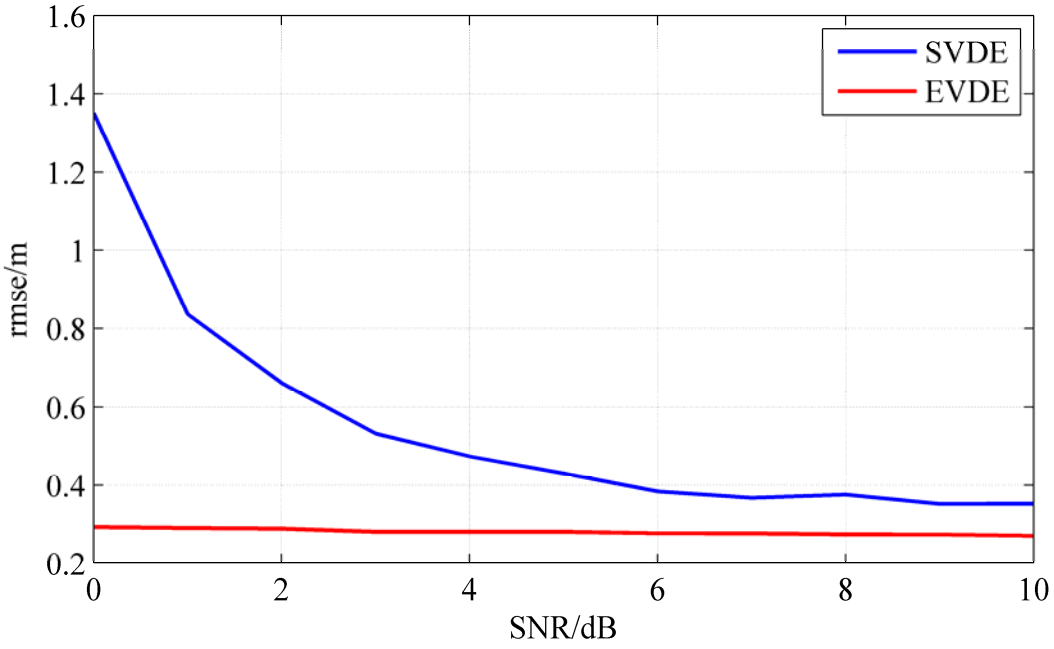

Figure 3.29: RMSE of distance estimation using SVDE and EVDE

Figure 3.29 shows that EVDE based distance estimation can achieve more accurate results than that of SVDE. EVDE based distance estimation depends slightly on SNR while SVDE based distance estimation shows a definitely better performance at a higher SNR.

4 Angle of Arrival (AoA) based Localization in Wireless LAN Systems

4.1 Overview

In chapter 4, AoA based localization in WLAN systems will be introduced. The main characteristics and advantages of WLAN localization systems have been mentioned in the chapter 1. This chapter is structured as follows. The employed antenna parameters shall be optimized in subchapter 4.2.1. Two criteria for antenna parameters optimization are deduced. Phase offset caused by PLL asynchronization can influence the accuracy of AoA estimation. Hence, the initial calibration process is introduced in 4.2.2. Existing AoA estimation algorithms: conventional beamforming technique and MUSIC will be introduced in subchapter 4.2.3. In subchapter 4.3, the Multi Path Components (MPC) suppression via channel estimation is proposed. The novel subspace based OFDM CFO (Carrier Frequency Offset) estimator and channel estimator has been investigated in the research. The simulation and measurement results will be given in 4.5.

4.2 AoA Estimation in WLAN Systems

4.2.1 Antenna Parameters Optimization

AoA estimation exploits the different phase shift among each antenna elements to estimate the arrived angle. From the antenna diagram, it is clear that the clarity area, Main Beam Width (MBW) and the Main lobe to Side lobe Ratio (MSR) play important roles on the angle estimation. Figure 4.1 illustrates the MBW, MSR and grating lobes of a Uniform Linear Array (ULA). Clarity area gives the scope from the main lobe to the first grating lobe. Any actual radiation direction θ beyond the clarity area will be estimated to a mirror direction θ'. The relation between θ and θ' can be expressed as

$$\theta = \begin{cases} \arccos\left(\frac{\lambda}{d}\left(\frac{d}{\lambda}\cos\theta' + 1\right)\right), \text{if } \frac{d}{\lambda}\cos\theta' < \frac{d}{\lambda} - 1 \\ \arccos\left(\frac{\lambda}{d}\left(\frac{d}{\lambda}\cos\theta' - 1\right)\right), \text{if } \frac{d}{\lambda}\cos\theta' > 1 - \frac{d}{\lambda} \end{cases}, \tag{4.1}$$

where λ is the wavelength and d is inter-elements spacing . θ is the angle between wave impinging direction and the antenna array, which is depicted in Figure 2.6. From (4.1), the clarity area can be calculated as

$$\arccos\left(\frac{\lambda}{2d}\right) \le \theta \le \arccos\left(-\frac{\lambda}{2d}\right). \tag{4.2}$$

From (4.2), it can be concluded that $d = \lambda / 2$ is the perfect case.

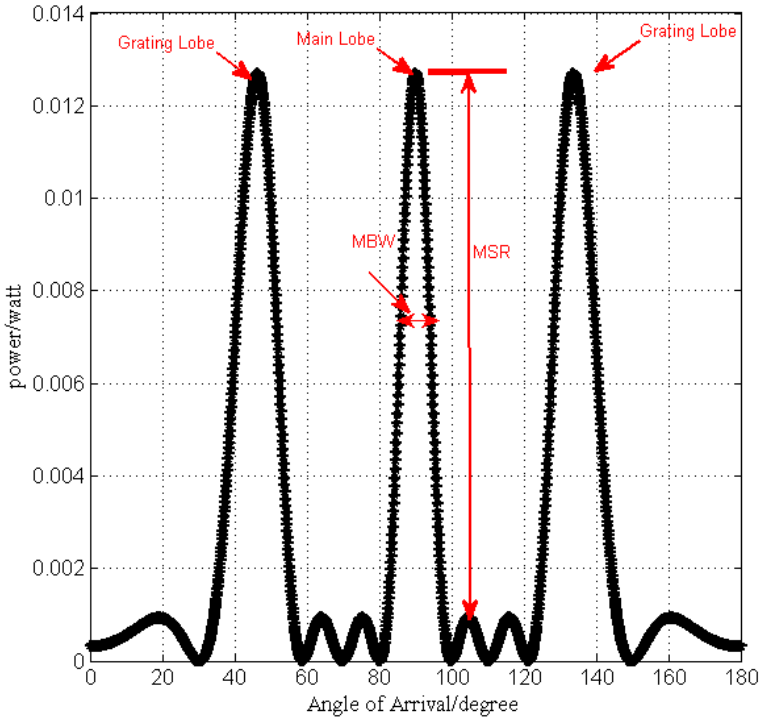

Figure 4.1: Radiation pattern of a Uniform Linear Array (ULA)

From Figure 4.1, we can see that the grating lobes may have the same radiation power as the main lobe. Hence, it is essential to investigate the relation between the antenna parameters and the angle distance from the main lobe to the grating lobe.

The following text gives the relation between radiation pattern and the inter-element spacing. It assumes that the number of antenna elements is N and the weighting vector of the beamformer is $\boldsymbol{w} = \begin{bmatrix} w_1 & w_2 & \cdots & w_N \end{bmatrix}^{\mathrm{T}}$. And the phase steering vector of the beamformer is $\boldsymbol{\beta} = \begin{bmatrix} 1 & \mathrm{e}^{j\frac{2\pi d \cos\theta_{\mathrm{b}}}{\lambda}} & \cdots & \mathrm{e}^{j\frac{2\pi(N-1)d\cos\theta_{\mathrm{b}}}{\lambda}} \end{bmatrix}^{\mathrm{T}}$, where θ_{b} is the desired direction of the beamformer. For the incoming angle θ, the output of the beamformer can be expressed as

$$\begin{aligned} \boldsymbol{r}(t) &= \sum_{n=1}^{N} w_n s_n(t) \mathrm{e}^{j\frac{2\pi(n-1)d\cos\theta_{\mathrm{b}}}{\lambda}} \\ s_n(t) &= s(t)\mathrm{e}^{-j\frac{2\pi(n-1)d\cos\theta}{\lambda}}, n = 1,2,\ldots,N \end{aligned} \tag{4.3}$$

The received signal power can be expressed as

$$P_{\mathrm{r}}=\frac{1}{T}\int_0^T\left|r(t)\right|^2\mathrm{d}t=\frac{1}{T}\int_0^T\left|\sum_{n=1}^{N}w_n s(t)\mathrm{e}^{-j\frac{2\pi(n-1)d\cos\theta}{\lambda}}\mathrm{e}^{j\frac{2\pi(n-1)d\cos\theta_{\mathrm{b}}}{\lambda}}\right|^2\mathrm{d}t$$
$$=\left(\sum_{n=1}^{N}w_n^2+2\sum_{n=1}^{N-1}\left(\sum_{m=1}^{N-n}w_m w_{m+n}\cos\left(n\frac{2\pi d}{\lambda}(\cos\theta-\cos\theta_{\mathrm{b}})\right)\right)\right)\frac{1}{T}\int_0^T\left|s(t)\right|^2\mathrm{d}t. \tag{4.4}$$

From (4.4), the location of main beam can be deduced as

$$\cos\theta=\cos\theta_{\mathrm{b}}+k\frac{\lambda}{d},k=-K,...,0,1,...,K. \tag{4.5}$$

k = 0 represents the location of the main lobe while k = 1, 2,…, K represent the location of grating lobes. It can be concluded from (4.2) and (4.5) that the clarity area can only be expanded by using arrays with narrow inter-elements spacing. However, smaller inter-element spacing can lead to a larger MBW, which can decrease the directivity of the antenna array. From (4.4) and (4.5), the maximum energy can be calculated as

$$P_{\max,\mathrm{r}}=\left(\sum_{n=1}^{N}w_n^2+2\sum_{n=1}^{N-1}\sum_{m=1}^{N-n}w_m w_{m+n}\right)\frac{1}{T}\int_0^T\left|s(t)\right|^2\mathrm{d}t. \tag{4.6}$$

The position of half power of the main beam can be calculated as

$$\cos\theta_{\mathrm{h}}-\cos\theta_{\mathrm{b}}\approx\pm\frac{\lambda}{2\pi d}\sqrt{\frac{2\sum_{n=1}^{N-1}p_n-q}{\sum_{n=1}^{N-1}n^2p_n}}$$
$$p_n=\sum_{m=1}^{N-n}w_m w_{m+n},n=1,2,...,N-1 \quad . \tag{4.7}$$
$$q=\sum_{n=1}^{N-1}\sum_{m=1}^{N-n}w_m w_{m+n}-\frac{1}{2}\sum_{n=1}^{N}w_n^2$$

The "≈" in (4.7) is used due to the Taylor Expansion. The MBW can be determined as

$$BW=\cos\theta_{\mathrm{l}}-\cos\theta_{\mathrm{r}}=\frac{\lambda}{\pi d}\sqrt{\frac{2\sum_{n=1}^{N-1}p_n-q}{\sum_{n=1}^{N-1}n^2p_n}}, \tag{4.8}$$

where $\left[\theta_{\mathrm{l}}\quad\theta_{\mathrm{r}}\right]$ represents the angle scope. The (4.7) and (4.8) give a conclusion that the MBW can be decreased with larger d and N. In addition, the weighting vector plays a windowing role, which can also influence the MBW. Due to the computational complexity, MSR will be derived only for the cases $N=3$ and $N=4$. Let's inspect the $N=3$ case firstly.

$$\theta_{\mathrm{s}}=\mathrm{LM}_{\theta}\left(\sum_{n=1}^{N-1}\left(\sum_{m=1}^{N-n}w_m w_{m+n}\cos\left(n\frac{2\pi d}{\lambda}(\cos\theta-\cos\theta_{\mathrm{b}})\right)\right)\right), \tag{4.9}$$

where "LM" represents Local Maximum operation. The derivation of (4.9) with respect to θ can be expressed as

$$\begin{aligned} & p_1 \sin\psi + 2p_2 \sin 2\psi = 0 \\ & \psi = \frac{2\pi d}{\lambda}\left(\cos\theta_s - \cos\theta_b\right) \end{aligned}. \tag{4.10}$$

p_1 and p_2 are from (4.7). Hence, position of the first side lobe can be expressed as

$$\cos\theta_s = \cos\theta_b \pm \frac{\lambda}{2\pi d}\arccos\left(-\frac{p_2}{4p_1}\right). \tag{4.11}$$

Then energy of the first side lobe can be determined as

$$\begin{aligned} & P_s = \left(\sum_{n=1}^{3} w_n^2 + 2\sum_{n=1}^{2}\left(\sum_{m=1}^{3-n} w_m w_{m+n}\cos(n\omega)\right)\right)\frac{1}{T}\int_0^T \left|s(t)\right|^2 \mathrm{dt} \\ & \omega = \arccos\left(-\frac{w_1 w_3}{4\left(w_1 w_2 + w_2 w_3\right)}\right) \end{aligned}. \tag{4.12}$$

Combining with (4.6), MSR can be calculated as

$$\mathrm{MSR}_{N=3} = \frac{P_{\max}}{P_s} = \frac{\sum_{n=1}^{3} w_n^2 + 2\sum_{n=1}^{2}\sum_{m=1}^{3-n} w_m w_{m+n}}{\sum_{n=1}^{3} w_n^2 + 2\sum_{n=1}^{2}\left(\sum_{m=1}^{3-n} w_m w_{m+n}\cos(n\omega)\right)}. \tag{4.13}$$

Now let us examine $N=4$ case. The derivation of (4.9) with respect to θ can be expressed as

$$\begin{aligned} & 12w_1 w_3 \cos^2\psi + 4\left(w_1 w_3 + w_2 w_4\right)\cos\psi - 2w_1 w_2 + w_2 w_3 + w_3 w_4 = 0 \\ & \cos\psi = \frac{-4\left(w_1 w_3 + w_2 w_4\right) \pm \sqrt{16\left(w_1 w_3 + w_2 w_4\right)^2 - 48 w_1 w_3\left(w_2 w_3 + w_3 w_4 - 2w_1 w_2\right)}}{24 w_1 w_3} \\ & = \beta \end{aligned}. \tag{4.14}$$

The position of the first side lobe can be expressed as

$$\cos\theta_s = \cos\theta_b \pm \frac{\lambda}{2\pi d}\arccos(\beta). \tag{4.15}$$

To reduce the computational complexity, first kind Chebshev polynomials are used. It defines

$$x = \frac{2\pi d}{\lambda}\left(\cos\theta - \cos\theta_b\right) = \arccos\alpha. \tag{4.16}$$

Then (4.9) can be rewritten as

$$\alpha_s = \underset{\alpha}{\mathrm{LM}}\left(p_1\alpha + p_2\left(2\alpha^2 - 1\right) + p_3\left(4\alpha^3 - 3\alpha\right)\right). \tag{4.17}$$

It is easy to get the local maximum positions from (4.17) that

$$\alpha_s = \frac{-4p_2 \pm \sqrt{16p_2^2 - 48p_3(p_1 - 3p_3)}}{24p_3} \tag{4.18}$$

Hence, MSR can be determined as

$$\mathrm{MSR}_{N=4} = \frac{P_{\max}}{P_s} = \frac{\sum_{n=1}^{4} w_n^2 + 2\sum_{n=1}^{3}\sum_{m=1}^{4-n} w_m w_{m+n}}{\sum_{n=1}^{4} w_n^2 + 2\sum_{n=1}^{3}\left(\sum_{m=1}^{4-n} w_m w_{m+n} \cos\left(n \arccos \alpha_s\right)\right)}. \tag{4.19}$$

(4.13) and (4.19) tell us that MSR depends on the number of antenna elements and the weighting vector but no inter-element spacing. In this research, a ULA with four antenna elements with inter-element spacing of approximate 4.4cm is used. (4.8) and (4.19) give two criterions to get the optimum weighting vector:

$$\begin{aligned} \boldsymbol{w}_{\mathrm{opt1}} &= \arg\min_{\boldsymbol{w}}\left(BW\right) \\ \boldsymbol{w}_{\mathrm{opt2}} &= \arg\max_{\boldsymbol{w}}\left(\mathrm{MSR}_{N=4}\right) \end{aligned}. \tag{4.20}$$

4.2.2 Calibration for the Phase Offset

Let us begin with a description of the hardware. The system consists of four WLAN receivers, each of which includes a RF frontend board, Virtex-5 FPGA (Field-Programmable Gate Array) module and a ULA. With four MAX2829 chips embedded in the RF frontend board, the receiver can transmit and receive OFDM signal from the ULA according to the 802.11a/g. After the down-mixture, the base band signal is digitalized using two Analog-to-Digital Converters (ADC). Finally, the digital signal is read by the FPGA module and transmitted to the server, on which a MATLAB program is running to perform the AoA estimation.

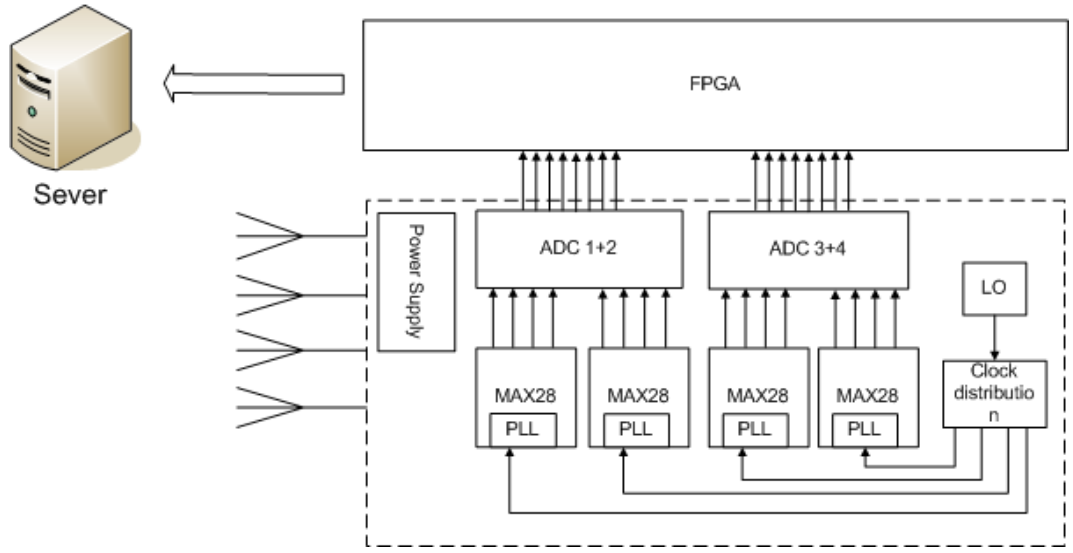

Figure 4.2: Block diagram of the WLAN receiver

Figure 4.2 illustrates the RF frontend and the base band signal processing module. One global Local Oscillator (LO) is deployed on each WLAN station to generate the reference clock with a constant phase offset while each MAX2829 is equipped with one independent Phase-Locked Loop (PLL). Ideally, the steady-state phase error shall be zero and each PLL shall output a clock with a constant phase offset since there is only one global LO. In practice, however, the average difference in time between the phases of two signals when the PLL has achieved lock is a random number. Therefore, phase offset caused by PLL is inevitable and that may seriously degrade the system performance. To mitigate the effect of phase jitter, initial calibration process shall be executed before localization. The calibration process consists of three parts:

1. Calibration of the phase offset generated by PLL
2. Calibration of the time offset generated by ADC
3. Signal power calibration

Figure 4.3 shows the calibration scenario

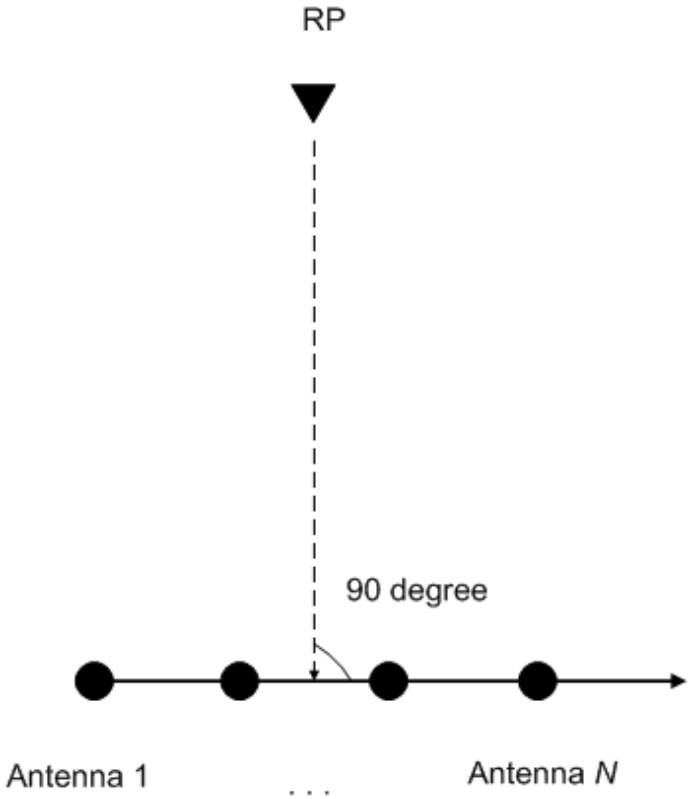

Figure 4.3: Initial calibration scenario

Before the localization process, each antenna element shall receive the signal transmitted from the WLAN transmitter located at the RP (see Figure 4.3). In the ideal case, each antenna element shall receive the signal with the same phase offset and time offset. With PLL phase offset, the received signal can be expressed as

$$\begin{aligned} r_n(t) &= a_n s(t-t_n) e^{j\phi_n} + w_n(t) \\ &= a_n e^{j\phi_n} \sum_{k=1}^{K} \underline{d}_k \exp\left(-j2\pi f_k (t-t_n)\right) + w_n(t) \end{aligned}, \tag{4.21}$$

where t_n , ϕ_n and a_n are the time offset, phase offset and power scaling factor, respectively. $w_n(t)$ is the additive Gaussian noise. The Cross Correlation Function (CCF) of two received signals can be written as

$$\begin{aligned} c_{n,m}(\Delta t) &= \frac{1}{T_s}\int_{-T_s/2}^{T_s/2} r_n^*(\tau) r_m(\tau+\Delta t)\,\mathrm{d}t \\ &= a_n a_m e^{j(\phi_m-\phi_n)}\frac{1}{T_s}\sum_{k=1}^{K}\int_{-T_s/2}^{T_s/2}\left|\underline{d}_k\right|^2 \exp\left(j2\pi f_k\left(t_m-t_n-\Delta t\right)\right)\mathrm{d}\tau+\sigma_n^2 \end{aligned} . \tag{4.22}$$

It is obvious that the absolute value of $c_{n,m}(\Delta t)$ will reach the maximum point if $\Delta t = t_m - t_n$. It denotes that the relative time offset between two adjacent antenna elements can be determined by the second-order statistics. Hence, the time offset of each channel can be calculated as

$$\begin{aligned} &\boldsymbol{t} = \boldsymbol{H}^{\dagger}\boldsymbol{\Delta t} \\ &\boldsymbol{H} = \underbrace{\begin{bmatrix} 1 & -1 & \cdots & 0 \\ 0 & 1 & \cdots & -1 \\ \vdots & \vdots & \ddots & \vdots \\ 1 & 0 & \cdots & -1 \end{bmatrix}}_{N}\Bigg\}\begin{pmatrix} 2 \\ N \end{pmatrix} \\ &\boldsymbol{t} = \begin{bmatrix} t_1 & t_2 & \cdots & t_N \end{bmatrix}^{\mathrm{T}} \\ &\boldsymbol{\Delta t} = \begin{bmatrix} \Delta t_1 & \Delta t_2 & \cdots & \Delta t_{\binom{2}{N}} \end{bmatrix}^{\mathrm{T}} \end{aligned} . \tag{4.23}$$

$\boldsymbol{H}^{\dagger}$ in (4.23) is the pseudo inverse of $\boldsymbol{H}$, which is a sparse matrix containing only 1 and -1. The relative phase offset can be determined by

$$\phi_m - \phi_n = \mathrm{angle}\left(\max\left(c_{n,m}(\Delta t)\right)\right). \tag{4.24}$$

The received signals shall have the same power as the distance between RP and the ULA is much larger than the inter-element spacing

$$\begin{aligned} &\frac{1}{T_s}\int_{-T_s/2}^{T_s/2}\left|r_n(t)\right|^2\mathrm{d}t = \frac{1}{T_s}\int_{-T_s/2}^{T_s/2}\left|r_m(t)\right|^2\mathrm{d}t \\ &\frac{1}{T_s}\int_{-T_s/2}^{T_s/2}\left|r_n(t)\right|^2\mathrm{d}t = \left|a_n\right|^2\sum_{k=1}^{K}\left|\underline{d}_k\right|^2+\sigma_n^2 \\ &\frac{1}{T_s}\int_{-T_s/2}^{T_s/2}\left|r_m(t)\right|^2\mathrm{d}t = \left|a_m\right|^2\sum_{k=1}^{K}\left|\underline{d}_k\right|^2+\sigma_m^2 \end{aligned} . \tag{4.25}$$

Hence, the relative power scaling factor can be expressed as

$$p_{nm} = \frac{\left|a_n\right|^2}{\left|a_m\right|^2} \approx \frac{\int_{-T_s/2}^{T_s/2}\left|r_n(t)\right|^2\mathrm{d}t}{\int_{-T_s/2}^{T_s/2}\left|r_m(t)\right|^2\mathrm{d}t} . \tag{4.26}$$

4.2.3 Implemented AoA Estimation Algorithms

Beamforming and MUSIC approaches are the most popular algorithms to estimate the AoA. A conventional beamformer can be considered as a spatial filter, which emphasizes the signal from a particular direction and suppress those from other directions by weighing process. In this research, the author uses conventional beamformer to sum up the weighted signal from regular spatial sampled direction which can be written as

$$\cos\boldsymbol{\theta}_{\mathrm{b}} = \left[-\frac{\lambda}{2d} \quad -\frac{\lambda}{2d} + \frac{\lambda}{(M-1)d} \quad \cdots \quad \frac{\lambda}{2d} \right]. \tag{4.27}$$

(4.27) denotes that the clarity area is regular spatial sampled into M specific desired directions toward which the beamformer is steered. The digitalized received data matrix can be expressed as

$$\underline{\boldsymbol{R}} = \left[\underline{\boldsymbol{r}}_1 \quad \underline{\boldsymbol{r}}_2 \quad \cdots \quad \underline{\boldsymbol{r}}_N \right], \tag{4.28}$$

which consists of N data vector with L data points. After the initial calibration process, $\underline{\boldsymbol{R}}_{\mathrm{c}}$ can be determined as

$$\begin{aligned}
&\underline{\boldsymbol{R}}_{\mathrm{c}} = \underline{\boldsymbol{R}}^{'}\underline{\boldsymbol{\varphi}} \\
&\underline{\boldsymbol{R}}^{'} = \left[p_{11}\underline{\boldsymbol{r}}_1^{'} \quad p_{12}\underline{\boldsymbol{r}}_2^{'} \quad \cdots \quad p_{1N}\underline{\boldsymbol{r}}_N^{'} \right] \\
&\underline{\boldsymbol{r}}_n^{'} = IFFT\left(FFT\left(\underline{\boldsymbol{E}}\underline{\boldsymbol{r}}_n \right) \right) \\
&\underline{\boldsymbol{\varphi}} = \begin{bmatrix} \mathrm{e}^{-j\phi_1} & 0 & \cdots & 0 \\ 0 & \mathrm{e}^{-j\phi_2} & \cdots & 0 \\ 0 & 0 & \ddots & 0 \\ 0 & 0 & \cdots & \mathrm{e}^{-j\phi_N} \end{bmatrix} \\
&\underline{\boldsymbol{E}} = \mathrm{diag}\left[1 \quad e^{j\frac{2\pi t_n}{L}} \quad \cdots \quad e^{j\frac{2\pi(L-1)t_n}{L}} \right]
\end{aligned} \tag{4.29}$$

Making $L \times M$ points two dimensional FFT operation on $\underline{\boldsymbol{R}}_{\mathrm{c}}$, it has

$$\begin{aligned}
\underline{\boldsymbol{F}}[u,v] &= \frac{1}{\sqrt{ML}} \sum_{m=0}^{M-1} \sum_{l=0}^{L-1} \underline{\boldsymbol{R}}_{\mathrm{c}}[m,l] \mathrm{e}^{-j2\pi\left(\frac{lv}{L}+\frac{mu}{M}\right)} \\
&= \frac{1}{\sqrt{M}} \left(\mathrm{FFT}_M \left(\left[\underline{\boldsymbol{r}}_1^{\mathrm{F}} \quad \underline{\boldsymbol{r}}_2^{\mathrm{F}} \quad \cdots \quad \underline{\boldsymbol{r}}_N^{\mathrm{F}} \right]^{\mathrm{T}} \right) \right)^{\mathrm{T}}
\end{aligned}, \tag{4.30}$$

where

$$\underline{\boldsymbol{r}}_n^{\mathrm{F}} = \frac{1}{\sqrt{L}} \mathrm{FFT}_L \left(p_{1n}\underline{\boldsymbol{r}}_n^{'} \right). \tag{4.31}$$

"FFT_L" denotes L-points FFT operation. The row vectors in $\underline{\boldsymbol{F}}$ give the information about the relative phase offset between two channels:

$$\Delta\phi = \frac{2\pi d \cos\theta_{\mathrm{i}}}{\lambda} = 2\pi \frac{v_{\mathrm{m}}}{M}$$
$$v_{\mathrm{m}} = \arg\max_{v} \left(\left(\sum_{u=1}^{L} \underline{\boldsymbol{F}}[u,v] \right)^2 \right). \tag{4.32}$$

The incoming angle θ_{i} can be easily determined by (4.32). It is obvious that the two dimensional FFT based conventional beamformer has the lower computational complexity. Subspace based approaches (MUSIC, root MUSIC and ESPRIT) are already known and investigated in many literatures. MUSIC can provide asymptotically unbiased estimation about number of present incident wave front and AoA. Root MUSIC is a variation of MUSIC, which is based on a polynomial formulation of the spectral search facilitated by the ULA structure. The signal zeros are found by their proximity to the unit circle. The performance and advantages over MUSIC has been discussed in [94]. In this research, the performance of AoA estimation via two dimensional FFT based conventional beamformer, MUSIC and root MUSIC are investigated and compared to each other und the dense multipath scenario.

4.3 Multi Path Components (MPC) Suppression

4.3.1 Perturbation Suppression

From the perturbation analysis in subchapter 2.3.10, we can conclude that the perturbation can be suppressed if the MPC information is available. Subspace approach requires $\underline{\boldsymbol{P}}$ being signal subspace, which is no more valid if $\underline{\boldsymbol{P}}$ is a square or fat matrix. Hence, some MPC portions shall be subtracted from the received signal in order to keep $\underline{\boldsymbol{P}}$ being a tall matrix. Let us define $\left(\hat{\underline{a}}_{1,n}, \cdots \hat{\underline{a}}_{L,n}; \hat{\tau}_1, \cdots \hat{\tau}_L\right)$ as the estimated decay factors and delays for the L resolvable paths at n-th antenna element, where $N \le L$. Subtracting the MPC portions $l = N \cdots L$ at each antenna element, (2.70) can be rewritten as

$$\underline{\boldsymbol{r}}'(t) = \underline{\boldsymbol{P}}' \boldsymbol{s}'(t) + \boldsymbol{n}(t), \tag{4.33}$$

where

$$\underline{\boldsymbol{r}}'(t) = \begin{bmatrix} \underline{r}_1(t) - \sum_{l=N}^{L} \hat{\underline{a}}_{l,1} s(t-\tau_{l,1}) \\ \vdots \\ \underline{r}_N(t) - \sum_{l=N}^{L} \hat{\underline{a}}_{l,N} s(t-\tau_{l,N}) \end{bmatrix}, \underline{\boldsymbol{P}}' = \begin{bmatrix} 1 & \cdots & 1 \\ \vdots & \ddots & \vdots \\ e^{j(N-1)\phi_1} & \cdots & e^{j(N-1)\phi_{N-1}} \end{bmatrix}.$$
$$\boldsymbol{s}'(t) = \begin{bmatrix} \underline{a}_1 s(t-\tau_1) \\ \vdots \\ \underline{a}_{N-1} s(t-\tau_{N-1}) \end{bmatrix} \tag{4.34}$$

In (4.34), $\underline{\boldsymbol{P}}^{'}$ becomes a tall matrix, which lets the determination of signal subspace become easy. Via ML method, (2.70) can be rearranged as

$$\begin{bmatrix}\underline{\boldsymbol{r}}_1 & \cdots & \underline{\boldsymbol{r}}_N\end{bmatrix}=\begin{bmatrix}\hat{\underline{a}}_1\hat{\boldsymbol{s}}_1 & \cdots & \hat{\underline{a}}_L\hat{\boldsymbol{s}}_L\end{bmatrix}\begin{bmatrix}1 & \cdots & e^{j(N-1)\varphi_1}\\ \vdots & \ddots & \vdots\\ 1 & \cdots & e^{j(N-1)\varphi_L}\end{bmatrix}+\begin{bmatrix}\underline{\boldsymbol{n}}_1 & \cdots & \underline{\boldsymbol{n}}_N\end{bmatrix}, \tag{4.35}$$

where $\underline{\boldsymbol{r}}_{n,n=1\cdots N}$ is the digitalized $r(t)$ at the n-th antenna element and $\hat{\boldsymbol{s}}_{l,l=1\cdots L}$ is the digitalized $s\left(t-\hat{\tau}_l\right)$. Summing each received vector up, it has

$$\sum_{n=1}^{N}\underline{\boldsymbol{r}}_n=\begin{bmatrix}\hat{\underline{a}}_1\hat{\boldsymbol{s}}_1 & \cdots & \hat{\underline{a}}_L\hat{\boldsymbol{s}}_L\end{bmatrix}\begin{bmatrix}1+\sum_{n=1}^{N-1}e^{jn\varphi_1}\\ \vdots\\ 1+\sum_{n=1}^{N-1}e^{jn\varphi_L}\end{bmatrix}+\sum_{n=1}^{N}\underline{\boldsymbol{n}}_n\,. \tag{4.36}$$

Define

$$\underline{\boldsymbol{r}}^{'}=\sum_{n=1}^{N}\underline{\boldsymbol{r}}_n,\underline{\boldsymbol{H}}^{'}=\begin{bmatrix}\hat{\underline{a}}_1\hat{\boldsymbol{s}}_1 & \hat{\underline{a}}_2\hat{\boldsymbol{s}}_2 & \cdots & \hat{\underline{a}}_L\hat{\boldsymbol{s}}_L\end{bmatrix}$$

$$\underline{\boldsymbol{w}}^{'}=\sum_{n=1}^{N}\underline{\boldsymbol{w}}_n,\underline{\boldsymbol{\varphi}}^{'}=\begin{bmatrix}1+\sum_{n=1}^{N-1}e^{jn\varphi_1}\\ 1+\sum_{n=1}^{N-1}e^{jn\varphi_2}\\ \vdots\\ 1+\sum_{n=1}^{N-1}e^{jn\varphi_L}\end{bmatrix}\,. \tag{4.37}$$

Thus, the phase vector can be estimated via ML

$$\underline{\boldsymbol{\varphi}}^{'}=\left(\underline{\boldsymbol{H}}^{'\mathrm{H}}\underline{\boldsymbol{R}}_{w}^{-1}\underline{\boldsymbol{H}}^{'}\right)^{-1}\underline{\boldsymbol{R}}_{w}^{-1}\underline{\boldsymbol{H}}^{'\mathrm{H}}\underline{\boldsymbol{r}}^{'}\,. \tag{4.38}$$

Adaptive sampling rate shall be selected to keep $\underline{\boldsymbol{H}}^{'}$ being a tall matrix. To suppress the perturbation, $\left(\hat{\underline{a}}_{1,n},\cdots\hat{\underline{a}}_{L,n};\hat{\tau}_1,\cdots\hat{\tau}_L\right)$ shall be known to the receiver.

4.3.2 Novel OFDM Channel Estimator

Suppose that the transmitter transmits OFDM signal, which conforms to 802.11a standard. Due to the narrow band characteristics, the OFDM signal shall be oversampled to enhance the multipath resolution. The double-sided bandwidth of WLAN signal is 20MHz, which lets the multipath resolution be approximate 50ns without oversampling. The ADCs on the main board can provide sampling rate of 80MHz, which denotes that the oversampling rate (OSR) is equal to four. Before the channel estimation, the Carrier Frequency Offset (CFO) shall be estimated. [99] introduces Non-Data-Aided CFO estimation with the consideration of CFO identifiability. However, computational effort will increase rapidly if the number of subcarriers goes high as it requires decomposing the covariance matrix to find its null

space. [100] and [101] describe the effective method, which exploits the virtual carriers to find the null spectra. However, the identifiability and the method to select the estimated CFO under the frequency selective channel are not described in them. In this research, the author proposes preamble-aided null-carrier CFO estimation approach, which requires lower computational complexity. CFO identifiability is also considered in the model. It defines $\underline{\boldsymbol{d}}_{\mathrm{s}}=\left[\underline{d}_{\mathrm{s},1}\quad \underline{d}_{\mathrm{s},2}\quad \cdots\quad \underline{d}_{\mathrm{s},N}\right]^{\mathrm{T}}$ and $\underline{\boldsymbol{d}}_{\mathrm{l}}=\left[\underline{d}_{\mathrm{l},1}\quad \underline{d}_{\mathrm{l},2}\quad \cdots\quad \underline{d}_{\mathrm{l},N}\right]^{\mathrm{T}}$ as the short preamble and long preamble vectors in Frequency Domain (FD), respectively. According to 802.11a, $\underline{\boldsymbol{d}}_{\mathrm{s}}$ and $\underline{\boldsymbol{d}}_{\mathrm{l}}$ contain P subcarriers and N-P null carriers, respectively. By the N_{s}-points IFFT (Inverse Fast Fourier Transform) operation, the preamble vector with the length of $N_{\mathrm{p}}=5N_{\mathrm{s}}$ in Time Domain (TD) can be expressed as

$$\begin{aligned}
&\underline{\boldsymbol{s}}_{\mathrm{t}}=\left[\left(\underline{\boldsymbol{M}}_{\mathrm{s}}\underline{\boldsymbol{d}}_{\mathrm{s}}\right)^{\mathrm{T}}\quad\left(\underline{\boldsymbol{M}}_{\mathrm{l}}\underline{\boldsymbol{d}}_{\mathrm{l}}\right)^{\mathrm{T}}\right]^{\mathrm{T}}\\
&=\left[\underline{s}_{0,\mathrm{t}}\quad \underline{s}_{1,\mathrm{t}}\quad \cdots\quad \underline{s}_{N_{\mathrm{p}}-1,\mathrm{t}}\right]\\
&\underline{\boldsymbol{M}}_{\mathrm{s}}=\begin{bmatrix}\underline{\boldsymbol{W}}_{N_{\mathrm{s}}\times N}\\ \underline{\boldsymbol{W}}_{N_{\mathrm{s}}\times N}\\ \left[\underline{\boldsymbol{I}}_{N_{\mathrm{s}}/2}\quad \boldsymbol{0}\right]\underline{\boldsymbol{W}}_{N_{\mathrm{s}}\times N}\end{bmatrix},\underline{\boldsymbol{M}}_{\mathrm{l}}=\begin{bmatrix}\left[\boldsymbol{0}\quad \underline{\boldsymbol{I}}_{N_{\mathrm{s}}/2}\right]\underline{\boldsymbol{W}}_{N_{\mathrm{s}}\times N}\\ \underline{\boldsymbol{W}}_{N_{\mathrm{s}}\times N}\\ \underline{\boldsymbol{W}}_{N_{\mathrm{s}}\times N}\end{bmatrix}
\end{aligned},\tag{4.39}$$

where $\underline{\boldsymbol{W}}_{N_{\mathrm{s}}\times N}$ is the $N_{\mathrm{s}}\times N$ IFFT matrix and $\underline{\boldsymbol{I}}_{N_{\mathrm{s}}/2}$ is the identity matrix with $N_{\mathrm{s}}/2$ elements, which is used to insert the Cyclic Prefix (CP). It assumes that the length of CP is larger than channel excess delay so that the Inter Carrier Interference (ICI) and Inter Symbol Interference (ISI) can be mitigated at the receiver. Through a time invariant frequency selective channel, the received preamble vector can be expressed as

$$\begin{aligned}
&\underline{\boldsymbol{s}}_{\mathrm{r}}=e^{j\Delta\theta}\underline{\boldsymbol{D}}_{N_{\mathrm{p}}}\underline{\boldsymbol{H}}_{\mathrm{t}}\underline{\boldsymbol{s}}_{\mathrm{t}}+\underline{\boldsymbol{w}}\\
&=e^{j\Delta\theta}\underline{\boldsymbol{D}}_{N_{\mathrm{p}}}\underline{\boldsymbol{H}}_{\mathrm{t}}\begin{bmatrix}\underline{\boldsymbol{M}}_{\mathrm{s}}\underline{\boldsymbol{d}}_{\mathrm{s}}\\ \underline{\boldsymbol{M}}_{\mathrm{l}}\underline{\boldsymbol{d}}_{\mathrm{l}}\end{bmatrix}+\underline{\boldsymbol{w}}\\
&=\left[\underline{s}_{0,\mathrm{r}}\quad \underline{s}_{1,\mathrm{r}}\quad \cdots\quad \underline{s}_{N_{\mathrm{p}}-1,\mathrm{r}}\right]^{\mathrm{T}}\\
&\underline{\boldsymbol{D}}_{N_{\mathrm{p}}}=\mathrm{diag}\left(\left[1\quad e^{j2\pi\Delta fT_{\mathrm{s}}}\quad \cdots\quad e^{j2\pi\Delta f\left(N_{\mathrm{p}}-1\right)T_{\mathrm{s}}}\right]\right)
\end{aligned},\tag{4.40}$$

where $\underline{\boldsymbol{D}}_{N_{\mathrm{p}}}$ is a $N_{\mathrm{p}}\times N_{\mathrm{p}}$ diagonal matrix containing the CFO Δf. $\Delta\theta$ is the constant phase offset caused by the imperfect time synchronization between signal carrier and the local oscillator. T_{s} is the sampling duration. $\underline{\boldsymbol{H}}_{t}$ is a Toeplitz matrix, which owns the size of $\left(N_{\mathrm{p}}+L-1\right)\times N_{\mathrm{p}}$ and its first column is $\left[\underline{h}_{0,t}\quad \underline{h}_{1,t}\quad \cdots\quad \underline{h}_{L-1,t}\quad 0\quad \cdots\quad 0\right]^{\mathrm{T}}$. L is the order of CIR and $\underline{h}_{l,t}$ is discrete-time expression of CIR. To mitigate the ISI and ICI caused by multipath channel, the CP shall be removed with a removing matrix $\underline{\boldsymbol{R}}_{\mathrm{cp}}$. It assumes that $L<N_{\mathrm{s}}/2$, which denotes interference post on the n-th OFDM symbol can only come from the (n-1)-th symbol and the long OFDM block suffers no interference from the short one due to its guard period. From (4.39), it can be seen that the short preamble block consists of two same consecutive OFDM symbol

followed by first half block. The long one contains second half OFDM symbol (CP) followed by two same consecutive OFDM symbols. To overcome the frequency selective effect on first short OFDM block, $\underline{\boldsymbol{s}}_{\mathrm{t}}$ shall be cut into: $\underline{\boldsymbol{s}}_{\mathrm{t},i}=\left[\underline{s}_{N_{\mathrm{s}}/2+(i-1)N_{\mathrm{s}},\mathrm{t}} \quad \underline{s}_{N_{\mathrm{s}}/2+(i-1)N_{\mathrm{s}}+1,\mathrm{t}} \quad \cdots \quad \underline{s}_{N_{\mathrm{s}}/2+iN_{\mathrm{s}}-1,\mathrm{t}}\right]^{\mathrm{T}}, i=1,2$ and $\underline{\boldsymbol{s}}_{\mathrm{t},i}=\left[\underline{s}_{3N_{\mathrm{s}}+(i-3)N_{\mathrm{s}},\mathrm{t}} \quad \underline{s}_{3N_{\mathrm{s}}+(i-3)N_{\mathrm{s}}+1,\mathrm{t}} \quad \cdots \quad \underline{s}_{3N_{\mathrm{s}}+(i-2)N_{\mathrm{s}}-1,\mathrm{t}}\right]^{\mathrm{T}}, i=3,4$. The $\underline{\boldsymbol{s}}_{\mathrm{r}}$ in (4.40) can be cut into

$$\begin{aligned}\underline{\boldsymbol{s}}_{\mathrm{r},i}&=\begin{cases}e^{j\left(2\pi\Delta f\left(N_{\mathrm{s}}/2+(i-1)N_{\mathrm{s}}\right)T_{\mathrm{s}}+\Delta\theta\right)}\underline{\boldsymbol{D}}_{N_{\mathrm{p}},i}\underline{\boldsymbol{H}}_{\mathrm{t},i}\underline{\boldsymbol{s}}_{\mathrm{t},i}+\underline{\boldsymbol{w}}_i, i=1,2\\ e^{j\left(2\pi\Delta f\left(3N_{\mathrm{s}}+(i-3)N_{\mathrm{s}}\right)T_{\mathrm{s}}+\Delta\theta\right)}\underline{\boldsymbol{D}}_{N_{\mathrm{p}},i}\underline{\boldsymbol{H}}_{\mathrm{t},i}\underline{\boldsymbol{s}}_{\mathrm{t},i}+\underline{\boldsymbol{w}}_i, i=3,4\end{cases},\\ \underline{\boldsymbol{D}}_{N_{\mathrm{s}},i}&=\mathrm{diag}\left(\left[1 \quad e^{j2\pi\Delta fT_{\mathrm{s}}} \quad \cdots \quad e^{j2\pi\Delta f\left(N_{\mathrm{s}}-1\right)T_{\mathrm{s}}}\right]\right)\end{aligned} \tag{4.41}$$

where $\underline{\boldsymbol{H}}_{\mathrm{t},i}$ is circulant matrix with the size of $N_{\mathrm{s}}\times N_{\mathrm{s}}$ and the first column of $\underline{\boldsymbol{H}}_{\mathrm{t},i}$ is $\underbrace{\left[\underline{h}_{0,t} \quad \underline{h}_{1,t} \quad \cdots \quad \underline{h}_{L-1,t} \quad 0 \quad \cdots \quad 0\right]^{\mathrm{T}}}_{N_{\mathrm{s}}}$. From (4.41), it can get

$$\begin{aligned}\underline{\boldsymbol{s}}_{r,\mathrm{m1}}&=\frac{1}{2}\left(\underline{\boldsymbol{s}}_{r,1}+\underline{\boldsymbol{s}}_{r,2}\right)\\ &=\frac{1}{2}e^{j\left(2\pi\Delta f\frac{N_{\mathrm{s}}}{2}T_{\mathrm{s}}+\Delta\theta\right)}\left(1+e^{j2\pi\Delta fN_{\mathrm{s}}T_{\mathrm{s}}}\right)\underline{\boldsymbol{D}}_{N_{\mathrm{s}},1}\underline{\boldsymbol{H}}_{\mathrm{t},1}\underline{\boldsymbol{s}}_{\mathrm{t},1}+\underline{\boldsymbol{w}}'\\ \underline{\boldsymbol{s}}_{r,\mathrm{m3}}&=\frac{1}{2}\left(\underline{\boldsymbol{s}}_{r,3}+\underline{\boldsymbol{s}}_{r,4}\right)\\ &=\frac{1}{2}e^{j\left(2\pi\Delta f3N_{\mathrm{s}}T_{\mathrm{s}}+\Delta\theta\right)}\left(1+e^{j2\pi\Delta fN_{\mathrm{s}}T_{\mathrm{s}}}\right)\underline{\boldsymbol{D}}_{N_{\mathrm{s}},3}\underline{\boldsymbol{H}}_{\mathrm{t},3}\underline{\boldsymbol{s}}_{\mathrm{t},3}+\underline{\boldsymbol{w}}'\end{aligned}. \tag{4.42}$$

Due to the uncorrelated characteristics of short preamble and long preamble, $\underline{\boldsymbol{s}}_{r,\mathrm{m1}}$ and $\underline{\boldsymbol{s}}_{r,\mathrm{m2}}$ are two uncorrelated vectors containing a unique Δf. It denotes that the freedom of estimation Δf from two vectors is two. The next task is to estimate Δf from each received vector and then compare them to each other. If $\Delta\widehat{f}_1\neq\Delta\widehat{f}_2$, it denotes these two values are not correct. $\underline{\boldsymbol{H}}_{\mathrm{t},1}$ and $\underline{\boldsymbol{H}}_{\mathrm{t},3}$ are circulant matrices, which can be diagonalized by FFT matrix. Hence, (4.42) can be rewritten as

$$\begin{aligned}\underline{\boldsymbol{s}}_{\mathrm{r,m1}}&=c_1\underline{\boldsymbol{D}}_{N_{\mathrm{s}},1}\underline{\boldsymbol{W}}_{N_{\mathrm{s}}\times N_{\mathrm{s}}}\underline{\boldsymbol{H}}_{\mathrm{f},1}\underline{\boldsymbol{W}}^{\mathrm{H}}_{N_{\mathrm{s}}\times N_{\mathrm{s}}}\underline{\boldsymbol{s}}_{\mathrm{t},1}+\underline{\boldsymbol{w}}'\\ \underline{\boldsymbol{s}}_{\mathrm{r,m3}}&=c_3\underline{\boldsymbol{D}}_{N_{\mathrm{s}},3}\underline{\boldsymbol{W}}_{N_{\mathrm{s}}\times N_{\mathrm{s}}}\underline{\boldsymbol{H}}_{\mathrm{f},3}\underline{\boldsymbol{W}}^{\mathrm{H}}_{N_{\mathrm{s}}\times N_{\mathrm{s}}}\underline{\boldsymbol{s}}_{\mathrm{t},3}+\underline{\boldsymbol{w}}'\\ \underline{\boldsymbol{H}}_{\mathrm{f},1}&=\mathrm{diag}\left(\underline{\boldsymbol{W}}^{\mathrm{H}}_{N_{\mathrm{s}}\times N_{\mathrm{s}}}\underline{\boldsymbol{H}}_{\mathrm{t},1}\boldsymbol{e}_1^{\mathrm{H}}\right),\underline{\boldsymbol{H}}_{\mathrm{f},3}=\mathrm{diag}\left(\underline{\boldsymbol{W}}^{\mathrm{H}}_{N_{\mathrm{s}}\times N_{\mathrm{s}}}\underline{\boldsymbol{H}}_{\mathrm{t},3}\boldsymbol{e}_1^{\mathrm{H}}\right).\\ c_1&=\frac{1}{2N_{\mathrm{s}}}e^{j\left(2\pi\Delta f\frac{N_{\mathrm{s}}}{2}T_{\mathrm{s}}+\Delta\theta\right)}\left(1+e^{j2\pi\Delta fN_{\mathrm{s}}T_{\mathrm{s}}}\right)\\ c_3&=\frac{1}{2N_{\mathrm{s}}}e^{j\left(2\pi\Delta f3N_{\mathrm{s}}T_{\mathrm{s}}+\Delta\theta\right)}\left(1+e^{j2\pi\Delta fN_{\mathrm{s}}T_{\mathrm{s}}}\right)\end{aligned} \tag{4.43}$$

$\boldsymbol{e}_1^{\mathrm{H}}$ is the unit column vector whose first element is equal to one. $\underline{\boldsymbol{s}}_{\mathrm{t},1}$ is a circulant shift vector of the short preamble block in TD and $\underline{\boldsymbol{s}}_{\mathrm{t},1}=\underline{\boldsymbol{s}}_{\mathrm{t},2}$. Hence, $\underline{\boldsymbol{s}}_{\mathrm{r,m1}}$ can be rewritten as

$$\begin{aligned}\underline{\boldsymbol{s}}_{\mathrm{r,m1}} &= c_1 \underline{\boldsymbol{D}}_{N_\mathrm{s},1} \underline{\boldsymbol{W}}_{N_\mathrm{s}\times N_\mathrm{s}} \underline{\boldsymbol{H}}_{\mathrm{f},1} \underline{\boldsymbol{W}}^{\mathrm{H}}_{N_\mathrm{s}\times N_\mathrm{s}} \underline{\boldsymbol{W}}_{N_\mathrm{s}\times N} \underline{\boldsymbol{E}}_N \underline{\boldsymbol{d}}_\mathrm{s} + \underline{\boldsymbol{w}}' \\ \underline{\boldsymbol{E}}_N &= \mathrm{diag}\left(\begin{bmatrix} 1 & e^{j\frac{\pi N_\mathrm{s}}{4N}} & \cdots & e^{j\frac{(N-1)\pi N_\mathrm{s}}{4N}} \end{bmatrix}\right)\end{aligned} . \tag{4.44}$$

As the OSR is an integer number, $\underline{\boldsymbol{W}}^{\mathrm{H}}_{N_\mathrm{s}\times N_\mathrm{s}} \underline{\boldsymbol{W}}_{N_\mathrm{s}\times N}$ can be considered as an N-rank matrix containing an $N\times N$ identity sub-matrix $\underline{\boldsymbol{I}}_N$ and a $(N_\mathrm{s}-N)\times N$ sub-matrix $\underline{\boldsymbol{R}}_{(N_\mathrm{s}-N)\times N}$, which is used to oversample the vector $\underline{\boldsymbol{E}}_N \underline{\boldsymbol{d}}_\mathrm{s}$. Recall that $\underline{\boldsymbol{d}}_\mathrm{s}$ contains N_v virtual carriers and $N-N_\mathrm{v}$ subcarriers in order to avoid the transmit filtering and $\underline{\boldsymbol{d}}_\mathrm{s}$ shall be filtered by $\underline{\boldsymbol{H}}_{\mathrm{f},1} \underline{\boldsymbol{W}}^{\mathrm{H}}_{N_\mathrm{s}\times N_\mathrm{s}} \underline{\boldsymbol{W}}_{N_\mathrm{s}\times N} \underline{\boldsymbol{E}}_N$ containing a diagonal sub-matrix because of the diagonal characteristics of $\underline{\boldsymbol{H}}_{\mathrm{f},1}$. It obtains the filter output $\underline{\boldsymbol{d}}'_\mathrm{s} = \underline{\boldsymbol{H}}_{\mathrm{f},1} \underline{\boldsymbol{W}}^{\mathrm{H}}_{N_\mathrm{s}\times N_\mathrm{s}} \underline{\boldsymbol{W}}_{N_\mathrm{s}\times N} \underline{\boldsymbol{E}}_N \underline{\boldsymbol{d}}_\mathrm{s}$ which contains at least N_v virtual carriers. The virtual carriers is reordered to the positions of $N_\mathrm{s}-N_\mathrm{v}+1$ to N_s and $\underline{\boldsymbol{W}}_{N_\mathrm{s}\times N_\mathrm{s}}$ is reordered to $\underline{\boldsymbol{W}}'_{N_\mathrm{s}\times N_\mathrm{s}} = \left[\underline{\boldsymbol{W}}'_{N_\mathrm{s}\times(N_\mathrm{s}-N_\mathrm{v}),\mathrm{s}} \quad \underline{\boldsymbol{W}}'_{N_\mathrm{s}\times N_\mathrm{v},\mathrm{n}}\right]$, where $\underline{\boldsymbol{W}}'_{N_\mathrm{s}\times(N_\mathrm{s}-N_\mathrm{v}),\mathrm{s}}$ and $\underline{\boldsymbol{W}}'_{N_\mathrm{s}\times N_\mathrm{v},\mathrm{n}}$ are the signal subspace and null space, respectively. Recalling that $\underline{\boldsymbol{W}}'_{N_\mathrm{s}\times(N_\mathrm{s}-N_\mathrm{v}),\mathrm{s}}$ is orthogonal to $\underline{\boldsymbol{W}}'_{N_\mathrm{s}\times N_\mathrm{v},\mathrm{n}}$, it can get

$$\underline{\boldsymbol{s}}^{\mathrm{H}}_{\mathrm{r,m1}} \underline{\boldsymbol{W}}'_{N_\mathrm{s}\times N_\mathrm{v},\mathrm{n}} \underline{\boldsymbol{W}}^{\mathrm{H}'}_{N_\mathrm{s}\times N_\mathrm{v},\mathrm{n}} \underline{\boldsymbol{s}}_{\mathrm{r,m1}} = 0, \tag{4.45}$$

if $\underline{\boldsymbol{D}}_{N_\mathrm{s},1}$ is an identity matrix ($\Delta f = 0$) and SNR is large enough. Under the case of $\Delta f \neq 0$ and SNR is relative small, Δf_1 can be estimated through $\underline{\boldsymbol{s}}_{r,\mathrm{m1}}$:

$$\begin{aligned}\widehat{\Delta \boldsymbol{f}}_1 &= \arg\min_{\Delta f}\left(\underline{\boldsymbol{D}}^{\mathrm{H}'}_{N_\mathrm{s},1} \underline{\boldsymbol{s}}^{\mathrm{H}}_{\mathrm{r,m1}} \underline{\boldsymbol{W}}'_{N_\mathrm{s}\times N_\mathrm{v},\mathrm{n}} \underline{\boldsymbol{W}}^{\mathrm{H}'}_{N_\mathrm{s}\times N_\mathrm{v},\mathrm{n}} \underline{\boldsymbol{s}}_{\mathrm{r,m1}} \underline{\boldsymbol{D}}'_{N_\mathrm{s},1}\right) \\ \underline{\boldsymbol{D}}'_{N_\mathrm{s},1} &= \mathrm{diag}\left(\begin{bmatrix} 1 & e^{-j2\pi\Delta f T_\mathrm{s}} & \cdots & e^{-j2\pi\Delta f (N_\mathrm{s}-1)T_\mathrm{s}} \end{bmatrix}\right)\end{aligned} . \tag{4.46}$$

The (4.46) gives the root MUSIC approach, which chooses the $N_\mathrm{s}-N_\mathrm{v}$ roots closet to the unit circle. It is clear that (4.46) is an $2N_\mathrm{s}$ - order polynomial, which has an extremely high computational cost if MUSIC polynomial is employed. A method is proposed to exploit spectrum of coefficients of polynomial to find the $N_\mathrm{s}-N_\mathrm{v}$ minimal positions. It assumes that the polynomial at the right hand side of (4.46) can be rewritten as

$$\begin{aligned} p(z) &= a_0 + a_1 z + a_2 z^2 + \cdots + a_{2N_\mathrm{s}-1} z^{2N_\mathrm{s}-1} \\ z &= e^{-j2\pi\Delta f T_\mathrm{s}} \end{aligned} . \tag{4.47}$$

The task is to find $N_\mathrm{s}-N_\mathrm{v}$ roots on the unit circle, which fulfills the condition in (4.46). It takes $2N_\mathrm{s}$ - points FFT for the coefficient vector $\underline{\boldsymbol{a}} = \left[\underline{a}_0 \quad \underline{a}_1 \quad \cdots \quad \underline{a}_{2N_\mathrm{s}-1}\right]^{\mathrm{T}}$ to get the spectrum vector $\underline{\boldsymbol{b}} = \left[\underline{b}_0 \quad \underline{b}_1 \quad \cdots \quad \underline{b}_{2N_\mathrm{s}-1}\right]^{\mathrm{T}}$. Then the $N_\mathrm{s}-N_\mathrm{v}$ roots can be expressed as

$$\boldsymbol{z} = \mathrm{LM}_{N_\mathrm{s}-N_\mathrm{v}}\left(|\underline{\boldsymbol{b}}|^2\right). \tag{4.48}$$

$\mathrm{LM}_{N_s-N_v}$ denotes the $N_s - N_v$ local minima points. Using (4.47) and (4.48), $N_s - N_v$ $\widehat{\Delta \boldsymbol{f}}_1$ can be estimated. Inconsistent CFO is caused by the unknown channel frequency response on the FFT grid, which can be solved by the asymptotic same operation on $\underline{\boldsymbol{s}}_{r,\mathrm{m3}}$ with only adjustment of (4.44):

$$\underline{\boldsymbol{s}}_{\mathrm{r,m3}} = c_3 \underline{\boldsymbol{D}}_{N_s,3} \underline{\boldsymbol{W}}_{N_s \times N_s} \underline{\boldsymbol{H}}_{\mathrm{f},3} \underline{\boldsymbol{W}}^{\mathrm{H}}_{N_s \times N_s} \underline{\boldsymbol{W}}_{N_s \times N} \underline{\boldsymbol{d}}_1 + \underline{\boldsymbol{w}}' . \tag{4.49}$$

It assumes $\underline{\boldsymbol{H}}_{\mathrm{f},1} = \underline{\boldsymbol{H}}_{\mathrm{f},3}$ due to the time invariant channel. $\widehat{\Delta \boldsymbol{f}}_1$ and $\widehat{\Delta \boldsymbol{f}}_2$ shall be compared to each other and the common values in two vectors will be selected to constitute the candidate estimation vector $\widehat{\Delta \boldsymbol{f}}_{\mathrm{c}}$. Each value in $\widehat{\Delta \boldsymbol{f}}_{\mathrm{c}}$ shall be used to compute $\widehat{\underline{\boldsymbol{H}}}_{\mathrm{f},1}$ and $\widehat{\underline{\boldsymbol{H}}}_{\mathrm{f},3}$. It has been asserted that $\underline{\boldsymbol{H}}_{\mathrm{f},1} = \underline{\boldsymbol{H}}_{\mathrm{f},3}$, one can find the correct estimation value $\Delta \widehat{f}$, which can fulfill this condition. From(4.44), (4.49) and the estimated CFO, the channel frequency response matrix $\underline{\boldsymbol{H}}_{\mathrm{f},1}$ and the discrete CIR vector $\underline{\boldsymbol{h}} = \begin{bmatrix} \underline{h}_0 & \underline{h}_1 & \cdots & \underline{h}_{L-1} \end{bmatrix}^{\mathrm{T}}$ can be determined. Recall that $\underline{\boldsymbol{H}}_{\mathrm{f},1}$ is a diagonalized matrix. The diagonal elements constitute a vector $\underline{\boldsymbol{h}}_{\mathrm{f}} = \begin{bmatrix} \underline{h}_{0,\mathrm{f}} & \underline{h}_{1,\mathrm{f}} & \cdots & \underline{h}_{N_s-1,\mathrm{f}} \end{bmatrix}^{\mathrm{T}}$. Then (4.44) can rewritten as

$$c_1^{-1} \underline{\boldsymbol{D}}^{-1}_{N_s \times 1} \underline{\boldsymbol{W}}^{-1}_{N_s \times N_s} \underline{\boldsymbol{s}}_{\mathrm{r,m1}} = \mathrm{diag}\left(\underline{\boldsymbol{W}}^{\mathrm{H}}_{N_s \times N_s} \underline{\boldsymbol{W}}_{N_s \times N} \underline{\boldsymbol{E}}_N \underline{\boldsymbol{d}}_{\mathrm{s}} \right) \underline{\boldsymbol{h}}_f + c_1^{-1} \underline{\boldsymbol{D}}^{-1}_{N_s \times 1} \underline{\boldsymbol{W}}^{-1}_{N_s \times N_s} \underline{\boldsymbol{w}}' . \tag{4.50}$$

With the LS estimator, $\underline{\boldsymbol{h}}_{\mathrm{f}}$ can be estimated as

$$\hat{\underline{\boldsymbol{h}}}_{\mathrm{f}} = c_1^{-1} \mathrm{diag}^{-1} \left(\underline{\boldsymbol{W}}^{\mathrm{H}}_{N_s \times N_s} \underline{\boldsymbol{W}}_{N_s \times N} \underline{\boldsymbol{E}}_N \underline{\boldsymbol{d}}_{\mathrm{s}} \right) \underline{\boldsymbol{D}}^{-1}_{N_s \times 1} \underline{\boldsymbol{W}}^{-1}_{N_s \times N_s} \underline{\boldsymbol{s}}_{\mathrm{r,m1}} . \tag{4.51}$$

Then the $\left(\hat{\underline{a}}_1, \cdots \hat{\underline{a}}_L ; \hat{\tau}_1, \cdots \hat{\tau}_L \right)$ can be determined through L peaks of IFFT of $\hat{\underline{\boldsymbol{h}}}_{\mathrm{f}}$.

4.4 Location Mapping via AoA Estimation

As known, the two dimensional localization via AoA measurements requires at least two WLAN stations. In this research, measurement campaigns are performed for M = 2 and M =4 cases, where M is the number of WLAN stations. For the M =2 case, it assumes the WLAN stations are located at (x_1, y_1) and (x_2, y_2), respectively. To overcome the effect of grating lobes, the antenna array of two stations are set to 45° and -45° deviated from the Y axis as the clarity area of each antenna array is from approximate 50° to 130° according to (4.2). (see Figure 4.4)

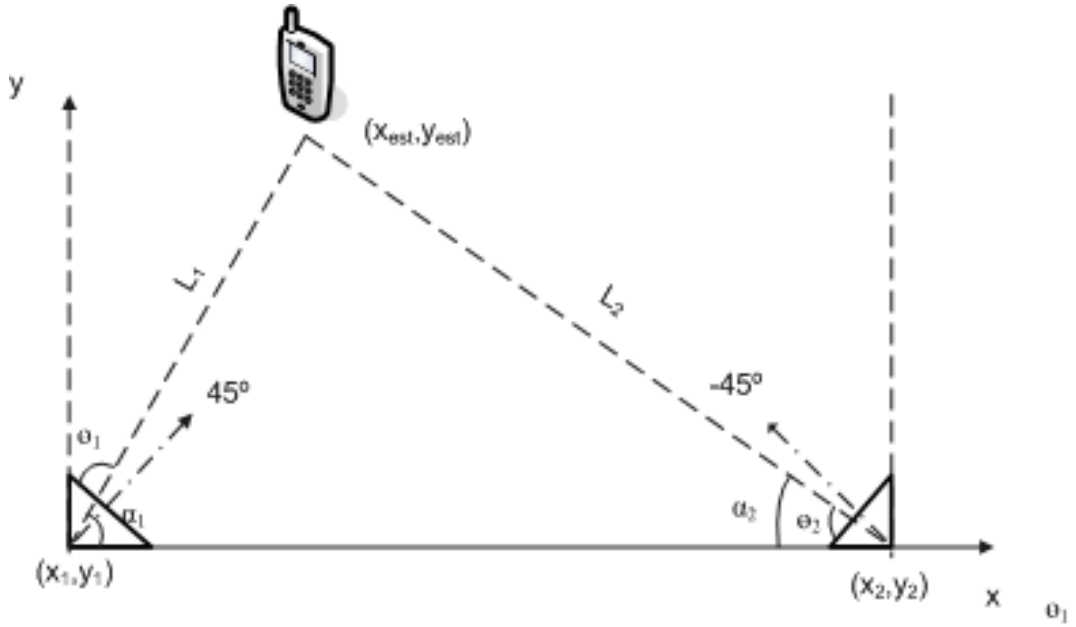

Figure 4.4: Location mapping via two AoA estimations

From Figure 4.4, $\hat{\theta}_1$ and $\hat{\theta}_2$ are estimated AoA from station 1 and station 2, respectively. α_1 and α_2 are angles deviated from wave incoming direction and the X axis. Relation between $\hat{\theta}$ and α can be expressed by $\alpha_1 = \frac{3\pi}{4} - \hat{\theta}_1$ and $\alpha_2 = -\frac{\pi}{4} + \hat{\theta}_2$, which depends on the position and direction of the antenna array. L is defined as the distance between two stations. Then the distance between transponder and the two stations can be calculated as $L_1 = \frac{L\sin(\alpha_2)}{\sin(\pi - \alpha_1 - \alpha_2)}$ and $L_2 = \frac{L\sin(\alpha_1)}{\sin(\pi - \alpha_1 - \alpha_2)}$. Solving the following equations:

$$\begin{cases} (x_{\text{est}} - x_1)^2 + (y_{\text{est}} - y_1)^2 = L_1^2 \\ (x_{\text{est}} - x_2)^2 + (y_{\text{est}} - y_2)^2 = L_2^2 \\ y_{\text{est}} - y_1 - \frac{y_2 - y_1}{x_2 - x_1}(x_{\text{est}} - x_1) > 0 \end{cases}, \tag{4.52}$$

the coordinate of transmitter $(x_{\text{est}}, y_{\text{est}})$ can be determined.

For M =4 case, the four WLAN stations are located at four corners of the localization area (see Figure 4.5).

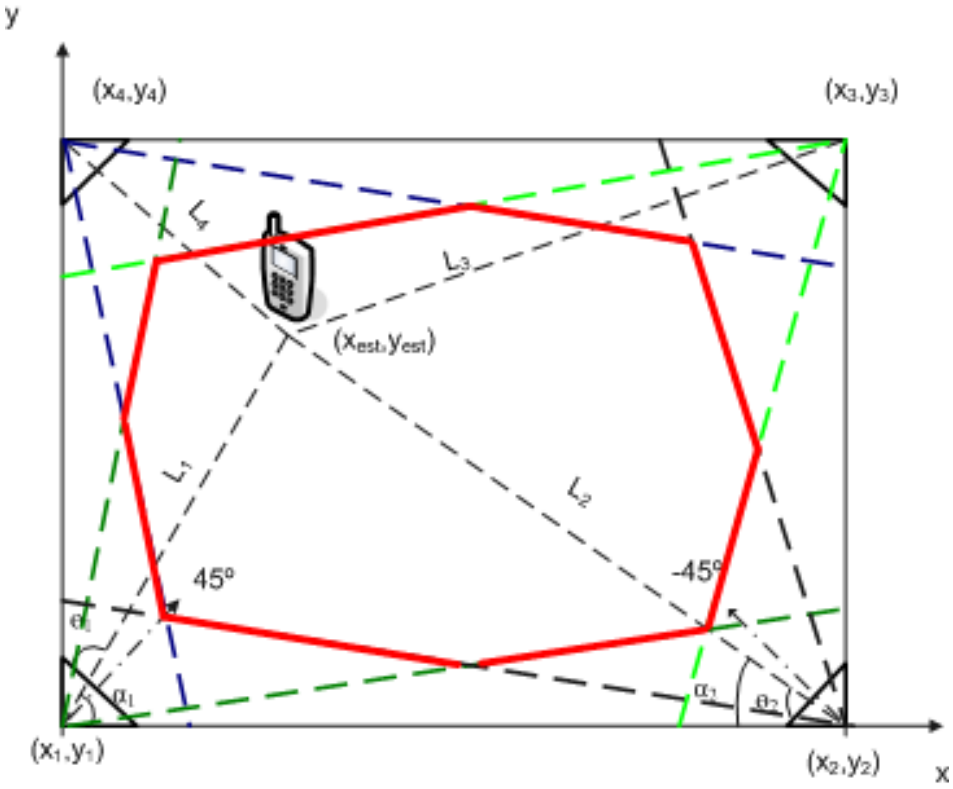

Figure 4.5: Location mapping via 4 AoA estimations

The same as Figure 4.4, the antenna array of the four stations are set to look toward to 45 or -45 degree deviated from the Y axis. The localization area is limited to be within the area *A*, which is enclosed by the red bold line, in order to avoid the mirror estimate caused by grating lobes. It defines the estimated AoA vector and mapped angle vector as $\hat{\boldsymbol{\theta}}$ and $\boldsymbol{\alpha}$. Ideally, the estimation directions from four stations shall intersect in a unique point. Generally, however, it will take place 16 intersections $p_{mn,m=1\cdots4,n=1\cdots4,m\neq n}$ due to the perturbation of estimation AoA. For the sake of simplicity, the four intersections are chosen: $p_{ij}, i=1,2\cdots,4.\ j=\mathrm{mod}(i,4)+1$ as the estimates from each pair of stations. The coordinates of the four intersections are $(x_{ij}, y_{ij}), i=1\cdots4,\ j=\mathrm{mod}(i,4)+1$, and $L_{mn,m=1\cdots4,n=1\cdots4,m\neq n}$ represents the range estimate from p_{mn} to *m*-th station. Using the LS algorithms, it has

$$(x_{\text{est}}, y_{\text{est}}) = \arg\min_{(x,y)} \left(\sum_{i=1,j=1,i\neq j}^{4} \left((x-x_{ij})^2 + (y-y_{ij})^2 \right) \right). \tag{4.53}$$

4.5 Simulation Results and AoA Measurements

Table **4.1** depicts the simulation and measurements parameters. In this research, the simulation and measurement campaigns are performed on an 802.11a system, which owns the carrier frequency range from 5GHz to 6GHz.

Table 4.1: Simulation and measurement parameters

Parameter	Definition	Value	Unit
d	Inter-element spacing	0.04425	meter
N	Number of antenna elements	4	
f_c	Carrier frequency	5.2	GHz
Δf	Subcarrier frequency spacing	0.3125	MHz
f_s	Sampling rate	80	MHz
W	Width of localization area	10	meter
L	Length of localization area	10	meter
M	The number of WLAN stations	2 and 4	
(x_1, y_1)	Location of the station 1	$(0,0)$	meter
(x_2, y_2)	Location of the station 2	$(10,0)$	meter
(x_3, y_3)	Location of the station 3	$(10,10)$	meter
(x_4, y_4)	Location of the station 4	$(0,10)$	meter
ϕ_m	Antenna mode	45	degree

Firstly, the optimum weighting vector for the ULA shall be found. The weighting vector is defined as

$$\boldsymbol{w}_{\mathrm{BF,w}} = \begin{bmatrix} k & ck & ck & k \end{bmatrix}, \tag{4.54}$$

where k is a random positive number and c is the coefficient between the first and second antenna element. The first criteria in (4.20) can be rewritten as

$$\begin{aligned} &\cos\left(\frac{6\pi d}{\lambda}\left(\cos\theta_h - \cos\theta_b\right)\right) + 2c\cos\left(\frac{4\pi d}{\lambda}\left(\cos\theta_h - \cos\theta_b\right)\right) + \\ &+\left(c^2 + 2c\right)\cos\left(\frac{2\pi d}{\lambda}\left(\cos\theta_h - \cos\theta_b\right)\right) - 2c = 0 \end{aligned} . \tag{4.55}$$

It can be concluded that the MBW shall increase with a larger c. Figure 4.6 shows the relation between the MBW and the coefficient c.

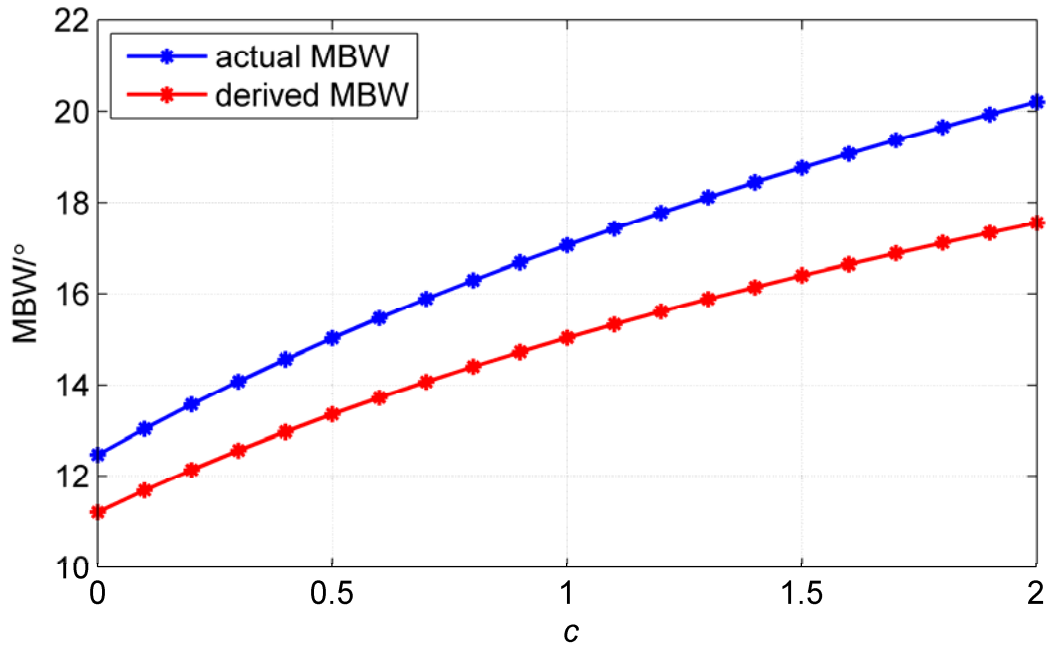

Figure 4.6: MBW vs. the coefficient *c*

As can be seen from Figure 4.6, MBW has the smallest value if $c = 0$, which denotes the second and third antenna elements have no contribution to the Beamformer. However, smaller c can cause a higher side lobe power, which can reduce the MSR. Figure 4.7 and Figure 4.8 illustrate the side lobe position and MSR with different coefficients.

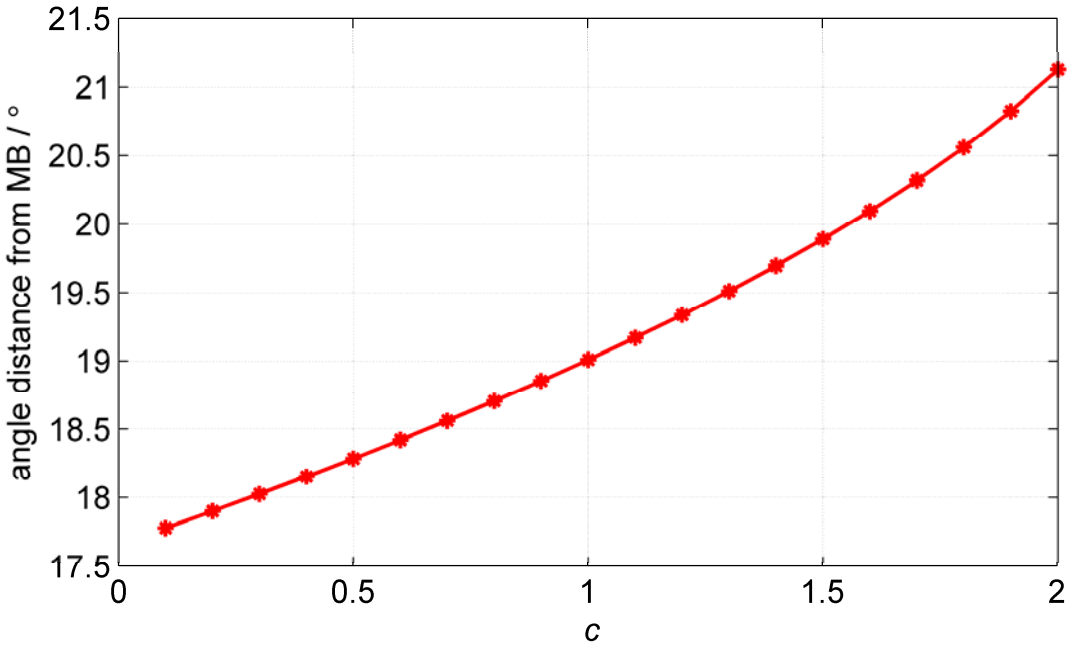

Figure 4.7: Position of the first side lobe vs. the coefficient *c*

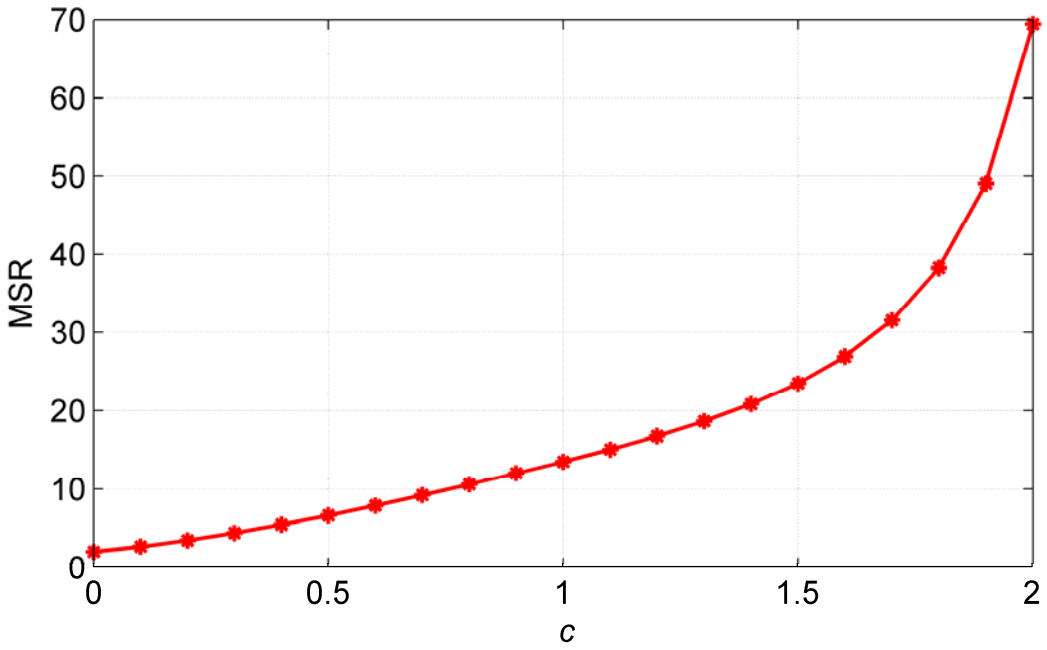

Figure 4.8: MSR vs. the coefficient *c*

To select the optimum coefficient, three factors shall be considered: MBW, side lobe position and MSR. In general, larger c shall be selected in the harsh environment as the receiver may receive copies of signal from random directions while smaller c may improve the performance of the beamformer in the outdoor environment.

To evaluate the novel channel estimator, the RMSE of estimated CIR can be written as

$$\text{rmse}=\sqrt{\frac{1}{NN_{\text{frame}}}\left(\sum_{i=1}^{N_{\text{frame}}}\left(\underline{\boldsymbol{h}}_{\text{est},i}-\underline{\boldsymbol{h}}_{\text{p},i}\right)^{\text{H}}\left(\underline{\boldsymbol{h}}_{\text{est},i}-\underline{\boldsymbol{h}}_{\text{p},i}\right)\right)}. \tag{4.56}$$

$\underline{\boldsymbol{h}}_{\text{est},i}$ and $\underline{\boldsymbol{h}}_{\text{p},i}$ are the estimated and perfect frequency CIR vector for the i-th Monte Carlo simulation, respectively. N_{frame} and N are the number of simulation and the vector length of CIR, respectively. Figure 4.9 illustrates the performance of the novel channel estimator

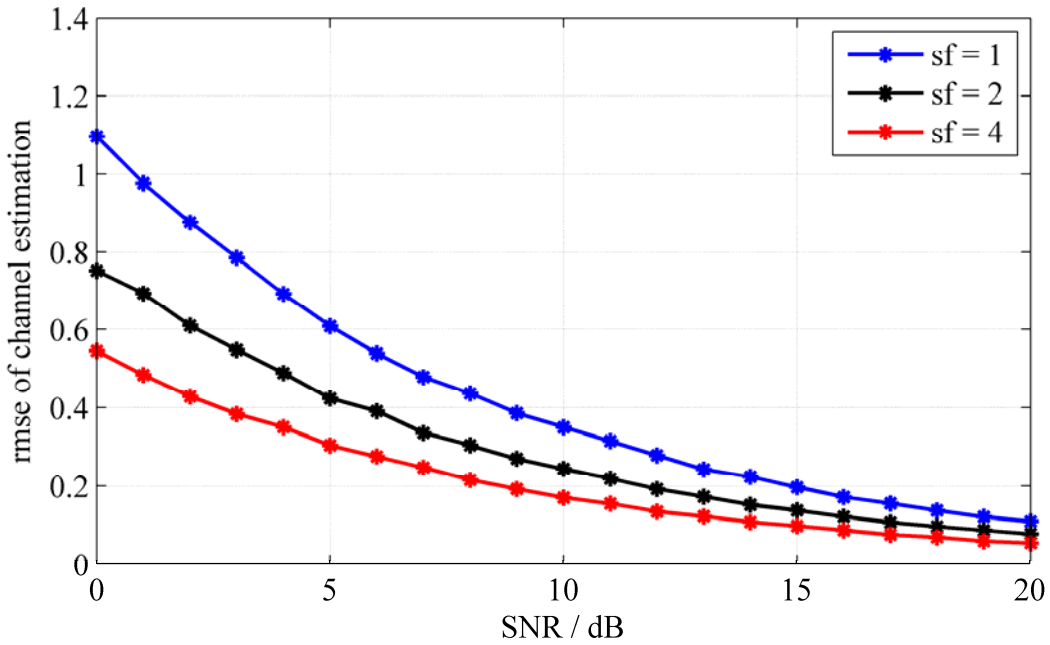

Figure 4.9: RMSE of estimated CIR vs SNR

It is clear that the estimation error can be suppressed with the increase of OSR, especially in a low SNR scenario. With the increase of SNR, higher OSR displays no dominant advantages over lower OSR.

The demonstrator consists of four WLAN stations, one notebook (server), one WLAN router and one transponder. The locations of the four WLAN stations and the antenna mode are depicted in Table **4.1**. The notebook as a processing server is connected to the station 1-4 using Ethernet cable. The measurements were carried out in the following way:

1. DHCP (Dynamic Host Configuration Protocol) server on the WLAN router allocates static IP address to stations 1 to 4 automatically.
2. Server sends commands to each station to carry out the calibration process.
3. Localization requirements are sent to each station
4. FPGA modules receive the WLAN signal and forward it to the server.
5. Server exploits the received signal to carry out the location estimation and display the result on the Graphic User Interface (GUI)

The 1st step will be performed immediately after the system power was on. The 2nd , 3rd and 5th steps are executed by MATLAB program running on the server. The location process is a real time procedure which shall be carried out in a “while” loop. The 4th step shall be finished by Microplaze module embedded in the VHDL code. The detailed localization process can be explained in the following flow chart:

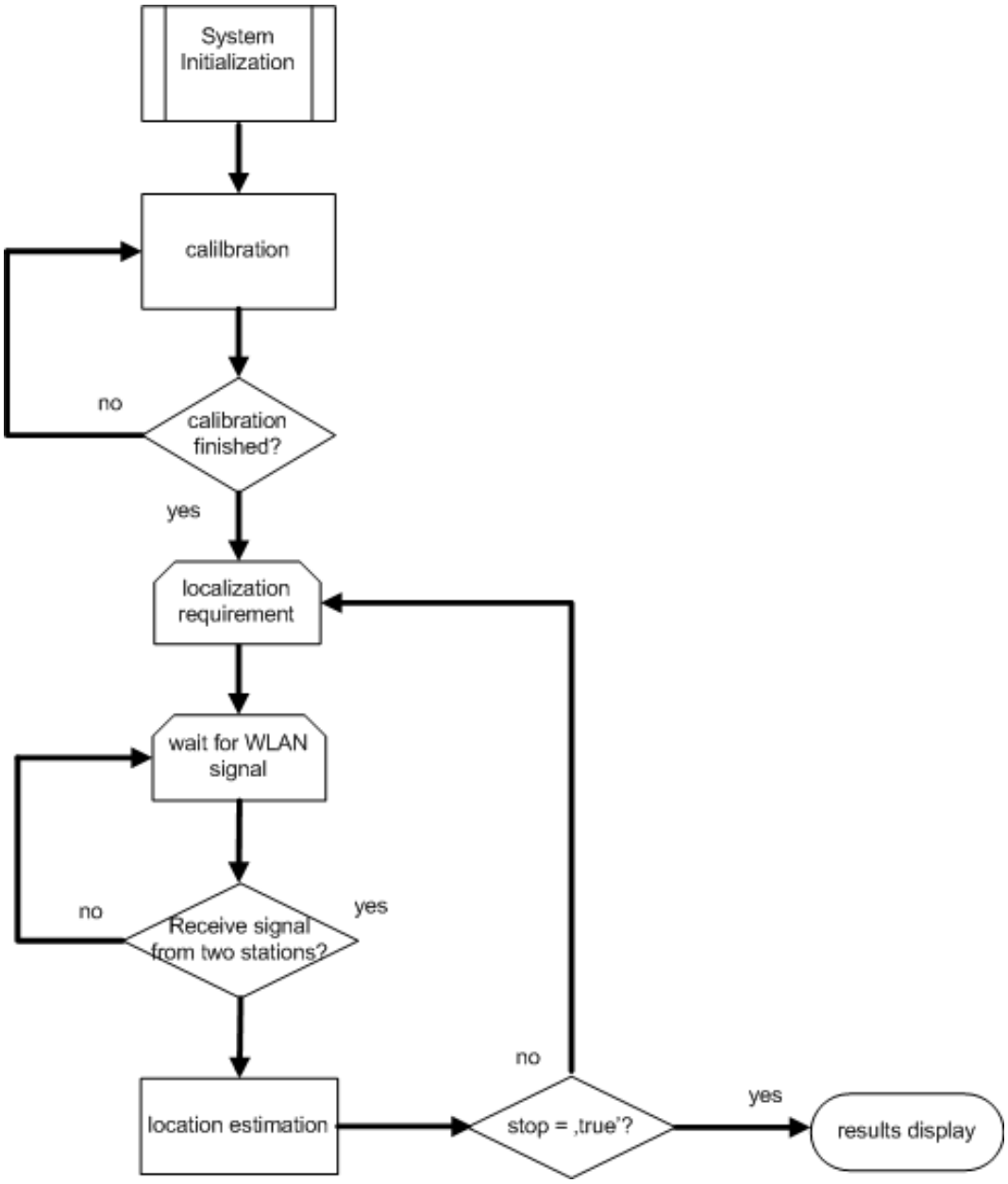

Figure 4.10: Flow chart of localization process

Before the localization is started, the effect of transmission distance on the AoA estimation shall be inspected. It takes 60° and 90° as the candidate AoAs. The blue and red lines in Figure 4.11 represent the 90° and 60°, respectively. On each line, the candidate measurement points with equi-distance of 60cm are selected. The AoA measurement results are depicted in Figure 4.14 and Figure 4.15.

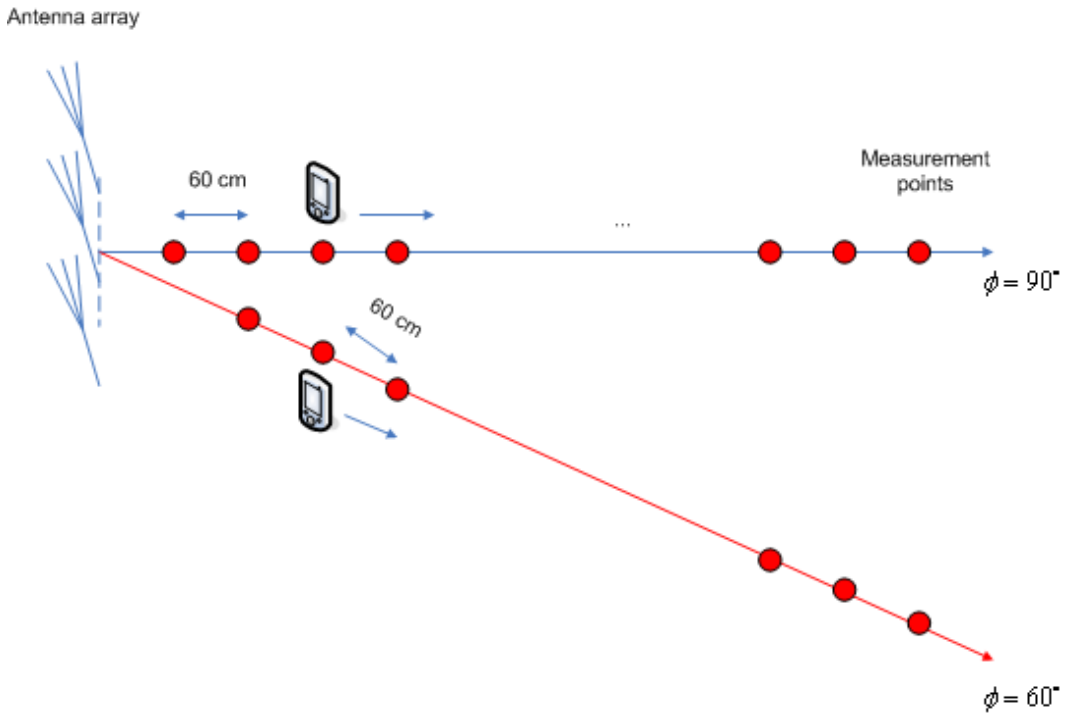

Figure 4.11: AoA measurement campaign

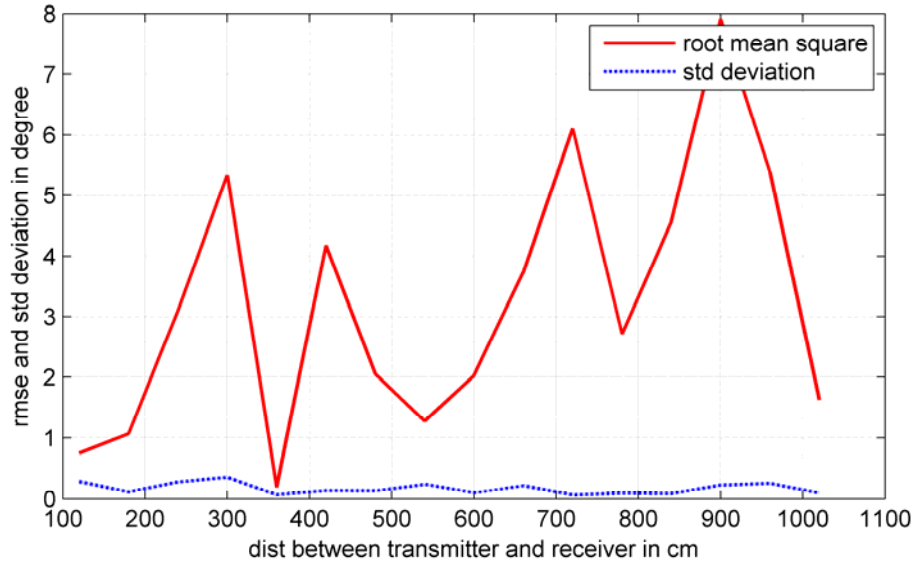

Figure 4.12: RMSE and std. deviation for different transmission distance (90 degree)

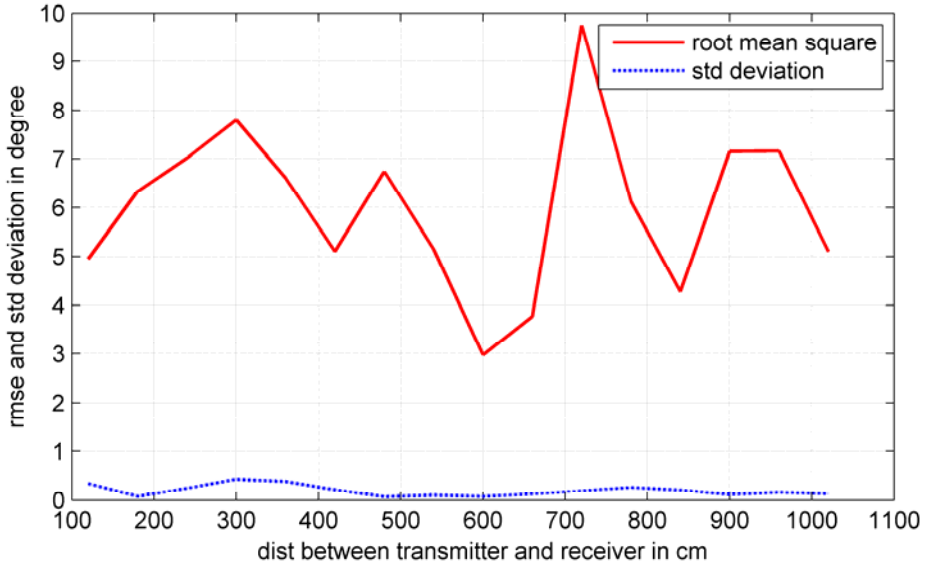

Figure 4.13: RMSE and std. deviation for different transmission distance (60 degree)

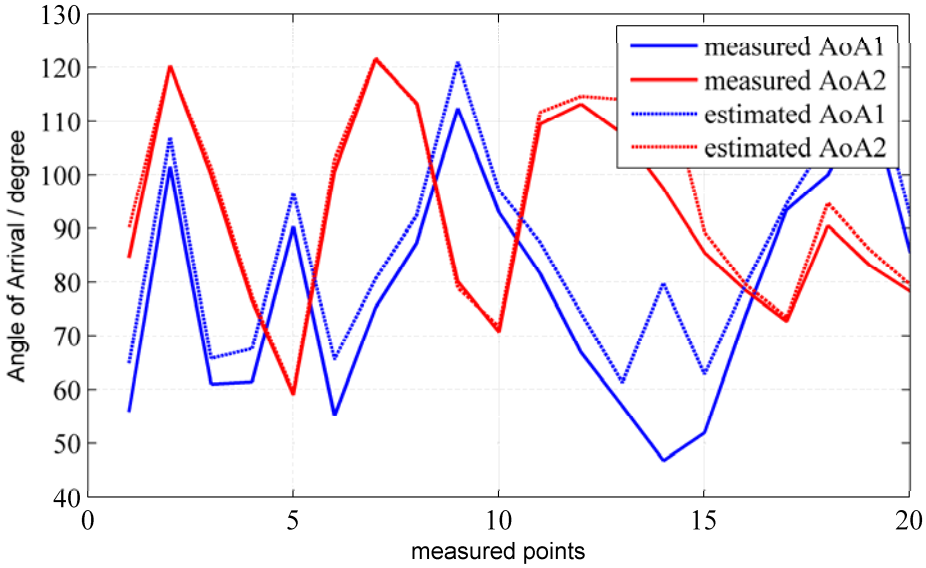

Figure 4.14: AoA measurement results for $M = 2$

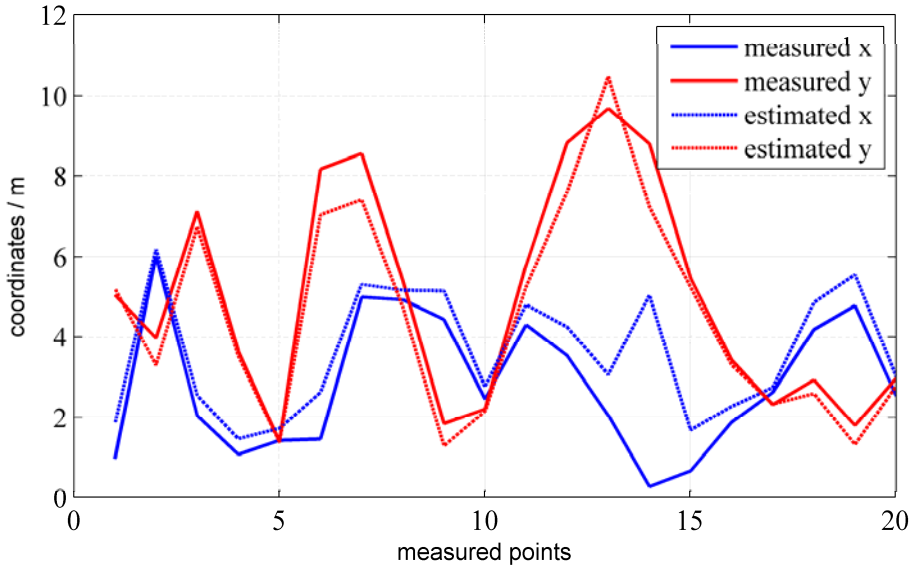

Figure 4.15: Location measurement results for $M = 2$

From Figure 4.14, it can be seen that the measured AoA conforms to the estimated one with the exception of the 14th point as the 14th reference points locates beyond the clarity area. The RMSE of location estimation for M =2 case is approximate 80cm.

The measurements shows that the RMSE of location estimation for M = 4 case can achieve 40cm. Figure 4.16 to Figure 4.19 give the AoA and location estimation results for M = 4 case.

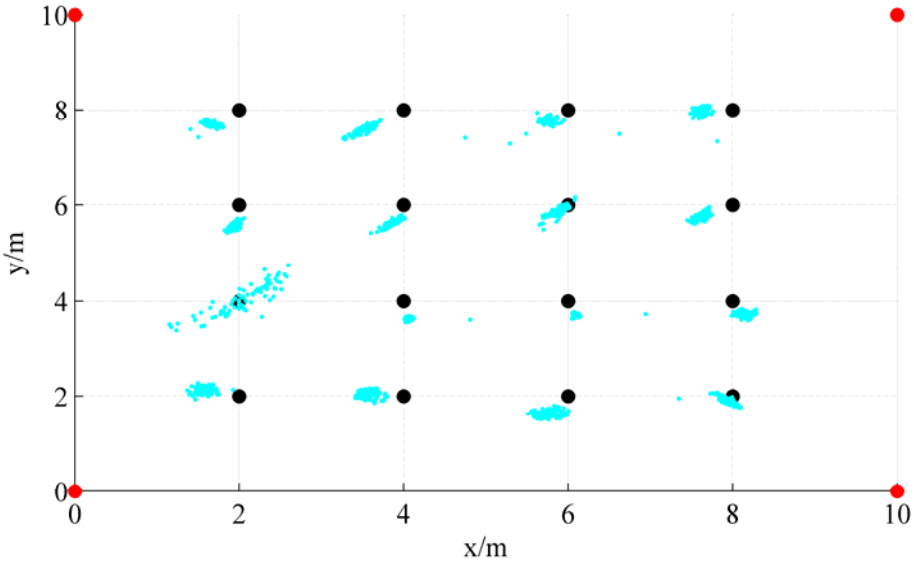

Figure 4.16: 100 measurements at each location for $M = 4$

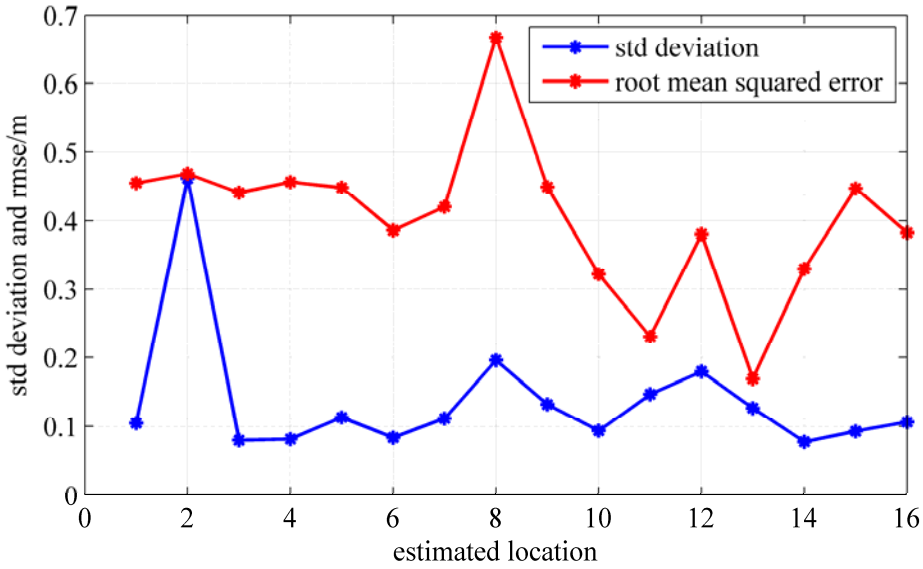

Figure 4.17: RMSE and std. deviation of location estimation for $M = 4$

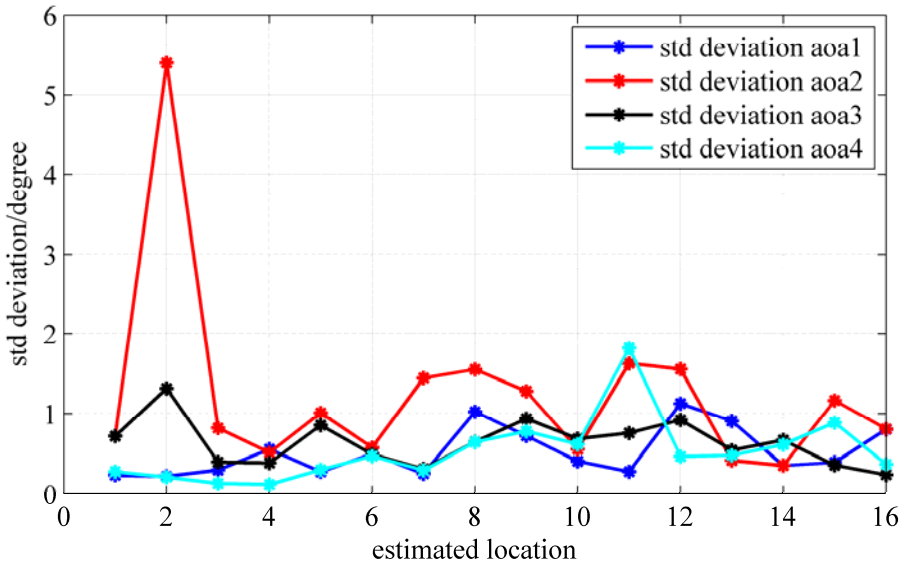

Figure 4.18: std. deviation of AoA estimation for $M = 4$

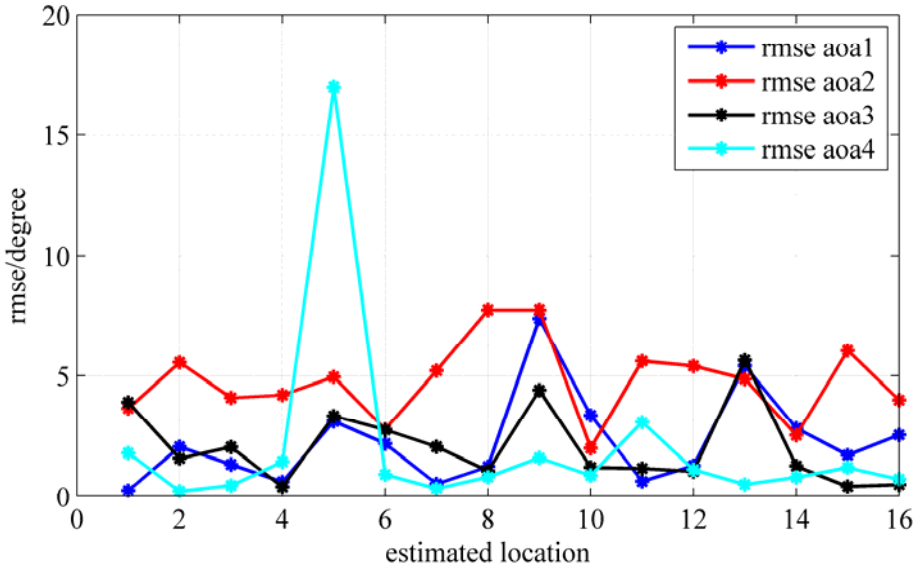

Figure 4.19: RMSE of AoA estimation for $M = 4$

Figure 4.16 shows the real time localization scenario. The four red points represent the four WLAN receivers, which are located at the four corners of the localization region. Within the localization region, there are 16 selected candidate positions with the known coordinates, which are represented with the black nodes. At each candidate position, 100 measurement campaigns are performed and the estimated positions of each measurement campaign are depicted via blue nodes. Figure 4.17, Figure 4.18 and Figure 4.19 illustrate the RMSE and standard deviation of the localization and AoA estimation at each candidate location. RMSE reflects the average deviation from the actual one while the standard deviation represents how much variation exists from the expected value. As can be seen from Figure 4.17, Figure 4.18 and Figure 4.19, RMSE values at most of candidate locations are larger than the standard deviation because of the imperfect antenna adjustment and the PLL calibration.

5 Hardware & Software Description and Measurement Setup

5.1 Overview

In chapter 5, the implemented UWB and WLAN demonstrators are described. The UWB description of hardware and the infrastructure of localization demonstrator will be given in the subchapter 5.2.1. In the subchapter 5.2.2, the UWB measurement setup in the indoor environment will be described. The subchapter 5.2.3 will describe the Java implementation of localization estimator. The WLAN transceiver will be described in the subchapter 5.3.1.

5.2 UWB Localization Demonstrator

5.2.1 Infrastructure of RSS based Location Tracking Demonstrator

The LT demonstrator consists of the following components:

- A 4 m² grid pattern is used during reference measurements to find a tag's position in the room.
- Four CWUSB dongles from IOGEAR of type GUWA U100 are distributed in the grid pattern. They use MB-OFDM UWB in accordance to ECMA-368.
- Four notebook computers with LT software are connected to and control the 4 UWB dongles. One of the four PCs is the LT master, whereas the other three are LT slaves. The LT slaves provide ranging measurement results to the LT master. The LT master performs the LT algorithm and operates as a LT server, providing LT information to the user.
- One Personal Digital Assistant (PDA) with a Graphical User Interface (GUI) to the LT application displays the actual position of the mobile tag, the target, to the user. The client PDA is a Blackberry 9000 Black Smartphone and is equipped with WLAN.

One WLAN access point allows the communication between the WLAN PDA and the LT master for acquisition of LT information to be displayed to the user.

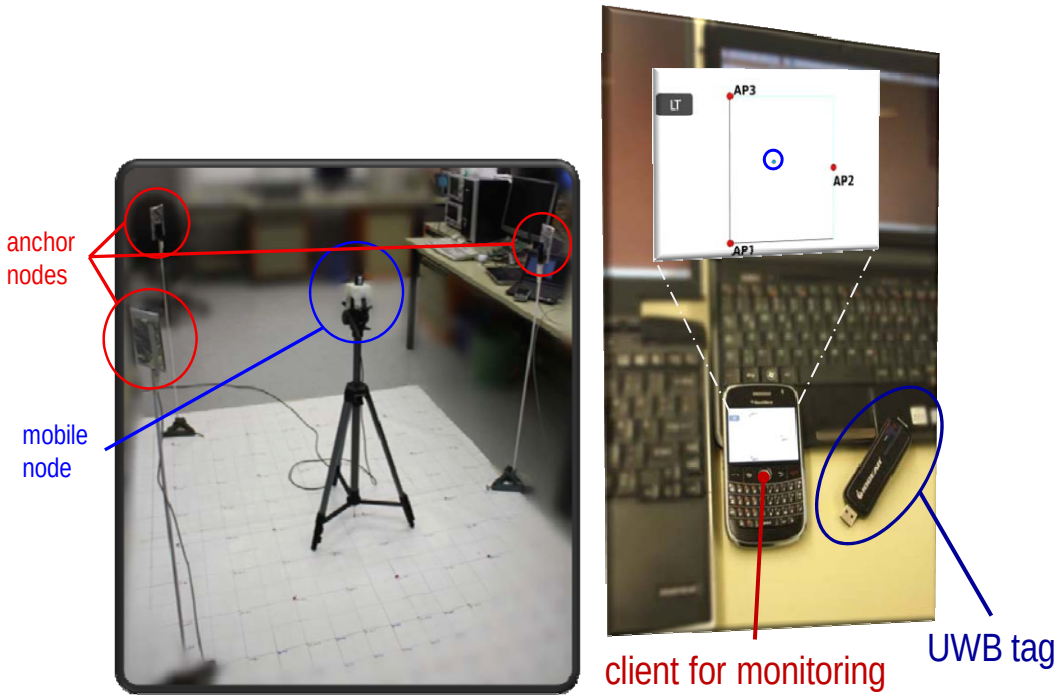

Pic. 5.1: Picture of the laboratory setup of the LT demonstrator for HDR UWB (left) and PDA with LT GUI and connection to the LT server (right)

5.2.2 Measurements Setup

The 3 red points in Figure 5.1 indicate the positions of the access points AP1, AP2 and AP3. They are the anchor nodes for the localization. In the displayed example, their coordinates are P_{AP1} (0.00 m, 0.00 m), P_{AP2} (1.76 m, 1.00 m) and P_{AP3} (0.00 m, 2.00 m). The three PCs Laptop 1 - Laptop 3 are connected to the anchor nodes AP1 - AP3 using USB cables. Laptop 4 is connected to the target device, the mobile node to be localized. The left side of Pic. 5.1 depicts a laboratory test setup of LT demonstrator. The right side of Pic. 5.1 shows a UWB dongle in more detail and the client PDA with the GUI. Then the measurements are carried out in the following way:

1. Initialize the UWB network with laptop 1 to laptop 4
2. Connect the PDA which acts as the application client to the server by WLAN connection
3. The PDA sends commands to the server requesting the server to execute the localization procedure
4. The results of the localization procedure are displayed on the screen of PDA

In the 1st step, the laptop 1 to laptop 4 configure the IP address of AP1 to AP4, respectively. PDA as the application client, is connected to the server (laptop 4) by WLAN in the 2nd step. In the 3rd step, the PDA sends the commands to the server to ask the server to execute the localization procedure. The server shall measure the RSSI from AP1 to AP3, and localize the UWB target with the aforementioned

algorithms. In the final step, the coordinates of the target shall be transmitted to the PDA with WLAN connection.

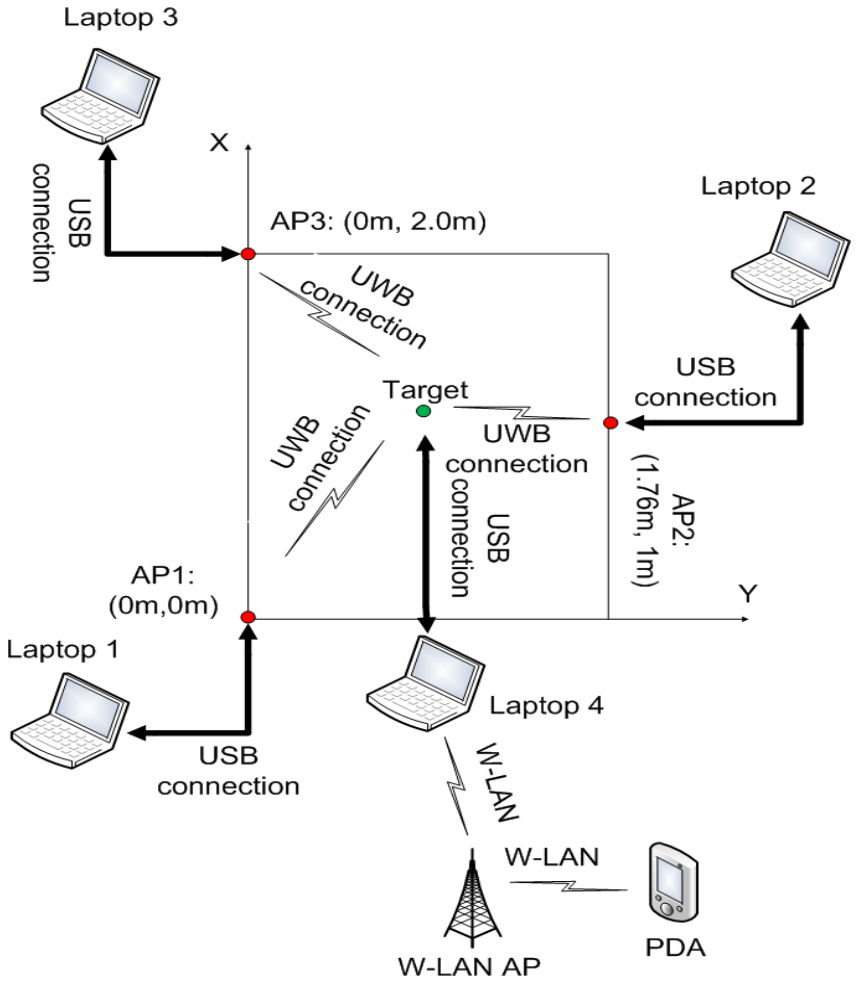

Figure 5.1: Infrastructure of HDR UWB localization demonstrator

5.2.3 Java Implementation of Location Estimators

In the passive localization, there is slave software running on the Laptop 2 and Laptop 3. Its structure is displayed in Figure 5.2. The software has a “while” loop, in which a function “ReceiveCommandStr()” is set to receive the command string from the LT master. The RSSI value stored in the slave will be read if the command string is equal to “RSSI_AP”. Then “SendRSSIToServer()” shall be called to send the RSSI value to the LT master.

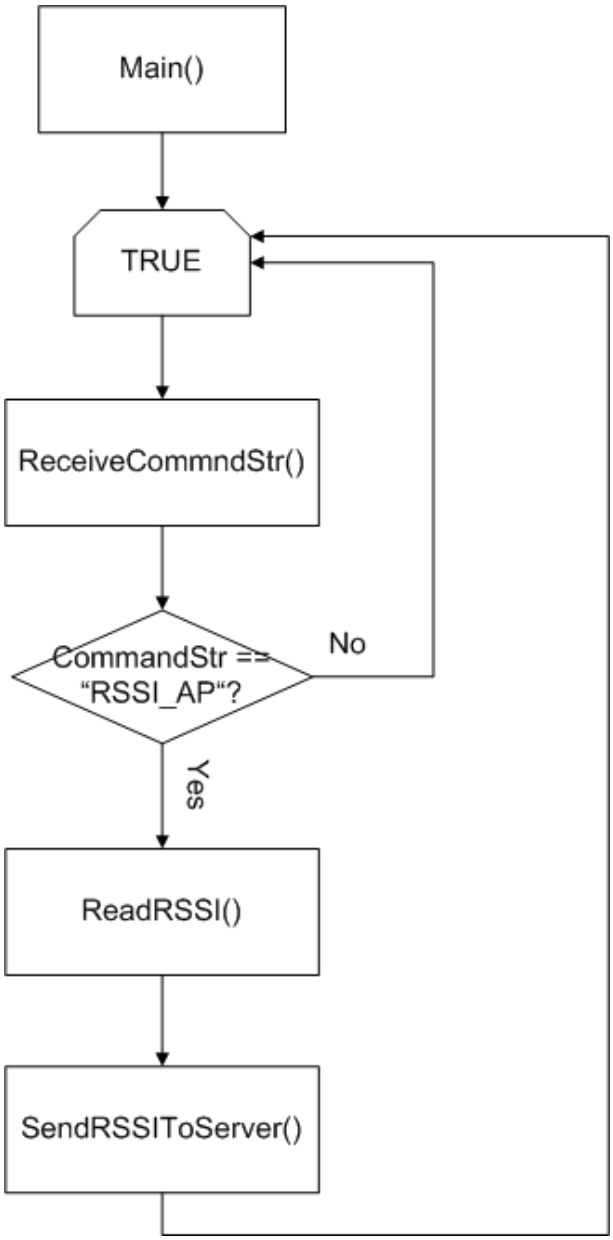

Figure 5.2: Structure of LT slave software

The master software runs on the Laptop 1, which is considered as the server. Its structure is illustrated in Figure 5.3. The master program consists of four threads: “PDA Listening”, “LT”, “AP2_listenning” and “AP3_listennming”. “PDA Listening” is responsible for listening the command from PDA client and executing the program according to the received command. If the “LT” command is received, the thread “LT” will be activated. The program will exit if the command “EXIT” is received from PDA client. The thread “LT” is used to execute the localization procedure and send the localization results back to the PDA client. The thread “AP2_listenning” and “AP3_listenning” are used to collect the RSSI values from AP2 and AP3.

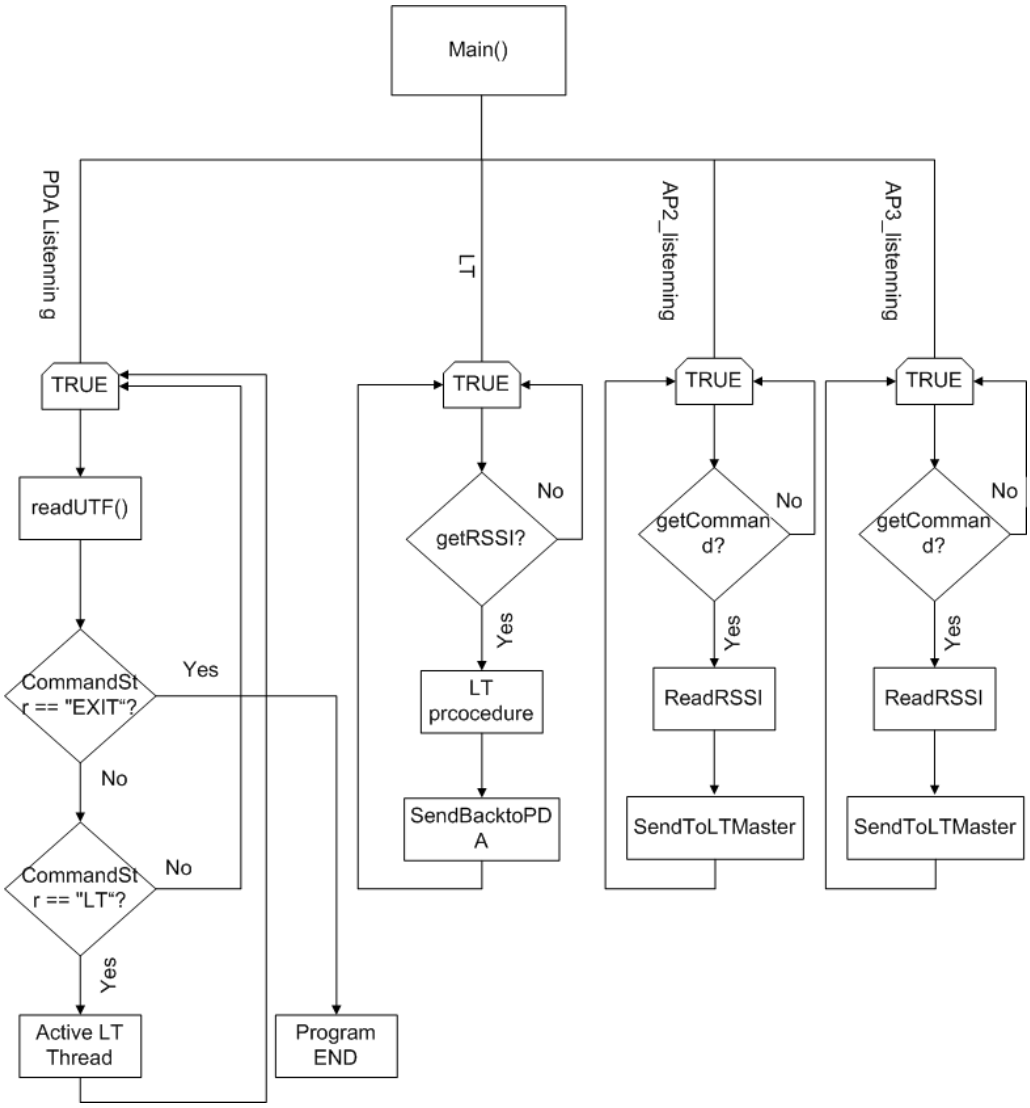

Figure 5.3: Structure of LT master software

Blackberry 9000 PDA is used as the client, on which the client program is running. Its function is to command the server to execute the localization procedure and display the localization results on PDA. Its structure is illustrated as follows:

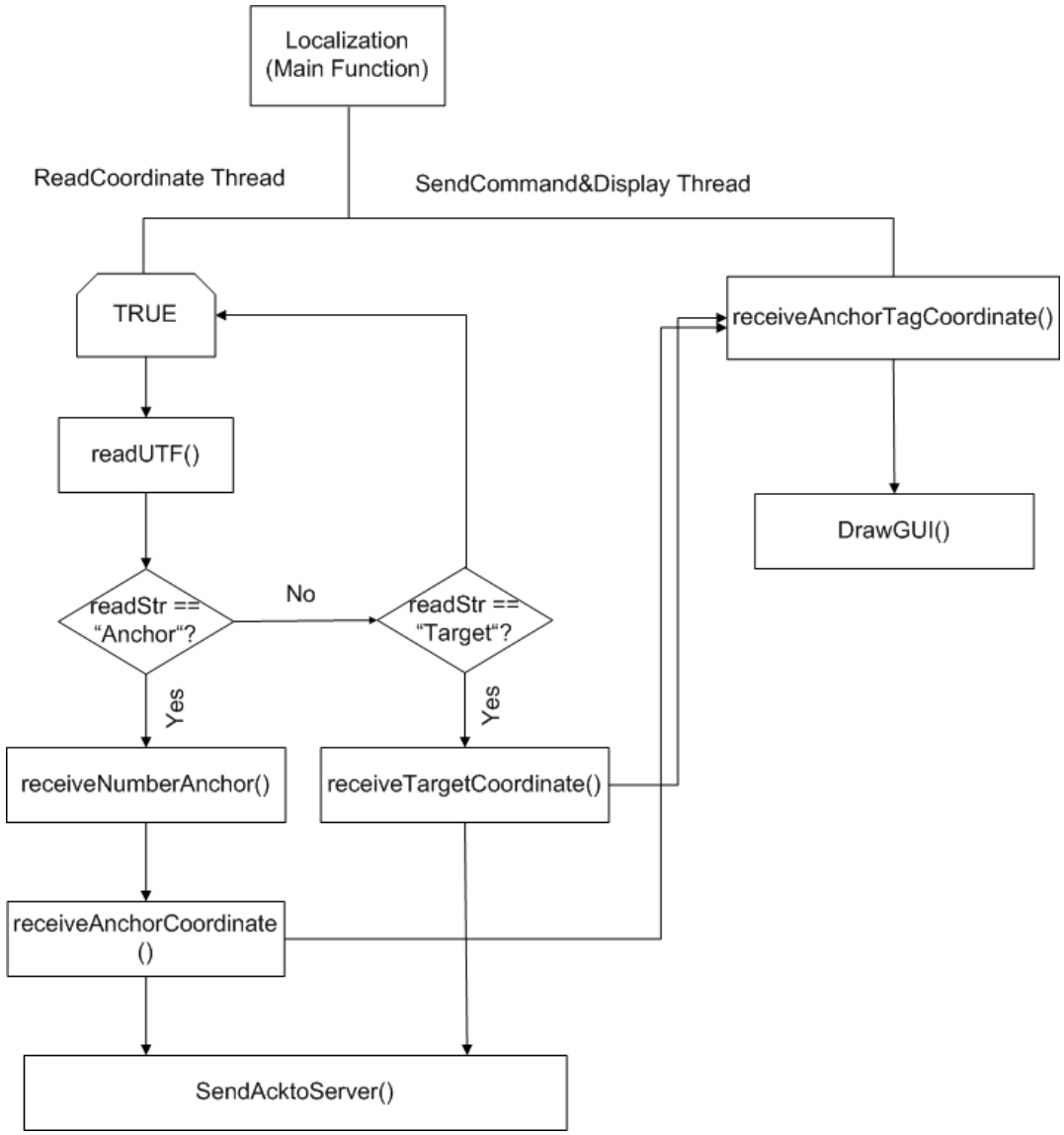

Figure 5.4: Structure of client program

It can be seen from Figure 5.4, the class "Localization" consists of two threads: "ReadCoordinate" and "SendCommand&Display". "ReadCoordinate" has a "while" loop which checks that whether the received string is equal to "Anchor" or "Target". If "Anchor" is received, the client software begins to receive the number of anchor nodes and the coordinates of anchor nodes. If "Target" is received, the client program begins to receive the coordinates of the UWB target. Then an acknowledgement shall be sent back to the server. If the anchor information and the target information are received by the client software, the semaphores "Anchor_received" and "Target_received" will be set to one, which active the thread "SendCommand&Display" to display the localization results on PDA screen.

5.3 WLAN Localization Demonstrator

5.3.1 Hardware Description

The WLAN RF frontend board is showed in Pic. 5.2.

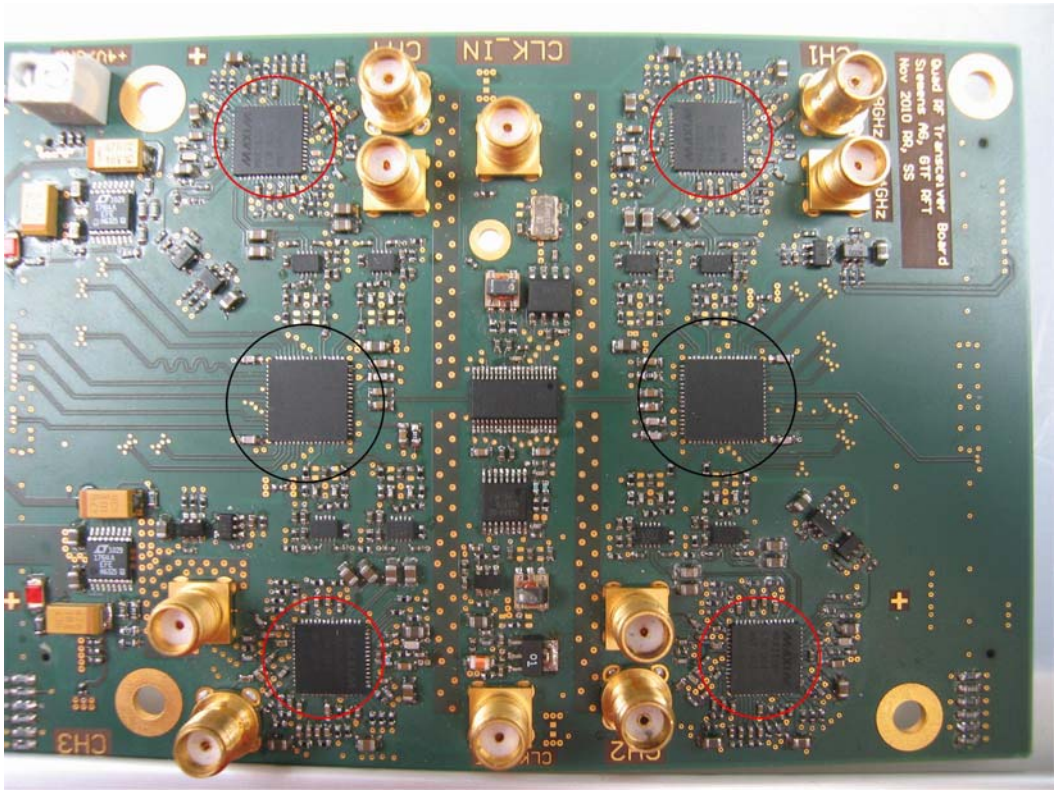

Pic. 5.2: WLAN RF frontend board

As can be seen from Pic. 5.2, the RF frontend board mainly consists of four MAX2829 chips (four red circles) and two ADS6443 (two black circles). The MAX2829 chip is responsible to down-sample RF signal to the analog base band signal. Two ADS6443 are 14-bit Analog-to-Digital-Converters (ADC), which are responsible to convert the analog signal to a digital base band signal. The output of ADS6443 can be found in Figure 5.5.

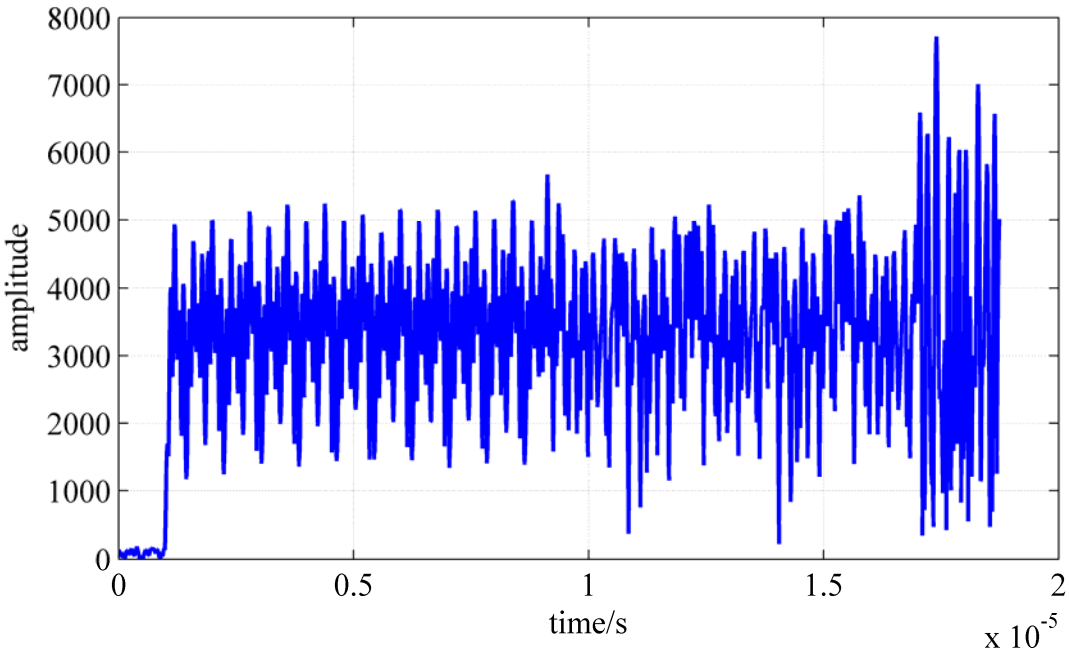

Figure 5.5: Received WLAN base band signal sampled with 80MHz

The Virtex-5 FPGA board is depicted in Pic. 5.3.

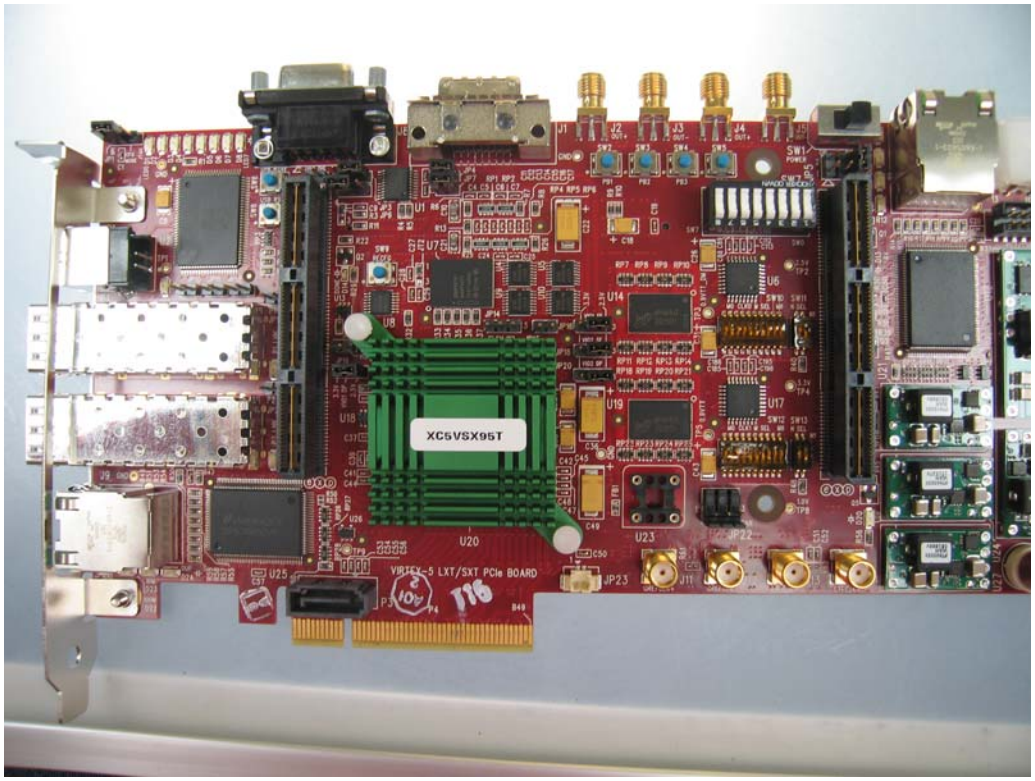

Pic. 5.3: Virtex-5 FPGA board

The FPGA module is responsible to extract the digital signal from ADS6443 and transmit it to the computer via Ethernet cable.

Pic. 5.4 and Pic. 5.5 show the measurement scenario.

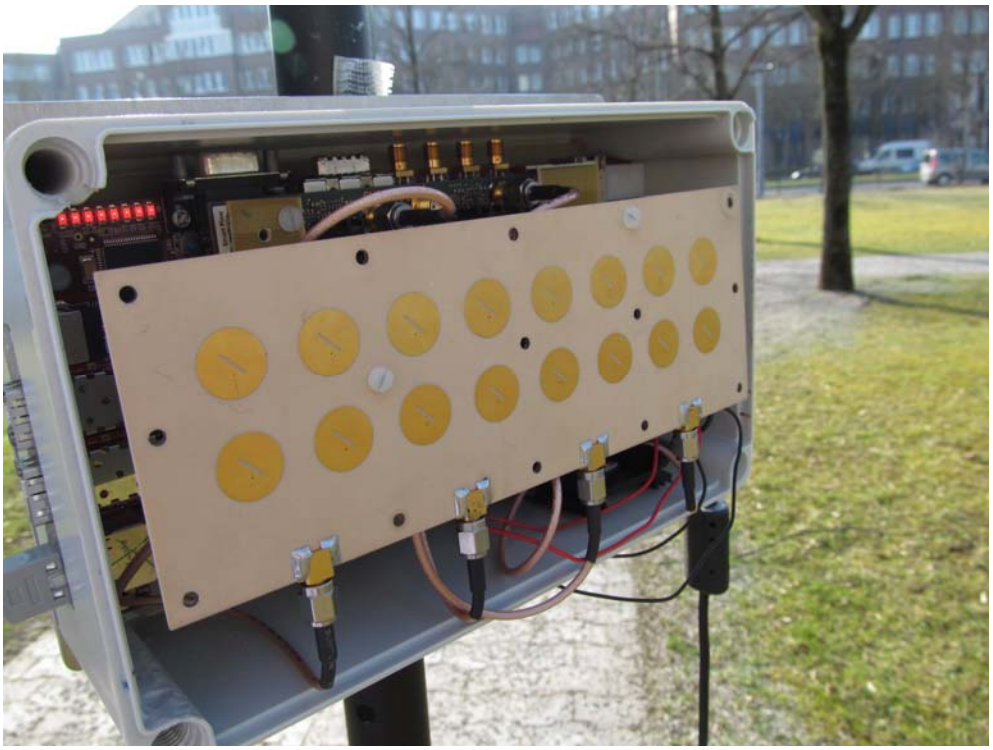

Pic. 5.4: Localization box

Pic. 5.5: WLAN station

5.3.2 Measurements Setup

The measurements setup of WLAN localization can be found in the subchapter 4.5.

5.3.3 FPGA Implementation

In the Virtex-5 FPGA, there were mainly six modules to be implemented: “power_up”, “clocking”, “MAX2829_control”, “ADC_control”, “AGC_control” and “Data_transmission”. The relation among each module is depicted in Figure 5.6.

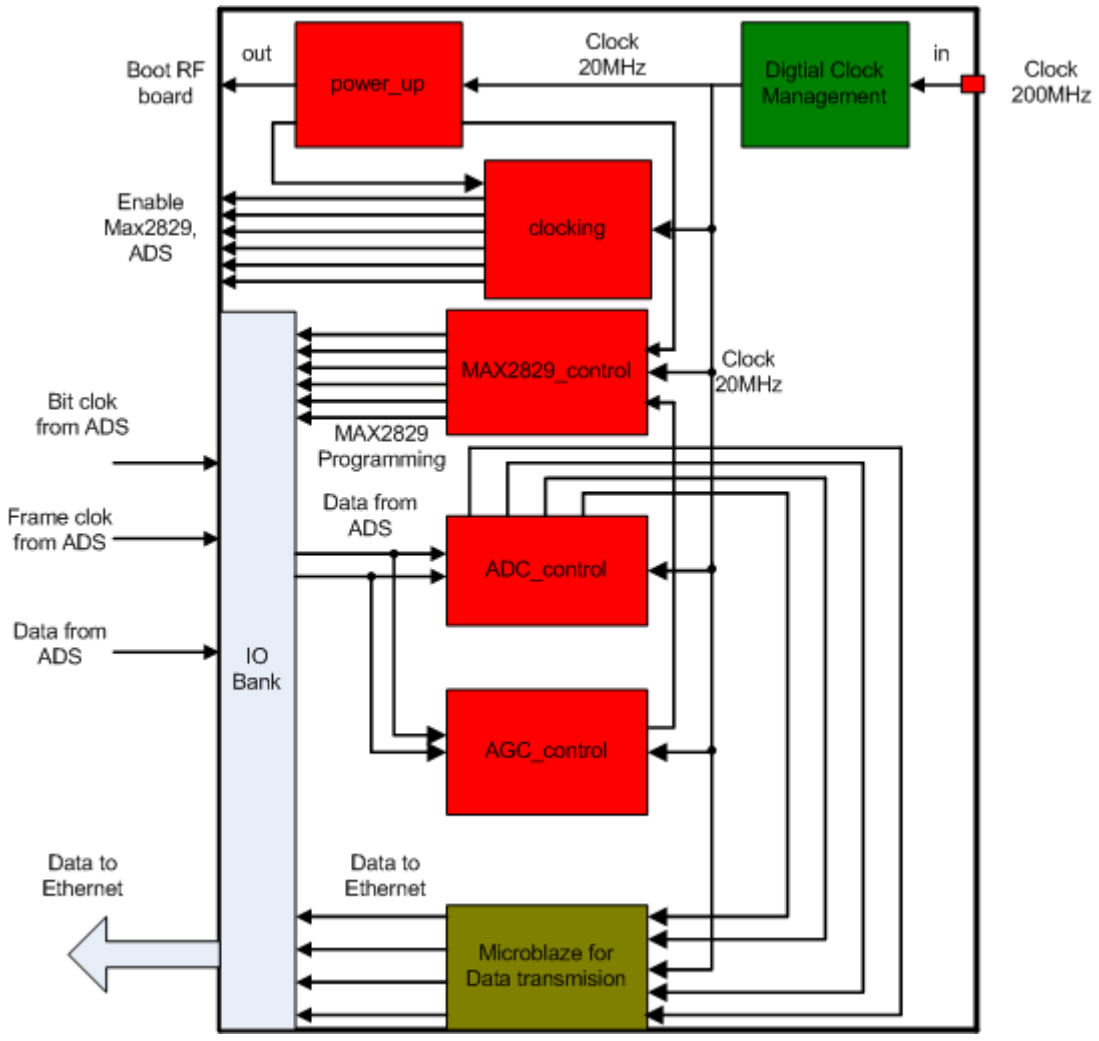

Figure 5.6: Implemented modules in FPGA

The “power_up” module has the input clock signal, which is with 20MHz. “power_up” module is responsible to boot the RF board and control the “clocking” and “MAX2829_control” modules. The “clocking” module is responsible to enable the four MAX2829 chips and the two ADS chips. The “MAX2829_control” is responsible to program the MAX2829 chips, adjust the power gain and the mixer frequency. “AGC_control” is used to determine the power gain according to the captured signals. “ADC_control” is used to convert the serial data from two ADS to

the parallel data and deliver them to the Microblaze. Finally, Microblaze delivers the data to the server by Ethernet.

6 Summary and Outlook

Within the framework of this thesis UWB localization and WLAN localization in the multipath environments were investigated in terms of design of the novel algorithms, error analysis, hardware and software implementation, etc. ToA based UWB localization can provide the best localization performance. In the multipath environments, the localization accuracy depends heavily on the detected leading edge. The presented dissertation introduced the novel leading edge detection approaches: JLED, IMLCE and SbA, which have shown the good performance in the multipath environment. For each algorithm, the estimation errors were analyzed and the estimation error probabilities were given. The RSS based localization as the additional localization strategy cannot provide good quality in general. However, RSS based localization requires no time synchronization between each stations. In this dissertation, the RSS based fingerprint approaches were presented and SSLS model was proposed. The simulation results showed that SSLS model can provide better performance as the LS model. In addition, the channel energy based distance estimator was investigated in this dissertation. SVDE and EVDE were investigated to estimate the noise power at the receiver. The simulation results showed that the EVDE can provide much better estimation performance than SVDE in the low SNR environment.

The AoA based WLAN localization was investigated in this dissertation. In comparison with UWB localization, WLAN localization cannot achieve better accuracy. However, WLAN localization has some advantages: standard device, larger coverage, etc. To get the most accurate localization results, antenna parameters were optimized through mathematical deduction. The calibration for phase offset was described. To overcome the problem caused by the multipath effect, the novel AoA estimator and the channel estimator were investigated. The measurements showed that the RMSE of AoA based WLAN localization can achieve approximate 80cm for the case with two stations and 40cm for the case with four stations.

Finally, the aforementioned RSS based fingerprint algorithms and the AoA based localization algorithms were implemented in the UWB demonstrator and WLAN demonstrator, respectively.

In this dissertation, all discussed issues are based on the single user mode. Hence, the author hopes that the future work can focus on the multiuser localization and the location based data communication. The FPGA implementation of the AoA estimation algorithms shall be another future work.

Abbreviations

ADC	Analog Digital Converter
AGC	Automatic Gain Control
AoA	Angle of Arrival
AP	Access Point
AWGN	Additive White Gaussian Noise
CACM	Channel Auto Correlation Matrix
CCF	Cross Correlation Function
CDF	Cumulative Distribution Function
CEE	Channel Energy Estimation
CFO	Carrier Frequency Offset
CIR	Channel Impulse Response
CP	Cyclix Prefix
CRLB	Cramer Rao Lower Bound
CSMA	Carrier Senses Multiple Access
CTS	Clear to Send
DA	Data Aided
DHCP	Dynamic Host Configuration Protocol
DP	Direct Path
DS-CDMA	Direct-Sequence Code Division Multiple Access
ED	Euclidean Distance
ESPRIT	Estimation of Signal Parameters via Rotational Invariance Techniques
EVD	Eigen Value Decomposition
FD	Frequency Domain
FPGA	Field Programmable Gate Array
GLRT	Generalized Likelihood Ratio Test
GMDL	Gaussian Minimum Description Length
GPS	Global Position System
GS	Grid Search
GUI	Graphic User Interface
ICI	Inter Carrier Interference
IMLCE	Improved Maximum Likelihood Channel Estimation
IPI	Inter Pulse Interference
IR	Impulse Radio
ISI	ISI Inter Symbol Interference
JLED	JLED Joint Leading Edge Detection
LBS	LBS Location Based Services
LDR	Low Data Rate
LEC	Leading Edge Combination
LO	Local Oscillator
LS	Least Squares
LT	Location Tracking
MA	Minimum Area
MAC	Media Access Control
MBW	Main Beam Width
MDL	Minimum Description Length

MED	Maximum Excess Delay
MEKF	Modified Extended Kalman Filter
MELER	Maximum Energy to Leading Energy Ratio
MF	Matched Filter
MLE	Maximum Likelihood Estimation
MMSE	Minimum Mean Squared Error
MPC	Multi Path Components
MPDU	MAC layer Protocol Data Unit
MRPF	Modified Regularized Particle Filter
MSR	Main lobe to Side lobe Ratio
MUA	Multi User Access
MUI	Multi User Interface
MUSIC	Multi Signal Classification
MVDR	Minimum Variance Distortionless Respones
NDA	Non Data Aided
NLOS	Non line of Sight
OFDM	Orthogonal Frequency Division Multiplexing
OSR	Oversampling Rate
PDA	Personal Digital Assistant
PDF	Probability Density Function
PLD	Peak to Leading Edge Delay
PLL	Phase Locked Loop
PN	Pseudo Noise
PRP	Pulse Repetition Period
PSD	Power Spectral Density
QoS	Quality of Service
RD	Range Doppler
RFID	Radio Frequency IDentification
RMSE	Root Mean Squared Error
RMUSIC	Root Music, Root Multiple Signal Classification
RSS	Received Signal Strength
RSSID	Received Signal Strength Indicator Difference
RTLS	Real Time Location System
RTS	Request to Send
SAGE	Space Alternating Generalized Expectation Maximization
SbA	Subspace based Approaches
SBA	Search Back Algorithms
SIR	Signal to Interference Ratio
SNR	Signal-to-Noise-Ratio
SPS	Standard Positioning Service
SSLS	Sub-Sampling Least Squares
SVDA	Singular Value Decomposition Approach
TDoA	Time Difference of Arrival
TFC	Time-Frequency Codes
THMA	Time Hopping Multiple Access
TH-PAM	Time Hopping - Pulse Amplitude Modulation
ToA	Time of Arrival
ToF	Time of Flight
ULA	Uniform Linear Array
UWB	Ultra Wide Band

WLAN	Wireless Local Area Network
WLSE	Weighted Least Squares Estimation
WSN	Wireless Sensor Network

List of Figures

References

[1] N. Alsindi, "Indoor Cooperative Localization for Ultra Wideband Wireless Sensor Networks", Ph.D. dissertation, Worcester polytechnic institute, 2008

[2] Harry L. Van Trees: *Optimum Array Processing*, John Wiley & Sons, January 2002.

[3] I. Oppermann, M. Hamalainen, J. Iinati: *UWB Theory and Applications*, John Wiley & Sons, 2004.

[4] Z. Sahinoglu, S. Gezici, I. Guvenc: *Ultra-wideband Positioning Systems*, Cambridge University Press, 2008.

[5] G. L. Turin: An Introduction to matched filters. *IRE Transactions on Information Theory*, IT-6: 3, pp. 311 – 329, June 1960.

[6] K. Siwiak and J. Gabig, *IEEE 802.15.4IGa informal call for application response, contribution#11, Doc.: IEEE 802.15-04/266r0, July 2003. [Online]*.

[7] S. Gezici and H. Poor, "Position estimation via ultra-wide-band signals", *Proceedings of the IEEE*, vol. 97, pp.386-403, February 2009.

[8] S. Gezici et all., "Localization via ultra-wideband radios: A look at positioning aspects for future sensor networks", *IEEE Signal Processing Magazine*, vol.22, pp.70-84, July 2005.

[9] F. Elbahhar, B. Fall, M. Heddebaut, A. Rivenq, J. M. Rouvaen, "Indoor positioning system based on the UWB technique", *2011 International Conference on Indoor Positioning and Indoor Navigation (IPIN)*, 21-23 September 2011, Guimaraes, Portugal.

[10] C. Botteron et all., "Cramer-Rao bound for location estimation of a mobile in asynchronous DS-CDMA systems", *IEEE International Conference on Acoustic, Speech and Signal Processing (ICASSP2001)*, vol.4, pp. 2221-2224, Salt Lake City, May 2001.

[11] G. Zhenghui and E. Gunawan, "Cramer-Rao bound for joint direction of arrival, time delay estimation in DS-CDMA systems", *IEEE Milit. Comm. Conf. Proceed.*, vol.2, pp.614-618, Oct. 2000.

[12] N. Liu, Z. Xu, B. M. Sadler, "Geolocation Performance with Biased Range Measurements", *IEEE Transactions on Signal Processing*, vol. 60, no.5, May 2012.

[13] G. Xu: *GPS Theory, Algorithms and Applications*, Springer, 2007.

[14] E.D. Kaplan, *Understanding GPS: Principles and Applications*, Artech House, Norwood, MA, 1996.

[15] S. M. Kay, *Fundamentals of Statistical Signal Processing: Estimation Theory*, Prentice Hall, Upper Saddle River, New Jersey, 1993.

[16] R. Negenborn, “Robot Localization and Kalman Filters”, MS.c Thesis, Utrecht University, 2003

[17] Yu, Chen, J. Juang, “Outlier-Detection-Based Indoor Localization System for Wireless Sensor Networks”, *International Journal of Navigation and Observation*, vol. 2012.

[18] O. Manu, “A Study of Indoor Localization Techniques”, *DOCT-US Journal*, vol 1, No 2, 2009.

[19] K. Muthukrishnan, G. Koprinkov, N. Meratnia, M. Lijding, “Using time-of-flight for WLAN localization: feasibility study”, *Centre for Telematics and Information Technology (CTIT) technical report*, TR-CTIT-06-28, June 2006, ISSN 1381-3625, 10 pages.

[20] L. E. Miller et all., “RFID-Assisted Indoor Localization and Communication for First Responders”, *First European Conference on Antennas and Propagation*, pp. 1-6, August 2008.

[21] K. Finkenzeller: *RFID Handbook*, Wiley, 2003.

[22] Wireless Medium Access Control (MAC) and Physical Layer (PHY) Specifications for Low-Rate Wireless Personal Area Networks (WPANs). IEEE Standard. 802.15.4a-2007.

[23] K. Pahlavan, P. Krishnamurthy and J. Beneat, “Wideband radio propagation modeling for indoor geolocation applications”, *IEEE Communications Magazine*, vol. 36, no.4,pp.60-65, April, 1998.

[24] K. Pahlavan, X. Li and J. Makela, “Indoor geolocation science and technology”, IEEE Communications Magazine, vol. 40, no.2, pp. 112-118, Feb. 2002.

[25] R. J. Vaccaro, C. S. Ramalingam, D. W. Tufts and R. L. Field, “Least-squares time-delay estimation for transient signals in a multipath environment”, 1*991 Conference Record of the Twenty-Fifth Asilomar Conference on Signals, Systems and Computers*, vol.2, pp. 1098-1102, 4-6 November 1991.

[26] T. G. Manickam, R. J. Vaccaro and D. W. Tufts, “A least-squares algorithm for multipath time-delay estimation”. *IEEE Transactions on Signal Processing*. vol. 42. No.11. November 1994.

[27] H. Saarnisaari, “ML time delay estimation in a multipath channel”. *In Proceeding IEEE Int. Symp. Spread Spectrum Techniques and Applications*, Mainz, Germany, Sep. 1996, pp. 1007-1011.

[28] A. P. Dempster, N. Laird, and D. B. Rubin, “Maximum Likelihood from incomplete data via the EM algorithm”, *Journal of the Royal Statistical Society*, B39;1-38, 1977

[29] B. Fleury, M. Tschudin, R. Heddergott, D. Dahlhaus, and K. Ingenman Pedersen, “Channel parameter estimation in mobile radio environments using the SAGE

algorithm ", *Selected Areas in Communications* , IEEE Journal on, vol. 17, no. 3, pp. 434-450, Mar 1999.

[30] M. Feder and E. Weinstein, "Parameter estimation of superimposed signals using the EM algorithm", *IEEE Transaction on acoustics speech and signal processing*, vol .36, pp. 477-489, April 1988.

[31] L. Reggiani and G. M. Maggio, "Rapid search algorithms for code acquisition in UWB impulse radio communications", *IEEE Journal on selected areas in communications*, vol. 23, No.5, May, 2005.

[32] Z. Tian and V. Lottici, "Efficient timing acquisition in dense multipath for UWB communications", *In Proceeding IEEE Vehicle Technology Conference*, vol.2, pp. 1318-1322. Orlando, FL, October 2003.

[33] C. Falsi, D. Dardari, L. Mucchi and M. Z. Win, "Time of Arrival Estimation for UWB Localizers in Realistic Environments", *EURASIP Journal on Applied Signal Processing*, 2006, pp. 1-13.

[34] E. R. Jativa and J. Vidal, "First arrival detection for positioning in mobile channels", in *Proceedings of 13th IEEE International Symposium on Personal, Indoor and Mobile Radio Communications (PIMRC'02)*, vol. 4, pp. 1540-1544, Lisbon, Portugal, September 2002.

[35] Z. Tian and L. Wu, "Timing acquisition with noisy template for ultra-wideband communications in dense multipath". *EURASIP Journal on Applied Signal Processing*, 2005, pp. 439-454.

[36] Z. Tian and G. B. Giannakis, "A GLRT approach to data-aided timing acquisition in UWB radios-Part I: Algorithms", *IEEE Transactions on Wireless Communications*, vol. 4, pp. 2956-2967. No.6, November 2005.

[37] Z. Tian and G. B. Giannakis, "A GLRT approach to data-aided timing acquisition in UWB radios-Part II: Training sequence design", *IEEE Transactions on Wireless Communications*, vol. 4, pp. 2994-3004, 2005.

[38] L. Yang and G. B Giannakis, "Blind UWB timing with dirty templates". *In Proc. IEEE Conf. On Acoust., Speech, Sig. Processing (ICASSP)*, vol. 4, Quebec, Canada, May 2004, pp. 509-512.

[39] J, Yu and Y. Yao, "Detection performance of time-hopping ultra-wideband LPI waveforms". *In Proc. IEEE Sarnoff Symp.*, Princeton, NJ, April 2005, pp. 147-140.

[40] A. Rabbachin and I. Oppermann, "Synchronization analysis for UWB systems with a low-complexity energy collection receiver". In *proc. IEEE Ultra-wideband Syst. Technol. (UWBST)*, Kyoto, Japan, May 2004, pp.288-292.

[41] J. Foerster and Q. Li, "UWB channel modeling contribution from Intel", *IEEE P802.15 Wireless Personal Area Networks*, IEEE P802.15-02/279r0-SG3a, June 2002.

[42] F. Coppens, “First arrival picking on common-offset trace collections for automatic estimation of static corrections”, *Geophysical. Prospecting*, vol.33, pp.1212-1231, December 1985.

[43] Y. Xie, Y. Wang, P. Zhu, X. You, “Grid-search-based hybrid ToA/AoA location techniques for NLoS environments”, *IEEE Communication Letters*, vol. 13, pp. 254-256, April, 2009.

[44] R. Fontana, A. Ameti, E. Richley, L. Beard, D. Guy, “Recent Advances in Ultra Wideband Communications Systems”, in *Proceedings IEEE Conference on Ultra Wideband Systems and Technologies*, May 2002.

[45] B. Denis, L. Ouvry, B. Uguen, F. Tchoffo-Talom, “Advanced Bayesian Filtering Techniques for UWB Tracking Systems in Indoor Environments”, *IEEE International Conference on Ultra-Wideband*, 2005.

[46] J. Ni, D. Arndt, P. Ngo, C. Phan, J. Gross, “UWB Tracking System Design for Free-Flyers”, *IEEE/ACES International Conference on Wireless Communications and Applied Computational Electromagnetics*, 2005.

[47] E. Dickerson, D. Arndt, J. Ni, “UWB Tracking System Design with TDoA Algorithm for Space Applications”, *ISSO Y2005 Annual Report*, 2005.

[48] Y. He, F. L. Chevalier, A. G. Yarovoy, “Range-Doppler Processing for Indoor Human Tracking by Multistatic Ultra-wideband Radar”, *13th International Radar Symposium (IRS)*, pp. 250-253, 23-25 May 2012.

[49] M. S. Arulampalam, S. Maskell, N. Gordon, T. Clapp, “A tutorial on particle filters for online nonlinear/non-Gaussian Bayesian tracking”, *IEEE Transactions on Signal Processing*, vol. 50, pp. 174 – 188, February 2002.

[50] Y. Bar-Shalom, T. E. Fortmann, “Tracking and Data Association”, *Academic Press, Inc., 1988.*

[51] N. Gvozdenovic, M. Eric, “Localization of users in multiuser MB OFDM UWB systems based on TDoA principle”, *Telecommunications forum(TELFOR)*, Nov. 2011

[52] A. E. Waadt, S. Wang, C. Kocks, A. Burnic, D. Xu, G. H. Bruck, „Positioning in multiband OFDM UWB utilizing received signal strength“, in *Proc. 7th Workshop positioning Navigation and Communication (WPNC)*, 2010, pp. 308-312.

[53] S. Wang, A. Waadt et al. “System implementation study on RSSI based positioning in UWB networks”, *7th International Symposium on Wireless Communication Systems (ISWCS)*, pp. 36-40, 19-22 September 2010.

[54] C. Steiner, “Location Fingerprinting for Ultra-Wideband Systems”, Ph.D. dissertation, Graz University of Technology, 2010.

[55] K. Kaemarungsi, “Design of Indoor Positioning Systems based on Location Fingerprinting Technique”, Ph.D. dissertation, University of Pittsburgh, 2005.

[56] M. Rehim, “Horus: A WLAN-Based Indoor Location Determination System”, Ph.D. dissertation, University of Maryland, 2004.

[57] Carl Monway Wong, “Investigation of Wireless Local Area Network Facilitated Angle of Arrival Indoor Location”, MS.c thesis, University of British Columbia, 2008.

[58] X. Li, K. Pahlavan, M. Latva-aho, M. Ylianttila, “Comparison of indoor geolocation methods in DSSS and OFDM wireless LAN systems”, *in IEEE VTC’2000*, September 2000.

[59] P. Prasithsangaree, P. Krishnamurthy, P.K. Chrysanthis. “On indoor position location with wireless LANs”, *13th IEEE International Symposium on Personal, Indoor, and Mobile Radio Communications*, 2002.

[60] S. Saha, K. Chaudhuri, D. Sanghi, P. Bhagwat, “Location determination of a mobile device using IEEE 802.11b access point signals”, *Wireless Communications and Networking*, 2003.

[61] P. Uthansakul and M. Uthansakul, “WLAN Positioning Based on Joint ToA and RSS Characteristics”, *World Academy of Science, Engineering and Technology*, 2009.

[62] A. Hatami, “Application of Channel Modeling for Indoor Localization Using ToA and RSS”, Ph.D dissertation, Worcester Polytechnic Institute, May 2006.

[63] A. Tayebi, J. Gomez, F. Saez de Adana, O. Gutierez, “The application of ray-tracing to mobile localization using the direction of arrival and received signal strength in multipath indoor environments”, *Progress In Electromagnetics Research*, 2009.

[64] H. Liu, H. Darabi, P. Banerjee, J. Liu, “Survey of Wireless Indoor Positioning Techniques and Systems”, *IEEE Transactions on Systems, Man, and Cybernetics-Part C: Applications and Reviews*, vol. 37, no.6, November 2007.

[65] S. Wang, A. Waadt, G. H. Bruck, P. Jung, “Quality of Service Parameters Optimization in Multi User Ultra Wideband Systems”, *International Conference on Communications, Computing and Control Applications (CCCA)*, pp.1-6, March, 2011.

[66] A. Ramirez, “Time-of-flight in Wireless Networks as Information Source for positioning”, Dr.-Ing Dissertation, 2011.

[67] Z. Sahinoglu, I. Guvenc, “Multiuser Interference Mitigation in Non-coherent UWB Ranging via Nonlinear Filtering”, *EURASIP Journal on Wireless Communications and Networking*, vol.2006, pp. 67-67, April 2006.

[68] M. Osborne and A. Rubinstein, “A Course in Game Theory”, MIT Press, 1994.

[69] G. Bacci, M. Luise, H. Poor, A. Tulino, "Energy Efficient Power Control in Impulse Radio UWB Wireless Networks", *IEEE Journal of selected topics in Signal Processing*, vol.1, no.3, October 2007.

[70] C. Kocks, E. Scheiber, A. Viessmann, Dong Xu, Shangbo Wang, Guido H. Bruck, Peter Jung, "A Low-Cost Protocol and Application for UWB Localization, Exploiting Cross-Layer Design and Cognitive Radio Aspects", *Second International Workshop on Cognitive Radio and Advanced Spectrum Management*. May 2009.

[71] W. Kim, J. G. Lee and G. I. Jee, "The interior-point method for an optimal treatment of bias in trilateration location", *IEEE Trans. Veh. Tecnol.*, 55: 4, (2006),1291-1301.

[72] Y. Qi, H. Kobayashi and H. Suda, "Analysis of wireless geolocation in a non-line-of-sight environment", *IEEE Trans. Wireless Commun.*, 5:3, (2006),672-681.

[73] J. J. Caffery, *Wireless Location in CDMA Cellular Radio Systems*. (Boston: Kluwer Academic Publishers, 2000).

[74] D. G. Manolakis, V. K. Ingle, S. M. Kogon, *Statistical and Adaptive Signal Processing*, Artech House, 2005.

[75] L. C. Godara, "Application of Antenna Arrays to Mobile Communications, Part II: Beam-Forming and Direct-of-Arrival Consideration", *Proceeding of the IEEE,* vol. 85, pp. 1195-1245, 1997.

[76] N. Kikuma, M. Fujimoto, "Adaptive Antennas". *IEICE Transactions on Communications*, vol. E86-B, pp. 968-979, 2003.

[77] L. C. Godara, *Handbook of Antennas in Wireless Communications*. Boca Raton: CRC Press, 2002.

[78] L. Ljung, *System Identification: Theory for the User*. Englewood Cliffs, NJ: Prentice-Hall, 1987.

[79] Y. Qi, Wireless geolocation in a non-line-of-sight environment. Ph.D Dissertation, Princeton University, December, 2004.

[80] H. V. Poor, *An Introduction to Signal Detection and Estimation*, Springer, 1994.

[81] I. Guvenc, Z. Sahingolu, A. F. Molisch and P. Orlink, "Non-coherent ToA estimation in IR-UWB systems with different signal waveforms". *In Proc. IEEE Int. Workshop on Ultra-wideband Networks (UWBNETs)*, Boston, MA, October 2005, pp. 245-251.

[82] I. Guvenc, Z. Sahinoglu, "Threshold-based TOA estimation for impulse radio UWB systems", In *Proc. IEEE Int. Conf. on Ultra-Wideband (ICUWB)*, 2005.

[83] M. R. Mahfouz, C. Zhang, B. C. Merkl, M. J. Kuhn and A. E. Fathy, "Investigation of High-Accuracy Indoor 3-D Positioning Using UWB

Technology", *IEEE Transactions on Microwave Theory and Techniques*, vol. 56, no. 6, June 2008.

[84] V. Dizdarevic and K. Witrisal, "On impact of topology and cost function on LSE position determination in wireless networks", In *Proc. Workshop on Positioning, Navigation, and Commun. (WPNC)*, Hannover, Germany, March 2006.

[85] M. J. Kuhn, J. Turnmire, M. R. Mahfouz and A. E. Fathy, "Adaptive Leading-Edge Detection in UWB Indoor Localization", *IEEE Radio and Wireless Symposium (RWS)*, pp. 268 – 271, 10 -14 January 2010.

[86] M. J. Kuhn, C. Zhang, S. Lin, M. R. Mahfouz and A. E. Fathy, "A System Level Design Approach to UWB Localization", *IEEE MTT-S International Microwave Symposium Digest*, pp. 1409-1412, Boston, MA, 7-12 June 2009.

[87] J. Riba and A. Urruela, "A non-line-of-sight mitigation technique based on ML-detection". In *Proc. IEEE Int. Conf. Acoust, Speech, and Sig. Processing (ICASSP)*, vol.2, Quebec, Canada, May 2004.

[88] R. Yao, W. Zhu and Z. Chen, "UWB multipath channel model based on time-domain UTD technique". In *Proc. IEEE Global Communication Conference*, vol. 3, San Francisco, CA, Dec 2003, pp. 1205-1210.

[89] R. Yao, W. Zhu and Z. Chen, "An efficient time-domain ray model for UWB indoor multipath propagation channel". In *Proc. IEEE Veh. Technol. Conf. (VTC)*, vol. 2, Orlando, FL, September 2003, pp. 1293-1297.

[90] A. Saleh and R. Valenzuela, "A statistical model for indoor multipath propagation", *IEEE Journal on Select. Areas Commun.*, vo. SAC-5, no.2, pp. 128-137, Feb. 1987.

[91] A. F. Molisch, K. Balakrishnan, C. C. Chong, et al., IEEE 802.15.4a channel model – final report. September 2004. Available: http://www.ieee802.org/15/pub/TG4a.html.

[92] M. Z. Win, R. A. Scholtz and L. W. Fullerton, "Time-Hopping SSMA Techniques for Impulse Radio with an Analog Modulated Data Subcarrier", *Proc. IEEE Int. Sym. on Spread Spectrum Techniques and Applications*, Sept. 1996, vol. 1, pp. 359-364.

[93] Ecma International: High Rate Ultra Wideband PHY and MAC Standard, Standard ECMA-368, 3rd Edition, December 2008.

[94] M. D. Zoltowski, G. M. Kautz and S. D. Silverstein, "Beamspace Root MUSIC", *IEEE Transactions on Signal Processing*. vol 41. No. 1, January, 1993.

[95] E. Fishler, H. V. Poor, "Estimation of the Number of Sources in Unbalanced Arrays via Information Theoretic Criteria", *IEEE Transactions on Signal Processing, vol. 53, pp. 3543-3553*, September 2005.

[96] J. G. F. Francis, "The QR Transformation: A Unitary Analogue to the LR Transformations-Part 1", The computer Journal, vol. 4(3), S. 265-271, doi:10.1093/comjnl/4.3.265.

[97] J. G. F. Francis, "The QR Transformation: A Unitary Analogue to the LR Transformation – Part 2", The Computer Journal, vol. 4, pp.332-345, 1962.

[98] Z. Xu, "Perturbation Analysis for Subspace Decomposition with Applications in Subspace-based Algorithms", IEEE Transactions on Signal Processing, vol. 50, no.11, November 2002.

[99] X. Ma, C. TepedTelenlioglu, G. B. Giannakis, S. Barbarossa, "Non-Data-Aided Carrier Offset Estimators for OFDM with Null Subcarriers: Identifiability, Algorithms, and Performance", *IEEE Journal on Selected Areas in Communications*, vol. 19, No. 12, December 2001.

[100] Q. Cheng, "Choice of Root in Root-MUSIC for OFDM Carrier Frequency Offset Estimation", *Asia-Pacific Conference on Communications*, Perth, Western Australia, 3-5 October 2005.

[101] D. Huang, K. B. Letaief, "Carrier Frequency Offset Estimation for OFDM Systems Using Null Subcarriers", *IEEE Transactions on Communications*, vol.54, no.5, May 2006.

[102] S. Li, G. Zhao and L. Liao, "User location service over an 802.11 ad-hoc network", Retrieved from http://www.cs.washingon.edu/homes/liaolin/Courses/netwoks02.pdf.

[103] C. M. Wong, G. G. Messier, "Evaluating Measurement-based AoA Indoor Location using WLAN Infrastructure", *Proceedings of the 20th International Technical Meeting of the Satellite Division of The Institute of Navigation (ION GNSS 2007)*, Fort Worth, TX, September 2007, pp. 1139 – 1145.

[104] Y. Xie, Y. Wang, P. Zhu and X. You, "Grid-Search-Based Hybrid ToA/AoA Location Techniques for NLOS Environments", *IEEE Communications Letters*, vol. 13, no.4, April 2009.

[105] Z. Yan, Y. Chang, Z. Shen and Y. Zhang, "A Grid-Scan Localization Algorithm for Wireless Sensor Network", *WRI International Conference on Communications and Mobile Computing*, vol. 2, 6-8 January 2009.

[106] M. Wallbaum. Wheremops, "An indoor geolocation system", *The 13th IEEE International Symposium on Personal, Indoor and Mobile Radio Communications*, vol. 4, pp. 1967-1971, 15-18 September 2002.

[107] P. Bahl and V. N. Padmanabhan, "RADAR: An in-building RF-based user location and tracking system", *IEEE INFOCOM 2000*, vol.2 pp. 775-784, 2000.

[108] P. Prasithsangaree, P. Krishnamurthy and P. K. Chrysanthis, "On indoor position location with wireless LANs", *The 13th IEEE International Symposium*

on Personal, Indoor and Mobile Radio Communications, vol. 2, pp.720-724, 15-18 September 2002.

[109] Ubisense website. [Online]. Available: http://www.ubisense.net

[110] Zebra Technologies website. [Online]. Available: http://www.zebra.com

[111] Aetherwire website. [Online]. Available: http://www.aetherwire.com